THÈSE

présentée par:

Weiwei SHU

soutenue le:
28 Mars 2024

pour obtenir le grade de:
Docteur de l'Université de Strasbourg

Discipline : **Sciences de la Terre et de l'Univers**
Spécialité : **Géophysique**

Analogical modelling of frictional slip on faults: implications for induced and triggered seismicity

THÈSE DIRIGEE PAR :
  M. SCHMITTBUHL Jean   Directeur de recherche CNRS, Université de Strasbourg
  M. LENGLINE Olivier   Maître de conférences, Université de Strasbourg

RAPPORTEURS :
  M. AMPUERO Jean-Paul   Directeur de recherche IRD, Université Côte d'Azur
  M. DUBLANCHET Pierre   Enseignant-chercheur, MINES ParisTech - PSL

AUTRES MEMBRES DU JURY :
  M. PASSELÈGUE François   Chargé de recherche CNRS, Université Côte d'Azur
  Mme. LASSERRE Cécile   Directrice de recherche CNRS, Université Claude Bernard Lyon 1

PRESIDENT DU JURY :
  M. HEAP Michael   Professeur, Université de Strasbourg

The dissertation of Weiwei Shu is approved:

_____

_____

_____

_____

_____

_____

Université de Strasbourg

2024

ACKNOWLEDGEMENTS

The journey of my PhD would not end with this dissertation without the help of many individuals.

I would like to sincerely thank my two advisors Jean Schmittbuhl and Olivier Lengliné for deciding to host me during the Covid pandemic, which allows me to pursue my PhD at Institut Terre & Environnement de Strasbourg. They are both kind, warm, and passionate about science. I enjoyed the sufficient freedom they provided, which made me think about my PhD project by myself and then develop an instinctual desire to explore science. They are not employing me to implement a project, but training me to become a researcher who can think about my interests independently. They also provided me so many opportunities for academic conferences, even during the Covid pandemic. I appreciate their efficient financial support for my experiments, as good experimental studies cannot be performed without sufficient support from the relevant facilities. Jean always brings me the experimental facilities that I need as soon as he can, such as the LED light, image scanner, acoustic sensors, etc. He is strict and responsible for my work. His comments always inspire me to learn how to rigorously describe my work with text that can be easily understood. I also appreciate Olivier for his patience in our casual daily meeting. Olivier has answered so many questions from me, and I guess some of them must be too simple and basic. But, he always explains with great patience to diminish my doubts. I remember that, at the beginning of my PhD, Olivier gave a lecture for me alone to explain the friction and derive the rate and state frictional law. He also helped a lot with coding during the early stage of my PhD. I cannot imagine how long would take to obtain some results without his generous help.

I would like to thank the monitoring committee members of my PhD: Hugo Perfettini, Michael J. Heap, and Paul A. Selvadurai. Hugo joined my first PhD monitoring meeting in 2022. He told me to learn to be an independent researcher and encouraged me to stay in academia. It is a huge pity that I have no chance anymore to collaborate with him on my numerical modeling work. Mike joined all the two monitoring meetings. He is always efficient in handling the administrative

procedures required by the doctoral school. His comments inspire me to think about how to give a clear and attractive presentation. I also shared the same laboratory with him during my first and a half years. He is so generous in sharing useful experimental tools with me. A special thanks needs to be given to Paul. Although I met him for the first time at EGU in 2023, his paper published in *Journal of Geophysical Research: Solid Earth* in 2015 is the first paper I read in detail since the start of my PhD. Paul is very interested in my work, and I received many comments and perspectives from him. Paul was invited to join my last monitoring meeting as a committee member in 2023. I am grateful that, after the meeting, he sent me some pressure-sensitive films to measure the normal stress and real contact of our analog fault interface and helped a lot with the data calibration and analysis.

I wish to thank Alain Steyer for the technical support of my experiments. I also would like to thank those colleagues in Strasbourg who overlap some time with me. The days during the week are always colorful because of the existence of every one of you.

I also wish to thank those people who I met and discussed with in the academic conferences, which include the 2021 Cargèse summer school, the 2022 joint summer school organized by EPFL and ETH, the 2023 ENS seminar, the 2023 workshop on mechanics of the earthquake cycle in ICTP, the EGU meetings from 2021 to 2023, and the 2023 AGU meeting. I would like to highlight my thanks to Harsha S. Bhat, who invited me to give a one-hour seminar at Laboratoire de Géologie in ENS after reading my preprint. Harsha not only discussed his research with me but also shared his suggestions for helping my early career.

I would like to thank my friends in China, Europe, and America. Without your accompany, I wouldn't be able to live a happy life during my PhD.

I wish to thank my PhD defense jury, although I still don't know who you are when I am writing this acknowledgment. I thank you in advance for reading my dissertation and discussing it with me.

Finally, I would like to dedicate this dissertation to my beloved parents, who give me infinite love and support. I owe all my achievements to my parents.

TABLE OF CONTENTS

LIST OF FIGURES

xiii

xvii

xxvii

LIST OF TABLES

VITA

2012 - 2016	B.Eng. in Mining Engineering, Central South University, Changsha, China
2016 - 2019	M.Eng. in Mining Engineering, Central South University, Changsha, China
2020 - 2024	Ph.D. in Geophysics, Université de Strasbourg, Strasbourg, France

PUBLICATIONS

Weiwei Shu, Olivier Lengliné, and Jean Schmittbuhl, "Collective Behavior of Asperities Before Large Stick-Slip Events", *Journal of Geophysical Research: Solid Earth*, e2023JB026696, 2023.

ABSTRACT OF THE DISSERTATION

Analogical modelling of frictional slip on faults: implications for induced and triggered seismicity

by

Weiwei Shu

Doctor of Philosophy in Geophysics

Université de Strasbourg, 2024

Faults are common geological discontinuities at different scales distributed at various depths within the Earth's crust, which can slip with diverse behaviors by accommodating the large-scale, far-field, slow tectonic loading: from aseismic creep to seismic slip. Such diverse slip behaviors of a fault are mainly controlled by the frictional stability of the fault interface sandwiched in the middle of the macroscopic fault zone system, in which viscoelastic rheology, particularly for faults at greater depth or within the high-temperature environment (e.g., geothermal reservoirs), might be aroused from the potential circulation of hot fluid in the heavily fractured damage zone. Through topographical measurements of exhumed geological faults, it has been widely recognized that the roughness of a fault interface exists at all scales and creates numerous discrete asperities that establish a complex set of real contacts. These asperities control the initiation and evolution of the fault slip since they offer greater than average resistance to the imposed shear stress. Investigating the intrinsic relationships between the collective behavior of local asperities and the frictional stability of the macroscopic fault enables a better understanding of the mechanical evolution of a fault and the physical process of resulting earthquake sources.

An analog fault model comprising multiple asperities is developed to overcome the difficulty of imaging an exhaustive spatiotemporal variability of a natural fault interface at depth and the limited computational efficiency of the numerical models when heterogeneities span a large time and space domain. Specifically, numerous

identical rigid spherical PMMA (poly-methyl-methacrylate) beads, which are used to model the discrete frictional asperities, are embedded with height variations and random spatial distribution in a soft viscoelastic silicone block to establish numerous micro-contacts with a thick transparent rigid PMMA plate on the top. During the entire shear process of such a heterogeneous fault interface, not only the subtle motion of each local asperity can be directly measured by the high-resolution optical monitoring system, but also the seismic characteristics emitted from dynamic ruptures that occurred at local asperities can be captured by the acoustic monitoring system.

By capturing the temporal evolution of the slip of each asperity, we link the mechanical response of the macroscopic fault with the collective behavior of local asperities. The synchronization of the local slips at all asperities is responsible for the unstable stick-slip of the macroscopic fault. Many destabilizing events at the local asperity scale are observed in the slip-strengthening stage which is conventionally considered as the stable regime of a fault. The slip behavior of asperities during the slip-strengthening stage is evaluated through the interseismic coupling, which can be affected by the nominal normal load, the local topography of the fault interface, and the elastic interactions between asperities through the embedding silicone block. The spatiotemporal interactions of asperities are quantified as slip episodes. Statistical analysis of the catalog of slip episodes reproduces the significant characteristics and scaling laws observed in natural faults, such as the magnitude-frequency distribution, the moment-duration scaling, and Omori's law, demonstrating the effective upscaling of the experimental results. The collective depinning of asperities in this slow-loading system is quantitatively illustrated through the evolution of the elastic energies. An unexpected persistency of a disordering of the asperities through the seismic cycles is evidenced despite the relaxation effect of the large slip events.

Additionally, such a multi-contact fault interface with normal stress variations at asperities and viscoelastic bulk rheology can be modeled numerically based on the modified two-dimensional Burridge-Knopoff model, where the viscoelastic interactions of asperities are quantified from the physical properties of our exper-

imental setup and the friction of each asperity is governed by the rate and state frictional law. The rate and state parameters of a single-asperity interface measured from slide-hold-slide and velocity step experiments are inputted into the numerical model. This physics-based numerical model is efficient in computation, and it allows a complementary understanding of the effects of some fault parameters (e.g., the viscosity of the silicone block, the spatial distribution of asperities, etc.) on the fault slip behavior.

Our results demonstrate that earthquake sequences are phenomenological manifestations of the diverse slip behaviors of a macroscopic fault controlled by the collective behavior of local asperities. The slow slip events clustered from spatiotemporal interactions of asperities are generated in our frictional-viscous experimental setup without the presence of fluid, which supports that the viscoelastic rheology of the complex fault zone could be an effective candidate for explaining the physical mechanism of the slow earthquakes observed worldwide. The slip intermittency of these slow events is also highlighted in our experiments. Such slip intermittency is consistent with the observations that a long-term slow slip event can be decomposed into multiple short-term slow slip events each acting for a limited duration. In addition, the initiation and arrest of the confined slip episodes taking place during the slip-strengthening phase are observed. This slip-strengthening phase with multiple small-size confined ruptures can be seen as the preparatory phase of a giant rupture that occurs in a natural fault. Besides, we evidence that the interseismic coupling on the analog interface is similar to that observed along subduction zones, where the coupling evolves with the normal stress and the topographical variation. All the reproduced magnitude-frequency distributions follow a typical Gutenberg-Richter distribution where events with multiple sizes are observed. Our moment-duration scaling indicates a best-resolved trend close to $M_0 \propto T$ that is in agreement with the observations of slow earthquakes using catalogs from multiple subduction zones. Similar temporal decay of our slow events is also evidenced when analyzing low-frequency earthquakes (LFEs) that occurred in several natural faults, as LFEs are mainly accounted for as the small shear ruptures confined on localized asperities.

Future work will focus on the relationships between the other features of such a group of asperities (e.g., asperities with varying sizes or different frictional properties on the same interface) and the development of seismicity, as well as the stress transfer and slip triggering among discrete asperities, which aims at better understanding the link of seismicity and the aseismic slip of asperities.

Chapter 1

Introduction

1.1 Stick-Slip of Crustal Faults

Large tectonic earthquakes are commonly felt as sudden violent shaking of the ground caused by the radiation of the seismic waves generated by the earthquake source in the Earth's lithosphere, which can induce tremendous damage to infrastructure and loss of human life (Fontiela et al., 2020). However, seismic radiation is only a small portion of the total energy released during such an earthquake (Aki & Richards, 2002). The energy of an earthquake is accumulated for years through the elastic strain localization acting on a crustal fault due to tectonic loading while being released in seconds through the rapid slip of the fault accompanied by a shear rupture instability (Scholz, 2019). Such a process is explained by the elastic rebound theory (Reid, 1911). During the long period when the fault is locked, the elastic strain slowly accumulates and the shear stress builds up on the fault with no earthquake occurrence. At one point, the accumulated shear stress is large enough to yield the fault, the shear strength of the fault suddenly drops and a rapid slip occurs to release the accumulated energy. This first locking and then slipping process is called stick-slip and has been universally recognized as the physical mechanism of earthquakes (Brace & Byerlee, 1966). The repeated occurrence of earthquakes also defines the seismic cycle over geological times, which mainly divides the temporal evolution of shear stress on the fault into three periods: interseismic, coseismic, and postseismic phases (Scholz, 2019). The interseismic phase

is the long sticking period for energy accumulation, while the rapid slip of the fault takes place during the short coseismic phase, which is followed by the postseismic phase where the stress redistributes around the earthquake source. Another seismic cycle will start with the interseismic phase when the shear stress slowly builds up again on the fault.
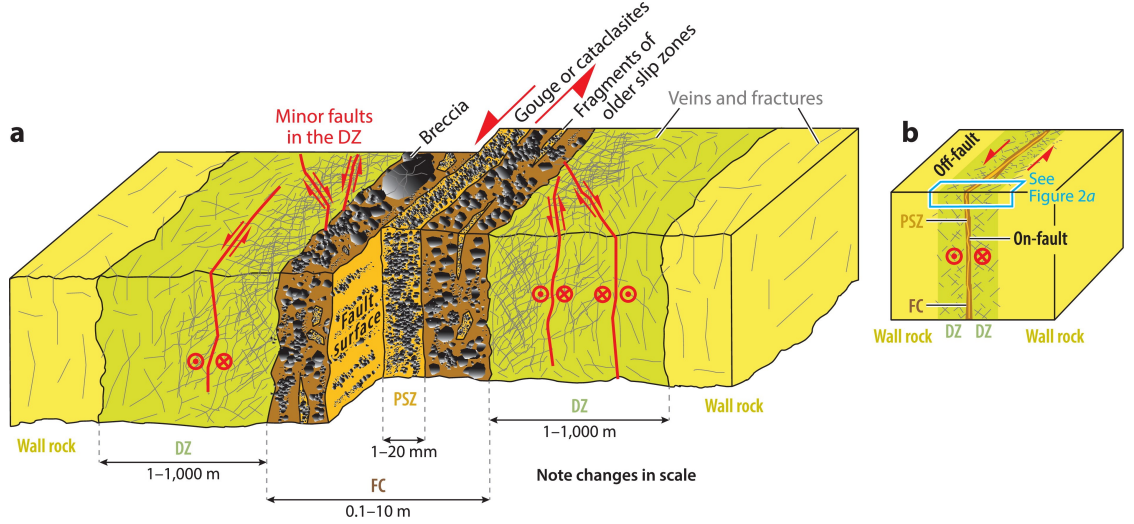
Figure 1.1: Typical geological model of a seismogenic strike-slip fault zone in different views. **a:** An exhaustive view shows that the fault zone structure contains a fault core that includes a thin principle slip zone where the fault slips and is surrounded by the heavily fractured damage zones. With the increase in the distance from the fault core, the number of fractures decreases. The compositions of the fault zone with much fewer fractures are represented by two stiffer wall rocks that host the whole fault. **b:** A global view of the fault zone shows that the sandwiched principal slip zone is extremely thin compared to the whole fault zone. Retrieved from Cocco et al. (2023).

Faults are common geological discontinuities at different scales distributed at various depths within the Earth's crust (Ben-Zion & Sammis, 2003). However, a unified geological model (e.g., Figure 1.1) is commonly used to describe the structure of these faults (Cocco et al., 2023). The structure of a fault zone is, from inward to outward, composed of the principal slip zone, fault core, and damage zone, hosted by two stiff wall rocks with few fractures (Mitchell & Faulkner, 2009;

Stierman, 1984). The principal slip zone is a thin fault surface (of a thickness of several millimeters) where the rapid slip motion of the fault takes place and also where the fault gouges or cataclasites are generated due to the wear effect (Engelder, 1974). The core of the fault, with a thickness of several meters, contains the principal slip zone and accommodates most of the displacement during the fault slip process, which is surrounded by a plastic zone consisting of heavily fractured rock mass with a thickness of several hundreds of meters, that is damage zone (Chester & Chester, 1998; Schulz & Evans, 2000).

Earthquakes are physically the results of the shear rupture instability along the thin principal slip zone embedded in the fault core. Such a thin principal slip zone is usually simplified as a slip plane, which is the fault interface, to study the relationship between earthquake characteristics and the frictional slip behaviors of the fault interface (Barbot, 2019).

1.2   Fault Roughness and Interfacial Contacts

The fault slip plane actually is not perfectly flat although the interface is idealized as a frictional slip plane (Barbot, 2019). The exhumed geological faults provide the opportunity to directly measure the roughness of the fault surface. For example, the roughness of the Corona Heights Fault in California was measured in scales varied by several orders of magnitude and corresponding adaptive resolutions (Candela et al., 2012), as shown in Figure 1.2. From the top to bottom panels of Figure 1.2, the measuring scales are decreased from dozens of meters to several millimeters, while the measuring resolutions are increased thanks to the topographical scanning devices employed with higher and higher resolutions. It is clear to see that this fault surface exhibits a complex topography characterized by height variations at all scales. It is not surprising that the same finding is concluded when similar measurements are performed on other exhumed faults (Candela et al., 2009; Power et al., 1987; Schmittbuhl, Gentier, & Roux, 1993). Moreover, the upscaling of the roughness of exhumed faults measured at laboratory scales allows a numerical model to successfully reconstruct the absolute normal stress fields of
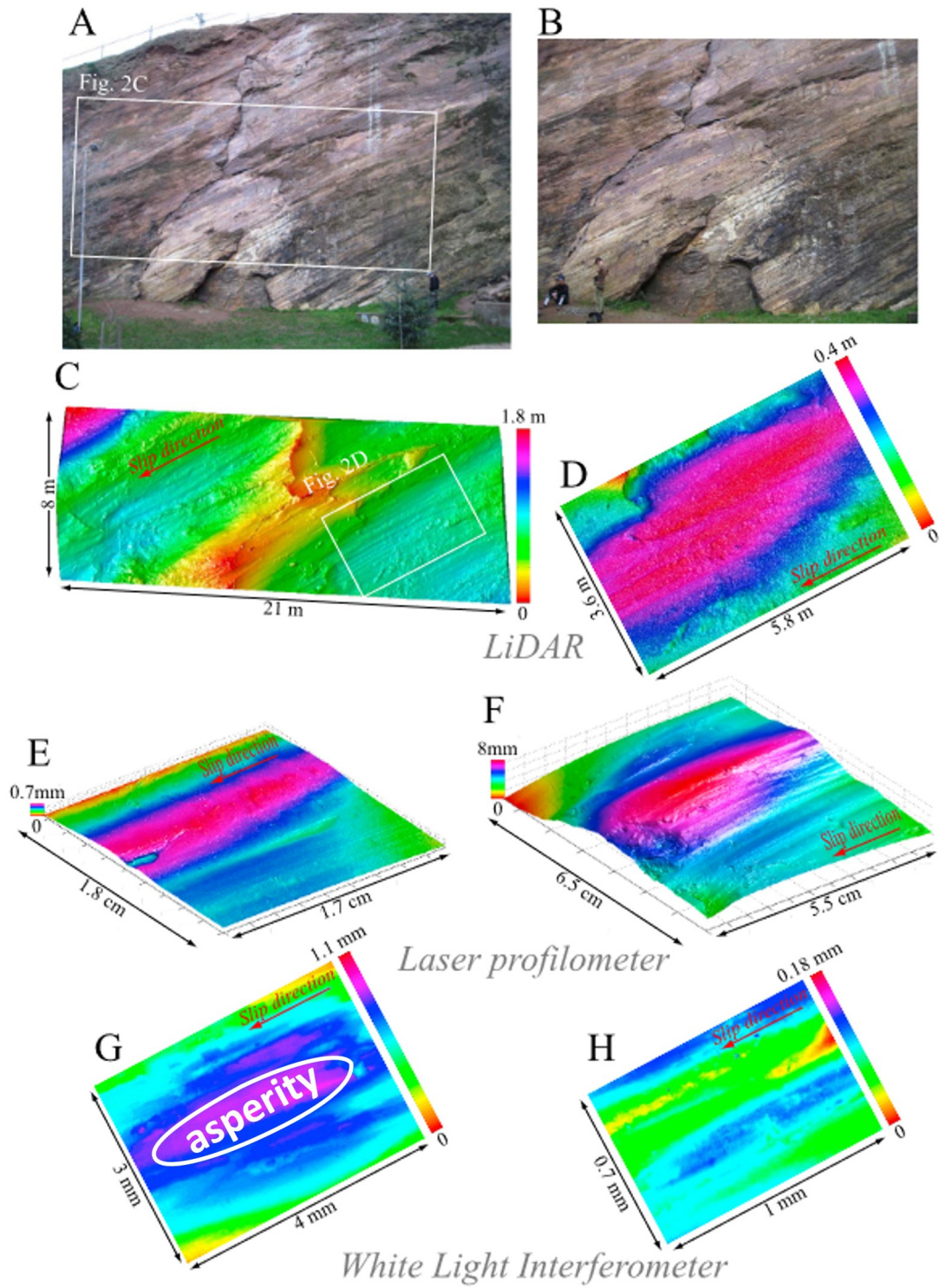
Figure 1.2: Roughness measurement of the exhumed Corona Heights Fault in California with decreasing scales and increasing resolution (from the top to bottom panels), with corresponding measuring devices indicated below each panel. The fault roughness exists at all scales. An elliptical asperity in millimeter-scale can be roughly evidenced in **G**. Modified from Candela et al. (2012).

the Nojima fault before and after the 1995 Kobe earthquake (Schmittbuhl et al., 2006).

Furthermore, the laboratory experiments performed by Dieterich and Kilgore (1994) using the transparent PMMA (poly-methyl-methacrylate) sample, a glassy material analogical to rock, clearly demonstrate the existence of a complex set of microcontacts on the frictional fault interface, which is responsible for establishing the fault roughness (Schmittbuhl et al., 2006) and commonly known as asperities (Bhushan, 1998). Recently, a series of laboratory experiments (Selvadurai & Glaser, 2015a, 2017) have taken advantage of the transparency of the PMMA-PMMA fault interface and the pressure-sensitive film to map the normal stress distribution of a seismogenic fault interface (Figure 1.3). It provides the identification of numerous discrete asperities with a complex and random distribution on this fault interface that serve as the real microcontacts. Since the real contact area is much smaller than the nominal contact area, these asperities sustain greater normal stress than the other parts of the interface and thus act as normal stress concentrators. Meanwhile, their resistance to the imposed shear stress is proved to control the initiation and evolution of the fault slip (Brener et al., 2018; Chen et al., 2020; de Geus et al., 2019; Scholz, 2019). By comparing the top and bottom panels in Figure 1.3, the number of generated asperities and the average normal stress of asperities increase with the normal load, which is also consistent with the prediction of the contact model (K. Johnson, 1987).

Such interfacial contacts of exhumed and analog faults can also be extrapolated to the active seismogenic faults at depth by supposing a similar topographical feature in which numerous discrete asperities sustaining higher normal stress establish the roughness of the fault surface. Indeed, the seismological observations of small repeating earthquakes in the San Andreas Fault (Nadeau & Johnson, 1998; Nadeau & McEvilly, 1999) and in the Japan Trench (Igarashi, 2020; Matsuzawa et al., 2002), as well as in other creeping plate boundary faults (Uchida & Bürgmann, 2019), interpreting them as the periodical failure of small locked patches driven by the constant aseismic creep on the surrounding fault surface, well support the presence of such asperities on the fault interface.
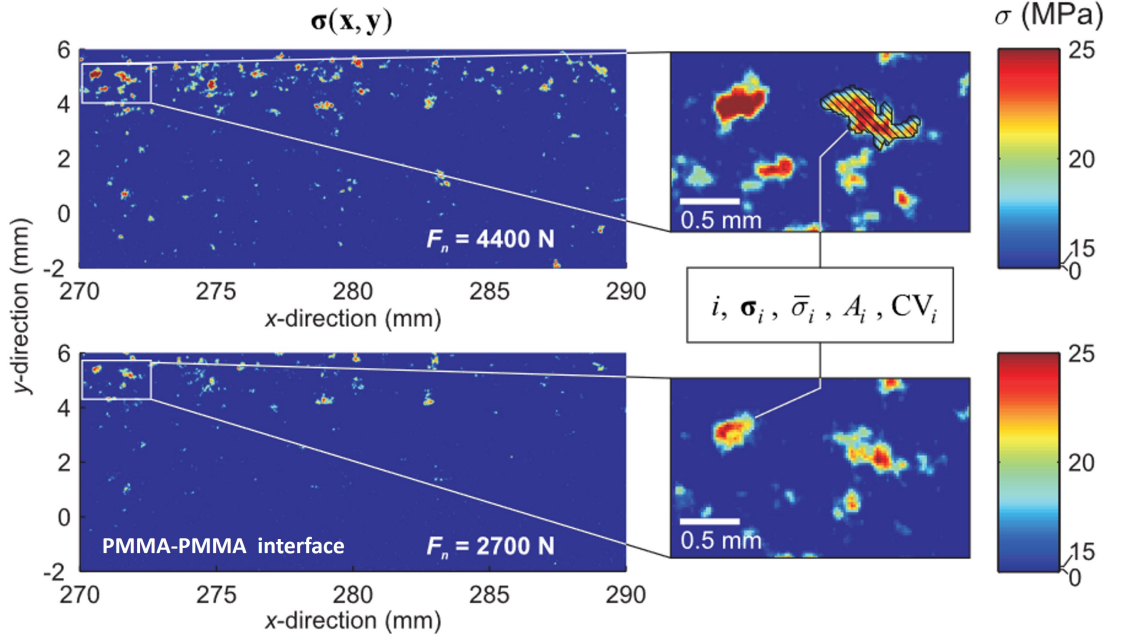
Figure 1.3: Maps of the normal stress distribution (color-coded) of the same segment of a seismogenic analog fault under the normal loads of 4400 N (top) and 2700 N (bottom). Modified from Selvadurai and Glaser (2017).

1.3   Diverse Slip Behaviors of Faults

According to the traditional end-member model of fault slip rate, the slip along the fault is thought to behave either in the fast seismic (unstable) way or in the slow aseismic (stable) way. It has been widely recognized that the seismic slip rates during earthquakes range approximately from 10^{-4} m/s to 1 m/s (Bürgmann, 2018; Sibson, 1986), while the aseismic slip rate during creep is around 10^{-10} m/s (Figure 1.4C) (Rowe & Griffith, 2015). However, with the discovery of a transition zone between the fast seismic slip and the slow aseismic creep, which is composed of slip events with intermediate slip rates of about $10^{-8} - 10^{-6}$ m/s (Dragert et al., 2001), it is suggested that faults actually can slip with various rates in a wide range (Rowe & Griffith, 2015), from fast seismic slip to slow aseismic creep, by accommodating lithosphere deformation (Bürgmann, 2018), thus presenting diverse slip behaviors: fast seismic slip, intermediate slow slip, and slow aseismic creep (Figure 1.4). These slip events with such intermediate slip rates are usually
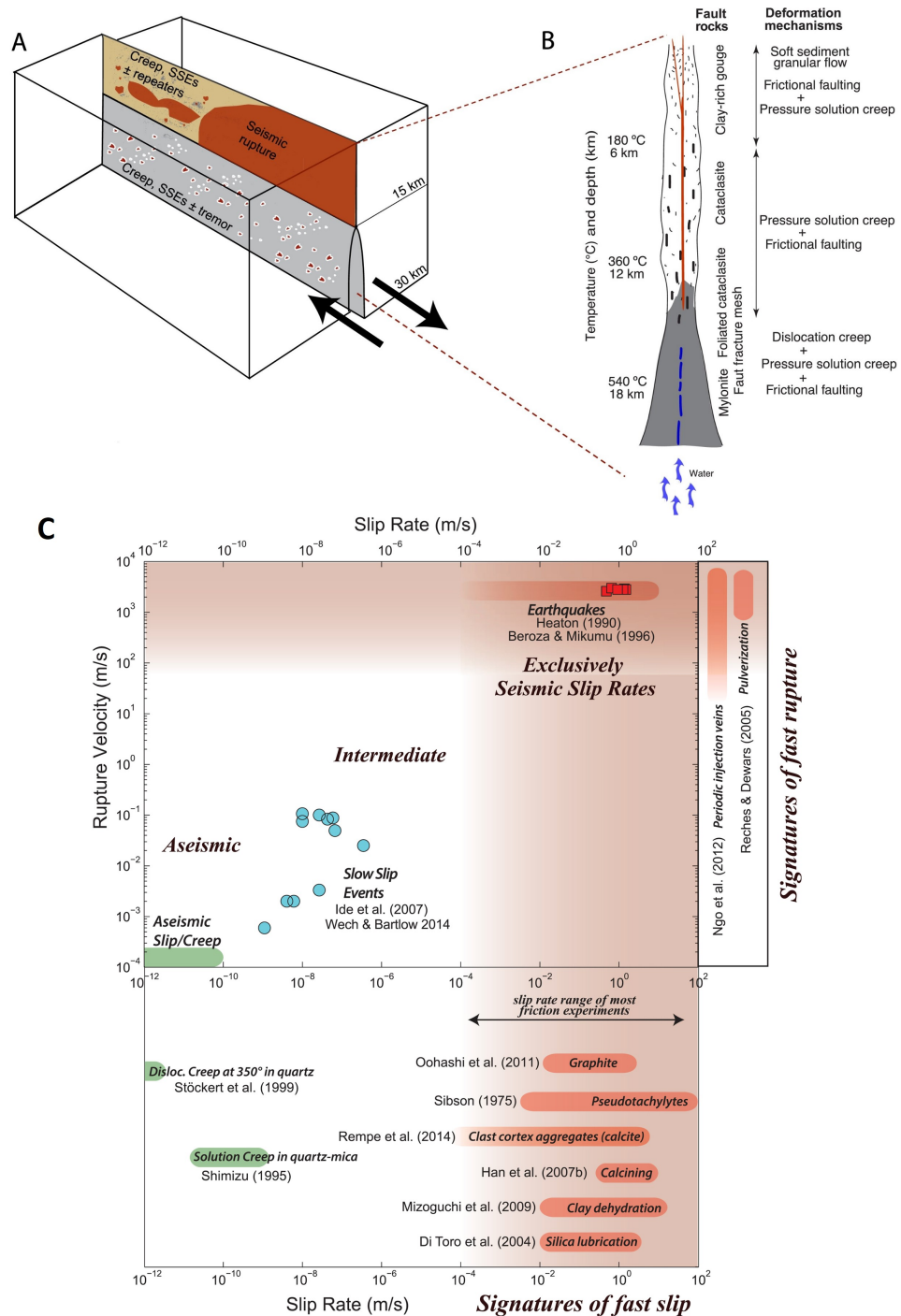
Figure 1.4: Slip behaviors and geological structure of a typical strike-slip fault. **A:** Schematic illustration of the distribution of seismic slip, aseismic creep, repeating earthquakes, SSEs, and tremors on the partially coupled San Andreas Fault near Parkfield. **B:** Conceptual section across strike-slip fault illustrating depth distribution of temperature, fault zone rocks, and deformation mechanisms accommodating different slip behaviors. Modified from Bürgmann (2018). **C:** Slip rates and rupture propagation speeds for different fault slip behaviors. Retrieved from Rowe and Griffith (2015).

called slow slip events (SSEs) (Dragert et al., 2001; Rogers & Dragert, 2003).

The distribution of seismic slip, repeating earthquakes, aseismic creep, SSEs, and tremors is schematically illustrated on the partially coupled San Andreas Fault near Parkfield (Figure 1.4A), while the deformation mechanisms on fault rocks in the conceptual section across the fault structure (Fagereng & Toy, 2011) correspond in Figure 1.4B (Bürgmann, 2018).

It is interesting to note that although SSEs can occur at all depths (Lay & Nishenko, 2022; Nishikawa et al., 2023) within the seismogenic zone of faults and below (Figure 1.4A), the related fault structure can be quite different due to the depth-varying factors of temperature, pore fluid pressure, fault rock, and the rheological deformation mechanisms integrated from all these factors (Fagereng & Beall, 2021). The complex fault structure and low-resolution frictional environment make the generation and physical process of SSEs and related seismologically observed slow earthquakes (will be briefly reviewed in Section 1.2.1) still elusive (Behr & Bürgmann, 2021). Regardless of considering such complexity, a fault capable of hosting SSEs is supposed to be at the transition state of the frictional equilibrium between seismic and aseismic slip (Scholz, 1998), which has also been evidenced on small-scale faults in geothermal reservoirs where high temperature and high pore fluid pressure (low effective normal stress) exist (Cornet, 2016; Wynants-Morel et al., 2020).

1.3.1 Brief Review of Slow Earthquakes

The geophysical signals observed at the fault transition state of the frictional equilibrium between seismic and aseismic slip are classified in the category of slow earthquakes. For convenience, the most commonly known regular earthquakes that generate significant ground shaking are termed "earthquakes" in this dissertation, in contrast to the "slow earthquakes" that gently release the accumulated energy. The mechanism for the occurrence of slow earthquakes remains largely a mystery. Currently, there are five major types of slow earthquakes (Nishikawa et al., 2023), which are low-frequency earthquakes (LFEs) (Figure 1.5a), tectonic tremors (Figure 1.5b), very-low-frequency earthquakes (VLFEs) (Figure 1.5c), long-term slow

slip events (SSEs) (Figure 1.5d), and short-term SSEs (Figure 1.5e). Among these five signals, long-term and short-term SSEs are observed by geodetic instruments, while the others are observed through seismological instruments. Here I briefly review some key features of the slow earthquakes according to the order shown in Figure 1.5.

Slow earthquake family
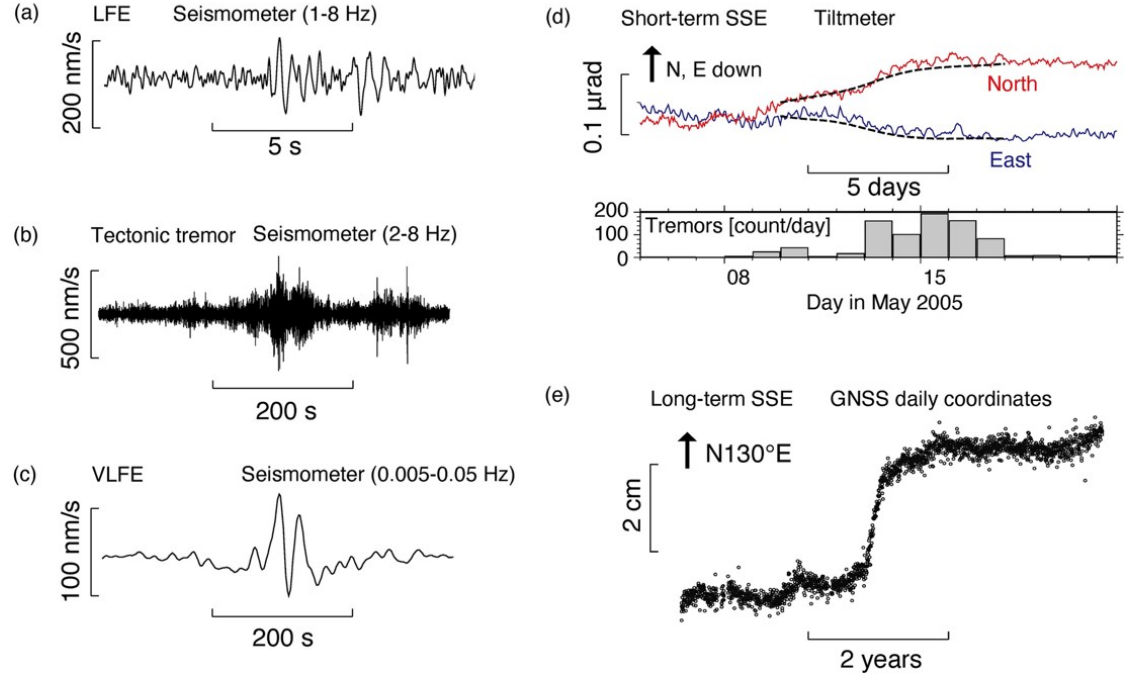
Figure 1.5: Typical geophysical signals of the observed slow earthquake family. **a:** Low-frequency earthquakes (LFEs) (Shelly et al., 2007). **b:** Tectonic tremors (Ide et al., 2008). **c:** Very-low-frequency earthquakes (VLFEs) (Ide et al., 2008). **d:** Short-term SSEs (Hirose & Obara, 2010), where the dashed lines indicate calculated tilt changes due to the short-term SSE. The daily count of concurrent tectonic tremors is presented below this signal (Hirose & Obara, 2010). **e:** Long-term SSEs (Takagi et al., 2016). Retrieved from Nishikawa et al. (2023).

LFEs are slow earthquakes with the smallest moment magnitudes (approximately M_W 1.5) and shortest source duration (about 0.2 s) (Ide, Beroza, et al., 2007; Ide, Shelly, & Beroza, 2007). They are characterized by low dominant frequencies (1–8 Hz) compared to micro-earthquakes of comparable moment release

(Shelly et al., 2007). Meanwhile, LFEs are thought as small shear ruptures (Beroza & Ide, 2011; Ide, Shelly, & Beroza, 2007) occurring on small localized asperities within a fault predominated by aseismic rheology (Thomas et al., 2018).

Tectonic tremors are detected as bursts of seismic signals without clear P- and S-wave arrivals. The dominant frequency band of tremors is 2-8 Hz (Shelly et al., 2007). It is suggested that a tremor can be decomposed into numerous individual LFEs concealed in this swarm (Shelly et al., 2007).

The waveforms of VLFEs present very weak amplitudes of high-frequency components, while VLFEs have greater seismic moments (of M_W 3-4) and longer source duration of tens to hundreds of seconds (Beroza & Ide, 2011; Ito et al., 2007; Obara, 2020). The occurrence of VLFEs in subduction zones is also frequently accompanied by tremors and LFEs.

Short-term SSEs are aseismic slip transients usually lasting from minutes to days and captured by the Global Navigation Satellite System (GNSS) (Dragert et al., 2001). According to the investigation of Dragert et al. (2001), the slow transient with a slip of ∼2 cm and a duration of about one month in the Cascadia subduction zone releases energy equivalent to the moment magnitude of M_W 6.7.

Long-term SSEs are aseismic transients that have the largest moment magnitudes (approximately M_W 6.5–7.5) and the longest characteristic time scales of several months to years (Kano et al., 2018; Nishikawa et al., 2023; Takagi et al., 2019). It is noteworthy that a long-term SSE can also be decomposed into a cluster of short-term SSEs by using a dense catalog of LFEs as a guide (Frank et al., 2018).

Although five major types of slow earthquakes are observed with different time scales and energy releases, they are often observed to occur in close time and spatial proximities. For example, episodic bursts of tremors, which can be decomposed into LFEs (Shelly et al., 2007), are found to coincide with the motions of short-term SSEs in the Cascadia subduction zone (Rogers & Dragert, 2003). It is also suggested by some recent reviews (Bürgmann, 2018; Obara & Kato, 2016) that the rupture fronts of SSEs can be represented by the tremor sequences.

It has been realized that slow earthquakes are ubiquitous in various environ-

ments (Saffer & Wallace, 2015) and characterized by a wide spectrum (Peng & Gomberg, 2010). Moreover, slow earthquakes play an important role in the earthquake cycle as they are thought to act as precursory sequences that trigger large earthquakes (Kato et al., 2012; Radiguet et al., 2016; Ruiz et al., 2014; Socquet et al., 2017). On the contrary, they also can be triggered due to the stress transfer from a mainshock (Alwahedi & Hawthorne, 2019; Uchida & Matsuzawa, 2013). The diverse slip behaviors of a fault interface are associated closely with slow earthquakes. Although many efforts have been made to explain these intriguing observations, a more comprehensive and detailed knowledge of the physical processes of diverse fault slip behaviors is still demanding.

1.4 Rate and State Friction

The frictional stability of a fault interface is usually quantified by the rate and state friction law, which is a constitutive law derived from laboratory rock friction experiments (Dieterich, 1979; Ruina, 1983). Figure 1.6 summarizes how the friction evolves with respect to the hold time and the slip rate using both bare rock samples and granular fault gouges in the laboratory (Marone, 1998b). With the quartz gouges, the friction strengthening is reproduced through the slide-hold-slide experiments and the frictional strength is greater with a larger hold time (Figure 1.6b). Such time-dependent friction strengthening using several experimental datasets is summarized in Figure 1.6a, which shows that the friction coefficient increases linearly with the logarithmic hold time. This strengthening of the fault frictional strength is usually called healing (Dieterich, 1978; Dieterich & Kilgore, 1994) and it describes the frictional strength increase (energy accumulation) of the seismogenic faults during slow creep (Marone, 1998a). Meanwhile, a velocity-weakening of the friction is also observed during a velocity-up-step experiment with quartz gouges (Figure 1.6d). Such weakening of the friction strength upon a slip rate increment is not only observed in quartz gouges but also bare rock faults (Figure 1.6c). This weakening characteristic also illustrates the origin of the slip instability, which is that the faster the slip rate, the weaker the fault interface,

resulting in accelerated slip and mechanical instability.

Based on the measurements of rock friction experiments, the rate and state frictional law is established by simultaneously modeling both the slip rate dependence and the state dependence on friction,

$$\mu = \mu_0 + a \ln(\frac{V}{V_0}) + b \ln(\frac{V_0 \theta}{D_c}), \tag{1.1}$$

where the friction coefficient, μ, is simultaneously dependent on the slip rate, V, and the state variable, θ. The state variable, θ is often interpreted as the average contact age of the frictional fault interface. μ_0 and V_0 are the reference values of the friction coefficient and the slip rate of the fault, respectively. D_c is the characteristic slip distance required for the fault to reach a new steady state. a and b are empirical parameters that indicate the direct effect and the evolution effect, respectively. Two different evolution laws of the state variable, θ, are commonly used to couple with equation 1.1:

$$\frac{d\theta}{dt} = 1 - \frac{V\theta}{D_c}, \tag{1.2}$$

and

$$\frac{d\theta}{dt} = -\frac{V\theta}{D_c} \ln(\frac{V\theta}{D_c}). \tag{1.3}$$

The equation 1.2 is called aging law (Dieterich, 1978, 1979) that emphasizes the time dependence on the restrengthening of friction during quasi-stationary contact while the equation 1.3 is the slip law that considers slip is necessary for any change in friction even during the restrengthening during quasi-stationary contact (Ruina, 1983). The differences between the aging law and the slip law have been compared in Marone (1998b) in detail and I will not dive deep into this topic in this dissertation.

Assuming a fault reaching the steady state which gives $d\theta/dt = 0$ and $\theta_{SS} = D_c/V$, then its friction is quantified as:

$$\mu = \mu_0 + (a - b) \ln(\frac{V}{V_0}). \tag{1.4}$$

Upon an increment of the slip rate, the frictional strength is strengthened and this leads to the aseismic slip of the fault if $(a - b) > 0$, which is usually called
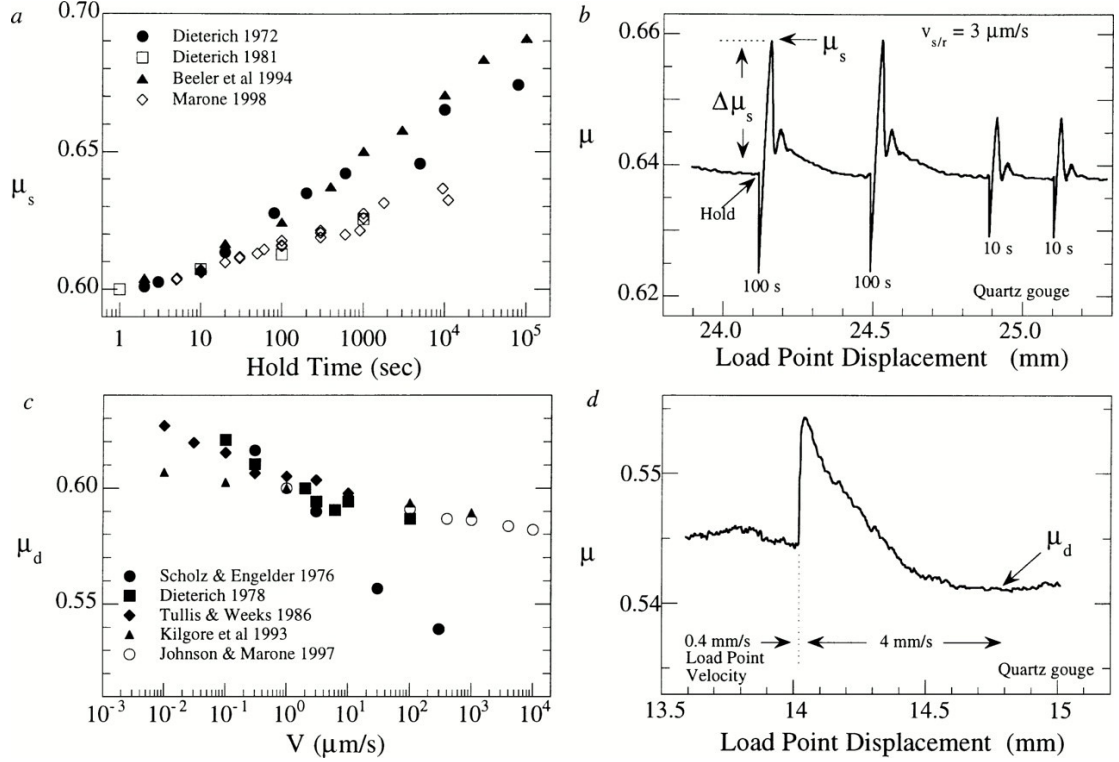
Figure 1.6: a: Relative static friction coefficient as a function of hold time using the bare rock fault (solid) and the granular fault gouges (open). **b:** Friction coefficient as a function of displacement during several slide-hold-slide experiments with hold time indicated below the spikes. **c:** Relative dynamic friction coefficient as a function of slip rate using the bare rock fault (solid) and the granular fault gouges (open). **d:** Friction coefficient as a function of displacement during a velocity-up-step experiment, which shows the friction coefficient transitions from a steady state to another steady state after sliding a characteristic distance. Retrieved from Marone (1998b).

velocity-strengthening behavior (Scholz, 1998). On the other hand, the fault shows velocity-weakening behavior and has the possibility to nucleate instability with unstable seismic slip due to the decrease of the frictional strength if $(a - b) < 0$ (Figure 1.7a).
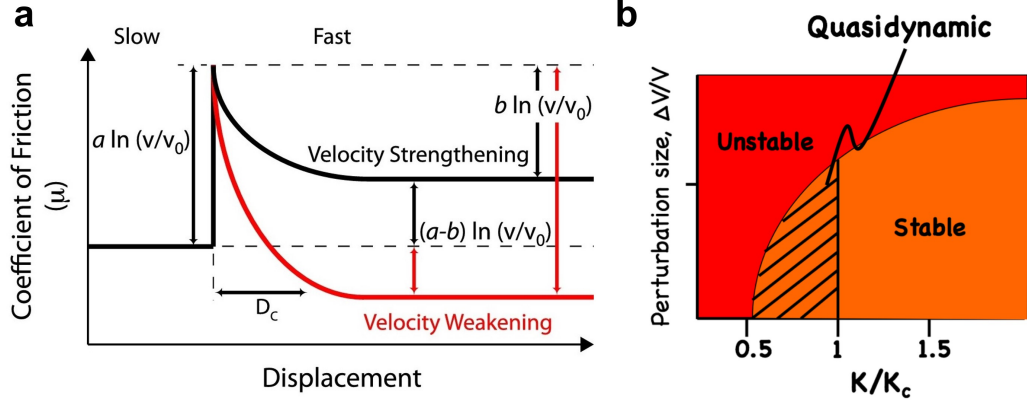
Figure 1.7: a: Two possibilities of friction evolution reacted to an increment of the slip rate of a fault. If $(a - b) > 0$, the frictional strength of the fault will be strengthened and lead to a stable aseismic slip behavior (black line). On the contrary, the frictional strength will be weakened and the unstable seismic slip is possible to nucleate, given the condition $(a - b) < 0$ (red line). Retrieved from Scuderi et al. (2017). **b:** Stability diagram of the velocity-weakening fault system governed by the rate and state frictional law. The fault system will be stable (red) if the loading stiffness, K, is greater than the critical rheological stiffness of the fault, K_c. The frictional instability can nucleate (orange) if $K < K_c$ while a narrow oscillation zone (shaded) which indicates the transition between stable and unstable emerges when the values of K and K_c are close. Modified from Gu et al. (1984) and Scholz (1998).

A velocity-weakening fault governed by the rate and state friction can nucleate dynamic instability when the stiffness of the loading system, K, is lower than its rheological critical stiffness, K_c:

$$K_c = \frac{\sigma_n{}'(b - a)}{D_c},$$

(1.5)

where $\sigma_n{'}$ is the effective normal stress equal to the difference between the normal stress, σ_n, and the pore fluid pressure, P_f. A stability diagram explaining different phases considering the ratio of K/K_c is shown in Figure 1.7b (Gu et al., 1984; Scholz, 1998). If $K > K_c$, the fault system will be stable whereas the fault will be unstable if $K \ll K_c$. It is noteworthy that a self-sustaining oscillatory motion will occur if values of K and K_c are close to each other (Scholz, 1998). Such oscillation marks a transition between seismic and aseismic slips which has been considered as a candidate to explain the physical mechanism of slow earthquakes (Leeman et al., 2016; Scuderi et al., 2016).

The rate and state friction law has been widely used to understand the mechanics of earthquakes and faulting, which enables the investigation of the whole seismic cycle (Lapusta et al., 2000) ranging from the nucleation phase (Ampuero & Rubin, 2008; Rubin & Ampuero, 2005) and precursory characteristics (Cattania & Segall, 2021; Dieterich, 1992) to the coseismic ruptures (Okubo, 1989; Tse & Rice, 1986) and to the afterslip (Perfettini & Avouac, 2007; Perfettini et al., 2010).

1.5   Role of Asperities during Fault Slip

1.5.1   Field Observations

The role of asperities in the behavior of earthquakes has been recognized since the proposal of the "asperity model" (Lay & Kanamori, 1981; Lay et al., 1982), which emphasizes a strong link between the rupture synchronization of asperities and the magnitude of the impending earthquake. This model is well supported by the evidence of the simultaneous rupture of multiple asperities observed in many huge interplate earthquakes, such as the 1960 M_W 9.5 Chile earthquake (Moreno et al., 2009), the 2004 M_W 9.2 Sumatra-Andaman earthquake (Subarya et al., 2006), and the 2011 M_W 9.0 Tohoku-Oki earthquake (S.-J. Lee et al., 2011). On the other hand, it is also suggested that small and scattered asperities on a subduction interface may lead only to a minor release of the seismic moment (Ruff & Kanamori, 1983).

The asperity model has progressively been updated by adding complexities of

diverse fault slip behaviors and of possible earthquake sequences since its proposal (Lay et al., 2012; Lay, 2015; Lay & Nishenko, 2022), especially after the dense investigations of the 2011 M_W 9.0 Tohoku-Oki earthquake (Lay, 2018; Kodaira et al., 2020, 2021; Nishikawa et al., 2023). Figure 1.8 presents the most up-to-date asperity model by taking the subduction zone off the northeast coast of Honshu, Japan, as an example. Four depth-varying domains representing different megathrust rupture characteristics on the subduction interface are indicated in Figure 1.8A, and features of the frictional slips for the corresponding domains are characterized in Figure 1.8B. Such four domains include the near-trench domain A where tsunami earthquakes or anelastic deformation and stable sliding occur, the central megathrust domain B where large slip occurs with low short-period seismic radiation, the down-dip domain C where moderate slip occurs with significant coherent short-period seismic radiation and the transitional domain D where SSEs, LFEs, and tremors occur. All these rupture characteristics actually are controlled by the frictional processes illustrated in Figure 1.8B, where numbers and sizes of asperities (in red), isolated or clustered asperities, and whether their distribution in conditional stable regions (in orange) or aseismic stable regions (in white), all impact the frictional behaviors of the fault interface in an individual and/or coupled way. It is noteworthy that, regardless of the depth of the frictional segment, the type of the triggered earthquakes and the duration and the amount of the corresponding seismic radiation, diverse slip behaviors of local asperities distributed on the macroscopic frictional interface and their complex interactions control the impeding slip behaviors of the frictional interface and the corresponding earthquake characteristics.

The very recent 2023 M_W 7.8 and M_W 7.6 Kahramanmaraş earthquake doublet that occurred in southeastern Turkey is an example that demonstrates the strong fault geometrical effect on the rupture dynamics of a complex fault zone system (Jia et al., 2023; L. Xu et al., 2023). It is suggested that geometric barriers could decelerate rupture propagation and enhance high-frequency wave radiations (Zhang et al., 2023). The multi-segment fault geometry is also thought as the most important reason for exciting the back-propagating rupture during the 2023 M_W
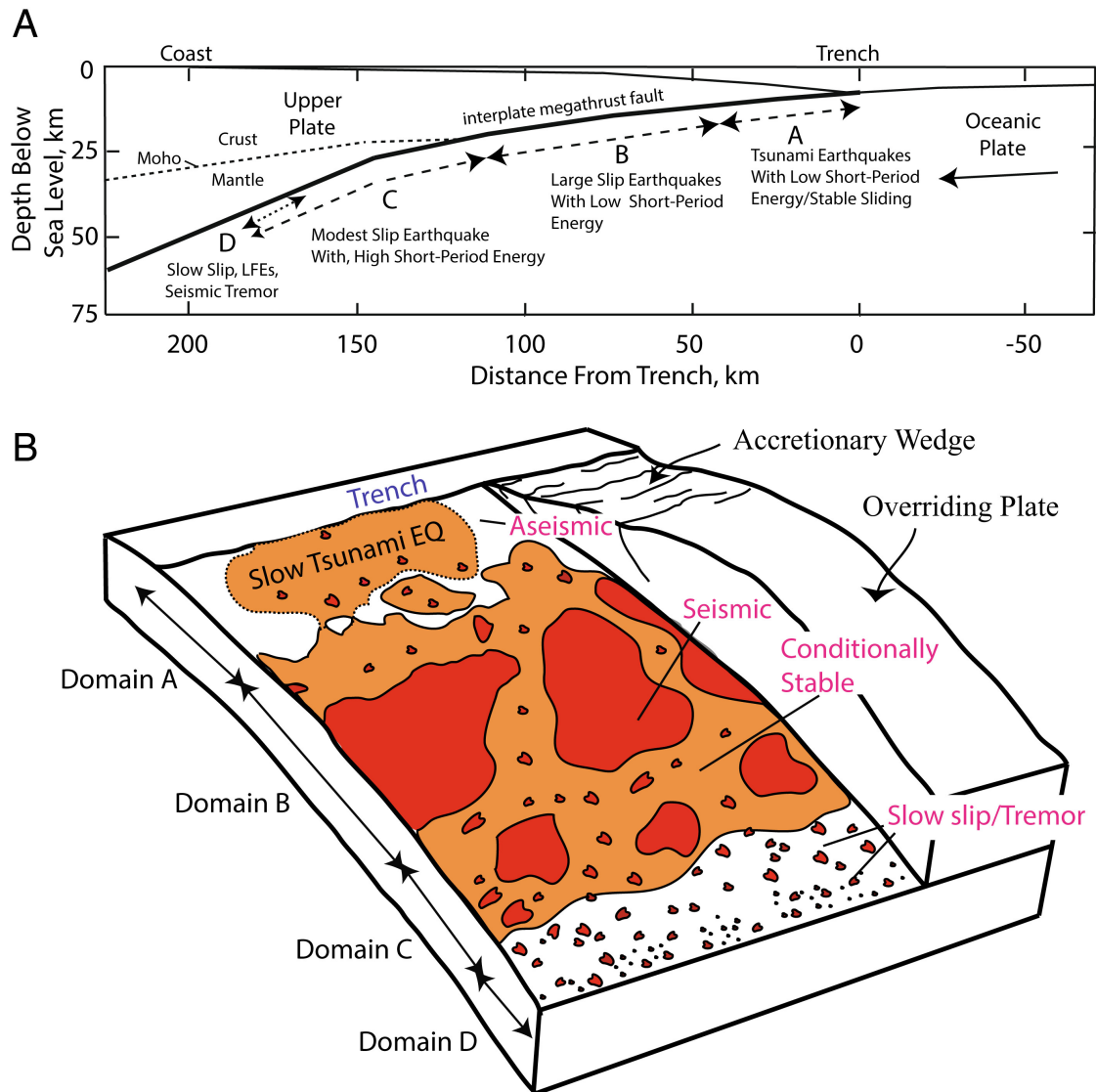
Figure 1.8: An updated asperity model. **A:** Cross-sectional scheme indicating the megathrust rupture characteristics of the subduction zone off the northeast coast of Honshu, Japan. Four depth-varying domains are presented with corresponding behaviors of the earthquake and fault slip illustrated. **B:** Cutaway schematic characterization of the megathrust frictional subduction interface related to the four domains defined. The regions in red, orange, and white indicate the seismic asperities slipping unstably, the conditional stable regions with aseismic slip that can also be accelerated by the ruptures of adjacent seismic asperities, and the stable aseismic or episodic slow slipping regions, respectively. It is noteworthy that the asperities are involved in all the complex and diverse behaviors of earthquake and fault slip. Retrieved from Lay and Nishenko (2022).

7.8 Kahramanmaraş earthquake (Ding et al., 2023). Such multi-segment geometrical complexities of a fault zone can be simplified to normal stress heterogeneities on a fault interface, which is controlled by the asperities establishing the interfacial contacts. Additionally, the observation of seismicity transients starting approximately 8 months before the 2023 M_W 7.8 Kahramanmaraş earthquake indicates that the nucleation of a large earthquake along rough heterogeneous faults is controlled by an intrinsically complex failure process of individual asperities of various sizes and strengths (Kwiatek et al., 2023).

Furthermore, the role of asperities on the behavior of the faulting interface is not limited to dynamic rupture events. Indeed, the interseismic phase is also strongly impacted by the presence of such strong contact areas. This notably arises as locked patches can create stress shadows that lead to reduced interseismic slip rates on the surroundings of the asperity (Bürgmann et al., 2005; L. R. Johnson & Nadeau, 2002), and thus a spatial modulation of the interseismic coupling (Perfettini et al., 2010), where the interseismic coupling is defined as the slip deficit over the long-term slip (Radiguet et al., 2016). Figures 1.9A-F show the slip rate map of a subduction interface under different scenarios of asperity distribution. In general, we observe that the stress shadows from the locked asperities cause the areas near to the asperities to slip aseismically at rates much less than the plate convergence rate. Figure 1.9G displays the interseismic coupling along the Peru megathrust. This heterogeneous spatial distribution of interseismic coupling emphasizes the important role of asperity in evaluating the slip behavior of the fault, the energy accumulation, and the assessment of potential seismic hazards. In addition, some other works (Lovery et al., 2024; Vaca et al., 2018; Villegas-Lanza et al., 2016) also evidence heterogeneous interseismic coupling that indicates the various locking degrees of the patches along the Peru megathrust.

1.5.2 Numerical Simulations

Numerical models are effective for prescribing multiple asperities on a fault interface and studying how the fault responds mechanically to the interactions of these asperities.
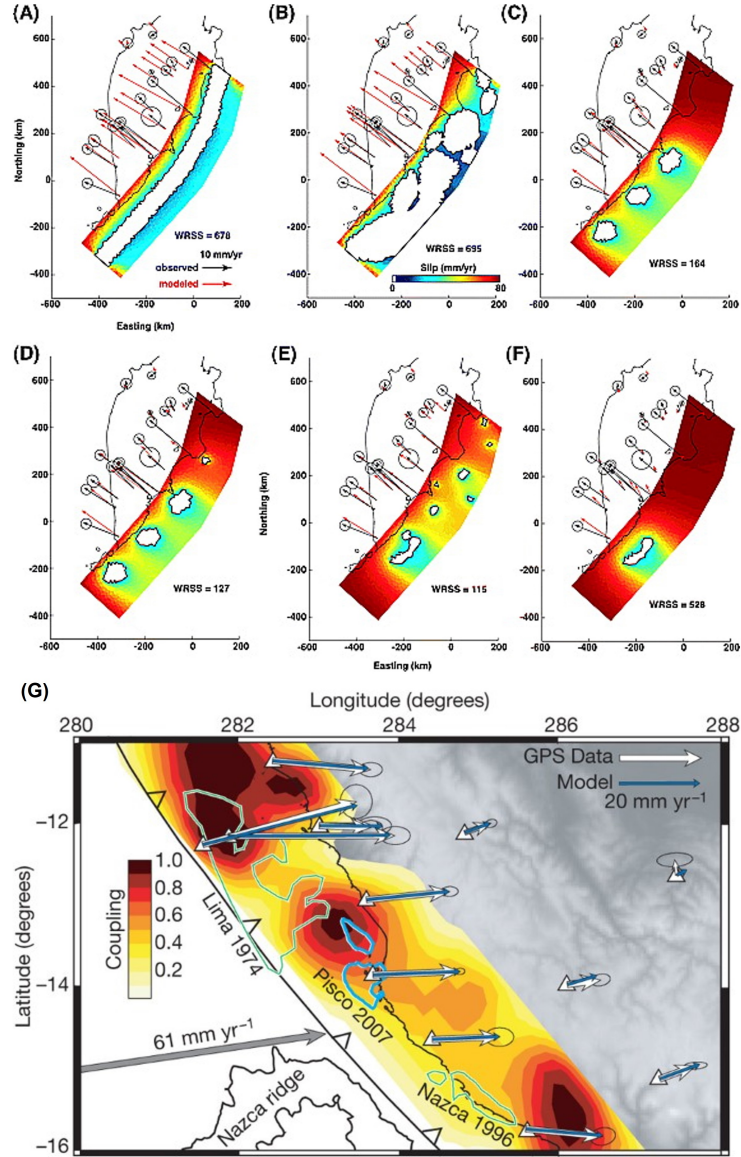
Figure 1.9: A-F: Slip rate maps computed from a forward boundary element method model by assuming different scenarios of asperity distribution. The white regions indicate the locked asperities with zero slip rate. The slip rates of the regions around the locked asperities are smaller compared to the regions far away from the asperities. Retrieved from Bürgmann et al. (2005). **G:** Spatially heterogeneous interseismic coupling map along the Peru megathrust, indicating the major role of asperity in the interseismic phase. Retrieved from Perfettini et al. (2010).

The original Burridge-Knopoff spring-block model, although proposed more than 50 years ago, is a simple mechanical model that can reproduce the first-order features of earthquakes observed worldwide (Burridge & Knopoff, 1967). This Burridge-Knopoff model is a one-dimensional system simulating an earthquake fault interface, which consists of a chain of identical blocks of mass M coupled to each other by the same coil springs of stiffness, k_c, and attached to a plate with a small constant loading rate of V by the identical leaf springs of a stronger stiffness, k_p (Figure 1.10a) (J. Carlson & Langer, 1989). Before the loading, the blocks are homogeneously distributed in space contacting on the rough surface with an equilibrium spacing, a. All the blocks are analogical to asperities that establish multiple contacts on a fault interface. These blocks obey Newton's laws of motion and the friction is dependent only on the slip rate of each block. Sequences of slip events with a wide range of sizes are reproduced using such a discrete model with only short-range elastic interactions, which particularly bears some analogy with the statistical magnitude distribution observed in natural earthquakes (J. M. Carlson & Langer, 1989; J. M. Carlson et al., 1991; J. Carlson, 1991a; J. M. Carlson et al., 1994; Schmittbuhl et al., 1996; Shaw et al., 1992). In addition to the chaotic motions of asperities, the solitary-wave solution that is not earthquake-like is also investigated through a 1D dynamic Burridge-Knopoff model (Schmittbuhl, Vilotte, & Roux, 1993), which can be correlated to the self-healing crack models for earthquake rupture.

These earlier simulations are then extended by considering a more realistic natural fault interface. For example, the one-dimensional chain of blocks is extended to the two-dimensional plane that includes lateral and longitudinal interactions of the blocks (J. Carlson, 1991b; Myers et al., 1996; Kawamura et al., 2019) while keeping the essential assumptions of the stick-slip spring-block oscillators unchanged (Figure 1.10b). Moreover, other strategies, such as considering the long-range interactions between blocks (Mori & Kawamura, 2008; Xia et al., 2005), taking account of the viscous effect (Myers & Langer, 1993; Shaw, 1994; Yoshino, 1998), and changing the friction law governing the motions of blocks (Cao & Aki, 1987; Kawamura et al., 2017; Ohmura & Kawamura, 2007), have been supplemented to
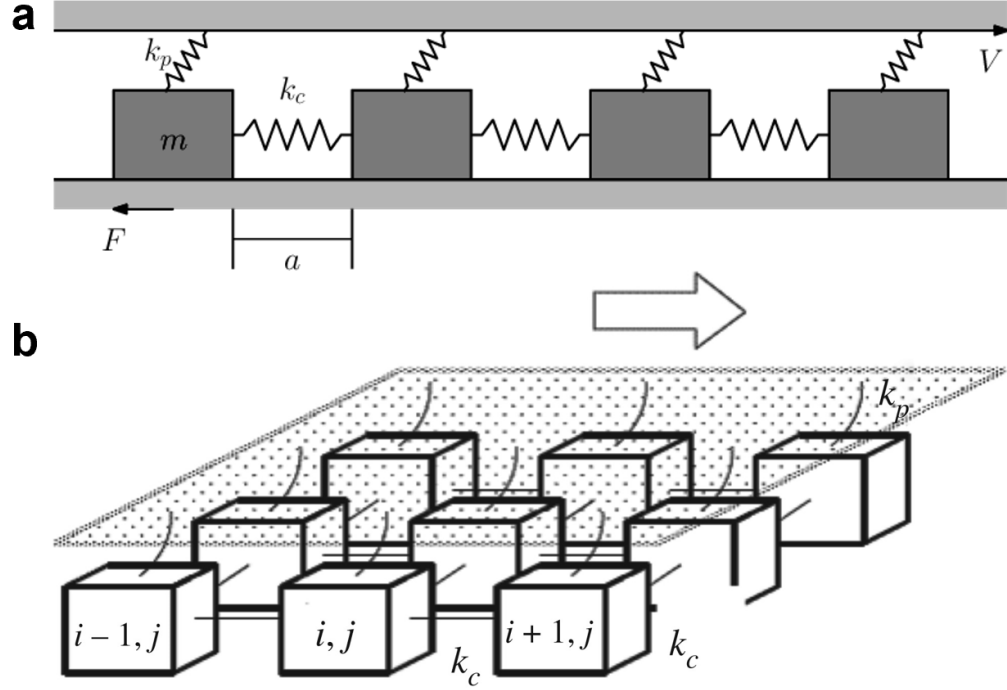
Figure 1.10: a: Scheme of the one-dimensional Burridge-Knopoff model. The spatially homogeneous system (with an equilibrium spacing, a) consists of a chain of identical blocks of mass m coupled to their nearest neighbors by the same harmonic springs of stiffness, k_c, and attached to the plate of a slow-loading rate of V by identical leaf springs of stiffness, k_p. These blocks are in contact with a rough substrate, and the friction of each block depends only on its slip rate. Modified from J. Carlson and Langer (1989). **b:** Scheme of the two-dimensional Burridge-Knopoff model. The original one-dimensional array of blocks is extended to the two-dimensional array of blocks that contains lateral and longitudinal interactions while keeping the other assumptions the same as the 1D model. Retrieved from Kawamura et al. (2019).

the Burridge-Knopoff model for better understanding how the interactions of these discrete blocks control the features of earthquakes observed in nature. Especially, recent simulations on the two-dimensional Burridge-Knopoff model governed by the rate and state friction law suggest that the rupture sometimes propagates in a manner of successive ruptures of neighboring asperities observed in large natural earthquakes (Kawamura et al., 2019).

Rather than the discrete models can only compute the interactions within a limited distance (i.e., the nearest neighboring asperities), the continuum models enable computing the interactions at any scale on a numerical fault interface. Nevertheless, whether the continuum models can correctly interpret the underlying physics of the fault motion is still affected by the size of the computation cell (Rice, 1993). For example, a system with a well-defined continuum limit may be forced to mimic an inherently discrete system given the too-large size of the computation cell (Rice, 1993). A large number of simulations have been conducted by setting multiple discrete asperities spatially distributed over a two-dimensional fault interface governed by the rate and state friction (Ariyoshi et al., 2009; Li & Rubin, 2017; Luo & Ampuero, 2018). Usually, these asperities are presented as velocity-weakening patches, thus they are defined to be potentially unstable and can initiate the seismic slip of the fault (e.g., Figure 1.11). It is demonstrated that the mechanical response of a fault is evidently affected by the interactions of discrete asperities surrounded by aseismic creep areas. For instance, Dublanchet et al. (2013) proposed a variable, namely density of asperities, which is the ratio between the total area covered by asperities and the total area of the fault plane to explain at which condition the fault will be ruptured entirely or locally (Figure 1.11). Such explanations regarding the local or entire rupture of the fault are not only consistent with the aforementioned asperity model that emphasizes the rupture synchronization of asperities distributed on the interface but also implies the existence of a collective effect of local asperities for controlling the rupture dynamics of a macroscopic fault.

Such asperities with distinct frictional properties can also be represented by varying roughness of a fault interface that indicates the different extents of the
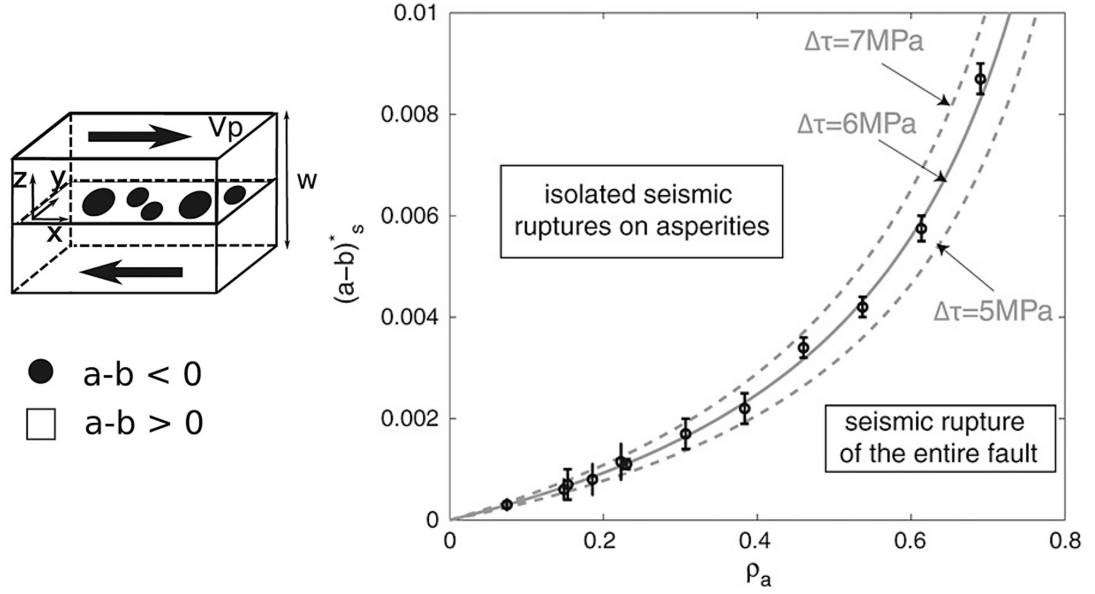
Figure 1.11: Schematic fault governed by the rate and state friction showing the individual velocity-weakening asperities surrounded by the velocity-strengthening creep areas (left). The rupture conditions of a fault are simultaneously controlled by the frictional properties and the density of asperity (right), which emphasizes the collective effect of local asperities on the slip behavior and frictional stability on the macroscopic fault. Modified from Dublanchet et al. (2013).

normal stress heterogeneities (Hansen et al., 2000; Schmittbuhl et al., 2006). It suggested that this heterogeneity affects the earthquake nucleation process (Ozawa et al., 2019; Tal et al., 2018), the precursory slip and foreshocks (Cattania & Segall, 2021), the transitions between seismic and aseismic slip (Tal et al., 2020), the coseismic slip and earthquake locations (Allam et al., 2019), the earthquake size and stress drop (Zielke et al., 2017), the distribution of aftershock (Aslam & Daub, 2018, 2019), and the development of the damage zone (Tal & Faulkner, 2022). Another noteworthy point is that new simulations now incorporate the geometrical complexity imaged from natural faults into numerical faults. For example, it is demonstrated that the diverse slip behaviors can be reproduced with such geometrical complexity alone (Romanet et al., 2018), without the need for the complexity of frictional laws (Hawthorne & Rubin, 2013) or effective normal stress (Luo & Liu,

2019, 2021). All these physics-based numerical simulations point out the significance of interfacial asperities and their interactions for controlling the mechanical evolution during the faulting process and the resulting earthquake triggering.

1.5.3 Laboratory Experiments

In the aspect of laboratory experiments focusing on the role of asperities, one mainly simulates the fault using rough rock samples with normal stress variations, while the other models the fault through transparent materials analogical to rock for imaging interfacial contacts.

For the experiments using rock samples, the role of asperities is usually translated to the normal stress heterogeneity resulting from the varying roughness of the simulated fault interface, as fault roughness controls the realistic stress conditions at contacting asperities (Aubry et al., 2020). Numerous laboratory experiments using simulated rock faults with pre-defined roughness (e.g., Figure 1.12c and Figure 1.12e) have proved the crucial role of asperities in different phases during the fault slip and resulting earthquake behaviors (Fryer et al., 2022; Dresen et al., 2020; Harbord et al., 2017; Goebel et al., 2017, 2023; Guérin-Marthe et al., 2023; Morad et al., 2022; S. Xu et al., 2023; Yamashita et al., 2021). However, these experiments, at the centimeter-scale fault (e.g., Figure 1.12b) or meter-scale fault (e.g., Figure 1.12d), share a common feature for analyzing the effects of asperities, which is that they can only compare the initial and final roughness of the fault interface or compare the results obtained from different fault samples with different roughness (e.g., Figure 1.12c and Figure 1.12e) since the nontransparent rock slabs cannot provide the possibility to directly observe the interfacial contacts. Even if a dense array of strain gages is employed along the two sides of the rock fault (e.g., Figure 1.12d), it is still difficult to completely capture what is happening on the two-dimensional fault interface during the fault slip process because these strain gages can only provide local measurements at limited points at the edge of the whole slip plane.

On the contrary, some other experiments employ transparent analog materials (e.g., PMMA) to model experimental faults that enable the direct optical observa-
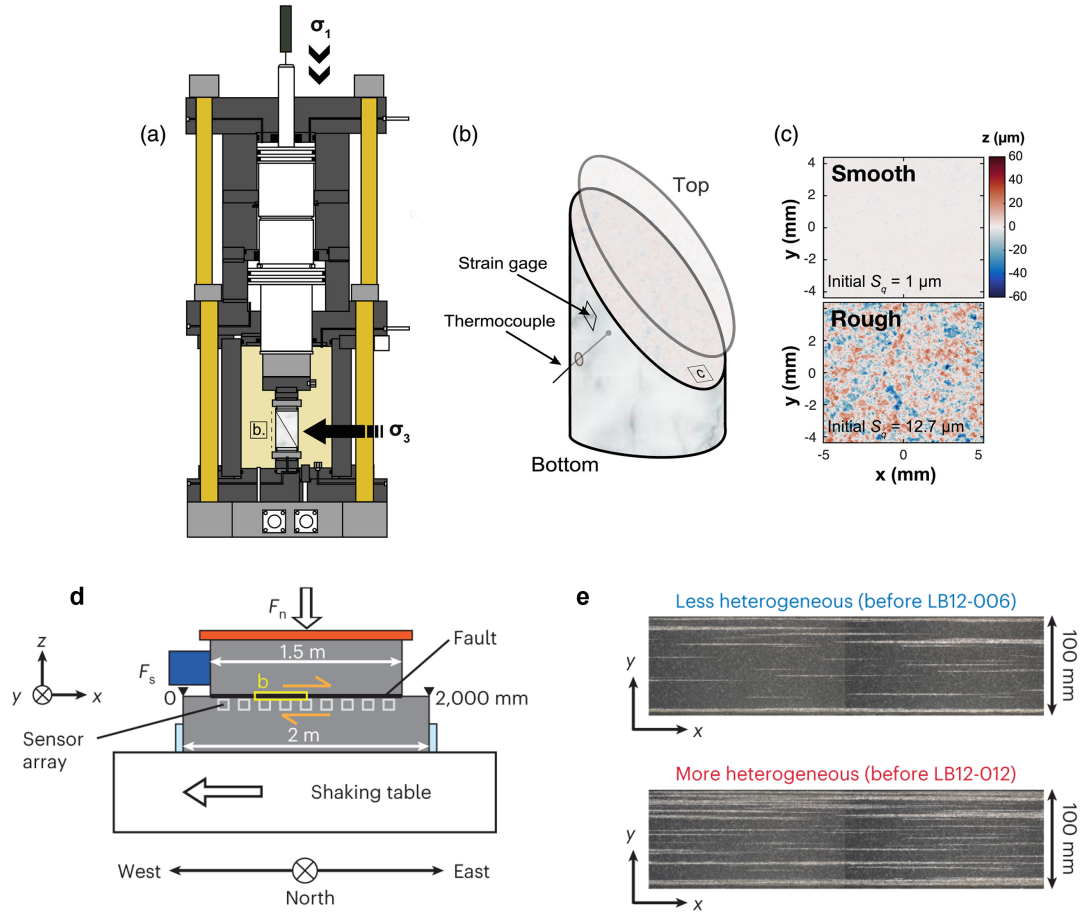
Figure 1.12: **a:** Schematic of the triaxial apparatus used for loading the centimeter-scale rough fault. **b:** Schematic of the saw cut fault sample. **c:** Initial roughness applied on the two parts of the fault before experiments. Two roughness maps are shown with the color bar indicating the altitude of asperities in μm. Retrieved from Aubry et al. (2020). **d:** Experimental setup of a meter-scale laboratory rock fault with a dense array of strain gages. **e:** Two fault surfaces are contrasted by the degree of topographic heterogeneity, where the transition from the less to the more heterogeneous fault is achieved by applying a fast-rate (1 mm/s) shear loading. Retrieved from S. Xu et al. (2023).
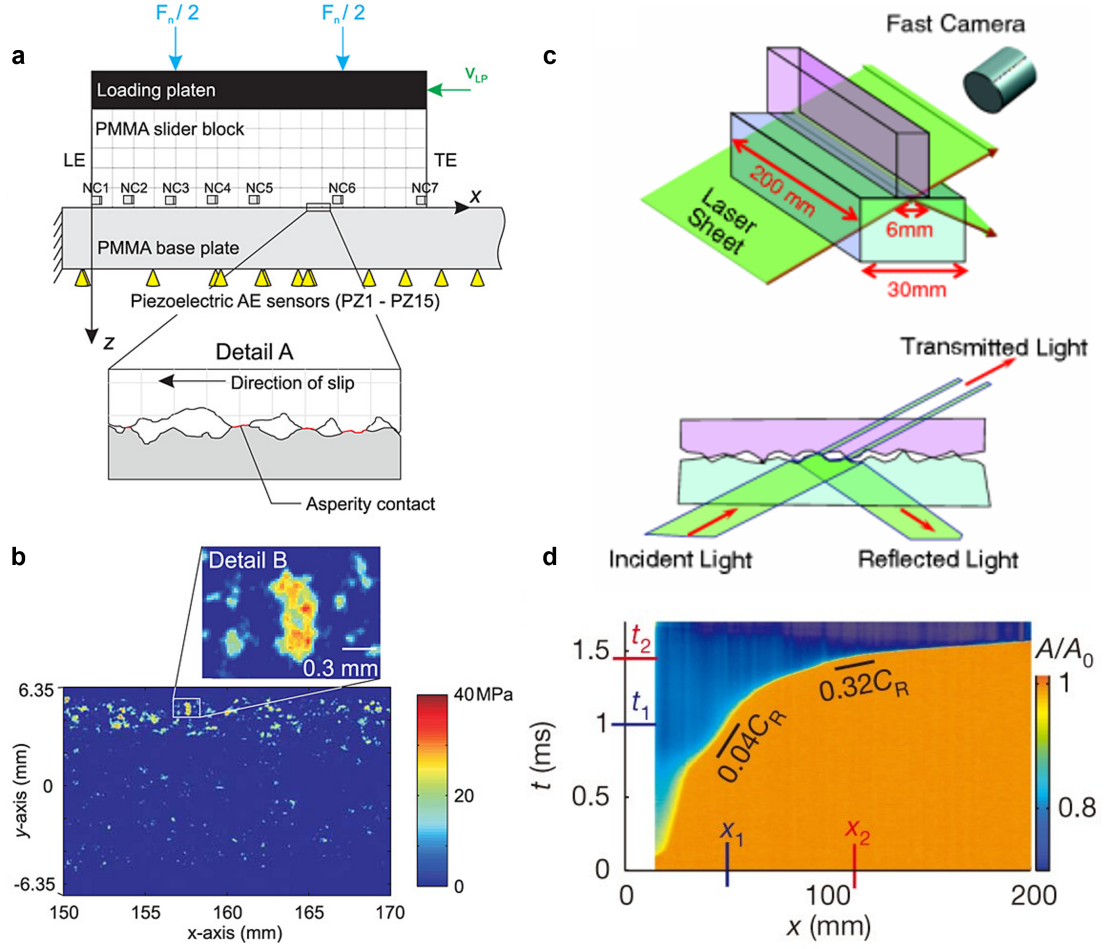
Figure 1.13: a: Side-view schematic of a PMMA-PMMA interface under the direct-shear loading. Detail A illustrates a cartoon representation of the multi-contact interface. **b:** A small section of the multi-contact interface showing initial asperity contact measured using the pressure-sensitive film. Retrieved from Selvadurai and Glaser (2015a). **c:** Scheme of a PMMA-PMMA fault interface under the direct-shear loading, where the real contact area along the entire interface is measured over time through a total internal reflection based method. A sheet of laser light, incident on the frictional interface, is totally reflected everywhere except at contact points. The intensity of the light transmitted at the real contact can be imaged by the fast camera and then converted to the real contact area. Retrieved from Ben-David, Cohen, and Fineberg (2010). **d:** An example showing the temporal evolution of the normalized real contact area along the fault interface. Retrieved from Svetlizky and Fineberg (2014).

tion of the asperities distributed on the interface (Ben-David, Cohen, & Fineberg, 2010; Ben-David, Rubinstein, & Fineberg, 2010; Jestin et al., 2019; Lengliné et al., 2012; Rubinstein et al., 2004; Selvadurai & Glaser, 2015a, 2017; Svetlizky & Fineberg, 2014). For instance, the multiple contacts of a PMMA-PMMA interface can be measured through the pressure-sensitive film (Figure 1.13a), which provides information including the location, real contact area, and normal stress of each asperity (Figure 1.13b) (Selvadurai & Glaser, 2015a). However, such experiments can only measure the interfacial contacts before the faulting, which is the initial interfacial contacts rather than the temporal evolution of these multi-contacts. Additionally, another experimental setup can quantify the asperity contact by measuring the spatiotemporal evolution of the real contact area of an entire PMMA-PMMA interface (Figure 1.13d) (Svetlizky & Fineberg, 2014). The principle of such measurement is that a sheet of light incident on the fault interface will be transmitted at the real contact points while being totally reflected at the other points. Consequently, the real contact area can be measured through the intensity of the transmitted light imaged by the fast camera (Figure 1.13c) (Ben-David, Cohen, & Fineberg, 2010; Svetlizky et al., 2019). Such types of experiments mainly focus on revealing the complexity of the dynamic ruptures along the fault interface (Gvirtzman & Fineberg, 2021; Ben-David, Rubinstein, & Fineberg, 2010; Svetlizky et al., 2019). Nevertheless, the motion of each discrete asperity and their interactions in time and space scales, especially before the rapid dynamic ruptures, are not well constrained.

1.6   Research Aim of the Dissertation

This dissertation aims to understand the intrinsic relationship between the collective behavior of local asperities and the frictional stability of the macroscopic fault through an analog fault model. Therefore, a novel experimental setup is developed to track the temporal evolution of the slip of each asperity on an analog fault interface during shearing. Specifically, numerous discrete rigid spherical PMMA beads, which are used to model the frictional asperities, are embedded

with height variations and random spatial distribution in a soft viscoelastic silicone block to establish numerous micro-contacts with a thick transparent rigid PMMA plate on the top. Such a multi-contact interface is much simpler than a complex fault zone system, which has no mineralogy, no fluid, and no chemical transformation, but the fundamental process of interest, how the collective behavior of local asperities control the frictional stability of the rough fault interface with normal stress heterogeneity and rheological heterogeneity, remains similar. In particular, growing geological evidence (Behr & Bürgmann, 2021; Kirkpatrick et al., 2021) and numerical simulations (Ando et al., 2010, 2012; Behr et al., 2021; Nakata et al., 2011) suggest that the rheological heterogeneity caused by the mixture of frictional and viscous deformation is responsible for the emerging diversity of fault slip behaviors, which could be a potential mechanism for explaining the physical process of slow earthquakes. During the whole shearing process, not only the subtle motion of each local asperity on the analog faulting interface can be directly recorded by the high-resolution optical monitoring system, but also the seismic characteristics emitted from dynamic ruptures that occurred at local asperities during slow transients can be captured by the acoustic monitoring system. An extension of the experimental efforts is the numerical modeling based on the physical properties of the analog fault model, which can be complemented to understand the effects of some fault parameters (e.g., the viscosity of the silicone block, the spatial distribution of asperities, etc.) on the fault slip behavior.

Integrating these studies enables explaining the slip behavior of a macroscopic fault and the resulting earthquakes through the collective behavior of local asperities. Furthermore, the aseismic slip transients clustered from the spatiotemporal interactions of local asperities are highlighted through the direct optical observation of the fault interface. Meanwhile, the link between such aseismic slip transients and the resulting seismicity also can be bridged by capturing the dynamic seismic characteristics recorded by acoustic monitoring. This can help to explore which fault properties are associated with the aseismic transients and how they influence the development of seismicity. The investigation of this dissertation is expected to better understand the transition between aseismic and seismic slips

of a heterogeneous fault interface, especially the physical process of aseismic transients preceding the rapid seismic slip. These studies have implications for the slip behavior and mechanical evolution of a macroscopic fault in natural earthquakes. On the other hand, since the seismicity induced by hydraulic stimulation within geothermal reservoirs is mainly the product of aseismic slip triggering (Guglielmi et al., 2015), these studies also provide insights into the occurrence and development of the induced seismicity in EGS (Enhanced Geothermal Systems) projects.

1.7   Structure of the Dissertation

This dissertation is dedicated to studying the relationship between the collective behavior of local asperities and the slip stability of a macroscopic fault through an analog fault model. In Chapter 2, I describe in detail all the experimental facilities required to perform the shear experiments of the analog fault. In Chapter 3, I explain the development of a numerical model of such an analog fault model and the benchmark work for validating the numerical model. In Chapter 4, I present the experimental results to demonstrate that the slip and mechanical response of the fault can be explained by the quantitative spatiotemporal interaction of asperities. This chapter is the content of a peer-reviewed article published in the *Journal of Geophysical Research: Solid Earth*. In Chapter 5, I discuss the implications for natural tectonic earthquakes and seismicity induced within geothermal reservoirs, as well as the conclusions and perspectives of my future work.

Chapter 2

Experimental Setup

The intrinsic relationships between the collective behavior of local asperities and the frictional stability of the global fault are still elusive due to the difficulty of imaging an exhaustive spatiotemporal variability of a fault interface at depth and the limited computational efficiency of the numerical models with heterogeneities span a large time and space domain. Analog modeling in the laboratory overcomes these difficulties, which can accurately capture the slip of all the asperities on a fault interface over time through a well-designed and controlled setup.

To conduct the experimental research on the analog fault model, a series of experimental facilities are employed to couple multiple measurements, which can precisely quantify the topographical map of the heterogeneous analog fault model, record the macroscopic mechanical evolution of the analogous fault over time, directly observe the subtle deformation of the fault interface, and capture the acoustic emissions emitted by dynamic ruptures that occurred at local asperities. These measurements enable a better understanding of the friction and mechanical dynamics at both asperity and fault scales during the whole faulting process.

In this chapter, I describe in detail all the experimental facilities required to perform the analog experiments, which include the preparation and characterization of the analog fault model, the mechanical loading of the direct-shear setup, the optical and acoustic monitoring of the interface, and the experimental measurements of the rate and state frictional parameters on the multi-asperity interface and the single-asperity interface.

2.1 Analog Fault Model

2.1.1 Sample Preparation

The analog fault model mainly consists of three components, which, from top to bottom, are a thick rigid PMMA plate with dimensions 20×17.5×3.0 cm, identical spherical rigid PMMA beads with a radius of 3 mm, and a soft viscoelastic silicone block with dimensions 10×10×~3.0 cm (Figure 2.1).
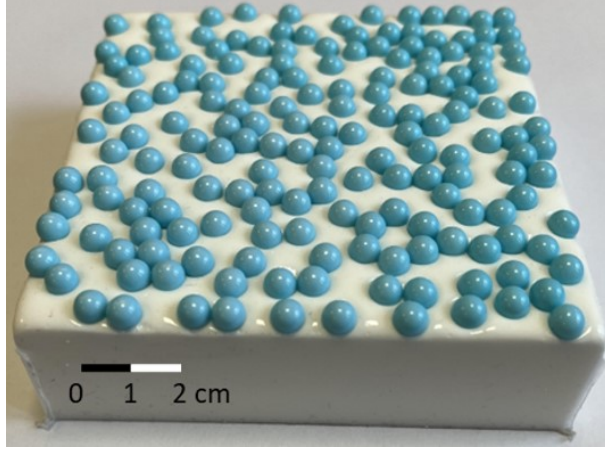
Figure 2.1: Picture showing numerous identical spherical rigid PMMA beads with a radius of 3 mm embedded in a soft viscoelastic block with dimensions 10×10×~3.0 cm. Modified from Shu et al. (2023).

The thick PMMA plate is flat and transparent. Before the direct-shear experiments, it is fixed to the aluminum frame (see Section 2.2 and Section 4.3) with its bottom surface contacting with the PMMA beads. The shear load is imposed on the plate during the faulting, which makes it act as the sliding slab, given the preset normal load has already been uniformly transferred on this PMMA plate (see also Section 2.2 and Section 4.3).

The identical spherical PMMA beads are embedded with small height variations in the silicone block to model the heterogeneous multi-contact with the PMMA plate (Figure 2.1). The detailed procedures for preparing such silicone block embedding numerous beads with height variations are summarized as follows: (1) We put the mixture containing about 4.20 g gelatin and 22 ml water at 70°C for 6

minutes using a water bath to melt it. The mixture is poured at the bottom of a mold of dimensions 10×10×10 cm to produce a thin layer of the thickness of a bead radius. (2) PMMA beads, as many as possible, are dropped randomly in this layer all over the interface and then about one hour wait at room temperature for the solidification of the thin layer. (3) The liquid silicon (BLUESIL RTV 3428 A&B product from the Elkem Company) is poured into the mold to cover the beads and for at least 24 hours at room temperature for its solidification. The liquid silicone is composed of 300 g component A and 30 g component B, and a slow stirring for 5 minutes is needed to minimize the introduction of air and to fully mix the two components before pouring. (4) The upside-down sample is taken out from the mold and the thin layer of gelatin is removed.

Following the procedures above, the viscoelastic silicone block embedding numerous frictional PMMA beads that are randomly scattered and with height variations is customized (Figure 2.1).

2.1.2   Sample Characterization

Another silicone block without PMMA beads is produced following similar procedures and used to characterize its physical properties. The physical characteristics of the silicone are derived from the technical datasheet, the relation of Gent (1958) for converting durometer values to Young's modulus, and direct laboratory measurements of the P-wave velocity of the material. A P-wave velocity of 1000 m/s, an S-wave velocity of 19 m/s, a Young's modulus of 1.1 MPa, and a density of 1100 kg/m^3, are obtained for the silicone.

The viscoelasticity of the silicone is measured through two sets of uniaxial compression experiments (Figure 2.2) performed using the MTS Model C43.104 (see Section 2.2.1 for details of this loading machine). The first set of experiments is controlled by the displacement of the normal loading piston. The piston is moved to load the silicone until the same displacement, 7 mm, is reached for all the displacement controlled experiments, at which the movement of the piston is terminated to stop the loading (Figure 2.2a). The force decay that presents the relaxation of the silicone block after stopping the piston is used to characterize
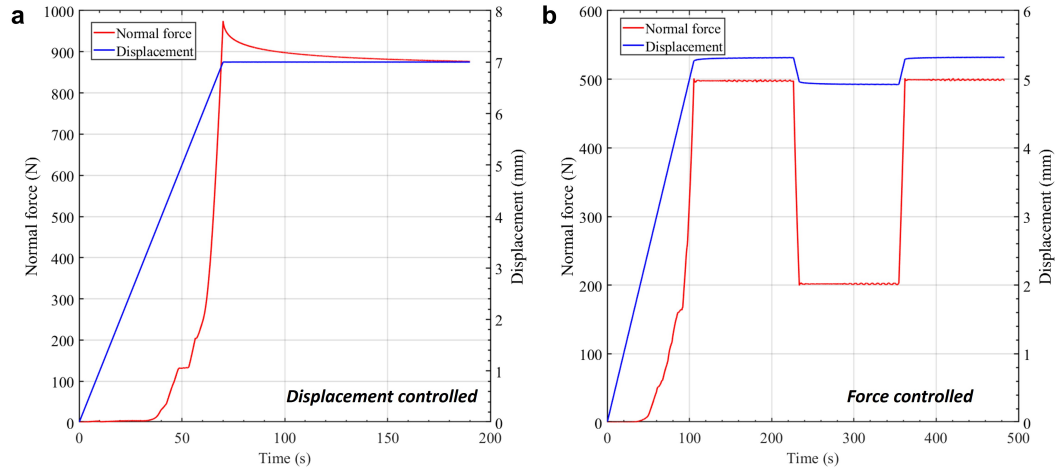
Figure 2.2: Typical temporal evolution of normal force (red) and displacement of the piston (blue) in the first set of experiments at imposed displacement (**a**) and the second set of experiments at imposed force (**b**).

its viscosity. The temporal evolution of the normal force is recorded as shown in Figure 2.3a. The second set of experiments is controlled by the applied normal force. We load the piston to reach a normal force of 500 N and keep it for 2 minutes, unload the normal force to 200 N and keep it for 2 minutes, and reload the normal force to 500 N and keep it for 2 minutes, which is a cycle process (Figure 2.2b). The temporal evolution of the displacement of the loading piston is recorded during each force step (Figure 2.3b). Note that the frequent oscillations come from the subtle motions of the piston that tries to maintain the preset normal load. Additionally, the reloading process during the second set of experiments can be used to characterize the elasticity of the silicone (Figure 2.3c).

The viscous rheology is quantified using a Maxwell model:

$$f(t) = a - b \exp^{(-t/\tau)} \tag{2.1}$$

where $\tau = \eta/E$ is the Maxwell characteristic time, η and E the viscosity and Young's modulus of the silicone block, respectively. $f(t)$ are the temporal evolution of force and piston displacement for Figure 2.3a and Figure 2.3b, respectively. a and b are empirical parameters for fitting the Maxwell model. The Maxwell
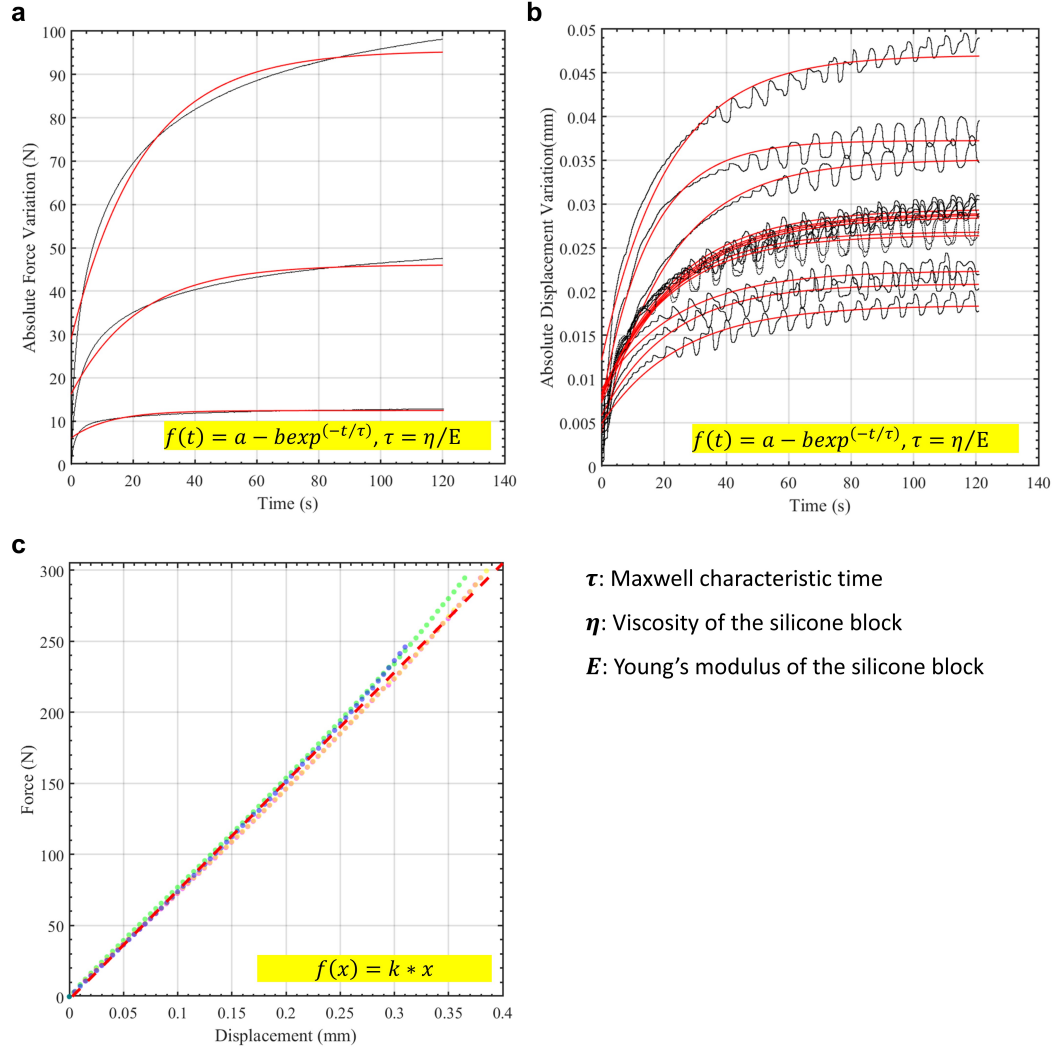
Figure 2.3: Characterizing the viscoelastic rheology of the silicone block. **a:** Temporal evolution of the normal force during the relaxation period (e.g., the force decay shown in Figure 2.2a). The black and red curves indicate the raw data and the best fitting, respectively. A Maxwell characteristic time of 19.08 ± 5.75 s is obtained. **b:** Temporal evolution of the displacement during the force step. The black and red curves indicate the raw data and the best fitting, respectively. A Maxwell characteristic time of 22.67 ± 2.65 s is obtained. **c:** Normal force as a function of the displacement of the loading piston during the loading stage. The circles and the red dashed line indicate the raw data color-coded by experiments and the best fitting, respectively. A stiffness of 767 N/mm is obtained for the silicone block. Retrieved from Shu et al. (2023).

characteristic time is estimated as 20 s, and a resulting viscosity of 2.2×10^7 Pa·s is obtained. The elasticity is fitted with Hooke's law, with a stiffness of 767 N/mm obtained.

PMMA has been widely used as an analogous material to rock to simulate numerous mechanical processes taking place within the Earth, which include not only fault creep and nucleation phases (McLaskey & Glaser, 2011; McLaskey et al., 2012; Selvadurai & Glaser, 2015a) but also dynamic ruptures (Ben-David, Cohen, & Fineberg, 2010; Gvirtzman & Fineberg, 2021). The values of shear modulus and Rayleigh wave speed of the PMMA used in my experiments are estimated from the corresponding typical values measured by Selvadurai and Glaser (2015a) and Gvirtzman and Fineberg (2021) by assuming little differences between PMMA materials, which are 2277.1 MPa and 1255 m/s, respectively.

To precisely quantify the height variations of the rough analog fault surface, its high-resolution topography is measured (Figure 4.3a) with a scan size of 10 cm×10 cm. A 3D digital microscopy (RH-2000, HIROX) and a non-contact Nano Point Scanner (NPS, HIROX) are employed. The system uses a white light confocal LED beam to measure the surface height with a resolution of 0.1 μm in real-time, combined with a high-precision motorized stage. For the measurements shown in Figure 4.3a, the scanning grids in the x and y directions are set as 28 and 10 μm, respectively.

2.1.3   Concluding Remarks

An analog fault model that generates a heterogeneous multi-contact interface is established using rigid PMMA and a soft viscoelastic silicone block. The heterogeneous multi-contact is created by contacting a thick flat PMMA plate on the top with numerous identical spherical PMMA beads, which are embedded with small height variations in the silicone block.

The physical characteristics of the silicone, including the P-wave velocity, S-wave velocity, Young's modulus, and density, are measured. In addition, the viscoelasticity of the silicone is also measured through two sets of uniaxial compression experiments, where one is controlled by the displacement of the loading piston and

the other by the applied normal force. The viscosity of the silicone is quantified through the Maxwell model, resulting a viscosity of 2.2×10^7 Pa·s. The elasticity is fitted through Hooke's law, with a stiffness of 767 N/mm.

The high-resolution topography of the rough analog fault interface is then measured with a 3D digital microscope profiler with a height resolution of 0.1 μm.

2.2 Mechanical Loading Configuration

To simulate the large-scale, far-field loading imposed on natural faults, a direct-shear experimental setup is designed to shear the whole analog fault interface by imposing small displacement rates on the PMMA plate under well-controlled normal loads (Figure 2.4).

Multiple normal loads (e.g., from 10 to 1000 N) and multiple displacement rates (e.g., from 5.0 to 15.0 μm/s) can be imposed in the experiments (e.g., Table 4.1). The normal force F_N is uniformly transferred to the PMMA plate through the ball bearing and the rigid aluminum frame (Figure 2.4c). A sensor is utilized to record the normal force and maintain a constant normal load throughout the whole duration of an experiment (Figure 2.4). A translation stage (MNT9, Axmo Précision) with a constant displacement rate, controlled by a combination of servo and stepper motor (National Instruments MID-7604), is run to drive the rigid loading cylinder to impose the shear force F_S while maintaining a normal force F_N on the PMMA plate (Figure 2.4c). The loading cylinder is composed of the aluminum alloy 2017A, with a stiffness of 78 N/μm. The shear force F_S is measured using a sensor placed between the cylinder and the translation stage, with a resolution of 0.01 N. The stiffness of this sensor is 1 N/μm (from the technical datasheet), thus most of the loading stage deformation is actually taking place within the force sensor. A laser (Keyence IL-S025), range 10 mm and resolution 0.1 μm, is employed to measure the displacement of the PMMA plate, d_P (Figure 2.4c). For all the experiments, the initial value of d_P is kept the same to ensure each fault slip starts from the same position.

Before performing the experiments, the PMMA plate is fixed to the aluminum
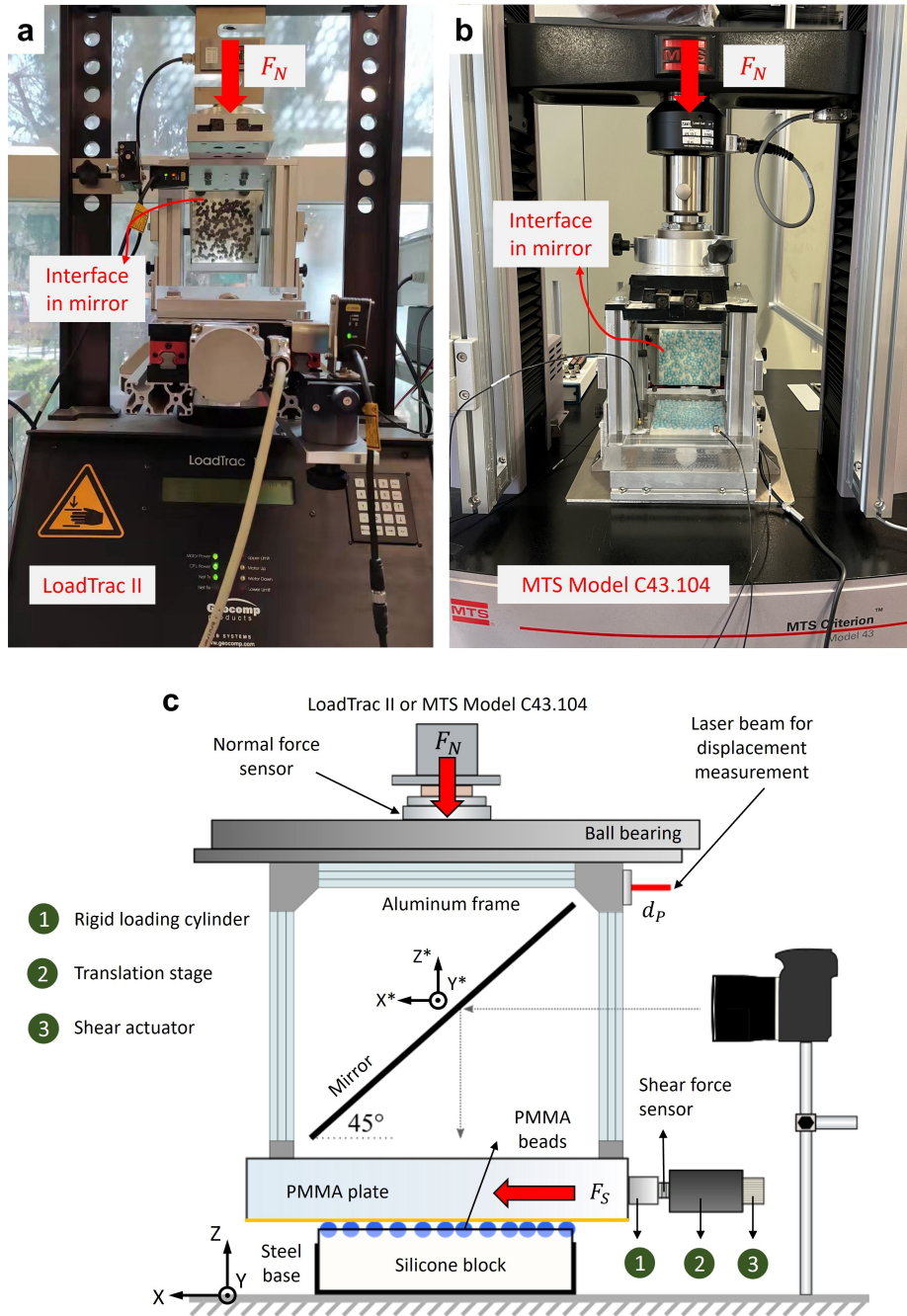
Figure 2.4: Technical experimental setups. **a:** Picture showing the experimental setup using the normal loading machine, LoadTrac II. Note that the fault interface reflected by the mirror comes from a preliminary analog fault model used for testing. **b:** Picture showing the experimental setup using the normal loading machine, MTS Model C43.104. **c:** Schematic side view of the same technical experimental setup, although two separate normal loading machines, LoadTrac II or MTS Model C43.104, are used in different experiments. Modified from Shu et al. (2023).

frame, and the silicone block is also clamped in the rigid steel base (Figure 2.4c). A digital level is used to make sure that the whole experimental system, especially the slip plane (indicated as the yellow line in Figure 2.4c), is flat horizontal. Each experiment begins at the moment when the shear force starts to increase on the PMMA plate, given the analog fault has been previously loaded by a stable normal load.

2.2.1   Normal Loading

Two machines imposing the normal loading were used in different experiments. The first one is LoadTrac II from Geocomp company (Figure 2.4a), and it is employed in all the experiments listed in Table 4.1. The second machine is MTS Model C43.104 (Figure 2.4b). It replaces the first machine (LoadTrac II) while keeping the original experimental setup the same (Figure 2.4c). The second one is employed in all the other experiments, including the viscoelastic characterization of the silicone, the experiments coupled with acoustic emission, and the experiments with pressure-sensitive films.

The first loading machine, LoadTrac II, is a hydraulic setup. It applies the normal load by the vertical movement of the rigid loading platen driven by a high-precision micro stepper motor (Figure 2.4a). The maximum normal load that can be applied is 12 kN. The sensor coupled with this machine has a resolution of 0.01 N.

The second loading machine, MTS Model C43.104, is a mechanical setup. The normal load is imposed by the displacement of the piston, which is driven by a high-speed, low-vibration electromechanical alternating current (AC) servo motor with integrated, digital closed-loop controls (Figure 2.4b). The maximum force capacity is 10 kN and the resolution of the recording sensor is 1×10^{-4} N.

2.2.2   Concluding Remarks

The well-controlled normal and shear loading were used in our direct-shear experimental setup to simulate the frictional slip on natural faults. For the normal

loading, two machines were employed in different experiments while keeping the fundamental process of frictional slip on the analog fault interface the same. The first machine is a hydraulic apparatus with a resolution of 0.01 N, whereas the second one is a mechanical apparatus with a resolution of 1×10^{-4} N. Various forces of the normal load imposed by both two machines can be uniformly transferred to the thick PMMA plate through the ball bearing and the rigid aluminum frame. The shear force can be imposed on the thick PMMA plate with multiple constant displacement rates while maintaining the preset normal load on the PMMA plate. The shear force is measured by a sensor with a resolution of 0.01 N that bears most of the loading stage deformation. The displacement of the PMMA plate, that is the displacement of the macroscopic fault, is measured through a laser with a resolution of 0.1 μm. We guarantee each friction experiment starts from the same position by keeping the same initial displacement of the PMMA plate.

2.3   Optical Monitoring Configuration

A high-resolution camera (Nikon D800) with a lens (Nikon 105 mm f/2.8D AF Micro-Nikkor) in automatic focus mode is employed as the optical device. Thanks to the mirror inclined at 45° that is fixed inside the aluminum frame, the camera fixed to the ground is able to capture the positions of asperities on the analog fault interface through the mirror reflection (Figure 2.4c). Two LED lights are placed behind the camera to supplement sufficient light for the clear observation of the interface. The main parameters for setting the optical system are as follows: aperture size f/14, exposure time 1/30 s, and photosensitivity (ISO) 100. For an entire experiment, the camera records a video of dimensions in 1920×1080 pixels with a sampling rate of 29.97 frames per second, during which the positions of asperities are always clearly captured (benefiting from the lens in automatic focus mode) though the mirror moves with the sliding of the PMMA plate. Besides, a function generator is used to manually trigger the recording of the camera by sending an electrical signal, thus synchronizing the force measurement and the optical monitoring by correcting the time base of each record.
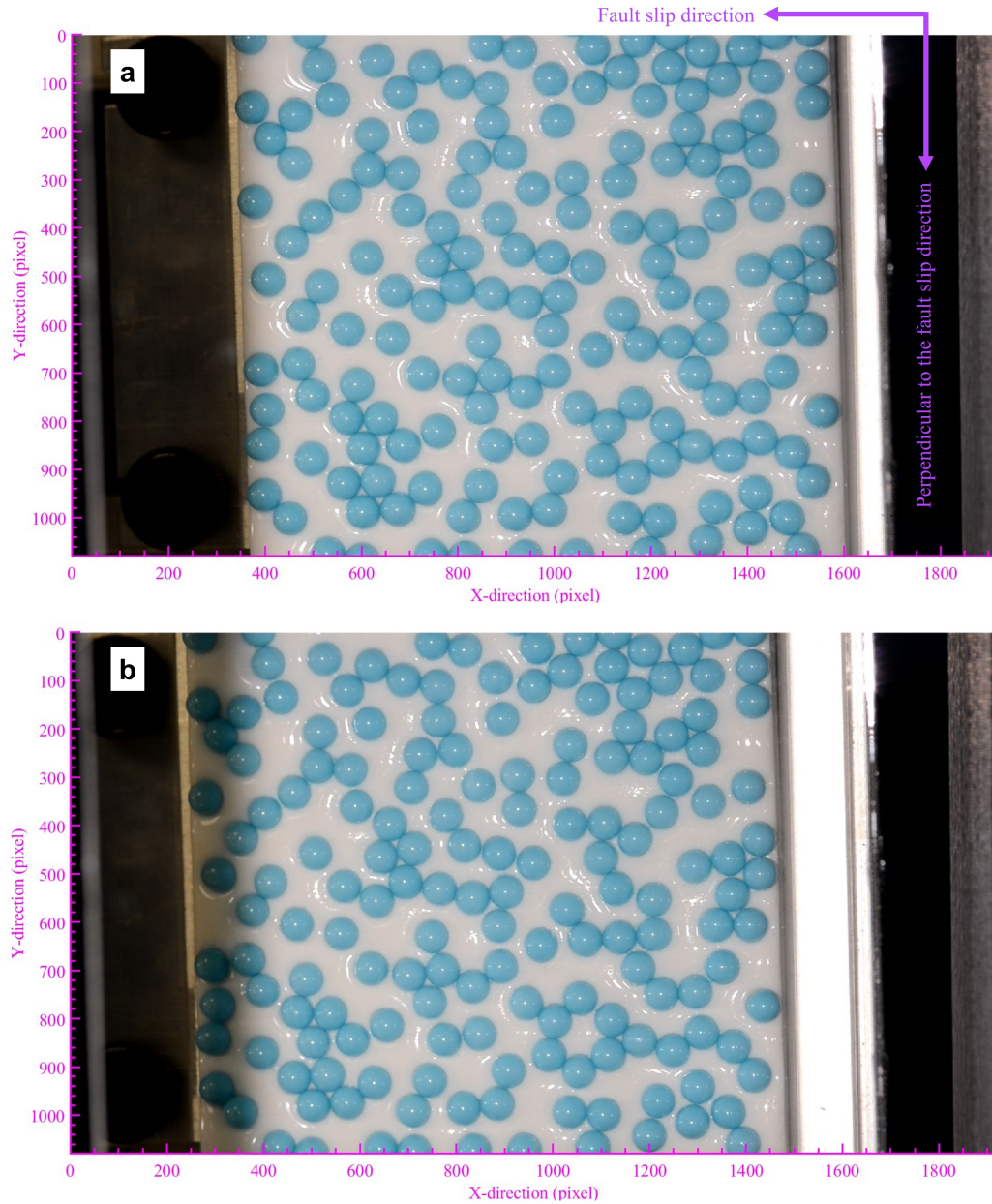
Figure 2.5: Raw images at the beginning (**a**) and the end (**b**) of an experiment extracted from the video recorded by the optical monitoring system. Both images clearly show the analog fault interface and the offset indicating the total slip of asperities during an experiment is also observed.

To compute the slip of each asperity during an entire experiment, the recorded video is decomposed into a series of successive images that range from times t_0 and t_f, which are the times at the beginning and the end of an experiment, respectively. The raw images recorded at such beginning and end of an experiment are presented as examples (Figure 2.5). Then, the aim is to extract the slip of each asperity as a function of time using this series of successive images. Denoting $x_i(t)$ and $y_i(t)$ the positions of the center of asperity i in the fixed reference frame (attached to the ground), the displacement of asperity i along the faulting direction in the same fixed reference frame is defined as,

$$d_i(t) = x_i(t) - x_i(t_0). \tag{2.2}$$

Similarly, denoting $x_P(t)$ as the position of the center of the mirror in the same fixed frame, and then its displacement is computed as:

$$d_P(t) = x_P(t) - x_P(t_0). \tag{2.3}$$

Such displacement, $d_P(t)$, is also the displacement of the PMMA plate in this fixed frame since the mirror moves with the sliding of the PMMA plate. The cumulative slip of asperity i at time t is defined as the difference in the displacements between the two sides of the interface, which is the difference in the displacements of asperity i and the PMMA plate:

$$u_i(t) = d_i(t) - d_P(t). \tag{2.4}$$

As mentioned before, the camera and the silicone block are both fixed to the ground while the mirror moves with the sliding of the PMMA plate. Thus, the positions of asperity i in the moving frame attached to the mirror (also the PMMA plate) are denoted as $x_i^*(t)$ and $y_i^*(t)$. Similarly, in this moving reference, the displacement of asperity i along the faulting direction is defined as

$$d_i^*(t) = x_i^*(t) - x_i^*(t_0). \tag{2.5}$$

Following the same definition of the cumulative slip of asperity i at time t, such displacement, $d_i^*(t)$, is exactly the cumulative slip of asperity i, as the sliding PMMA plate is the moving reference frame.

$$u_i(t) = d_i^*(t) - d_P^*(t) = d_i^*(t). \tag{2.6}$$

Consequently, the cumulative slip of each asperity along the two directions (i.e., faulting direction and perpendicular to faulting) is obtained by tracking the temporal evolution of its positions, $x_i^*(t)$ and $y_i^*(t)$, between time t_0 and time t_f.

2.3.1 Asperity Detection

A two-step procedure is developed to track the temporal evolution of the positions of each asperity ($x_i^*(t)$ and $y_i^*(t)$) during the whole experiment.

The first step is the automatic detection of the positions of each asperity at times t_0 and t_f. Prior to the detection, all the extracted RGB images are converted to the grayscale. A region of interest of dimensions 1300×1080 pixels (i.e., 108.33×90 mm, see the conversion between pixel and mm described below) is selected to include the whole fault interface (Figure 2.6). The circular Hough transform algorithm, the function *imfindcircles* implemented in MATLAB, enables the automatic detection of circular objects in an input image along with estimating their center coordinates and radius (Davies, 2005; Yuen et al., 1990). Thus, the initial positions, $x_i^*(t_0)$ and $y_i^*(t_0)$, at time t_0 and the final positions, $x_i^*(t_f)$ and $y_i^*(t_f)$, at time t_f, of each asperity are determined.

Figure 2.6a shows the initial positions of asperities, $x_i^*(t_0)$ and $y_i^*(t_0)$, detected at time t_0. The asperities marked by red and blue are respectively retained and discarded in the subsequent image correlation, as the image correlation windows of the blue ones exceed the image boundary. The number of retained asperities is $N = 144$ here. The value of N may change with different experiments mainly due to the field view of the camera, but it fluctuates around 140. The radius of asperities is estimated as 36 pixels, and it gives the scaling of the image from the known radius of the PMMA beads ($R = 3$ mm), 12 pixels/mm.

In addition, the total slip of each asperity along the faulting direction (see also Figure 2.5 for a rough total slip of each asperity) can be estimated based on their initial and final positions:

$$u_i(t_f) = x_i^*(t_f) - x_i^*(t_0). \tag{2.7}$$

Due to the constant loading rate in an experiment, a simple linear trend between

the initial and final positions gives an approximate position, $x_i^*(t)$, of each asperity i at each time step t:

$$x_i^*(t) = \frac{u_i(t_f)}{t_f - t_0} \times t + x_i^*(t_0), \tag{2.8}$$

which provides a first-order estimate of the position of each asperity during the experiment.

2.3.2 Image Correlation Technique

The second step is applying an image correlation technique (Sutton et al., 2009) to refine the estimations obtained in the first step (see Equation 2.8) to compute the most accurate positions of asperities.

To proceed with the image correlation, a square window with a size of $\sqrt{2}R$ is defined at the center of each asperity since their initial positions, $x_i^*(t_0)$ and $y_i^*(t_0)$, are estimated before. The image defined by the square correlation window of each asperity at all frames is extracted (Figure 2.6a). For each asperity, the FFT (fast Fourier transform)-based two-dimensional cross-correlation map between the extracted windows defined at two successive time frames, t_{k-1} and t_k, is computed (Figure 2.6b). The position of the maximum value in the correlation map that gives the displacement of the asperity is isolated. The correlation window of the second frame (t_k) is then shifted based on this displacement and the procedure is repeated until the computed displacement is null. During this last stage, a sub-sample displacement is extracted by interpolating the correlation map around its maximum. The final displacement of the asperity between the two successive time frames is obtained by summing all displacements computed during this iterative process. By repeating this procedure for all time frames and for each asperity, the cumulative slip of each asperity during an entire experiment can be obtained. The typical resolution of the resolved displacement in each direction is of the order of 0.01 mm.

The non-perfect 45° inclination of the mirror and/or the non-parallel view between the camera lens and the slip plane (Figure 2.4c) may result in the non-parallelism that can create a non-linear scaling along the x axis (i.e., the faulting direction). To eliminate such an effect, the cumulative slip of each asperity, $u_i(t)$,
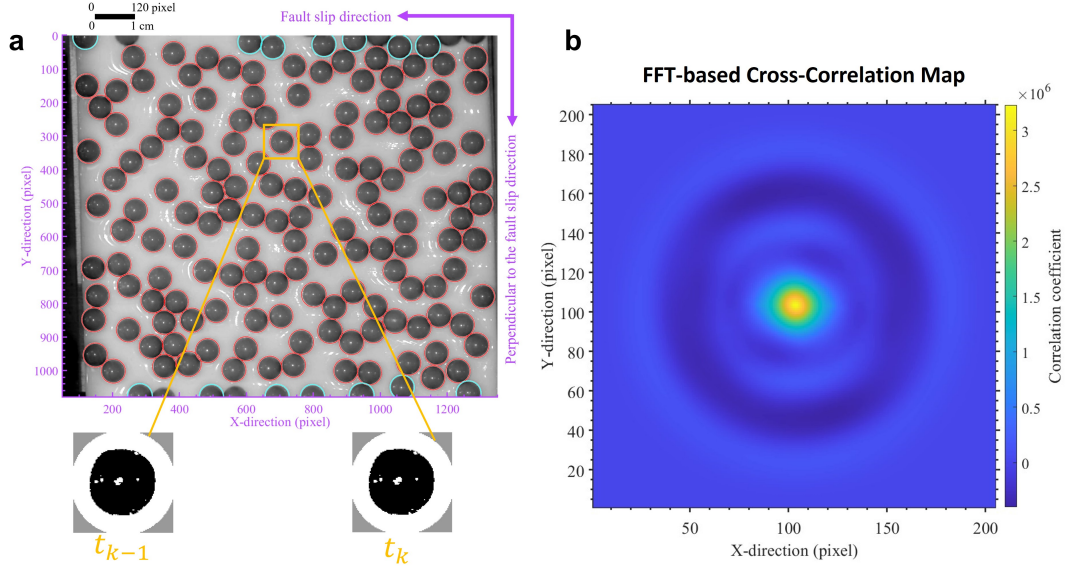
Figure 2.6: a: Typical automatic detection results indicate the initial positions of asperities at time t_0 within the selected region of interest, 1300×1080 pixels. The asperities without markers represent the undetected ones while the asperities with blue circles correspond to the excluded ones as their correlation windows exceed the image boundary. A total of $N = 144$ asperities marked by red circles are kept and their positions, $x_i^*(t_0)$, are taken as the initial positions for computing the slip through the subsequent image correlation. The square correlation window with a size of $\sqrt{2}R$ for an arbitrary retained asperity is marked by the orange square. Two images are extracted from the square correlation window at times t_{k-1} and t_k, and then the contrast is increased, and the neighbor asperities are excluded from the window (see the four gray tapers in the corners). **b:** The two-dimensional FFT-based cross-correlation map between the two extracted images at times t_{k-1} and t_k. The final displacement of this asperity between the two successive time frames is refined through an iterative interpolation process implemented around the position of the maximum value of this correlation map.

is corrected using its total slip $u_i(t_f)$, which should never be greater than the displacement of the PMMA plate, $d_P(t_f)$ at the same time t_f. Accordingly, the displacement of each asperity, $d_i(t)$, also can be updated following Equation 2.4.

The image correlation technique explained above allows us to quantify the temporal evolution of the slip of each asperity during the whole faulting process. For each asperity, the slipping events, which can be called individual asperity slippings, can be defined through a slip rate threshold computed by specifically considering its slip history. Since numerous asperities are present on the 2D analog fault interface, the individual asperity slippings originating from different asperities are clustered in both time and space scales to quantify the spatiotemporal interactions of asperities, which are defined as slip episodes to mimic the ruptures over the 2D fault interface. Here is only a brief introduction, please refer to Section 4.5.1 for more details about the definition and the generation of the spatiotemporal slip episodes.

2.3.3 Concluding Remarks

A high-resolution camera recording a video of dimensions in 1920×1080 pixels with a sampling rate of 29.97 frames per second is employed as the optical device, along with a 45° inclined mirror fixed inside the aluminum frame and two LED lights, to monitor the subtle deformation of the analog fault interface. Aiming to extract the slip of each asperity as a function of time, the recorded video is decomposed into a series of successive images between t_0 and t_f. According to the fixed and moving reference frames in our experimental setup, the cumulative slip of each asperity along the faulting direction and the direction perpendicular to faulting can be obtained by respectively tracking the temporal evolution of its x^* and y^* positions in the moving reference frame, which are the positions recorded in the video.

A two-step procedure is developed to track the temporal evolution of the positions of each asperity. The automatic detection of the positions of each asperity at times t_0 and t_f is the first step. To this end, all the extracted RGB images are converted to the grayscale, and a region of interest of dimensions 1300×1080 pixels

are applied to all the grayscale images. The automatic detection is implemented through the circular Hough transform algorithm to give the initial positions, $x_i^*(t_0)$ and $y_i^*(t_0)$, at time t_0 and the final positions, $x_i^*(t_f)$ and $y_i^*(t_f)$, at time t_f, for each asperity within the region of interest. The difference between the initial and final positions gives the estimation of the total slip of each asperity, which in first-order estimates the position of each asperity at each time since the constant loading rate in our experiments is responsible for a simple linear trend between the initial and final positions.

To compute the most accurate positions of each asperity, the second step is to refine the estimations obtained in the first step by applying an image correlation technique. Specifically, the FFT (fast Fourier transform)-based two-dimensional cross-correlation map between the square correlation windows, which are of a size of $\sqrt{2}R$ centered at the position of each asperity, at two successive time frames, t_{k-1} and t_k, are computed. The final displacement of this asperity between the two successive time frames is refined through an iterative interpolation process implemented around the position of the maximum value in this correlation map.

The non-perfect $45°$ inclination of the mirror and/or the non-parallel view between the camera lens and the slip place may lead to non-parallelism, which can create a non-linear scaling along the faulting direction and thus distort the result of the cumulative slip of each asperity. Such an effect is corrected by the fact that the total slip of each asperity should never be larger than the displacement of the PMMA plate.

2.4   Acoustic Emission Configuration

A preliminary acoustic acquisition test was performed by deploying an array of four identical piezoelectric accelerometers (Miniature DeltaTron Type 4519-003, Brüel & Kjær company). These accelerometers were mounted on the top of the thick PMMA plate (which moves with shearing) to monitor the seismic characteristics emitted from dynamic ruptures during the experiments (Figure 2.7). The initial position of each sensor is roughly located above each corner of the silicone

block with a separation distance of about 10 cm along both x and y directions (Figure 2.7b). The precise initial position of each sensor is not measured since the current acoustic configuration is still under test. The peak frequency response of these sensors is 20 kHz, and all four channels are continuously recorded at 100 kHz. For each experiment, an function generator is used to manually trigger the acquisition of the acoustic data and synchronize the acoustic recording with both the shear force measurement and the optical monitoring. Due to the limited volume of the acoustic acquisition cards, the maximum duration of such an experiment is 160 s at the current configuration.
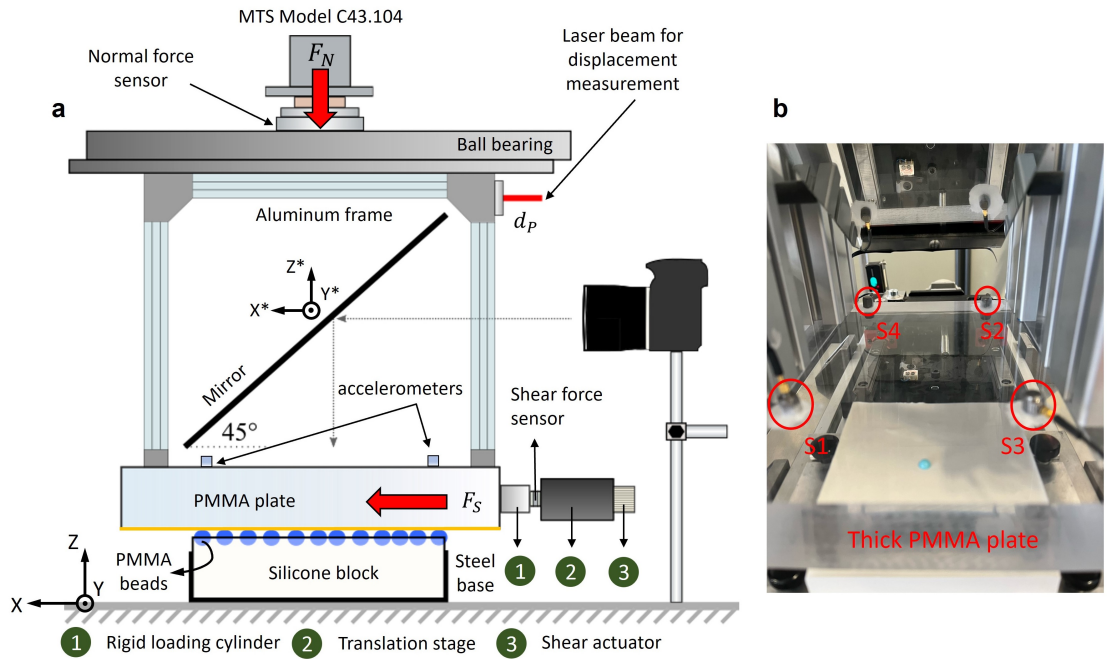
Figure 2.7: a: Schematic side view of the technical experimental setup coupled with acoustic monitoring. Four identical accelerometers are deployed by vertically gluing them on the top of the thick PMMA plate. **b:** Picture showing the four accelerometers glued to the PMMA plate. Note that the analog fault model here is a single-asperity interface used for measuring the parameters in the rate and state frictional law.

2.4.1 Acoustic Data Processing

Figure 2.8 presents a typical example of acoustic signals recorded by the deployed sensor array during the whole duration of an experiment (normal load 500 N and loading rate 25 μm/s). The acoustic signals recorded by the accelerometers
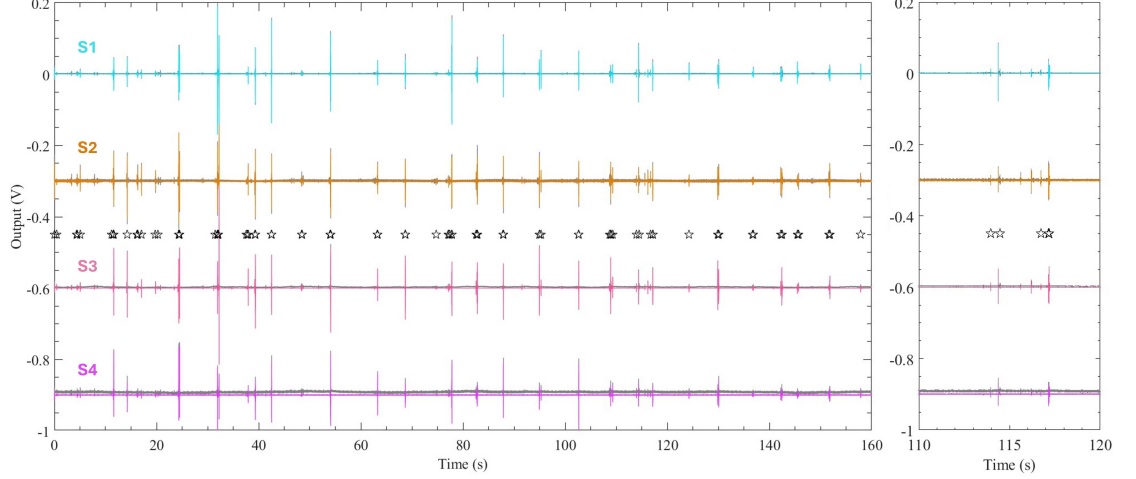
Figure 2.8: Superposition of the raw seismograms (in gray) recorded by each accelerometer and the corresponding highpass-filtered and denoised seismogram color-coded by the accelerometer index. Each black pentagram indicates a STA/LTA detected acoustic event that simultaneously triggers all four accelerometers, where the P-wave arrival time differences among any pairs of accelerometers are all smaller than the preset threshold, 2.0×10^{-4} s. The acoustic signals recorded by the accelerometers S2, S3, and S4 are offset by -0.3 V, -0.6 V, and -0.9 V for better visualization. The right panel shows a zoom-in view for the period ranging from 110 s to 120 s to show the comparison between the raw seismograms and the processed ones. This experiment is performed under a normal load of 500 N with a constant loading rate of 25 μm/s.

S2, S3, and S4 are offset by -0.3 V, -0.6 V, and -0.9 V for better visualization. The raw acoustic signals recorded by the four sensors are all shown in gray (Figure 2.8). A good synchronized triggering of the four sensors is observed for all the large and intermediate amplitude events, as well as most of the small amplitude events. The sensors S2 and S4 record greater noise, compared to the others, since

they are located closer to the shear actuator.

For the acoustic data recorded by each channel, an 8th-order highpass Butterworth filter with a cutoff frequency of 5 kHz is designed to filter all the raw acoustic data. Subsequently, the highpass-filtered acoustic signal of the first three seconds is sampled as noise to obtain the frequencies corresponding to its spectral estimation. Finally, an infinite impulse response bandstop filter is designed to filter the noise based on the previous frequency estimation. The resulting acoustic signals color-coded by the accelerometer index are displayed in Figure 2.8. From the superposition of the raw (in gray) and the highpass-filtered and denoised (in color) seismograms (right panel in Figure 2.8), it is clear that the noise components are evidently diminished for all four channels, especially for channels S2 and S4.

The short-term-average to long-term-average ratio (STA/LTA) algorithm (Earle & Shearer, 1994) is applied to automatically detect acoustic events triggered in the experiments. This procedure is similar to that applied to earthquake sequences in nature. According to the short signal duration and high frequency acquisition rate in such experimental configuration, the window lengths of STA and LTA are tailored as 0.4 ms and 2.0 ms, respectively. Meanwhile, the threshold for triggering a STA/LTA detection is set to be 3.0. In our detection, only an event simultaneously triggers all four accelerometers, and the P-wave arrival time differences among any pairs of accelerometers are all smaller than the preset threshold, 0.2 ms, which can be considered as an acoustic event. The detection of acoustic events is illustrated in Figure 2.8, where a total of 144 acoustic events indicated by the black pentagram are detected in this experiment. These acoustic events capture the dynamic ruptures at different amplitude scales that occurred on the fault interface.

2.4.2   Synchronization of Multiple Measurements

The temporal evolution of the shear force measurement of the macroscopic fault system, the mean acoustic data averaged over the four channels, and the optically derived average cumulative slip of asperity over all asperities are presented in Figure 2.9. Moreover, the detected acoustic events are also marked as black pentagrams to correspond to the temporal evolution of these multiple measure-
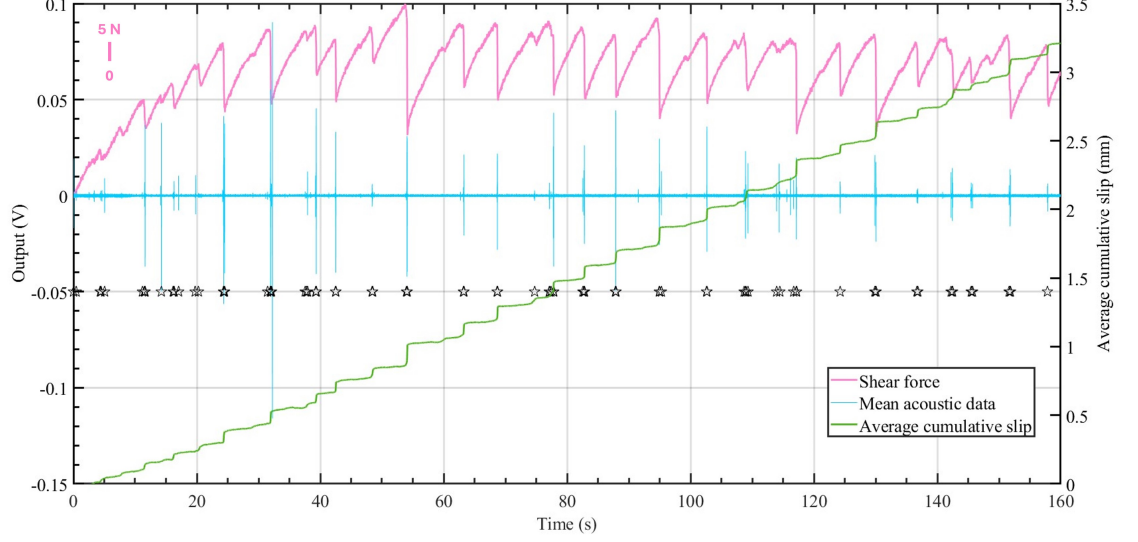
Figure 2.9: Synchronization of the shear force measurement of the macroscopic fault system, the mean acoustic data averaged over the four accelerometers, and the average cumulative slip of asperity over all asperities computed from optical monitoring. Black pentagrams indicate the seismic events detected through the acoustic data, and these events track the shear force drops and average cumulative slip increments at both small and large scales. This experiment is performed under a normal load of 500 N with a constant loading rate of 25 μm/s.

ments. In general, we observe good synchronization and correlation between the shear force drops, amplitudes of the detected acoustic events, and the increment of the average cumulative slip of asperity. Specifically, these acoustic events can not only track the large-scale stick-slip events with large shear force drops (e.g., the large event at around 55 s with a force drop of about 40 N) but also the small-scale local events with small shear force drops (e.g., the small event at around 20 s with a force drop of about 7 N).

We also present the typical acoustic signals of noise, a small-scale event, and a large-scale stick-slip event, as well as their corresponding short-time Fourier transform-based spectrograms (Figure 2.10). The aforementioned acoustic signals (left panel, Figure 2.10) of noise, the small-scale event, and the large-scale event are respectively extracted at times 0.8-1.8 s, about 19.810 s, and about 54.055
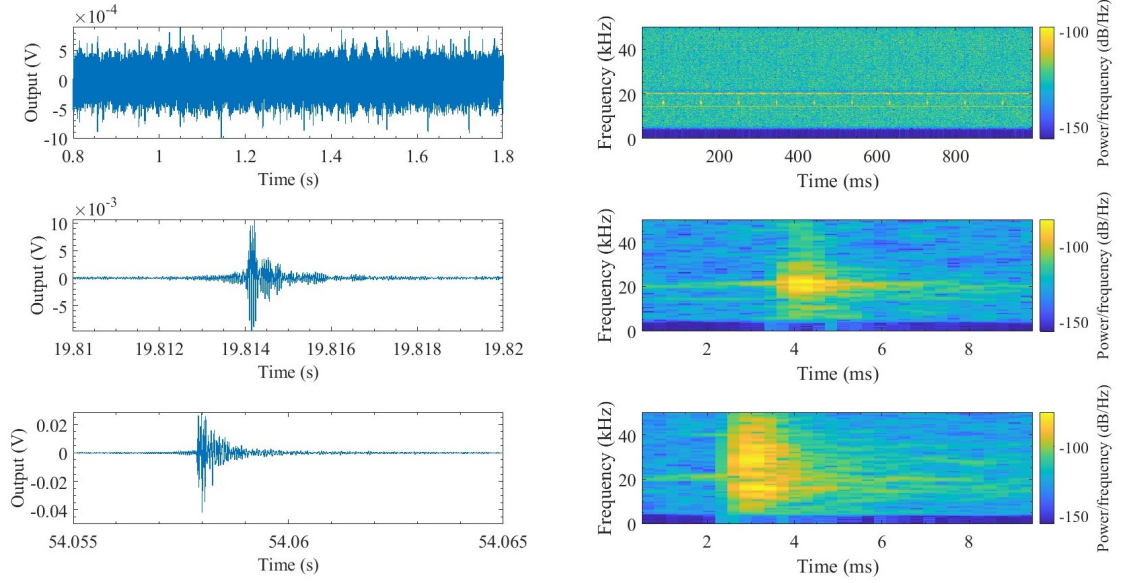
Figure 2.10: Typical examples of the highpass-filtered (5 kHz) and denoised acoustic signals and corresponding short-time Fourier transform-based spectrogram of noise (**a**), a small-scale event (**b**), and a large-scale event (**c**). Note that the scales in the y axis are different for the three signals that are extracted from the same acoustic data (the mean acoustic signal averaged over the four accelerometers) shown in Figure 2.9. A large-scale event presents more high-frequency characteristics, whereas a small-scale event is dominated by the intermediate frequency band. No dominant frequency is shown in the spectrogram of noise except a peak is observed at 20kHz.

s, from the mean acoustic data shown in Figure 2.9. It is noteworthy that the amplitudes of the three signals vary by several orders of magnitude, where the amplitude of the noise is the smallest and relatively constant while the large-scale event presents an energetic burst in amplitude and then decays rapidly. According to the spectrogram of the large-scale event, the duration is about 2.0 ms, and such an event presents a burst of high-frequency characteristics (up to 50 kHz) followed by rapid energy decay. On the contrary, the spectrogram of the small-scale event is dominated by an intermediate frequency of about 20 kHz. Its duration is about 3 ms, which lasts longer than the burst-like large-scale stick-slip events. No dominant frequency is observed for the acoustic signal of the noise except a peak is observed

at 20kHz. Note that the cutoff frequency of 5 kHz shown in all three spectrograms comes from the highpass filtering previously performed.

To quantitatively illustrate the time synchronization between the optical monitoring and the acoustic monitoring, the cross-correlation between the initial times of optical events and detected acoustic events are computed (Figure 2.11). The
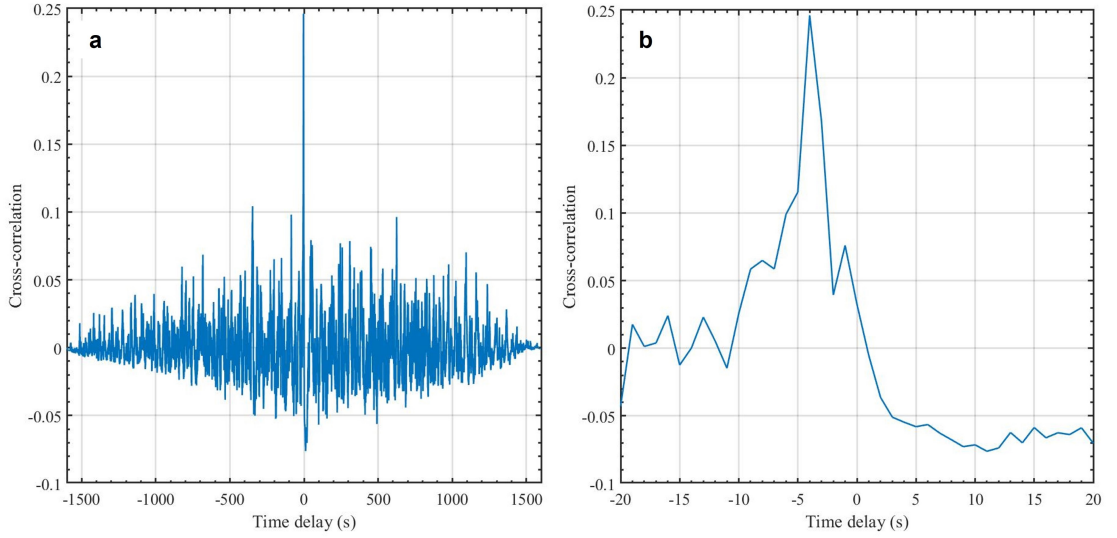
Figure 2.11: **a:** Cross-correlation between the initial times of optical and acoustic events, where the mean initial time is removed from both the optical and acoustic catalogs before the cross-correlation. The acoustic events are the seismic events detected before, while the optical events are the slip episodes clustered from the spatiotemporal interactions of different asperities. A nearly symmetric distribution of the cross-correlation function is observed. According to the zoom view (**b**), the maximum cross-correlation is found at -4 s time lag, indicating a time synchronization issue that needs to be optimized in further tests.

acoustic events are the detected events (black pentagrams) shown in Figure 2.9. The optical events are the slip episodes clustered from the spatiotemporal interactions of different individual asperity slips, which are defined from the slip history of each asperity and obtained solely by optical monitoring (see also Section 4.5.1 for more details). The maximum cross-correlation, for this single experiment, is found at -4 s time lag. This large time delay indicates a time synchronization issue

with the current technical configuration, which needs to be improved in our further tests.

2.4.3 Concluding Remarks

Although with the current technical configuration of acoustic emission, the high-quality acoustic signals at local asperity and global fault scales, and the accurate detection of acoustic events are achieved in the preliminary results of a single experiment. However, a time synchronization issue between the optical monitoring and the acoustic monitoring is found, which needs to be improved through further tests. At present, two high-speed acquisition cards (PCIe3660, ADDI-DATA) which enable the recording of up to 8 signals at 24 bits up to 4 MHz, as well as a set of 8 accelerometers from Brüel & Kjær company are under testing, which will contribute better acoustic data acquisition related to the slip of the analog fault interface. In addition to developing the best acoustic acquisition system adaptive to our experimental setup, we will also find the relevant acquisition frequency range, the number of channels to be used, and the most appropriate positions of the sensors for monitoring the acoustic signal linked to the sliding of the asperities. The aforementioned tests of acoustic monitoring are expected to improve the amplitude quantification and precisely locate the acoustic events, for better coupling with the optical monitoring, as well as illustrating the link between seismicity and slips of asperities.

2.5 Rate and State Frictional Parameters of the Multi-Asperity Interface

To measure the rate and state frictional parameters of the multi-asperity interface, which include the direct effect a, the evolution effect b, and the critical slip distance D_c, the slide-hold-slide experiments and velocity-step experiments are subsequently performed with this interface.

2.5.1 Slide-Hold-Slide Experiments

The slide-hold-slide experiments are used to measure the static friction of a fault interface (Marone, 1998b). In particular, the sliding of the interface is interrupted for a specific time, here the holding time sequence, after which the original loading is recovered to slide the interface again and measure the maximum friction coefficient (e.g., Figure 1.6b). By repeating the slide-hold-slide process, the static friction of the interface at the predefined holding time sequence can be measured by picking up the corresponding maximum friction coefficient. A linear increase of the static friction with the logarithmic hold time is expected. This linear relation explains the healing of the fault interface, and its slope corresponds to the evolution effect b in the rate and state frictional law (e.g., Figure 1.6a).
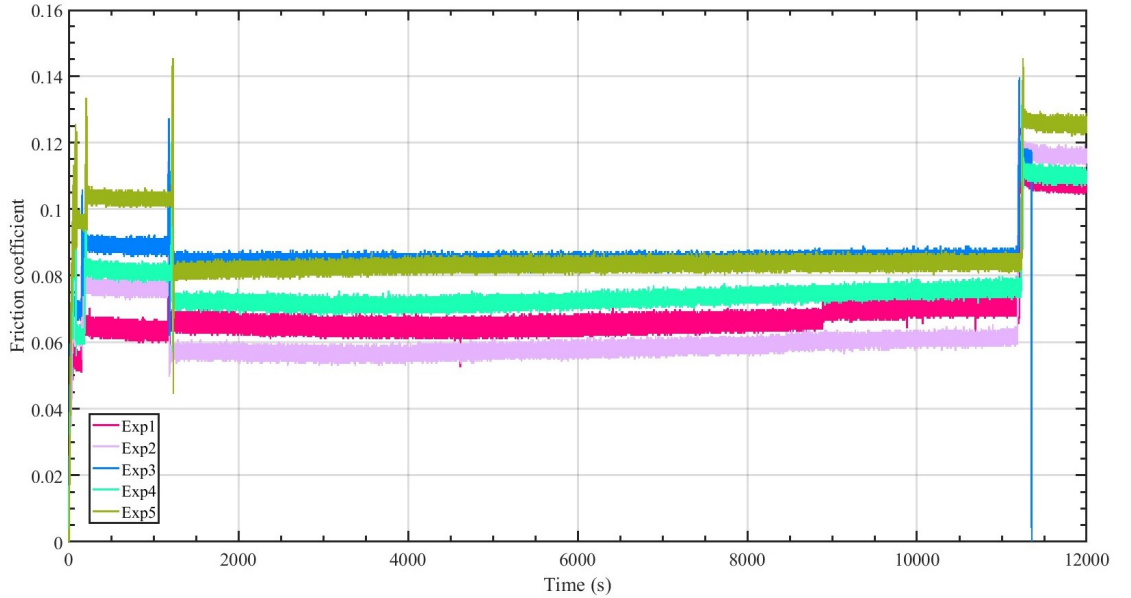
Figure 2.12: Temporal evolution of the friction coefficient of the multi-asperity interface during the five slide-hold-slide experiments. All the experiments are performed under a normal load of 500 N and a loading rate of 15 μm/s. All the experiments have a holding time sequence of 10 s, 100 s, 1000 s, and 10000 s. Each experiment is coded by color. Note the sudden friction coefficient drop of Exp3 at about 11300 s is due to the stop of the shear loading.

Five slide-hold-slide experiments were conducted using the multi-asperity in-

terface under a normal load of 500 N and a loading rate of 15 μm/s, where all experiments have a holding time sequence of 10 s, 100 s, 1000 s, and 10000 s. Figure 2.12 presents the temporal evolution of the friction coefficient. Each experiment is coded by color. Note the sudden friction coefficient drop of Exp3 at about 11300 s is due to the manual stop of the shear loading. Variations of the absolute friction coefficient are observed among the five experiments, which could be a result of the variations of the experimental environment. For example, our experimental setup cannot maintain the same temperature and humidity for all experiments. The increase of the friction coefficient with the holding time is evidenced for all experiments, though variations of the absolute friction coefficient exist.

The maximum friction coefficient followed by holding the interface for each specific time is selected for each slide-hold-slide experiment. Figure 2.13 shows the measurements of the static friction coefficients of the multi-asperity interface at different holding times in the five experiments, where the color coding is the same as Figure 2.12. Variations of the absolute static friction coefficients are observed among all five experiments. In general, a consistent trend that the static friction coefficient increases linearly with the logarithmic hold time is observed for all five experiments. The values of the evolution effect b of the five experiments are given by the best linear fits (shown as the color-coded lines), with a minimum value of 0.0071 and a maximum value of 0.0197, where the values of the evolution effect b of Exp1, Exp2, and Exp3 are close to each other. An outlier is found at the holding time of 10000 s for Exp5. The friction coefficient at the holding time of 1000 s should never be less than the friction coefficient at the holding time of 1000 s if we assume the friction coefficients at 10 s, 100 s, and 1000 s are robust. Given this unreasonable measurement, Exp5 is excluded from further analysis. The values of the evolution effect b of the four retained experiments (i.e., Exp1, Exp2, Exp3, and Exp4) are averaged as 0.0171±0.0030, which is the estimation of the evolution effect b of the multi-asperity interface.
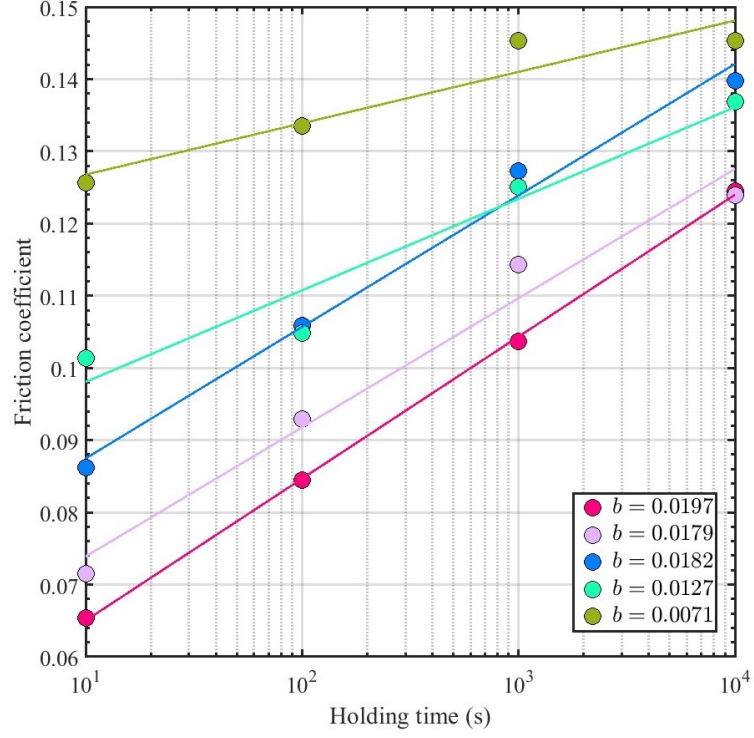
Figure 2.13: Measurements of the static friction of the multi-asperity interface at different holding times for all five slide-hold-slide experiments. Each experiment is color-coded the same as Figure 2.12. Each circle denotes the static friction coefficient, whereas each line represents the best linear fit of the fault healing for each experiment. Exp5 is excluded due to the outlier at the holding time of 10000 s. The mean value of the evolution effect b averaged over the four retained experiments is 0.0171 ± 0.0030.

2.5.2 Velocity Step Experiments

The velocity step experiments measure the dynamic friction of a fault interface in response to the abrupt change in the sliding rate (Marone, 1998b). Specifically, the initial sliding rate of the interface is abruptly increased or decreased by imposing a new loading rate will lead to a change in the friction coefficient. The friction evolves over a critical slip distance, D_c, upon a sudden change in the sliding rate and then to the dynamic friction in a new state to be measured (e.g., Figure 1.6d). If this dynamic friction coefficient is smaller than the initial friction

coefficient in response to the sliding rate increment, the interface is defined as velocity-weakening. By changing the variations of the velocity steps, the dynamic friction coefficients at different sliding rates can be measured. Moreover, a linear relationship between the dynamic friction coefficient and the logarithmic slip rate of the interface is expected (e.g., Figure 1.6c) to derive the direct effect a in the rate and state framework.

Five velocity step experiments were performed with the multi-asperity interface under a normal load of 200 N. Each experiment highlights the velocity up-step from 15 μm/s to 150 μm/s and the velocity down-step from 150 μm/s to 15 μm/s. Figure 2.14 displays a typical experimental result, in which the friction coefficient evolves as a function of time (top) and as a function of the displacement of the shearing point (bottom). The inset shows the temporal evolution of the loading rate (indicated by the slope). Each experiment starts with a loading rate of 15 μm/s for about 120 s followed by the velocity up-step. At the velocity up-step, the velocity-weakening behavior of the interface is evidenced. Equivalently, the strength of the interface increases at the velocity down-step. According to the rate and state friction (Figure 1.7a), the critical slip distance, D_c, can be evidenced as the evolution distance at the velocity step. Meanwhile, the friction coefficient variation due to the velocity step is equal to $(a - b)\ln(V/V_0)$, which can be used to compute the value $(a - b)$ since friction coefficient variation and $\ln(V/V_0)$ are known.

To show more details at the velocity steps, the zoom view of the friction coefficient evolution as a function of time (Figure 2.15 a and b) and as a function of shearing point displacement (Figure 2.15 c and d) are presented for the first velocity up-step. Figure 2.15b and Figure 2.15d are the zoom views of Figure 2.15a and Figure 2.15c with finer resolution, respectively. We observe an evident decrease of the friction coefficient during the velocity up-step (Figure 2.15b). Meanwhile, the characteristic slip distance involving the evolution of the friction coefficient is also observed (Figure 2.15d).

However, the large normal load (i.e., 200 N) imposed on the multi-asperity interface makes it experience sequences of stick-slip before and after the velocity
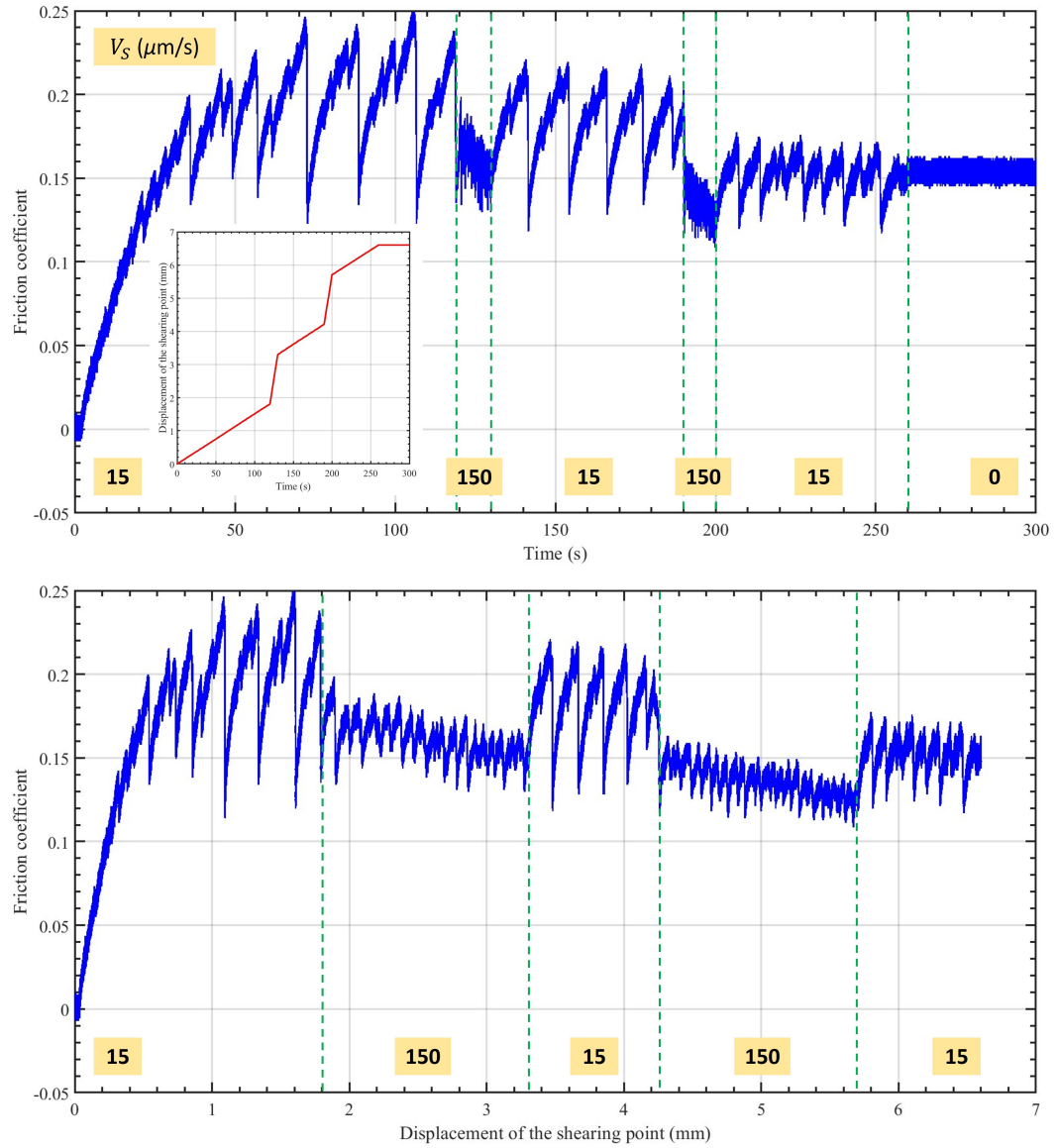
Figure 2.14: Typical evolution of the friction coefficient as a function of time (top) and as a function of the shearing point displacement (bottom). The green dashed lines roughly divide the evolution into several periods corresponding to different loading rates that are indicated in μm/s. The inset shows the temporal evolution of the displacement of the shearing point to indicate the history of the loading rate. The velocity up-step from 15 μm/s to 150 μm/s and the velocity down-step from 150 μm/s to 15 μm/s are highlighted in this experiment.
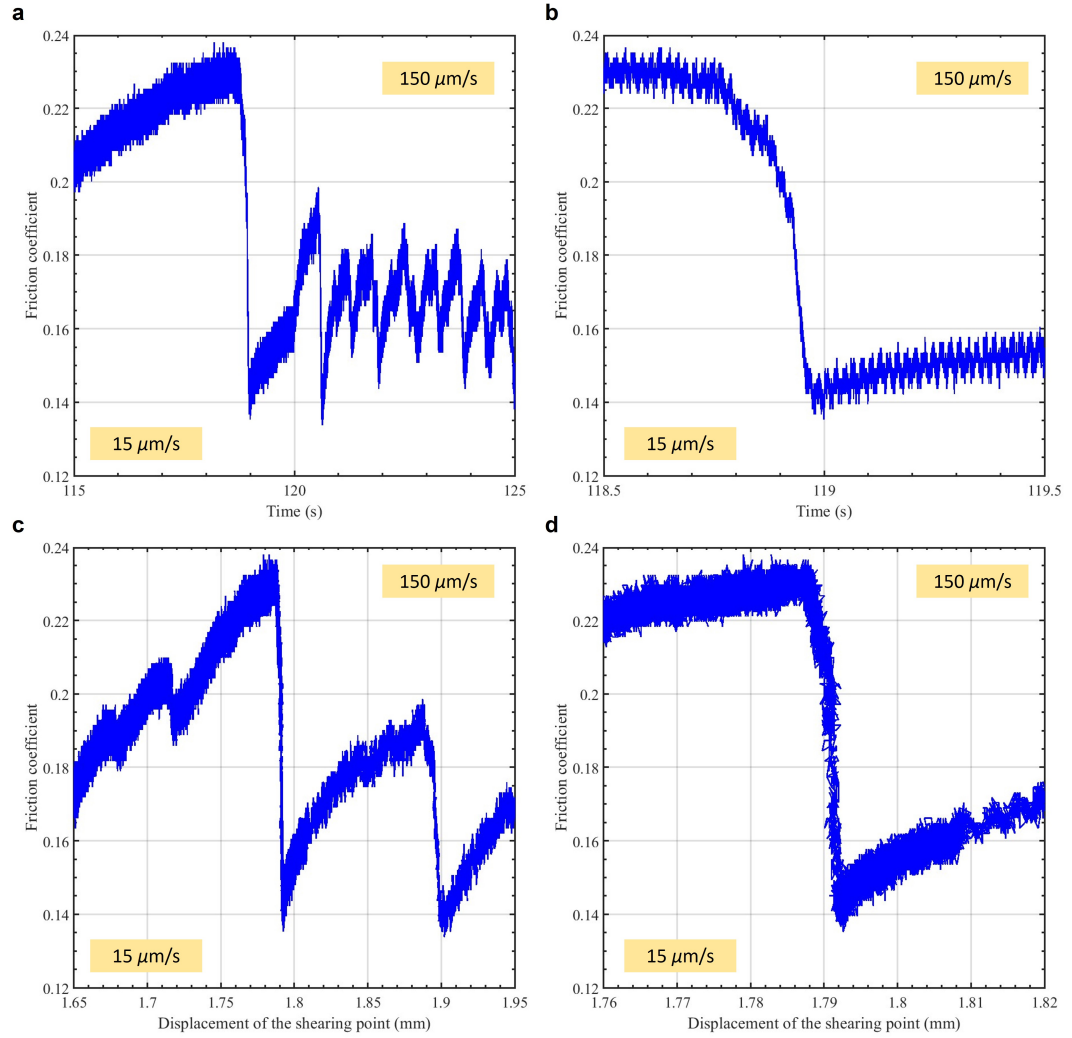
Figure 2.15: a: Zoom view of the evolution of the friction coefficient as a function of time during the first velocity up-step shown in Figure 2.14. **b:** Zoom view of Figure 2.15a with higher resolution. **c:** Zoom view of the evolution of the friction coefficient as a function of shearing point displacement during the first velocity up-step shown in Figure 2.14. **d:** Zoom view of Figure 2.15c with higher resolution.

steps (Figure 2.14). Therefore, it is difficult to determine an accurate value of the direct effect a with small uncertainty, since no accurate friction coefficients of the steady states before and after the velocity step can be obtained. Further experiments should be performed with a normal load of less than 50 N because this range of normal load can induce the steady sliding of the multi-asperity interface (see the temporal evolution of the shear force under different normal loads of the multi-asperity interface in Figure 4.4). With appropriate normal loads, the values of the direct effect, a, and the critical slip distance, D_c, can be better constrained through the velocity step experiments.

2.5.3 Concluding Remarks

The slide-hold-slide experiments and velocity step experiments were performed on the multi-asperity interface to measure its rate and state frictional parameters, which are the direct effect a, the evolution effect b, and the critical slip distance D_c.

Five slide-hold-slide experiments were performed with the multi-asperity interface, where all the experiments have a holding time sequence of 10 s, 100 s, 1000 s, and 10000 s. Fault healing is observed for all the experiments. One experiment with an outlier that is contradictory to the fault healing mechanism is excluded. The value of the evolution effect b is estimated as 0.0171±0.0030 by averaging the evolution effects of all the retained slide-hold-slide experiments.

Five velocity step experiments were performed one the same interface, where each one highlights the velocity up-step from 15 μm/s to 150 μm/s and the velocity down-step from 150 μm/s to 15 μm/s. Velocity-strengthening is evidently observed in all the experiments. Yet, due to the large applied normal load, the interface is always in the stick-slip regime rather than the steady state, which causes large uncertainty for estimating the robust values of the direct effect a and the critical slip distance D_c. Further velocity step experiments should be conducted with a normal load of less than 50 N, which can make sure the interface slips steadily. In this circumstance, the values of $a\ln(V/V_0)$, $b\ln(V/V_0)$, and $(a-b)\ln(V/V_0)$ could be better estimated from the clear friction coefficient variation and known velocity

step, which results in a much more precise estimation of the direct effect a and the critical slip distance D_c.

2.6 Rate and State Frictional Parameters of the Single-Asperity Interface

The analog fault model with numerous asperities (i.e., Figure 2.1) presents an effective friction rather than the friction of a single asperity. Therefore, a single-asperity interface needs to be prepared to experimentally measure the rate and state frictional parameters. To this end, a rigid embedding material with little impact on the rheology of the contact is needed for such an interface. Otherwise, the thick PMMA plate will easily contact with the silicone when only one single asperity is embedded, which will modify the physical process from friction to adhesion. More importantly, the time effect of friction will be mixed with the time effect of the silicone block.

Plaster is employed as the embedding substrate to replace the soft silicone block. Compared to the preparation of the multi-asperity analog fault model, the procedures for preparing such a rigid plaster block embedded with a single asperity are much easier: The plaster powder (from Esprit Composite) is fully mixed with water at room temperature, and then the mixture is poured into the same mold (of dimensions 10×10×10 cm) to form a layer of about 3 cm thickness. A single PMMA bead, the same as the beads used in the analog fault model, is embedded into the mixture with a depth approximately equal to its radius. After waiting for at least 24 hours, the solidified plaster block embedded with a single asperity is removed from the mold. Figure 2.16 displays the picture of the resulting plaster block with a single asperity.

A single-asperity interface is achieved by contacting the thick PMMA plate with the single asperity embedded in the rigid plaster block. Slide-hold-slide experiments and velocity-step experiments are subsequently performed with this interface to measure the rate and state frictional parameters of a single asperity.
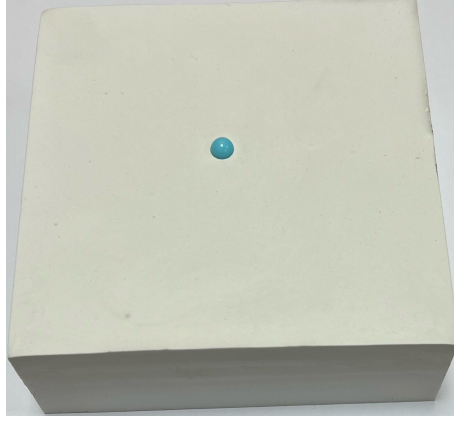
Figure 2.16: Picture showing a single rigid PMMA bead, the same as the beads used in the analog fault model shown in Figure 2.1, embedded in a rigid plaster block with dimensions 10×10× ∼3 cm.

2.6.1   Slide-Hold-Slide Experiments

Six slide-hold-slide experiments were performed with the single-asperity interface under a normal load of 200 N and a loading rate of 15 μm/s, where four of them have a holding time sequence of 10 s, 100 s, 1000 s, and 10000 s and the other two have a holding time sequence of 10 s, 50 s, 100 s, 500 s, 1000 s, 5000 s, and 10000 s. The temporal evolution of the friction coefficient is presented in Figure 2.17, where each experiment is color-coded. We observe that variations of the absolute friction coefficient exist among the six experiments. Such variations may be due to the variations of the experimental environment, such as the temperature and humidity since our experimental setup is incapable of maintaining the same environment for all the experiments. Despite variations of the absolute friction coefficient, an increment of the friction coefficient is also observed after each holding for all the experiments.

For each slide-hold-slide experiment, we pick up the maximum friction coefficient after holding the interface for each specific time. Figure 2.18 summarizes the measurements of the static friction coefficients after holding the single-asperity interface at different times in the six experiments. The absolute static friction coefficients of the four experiments (i.e., Exp1, Exp2, Exp3, and Exp4) are very
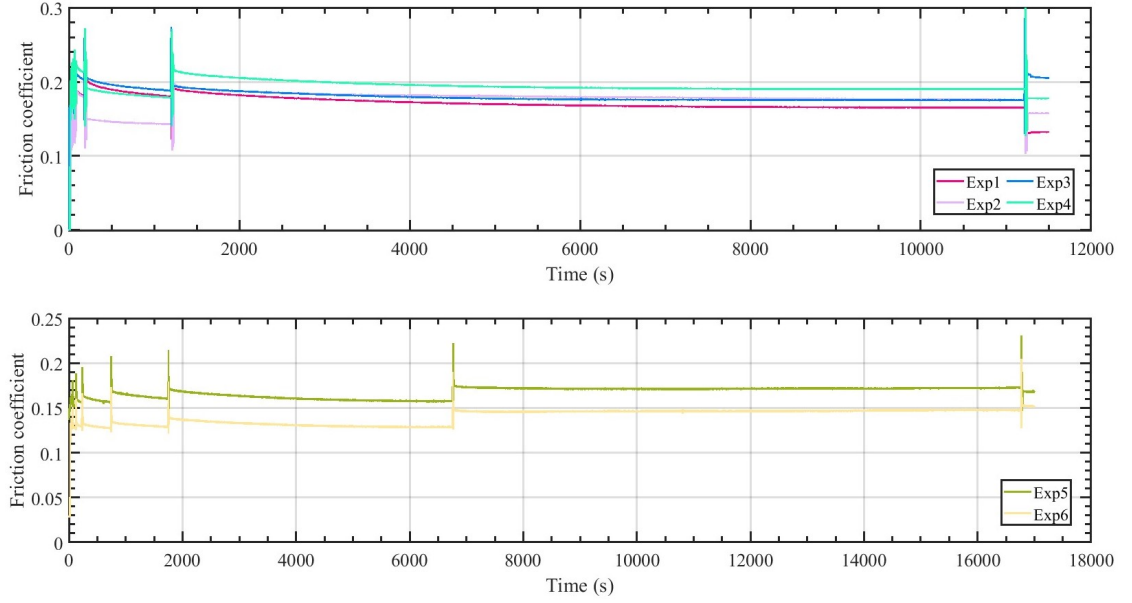
Figure 2.17: Temporal evolution of the friction coefficient of the single-asperity interface during the six slide-hold-slide experiments. All the experiments are performed under a normal load of 200 N and a loading rate of 15 μm/s. Four experiments (top) have a holding time sequence of 10 s, 100 s, 1000 s, and 10000 s and the other two (bottom) have a holding time sequence of 10 s, 50 s, 100 s, 500 s, 1000 s, 5000 s, and 10000 s. Each experiment is coded by color.

close to each other, while the corresponding ones of the other two experiments (i.e., Exp5 and Exp6) are much smaller. In general, all six experiments presents a consistent trend that the static friction coefficient increases linearly with the logarithmic hold time. The values of the evolution effect b of the six experiments are given by the best linear fits (shown as the color-coded lines), with a minimum value of 0.0165 and a maximum value of 0.0222. These six values are averaged as 0.0183±0.0022, which is the value of the evolution effect b in the rate and state frictional law governing the motion of a single asperity.

2.6.2 Velocity Step Experiments

Five velocity step experiments were performed with the same single-asperity interface under a normal load of 200 N. Each experiment highlights the velocity up-
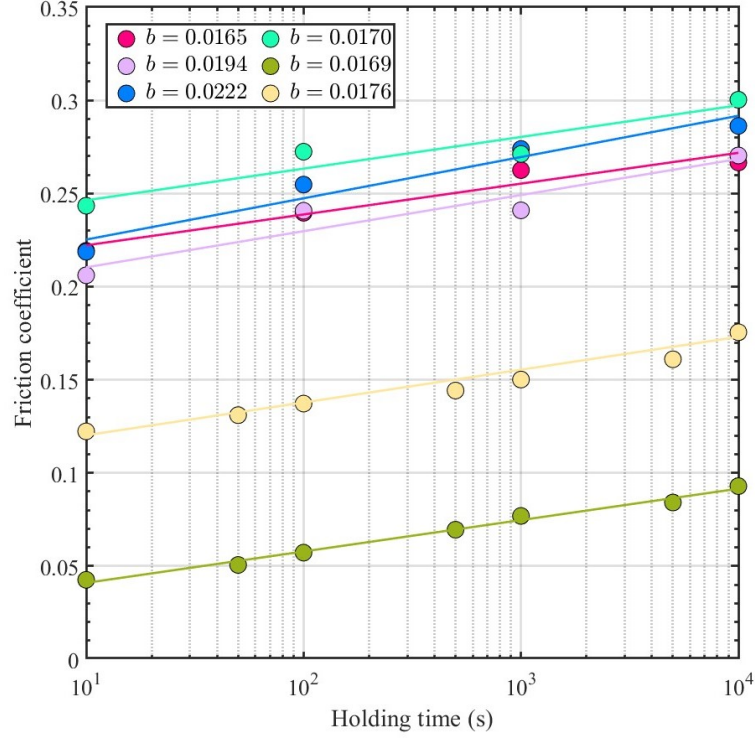
Figure 2.18: Measurements of the static friction of the multi-asperity interface at different holding times for all six slide-hold-slide experiments. Each experiment is color-coded the same as Figure 2.17. Each circle denotes the static friction coefficient, whereas each line represents the best linear fit of the fault healing for each experiment. The mean value of the evolution effect b averaged over all six experiments is 0.0183 ± 0.0022.

step from 5 μm/s to 50 μm/s and the velocity down-step from 50 μm/s to 5 μm/s. Figure 2.19 illustrates a typical experimental result, in which the friction coefficient evolves as a function of time (top) and as a function of the displacement of the shearing point (bottom). The inset displays the temporal evolution of the loading rate (indicated by the slope) imposed on the fault interface. Each experiment starts with a sliding stage at 15 μm/s for about 60 s to achieve a steady state of the interface. At the velocity up-step, the velocity-weakening behavior of the interface is evidenced. Equivalently, the strength of the interface increases at the velocity down-step. According to the rate and state friction (Figure 1.7a), the critical slip distance, D_c, can be evidenced as the evolution distance at the velocity
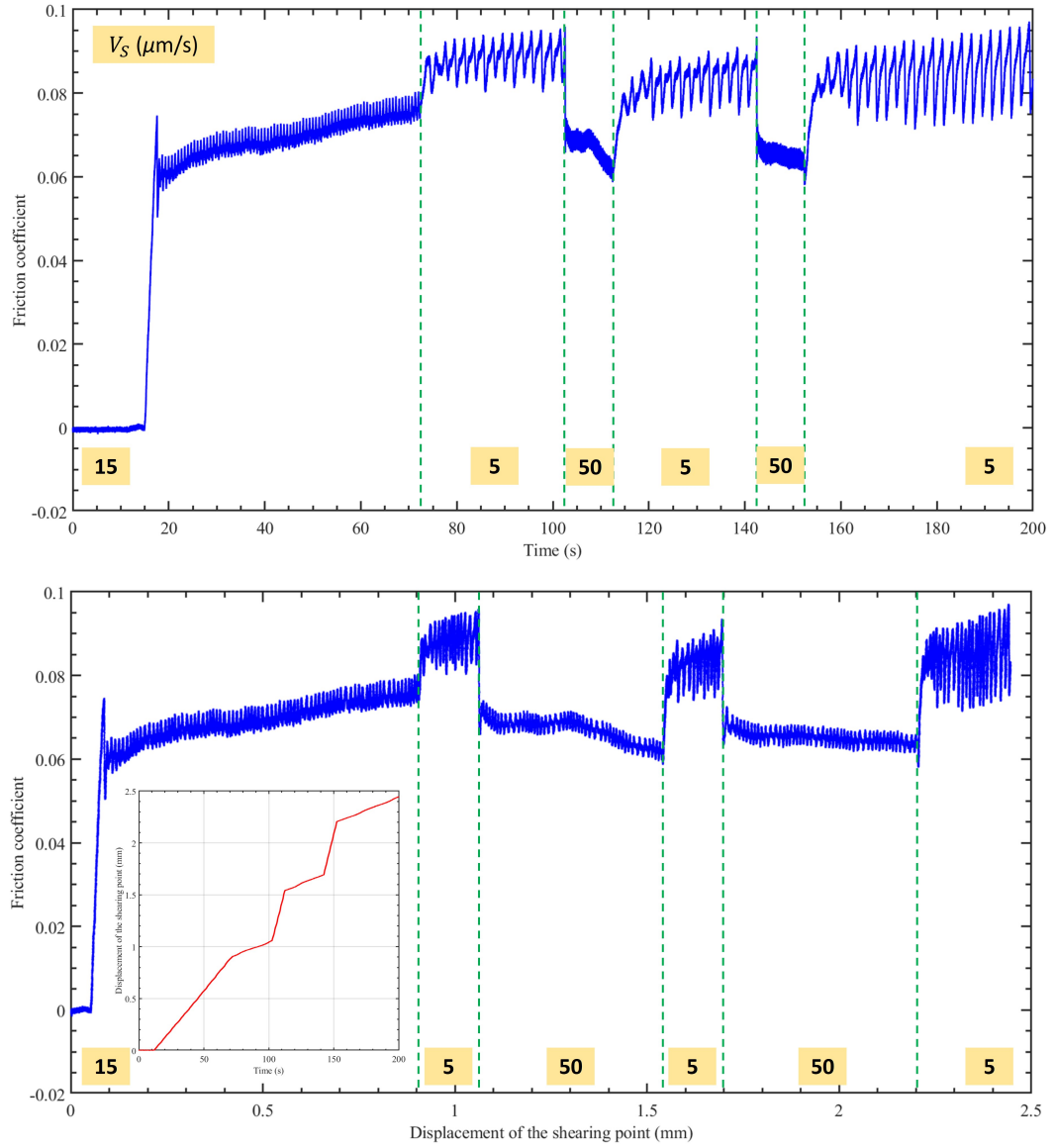
Figure 2.19: Typical evolution of the friction coefficient as a function of time (top) and as a function of the shearing point displacement (bottom). The green dashed lines roughly divide the evolution into several periods corresponding to different loading rates that are indicated in μm/s. The inset shows the temporal evolution of the displacement of the shearing point to indicate the history of the loading rate. The velocity up-step from 5 μm/s to 50 μm/s and the velocity down-step from 50 μm/s to 5 μm/s are highlighted in this experiment.

step. Meanwhile, the friction coefficient variation due to the velocity step is equal to $(a - b) \ln(V/V_0)$, which can be used to compute the value $(a - b)$ since friction coefficient variation and $\ln(V/V_0)$ are known.

To show more details at the velocity steps, the zoom view of the friction coefficient evolution as a function of time (Figure 2.20 a and b) and as a function of shearing point displacement (Figure 2.20 c and d) are presented for the first velocity up-step. Figure 2.20b and Figure 2.20d are the zoom views of Figure 2.20a and Figure 2.20c with finer resolution, respectively. We observe an evident decrease of the friction coefficient during the velocity up-step (Figure 2.20b). Meanwhile, the characteristic slip distance involving the evolution of the friction coefficient is also observed (Figure 2.20d).

For all the ten velocity up-steps in the five experiments, we superimpose them by setting both the friction coefficient peak and its time as zero and present the friction coefficient variation as a function of time variation (Figure 2.21a) and as a function of shearing point displacement variation (Figure 2.21b). It is found that deviations of the initial friction coefficient variation, which is the difference between the initial friction coefficient and the minimum friction coefficient, exist among these ten velocity up-steps. Assuming the initial friction coefficient variation corresponding to $(a-b) \ln(V/V_0)$ (Figure 1.7), such large deviations will result in a large uncertainty in the estimation of the direct effect a. A preliminary value of about 2-3 μm for the critical slip distance, D_c, can be estimated from Figure 2.21b if we assume the minimum friction coefficient variation corresponds to the initiation of the new state of the fault interface.

To measure the direct effect a in the rate and state friction with velocity step experiments, the most used way is to steadily slide the fault interface before the velocity step, which makes it easy to determine the value of $a \ln(V/V_0)$ by computing the difference between the relatively constant friction coefficient before the velocity step and the peak friction coefficient during the velocity step (Figure 1.7). The fault evolves to another steady state with another relatively stable friction coefficient through a critical slip distance. Similarly, the relatively stable friction coefficient under the new steady state makes it easy to determine the values of
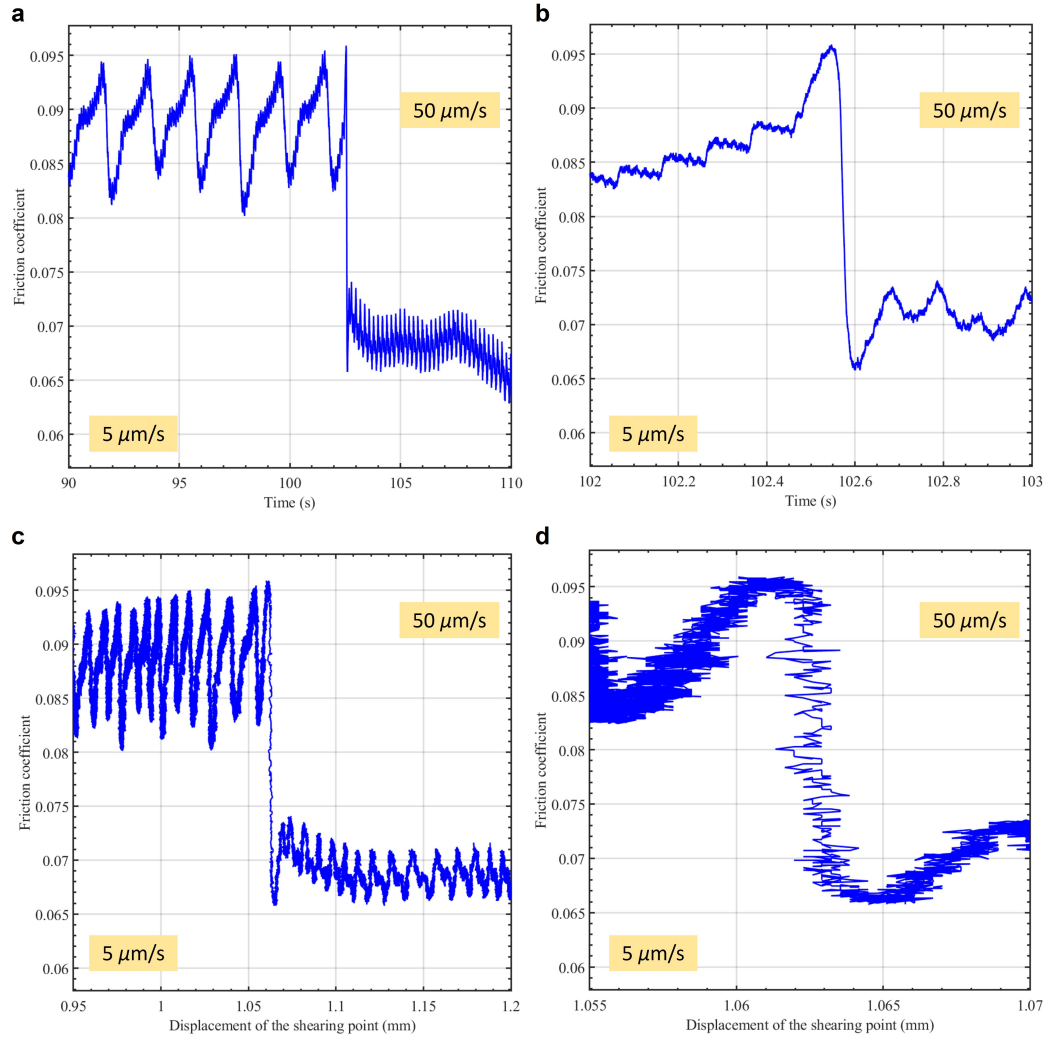
Figure 2.20: a: Zoom view of the evolution of the friction coefficient as a function of time during the first velocity up-step shown in Figure 2.19. **b:** Zoom view of Figure 2.20a with higher resolution. **c:** Zoom view of the evolution of the friction coefficient as a function of shearing point displacement during the first velocity up-step shown in Figure 2.19. **d:** Zoom view of Figure 2.20c with higher resolution.
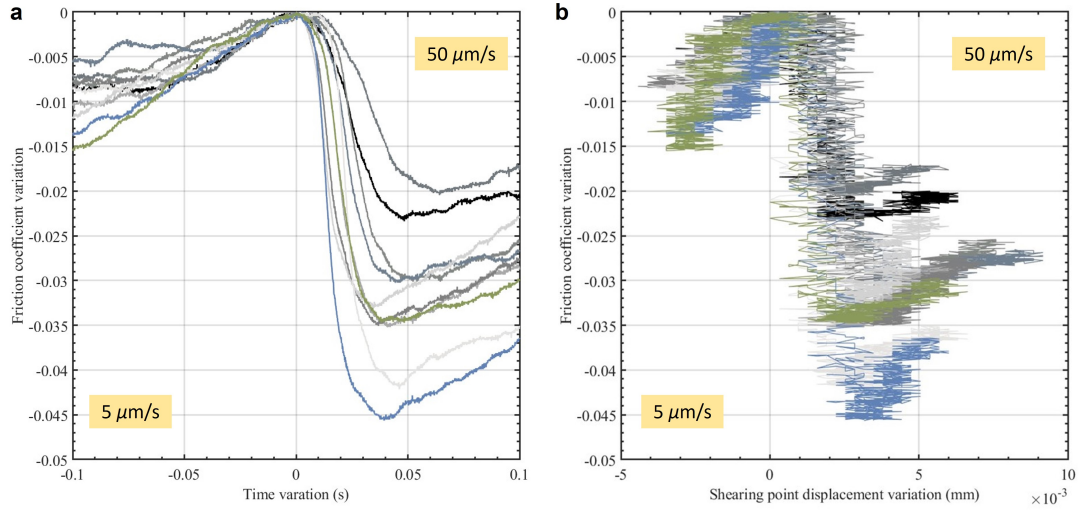
Figure 2.21: Superposition of the friction coefficient variation as a function of time variation (**a**) and as a function of shearing point displacement variation (**b**) for all the velocity up-steps in the five experiments, by setting both the friction coefficient peak and its time as zero.

$b \ln(V/V_0)$ and $(a-b) \ln(V/V_0)$. Unfortunately, the single-asperity interface experienced sequences of stick-slip before and after the velocity steps (Figure 2.19) due to the employment of a large normal load (i.e., 200 N), which makes it difficult to determine an accurate value of the direct effect a with small uncertainty. Experiments under the same loading rate and different normal loads need to be performed with the single-asperity interface to find the range of normal load for the steady sliding. Based on this range of normal load, the velocity step experiments can be proceeded with the single-asperity interface to better constrain the values of $a \ln(V/V_0)$, $b \ln(V/V_0)$, and $(a-b) \ln(V/V_0)$, since the steady states of the interface can be achieved before and after the velocity step.

To estimate the direct effect, a, and the critical slip distance, D_c, another possibility is to employ the validated spring-block numerical model (see Section 3.1 for details) to simulate earthquake sequences under loading characteristics the same as those applied in our experiments. Since a robust estimation of the evolution effect, $b = 0.0183 \pm 0.0022$, is known, we could compare the numerical and experimental

earthquake sequences by setting different values for a and D_c. Among the values of a and D_c for numerically producing the frictional behavior of this single-asperity interface, the one that best matches our experimental measurements could be the robust estimation of the frictional parameters.

2.6.3 Concluding Remarks

To measure the rate and state frictional parameters of a single asperity (i.e., the direct effect a, the evolution effect b, and the critical slip distance D_c), the single-asperity interface was prepared by replacing the silicone block with the rigid plaster as the embedding substrate.

Six slide-hold-slide experiments were performed with the single-asperity interface, where four of them have a holding time sequence of 10 s, 100 s, 1000 s, and 10000 s and the other two have a holding time sequence of 10 s, 50 s, 100 s, 500 s, 1000 s, 5000 s, and 10000 s. A robust experimental estimation of the evolution effect b, which is 0.0183±0.0022, is obtained by averaging the evolution effects of all six slide-hold-slide experiments.

Five velocity step experiments were performed with the same single-asperity interface, where each one features the velocity up-step from 5 μm/s to 50 μm/s and the velocity down-step from 50 μm/s to 5 μm/s. However, with current datasets of the velocity step experiments, it is not easy to constrain the robust values of the direct effect, a, and the critical slip distance, D_c, because the applied large normal load (i.e., 200 N) makes the interface be in the stick-slip regime rather than the steady state. More velocity step experiments under a range of normal loads that lead to the steady sliding of the interface are preferred to determine the values of $a \ln(V/V_0)$, $b \ln(V/V_0)$, $(a-b) \ln(V/V_0)$, and D_c from the clear friction coefficient variation and known velocity step. The values computed above can also cross-validate the evolution effect b measured from the slide-hold-slide experiments, which all together enable the robust estimation of the rate and state frictional parameters for each asperity.

2.7   Contributions

Such a novel experimental setup, which can directly capture the subtle motions of hundreds of asperities on a faulting interface, is a significant bedrock for our subsequent experimental and numerical works. The first version of this setup was established by a former PhD student, Camille Jestin, of my supervisors, which only achieved a very preliminary optical monitoring of the faulting interface but without the high-quality capture of the subtle motions of all the asperities.

Since the start of my PhD, I found a better silicone product to produce the silicone block, and the PMMA beads with suitable sizes and colors. I then produced the analog fault model comprising numerous asperities with height variations and random spatial distribution. Based on the first version of the setup, I assembled all the individual experimental elements, supplemented more measuring devices, and calibrated all the devices. In particular, I supplemented the laser for measuring the displacement of the PMMA plate. I calibrated the shearing system including the translation stage and shear force sensor. I also found the loading cylinder with suitable stiffness. In addition, I updated the optical monitoring and determined the best monitoring parameters for the experiments. For the acoustic aspect, it was totally developed by myself. For measuring the rate and state frictional parameters of both multi-asperity and single-asperity interfaces, it was totally implemented by myself. Furthermore, for the setup related to the MTS machine, it was totally developed by myself.

Chapter 3

Modeling of the Analog Fault Interface

The heterogeneous analog fault model, which comprises numerous discrete frictional asperities with normal stress variations randomly embedded in a viscoelastic silicone block, leads to a multi-contact fault interface with a mixture of frictional-viscous deformation and normal stress variations at asperities. Numerical modeling of this interface can complement the understanding of the effects of some fault parameters on the fault slip behavior, such as the viscosity of the silicone block or the spatial distribution of asperities.

A numerical model of such an analog fault interface is developed based on the modified two-dimensional Burridge-Knopoff model, where viscoelastic interactions of asperities are quantified from the physical properties of our experimental setup. Meanwhile, the friction of each asperity is assumed to be governed by rate and state frictional law, in which the rate and state parameters are measured from slide-hold-slide and velocity step experiments using a single-asperity interface. In this chapter, I start the numerical modeling with a single-degree-of-freedom spring-block model that is validated through the benchmark with the Quasi-DYNamic (QDYN) earthquake simulator. I then extend this zero-dimensional model to a one-dimensional model containing two viscoelastically interacting asperities. Finally, a two-dimensional numerical model of the analog fault interface is developed, which considers the viscoelastic interactions among all asperities.

3.1   Spring-Block Model

A spring-block model is established following a single-degree-of-freedom oscillator (Erickson et al., 2008; Madariaga, 1998) to describe the slip behavior of a single asperity on the rough surface (Figure 3.1), where the friction of the block is governed by the rate and state constitutive friction with aging law (Dieterich, 1978, 1979). We consider the block with unit basal area and mass M, coupled by an elastic spring of stiffness K_S to a loading plate with a constant rate, V_S (Figure 3.1). The radiation damping term proposed by Rice (1993) is also included to approximately represent radiated energy loss during earthquake sequences.
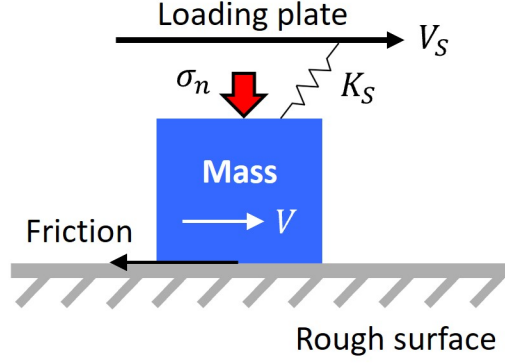
Figure 3.1: Scheme of the single-degree-of-freedom spring-block system. The slider of mass (analogical to an asperity) is coupled by a spring with a stiffness of K_S to a plate with a constant loading rate of V_S, which represents the other side of the fault and the thick PMMA plate in our experimental setup. The friction between the slider and the rough surface is governed by the rate and state friction with aging law in our modeling.

The behavior of this model is described by the following system of ordinary differential equations (ODEs):

$$\begin{cases} \dot{u} = V - V_0 \\ \dot{V} = -\dfrac{1}{M}\left(K_S \cdot u + \mu\sigma_n + \dfrac{G}{2C_S}V\right) \\ \dot{\theta} = 1 - \dfrac{V\theta}{D_c} \end{cases} \tag{3.1}$$

where u, V, and M are respectively the slip, the slip rate, and the mass of the block, σ_n is the normal stress, G is the shear modulus, and C_S is the shear wave speed. μ is the friction coefficient defined by the rate and state friction law,

$$\mu = \mu_0 + a\ln(\dfrac{V}{V_0}) + b\ln(\dfrac{V_0\theta}{D_c}) \tag{3.2}$$

where all these variables have already been explained in equation 1.1 in Section 1.3. We emphasize that the evolution of the state variable, θ, here is defined by the aging law (Dieterich, 1979).

A non-dimensionalization is implemented as follows before numerically solving the system of ODEs (Bolotskaya & Hager, 2022; Erickson et al., 2008):

$$\begin{cases} u_{nd} = \dfrac{u}{u_d} = \dfrac{u}{D_c} \\ V_{nd} = \dfrac{V}{V_d} = \dfrac{V}{V_0} \\ \theta_{nd} = \dfrac{\theta}{\theta_d} = \dfrac{\theta}{a\sigma_n} \\ t_{nd} = \dfrac{t}{t_d} = t\dfrac{V_d}{u_d} = t\dfrac{V_0}{D_c} \end{cases} \tag{3.3}$$

where the variables marked by the subscripts 'nd' and 'd' indicate the non-dimensionalized and dimensional variables, respectively. With these non-dimensionalization equations, the original ODE system (equation 3.1) can be derived into the non-dimensionalized system as:

$$\begin{cases} \dot{u_{nd}} = V_{nd} - 1 \\ \dot{V_{nd}} = -\gamma^2\left(\zeta V_{nd} + u_{nd} + \dfrac{1}{\xi}\left(\dfrac{\mu_0}{a} + \ln(V_{nd}) + (1+\epsilon)\ln(\kappa\theta_{nd})\right)\right) \\ \dot{\theta_{nd}} = \dfrac{1}{\kappa} - V_{nd}\theta_{nd} \end{cases} \tag{3.4}$$

with

$$
\begin{cases}
\gamma = \sqrt{\dfrac{K_S}{M}}\dfrac{D_c}{V_0} \\[2mm]
\zeta = \dfrac{G}{2C_S}\dfrac{V_0 D_c}{K_S} \\[2mm]
\xi = \dfrac{K_S D_c}{a\sigma_n} \\[2mm]
\epsilon = \dfrac{b-a}{a} \\[2mm]
\kappa = a\sigma_n \dfrac{V_0}{D_c}
\end{cases}
\tag{3.5}
$$

This non-dimensionalized ODE system is then solved numerically in MATLAB using a variable-step, variable-order stiff solver (Shampine & Reichelt, 1997; Shampine et al., 1999).

3.1.1 Benchmark with QDYN

The widely used Quasi-DYNamic earthquake simulator (QDYN) (Luo et al., 2017) is applied to simulate the earthquake sequences with the spring-block model. By comparing the earthquake sequences produced by our model and QDYN using the same set of parameters, our spring-block model can be benchmarked.

A set of parameters listed in Table 3.1 is used both in our numerical spring-block model and QDYN. The mass is estimated from the mass of a single PMMA bead used for modeling the asperity, and the shear modulus and shear wave speed of PMMA are respectively estimated by Selvadurai and Glaser (2015a) and Selvadurai, Galvez, Mai, and Glaser (2023). Since the robust estimation of the rate and state frictional parameters have not been obtained through the experiments on the single-asperity interface, the direct effect a and the evolution effect b are extracted from the studies on PMMA interface (Berthoud et al., 1999), and the critical slip distance D_c is represented by a preliminary value. We note that, for the moment, these parameters (Table 3.1) are capable of testing the performance of our spring-block model, although some of them are not perfectly true for our analog fault interface.

With the same set of parameters (Table 3.1), the earthquake sequences produced by our model and QDYN are compared in Figure 3.2. We observe that,

after one earthquake cycle, the evolution of the two sequences achieves the same during the subsequent dozens of cycles. This simple benchmark demonstrates the effectiveness of our developed spring-block model. We note that the inertia term is not included in the governing equations in QDYN, though a good consistency between our model and QDYN is observed. The reason is that in our spring-block model, the mass value is set based on the mass of a PMMA bead, which is about 6×10^{-3} kg, thus only a negligible inertia effect will be considered.

Table 3.1: Parameters used in the spring-block model

Parameter	Symbol	Value
Mass	M	6×10^{-3} kg
Shear modulus	G	2.28 GPa
Shear wave speed	C_S	1330 m/s
Normal stress	σ_n	20 MPa
Loading rate	V_S	10.0 μm/s
Direct effect	a	0.00936
Evolution effect	b	0.01440
Critical slip distance	D_c	1×10^{-5} m
Stiffness of the loading	K_S	1.0 GPa
Reference friction coefficient	μ_0	0.6
Reference slip rate	V_0	10.0 μm/s
Simulation time	t	3000 s
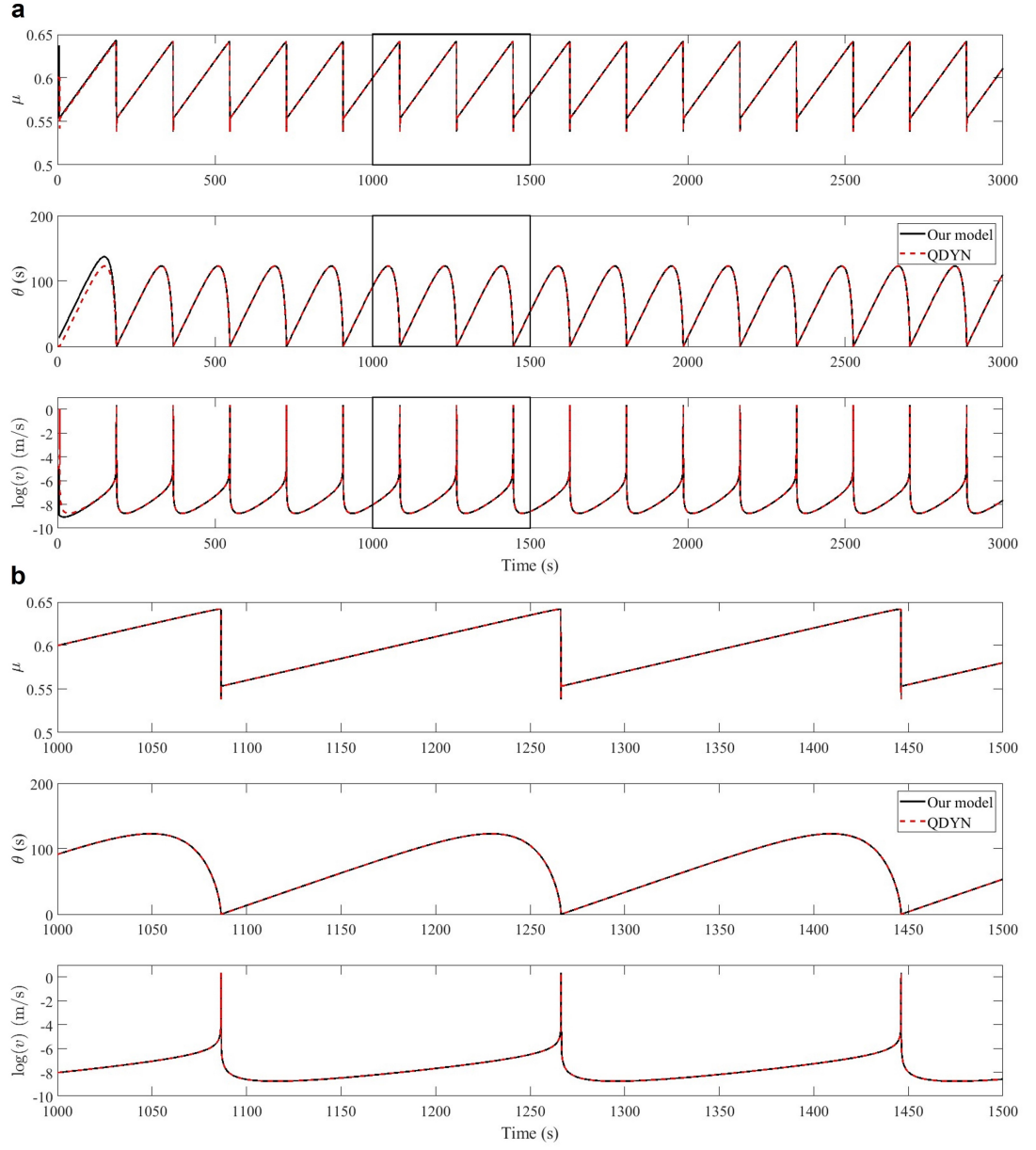
Figure 3.2: a: Earthquake sequences simulated by our spring-block model (black solid line) and QDYN (red dashed line) using the same set of parameters listed in Table 3.1. The two earthquake sequences present the same evolution after the first earthquake cycle. **b:** Zoom-in view of Figure 3.2 ranging from 1000 s to 1500 s.

3.1.2 Tests with Varying Parameters

We conduct a series of tests by separately varying the normal stress, the loading rate, the ratio between the direct effect a and the evolution effect b, and the critical slip distance while keeping the other parameters the same as Table 3.1 to further test the established spring-block model.

Varying the Normal Stress
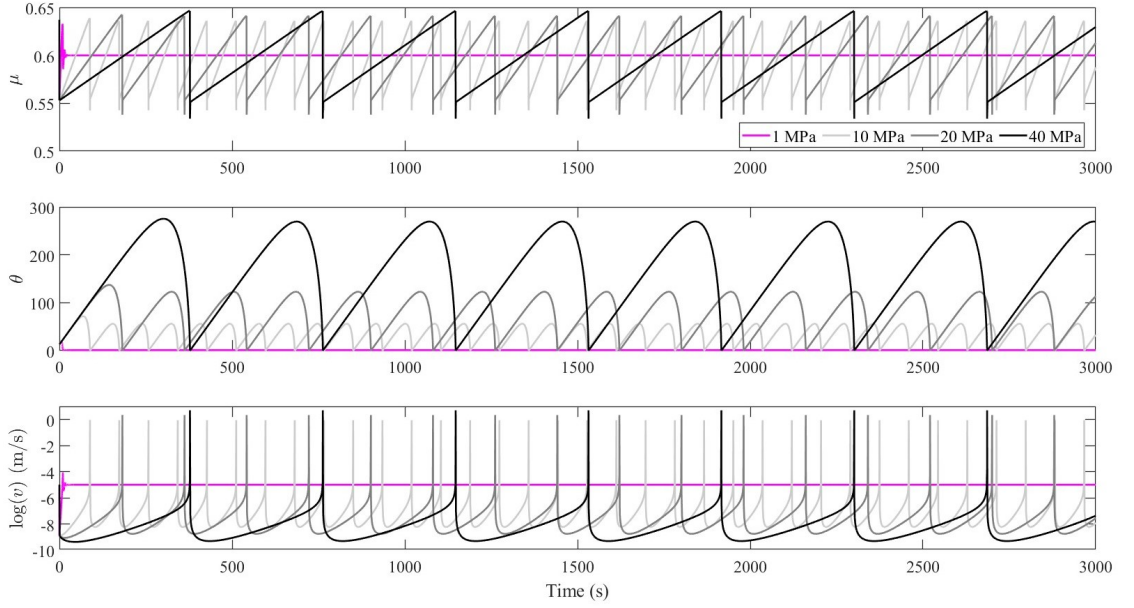
Figure 3.3: Earthquake sequences simulated by the spring-block model under four different normal loads. The steady sliding of the system is observed at 1 MPa. The recurrence time, the maximum stress drop, and the maximum slip rate increase with the normal stress.

Figure 3.3 presents the simulated earthquake sequences under four different normal stresses of 1 MPa, 10 MPa, 20 MPa, and 40 MPa. We observe that the recurrence time, the maximum stress drop, and the maximum slip rate increase with the normal stress, which is consistent with the experimental and field observations (Rivière et al., 2018; Zhou et al., 2021). The steady sliding of the system is observed when the normal load is 1 MPa, during which the slip rate and the fric-

tion coefficient are equal to the loading rate and the reference friction coefficient, respectively.

With the earthquake sequences produced by our spring-block model, the variables including recurrence time, maximum slip rate, peak strength, and maximum stress drop are plotted as a function of the normal stress in Figure 3.4. The thick gray dashed line in the right top panel represents the reference slip rate of the system (i.e., 1×10^{-5} m/s). All the four variables increase with the normal stress. The steady sliding of the system, which has zero stress drop and a slip rate equal to the reference slip rate, is evidenced at a normal stress of 1 MPa. Thus, no recurrence time is plotted at the 1 MPa normal stress. Such evolution also highlights the transition from steady sliding to stick-slip of the spring-block system with increasing normal stress.
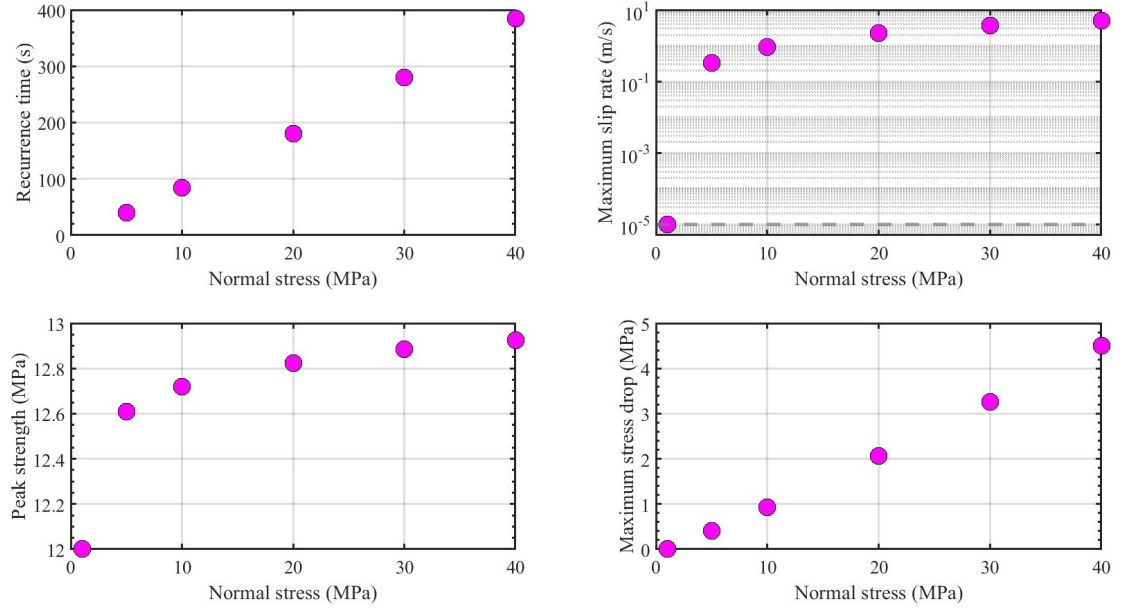
Figure 3.4: Recurrence time, maximum slip rate, peak strength, and maximum stress drop of the earthquake sequences simulated under different normal loads. The thick gray dashed line indicates the reference slip rate of the spring-block system. No recurrence time is plotted at the 1 MPa normal stress due to the steady sliding of the system.

Varying the Loading Rate

We also test the earthquake sequences under three different loading rates (Figure 3.5). An evident decrease in the recurrence time is observed for the increment of the loading rate. This is also consistent with experimental observations (Zhou et al., 2021). Nevertheless, the loading rate shows no dominant effect on the maximum slip rate.
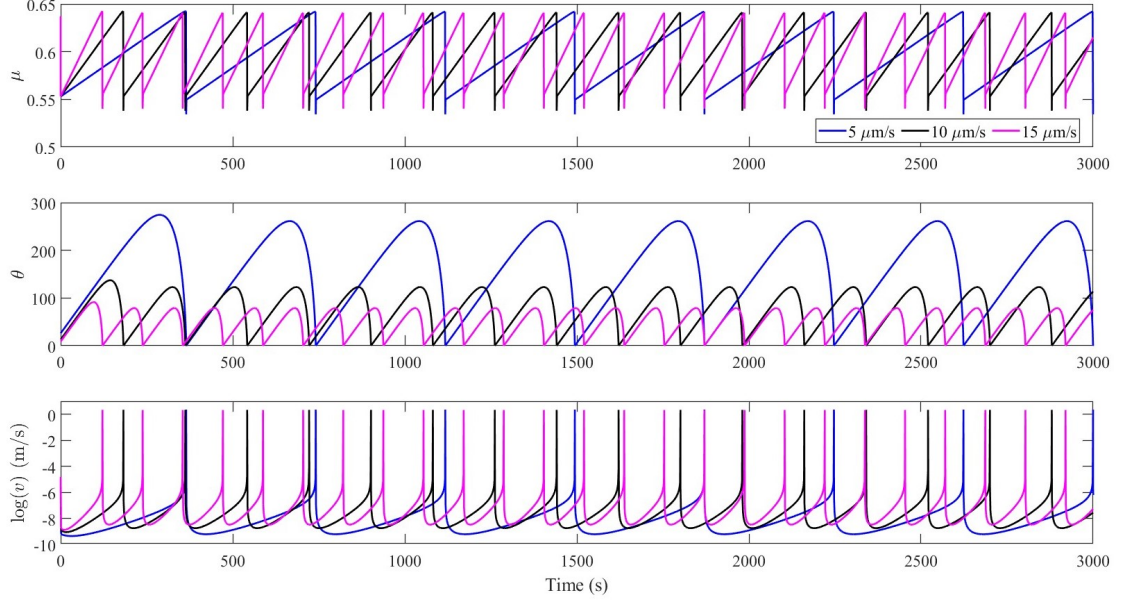
Figure 3.5: Earthquake sequences simulated by the spring-block model under three different loading rates. The recurrence time decreases with the loading rate.

The effect of the loading rate on the recurrence time, maximum slip rate, peak strength, and maximum stress drop is also investigated through multiple earthquake sequences simulated by the spring-block model. As shown in Figure 3.6, the recurrence time evidently decreases with the loading rate, whereas the maximum slip rate is invariant to the loading rate. The peak strength and the maximum stress drop slightly decrease with the loading rate.
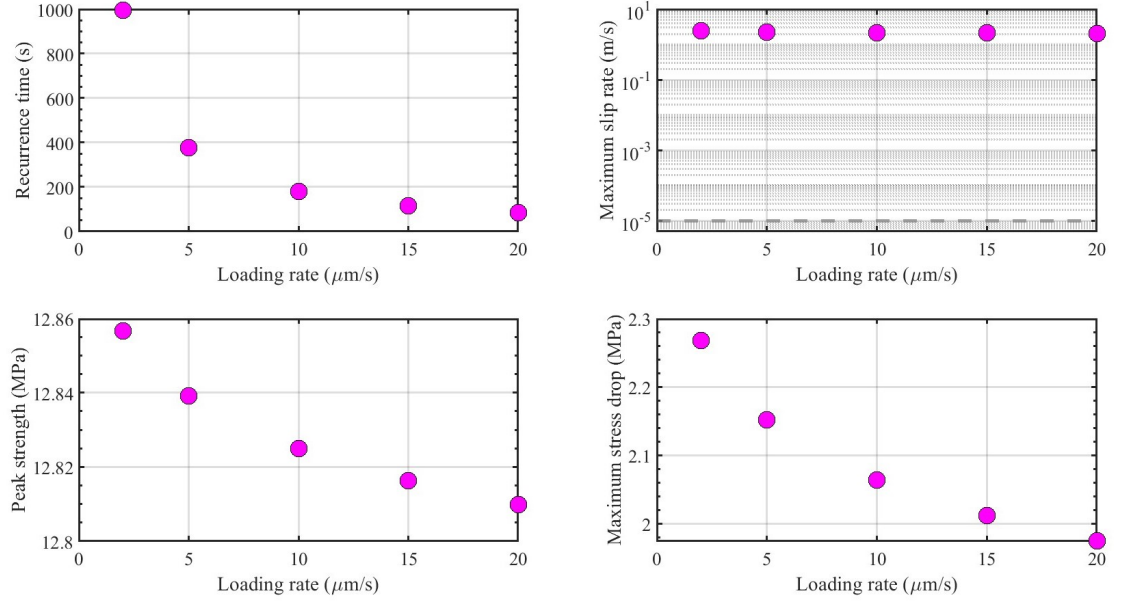
Figure 3.6: Recurrence time, maximum slip rate, peak strength, and maximum stress drop of the earthquake sequences simulated under different loading rates. The thick gray dashed line in the right top panel indicates the reference slip rate of the spring-block system. The recurrence time decreases with the loading rate, while the maximum slip rate shows no dependency on the loading rate. The peak strength and the maximum stress drop slightly decrease with the loading rate.

Varying the Ratio a/b

By keeping b fixed to 0.0144, we vary the ratio a/b as 0.50, 0.65, and 0.80 to simulate the corresponding earthquake sequences (Figure 3.7). We find that the recurrence time, the peak strength, and the maximum stress drop all decrease with the increase of the ratio. Indeed, the proportional relationship between the variable $(a - b)\sigma_n$ and the stress drop has long been recognized (Cao & Aki, 1987; Tullis et al., 2012) and indicated in the rate and state frictional law (Figure 1.7a), which means that a smaller difference between a and b (given $a < b$) will lead to a smaller stress drop. Thus, a larger value of the ratio a/b will result in a smaller stress drop. Since a smaller energy will be released during an earthquake, the time required for accumulating strain energy will be less, which causes a smaller strength of the system and a smaller recurrence time.
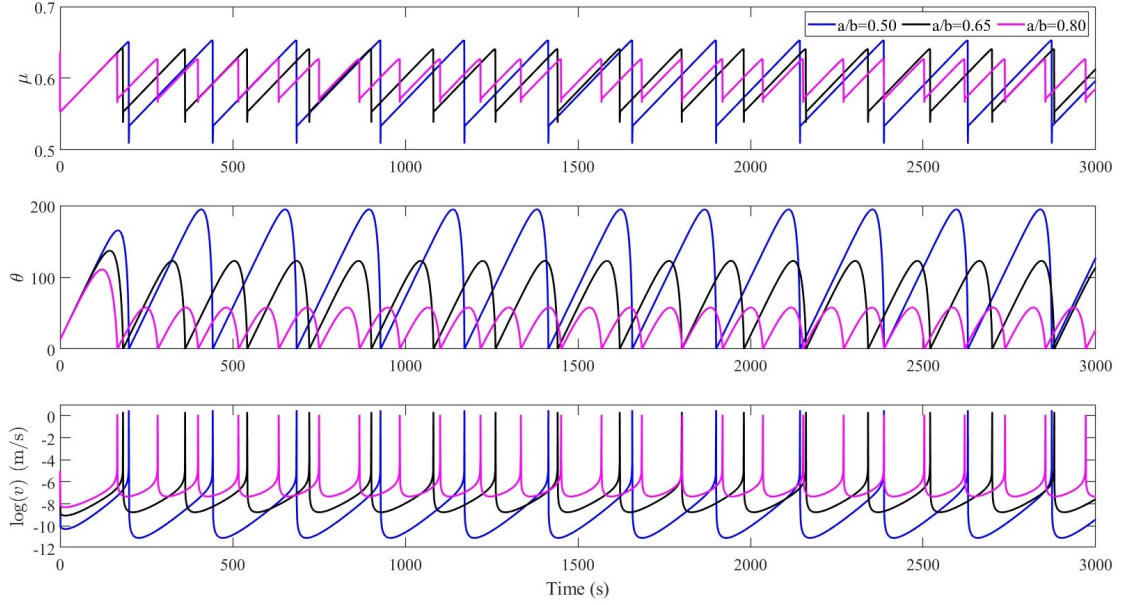
Figure 3.7: Earthquake sequences simulated by the spring-block model under three different values of a/b by keeping b fixed as 0.0144. The recurrence time, the peak strength, and the maximum stress drop decrease with the ratio.

Such an explanation is well supported by Figure 3.8, which shows the evolution of recurrence time, maximum slip rate, peak strength, and maximum stress drop along with multiple values of the ratio a/b. The recurrence time, the peak strength, and the maximum friction drop are observed to clearly decrease with the a/b ratio, whereas the maximum slip rate slightly decrease with this ratio.
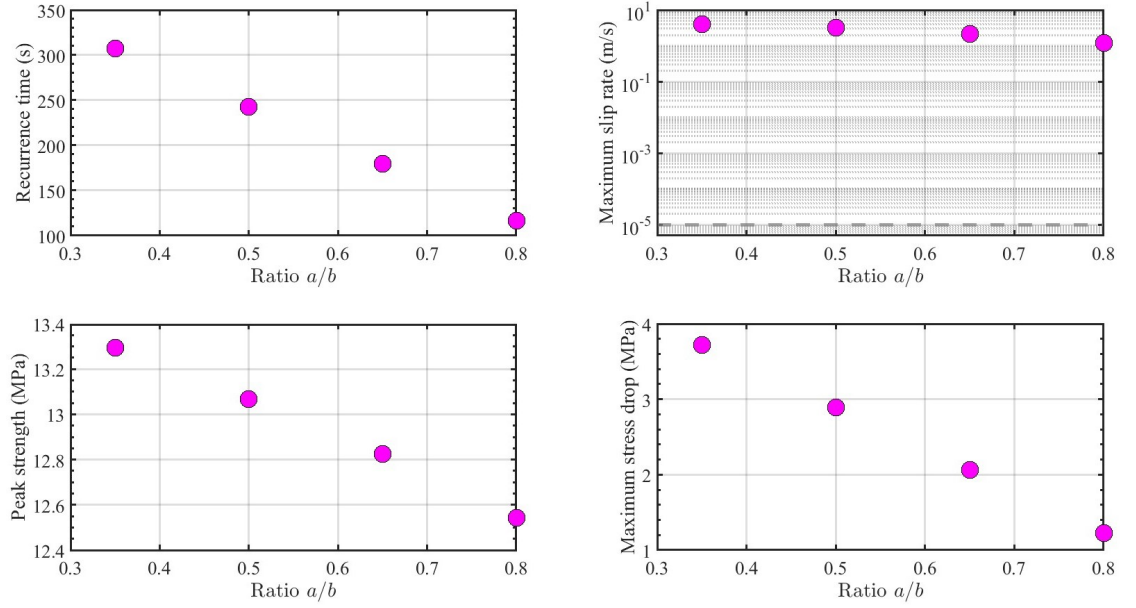
Figure 3.8: Recurrence time, maximum slip rate, peak strength, and maximum stress drop of the earthquake sequences simulated under different values of the ratio a/b. The thick gray dashed line in the right top panel indicates the reference slip rate of the spring-block system. The recurrence time, the peak strength, and the maximum friction drop evidently decrease with the ratio a/b, while the maximum slip rate slightly decrease with the ratio a/b.

Varying the Critical Slip Distance

In addition, we vary the critical slip distance, D_c, at three orders of magnitude to check its effect on the earthquake sequences (Figure 3.9). The system will be stable (i.e., steady sliding) if the critical slip distance is large to result in a large enough nucleation length (Ampuero & Rubin, 2008), which can prohibit the occurrence of the stick-slip behavior. The steady sliding of the system is found when the critical slip distance is 1000 μm. In the regime of stick-slip of the system, the peak strength, the recurrence time, the maximum slip rate, and the maximum stress drop decrease with the critical slip distance , D_c.
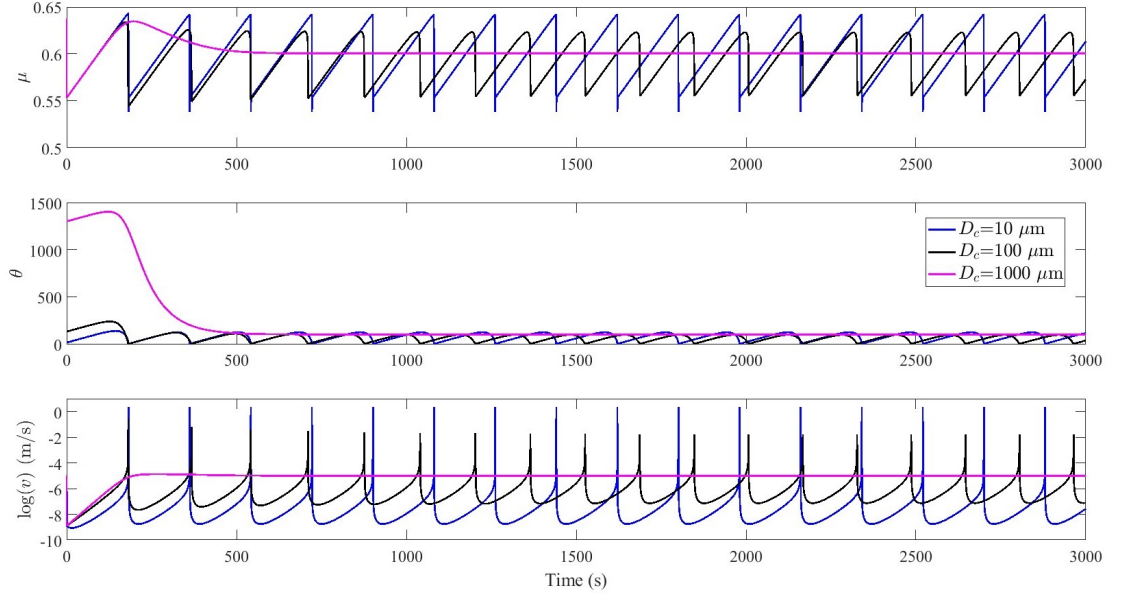
Figure 3.9: Earthquake sequences simulated by the spring-block model under three different critical slip distances. The steady sliding of the system is observed when the critical slip distance is large enough. For the system with stick-slip sequences, the peak strength, recurrence time, the maximum slip rate, and the maximum stress drop decrease with the critical slip distance.

Similarly, our spring-block model simulates multiple earthquake sequences with critical slip distances ranging five orders of magnitude. Five sets of recurrence time, maximum slip rate, peak strength, and maximum stress drop are extracted

from the corresponding earthquake sequences and summarized in Figure 3.10. The steady sliding of the system, which has zero stress drop and a slip rate equal to the reference slip rate, is evidenced when the critical slip distance is 1000 μm, thus no recurrence time is plotted here. Recurrence time, maximum slip rate, peak strength, and maximum stress drop all decrease with the critical slip distance. However, the maximum slip rate just slightly decreases when the critical slip distance is less than 10 μm, and it decreases sharply since the critical slip distance is greater than 10 μm. The transition of the spring-block system from stick-slip to steady sliding is also highlighted with the increment of the critical slip distance.
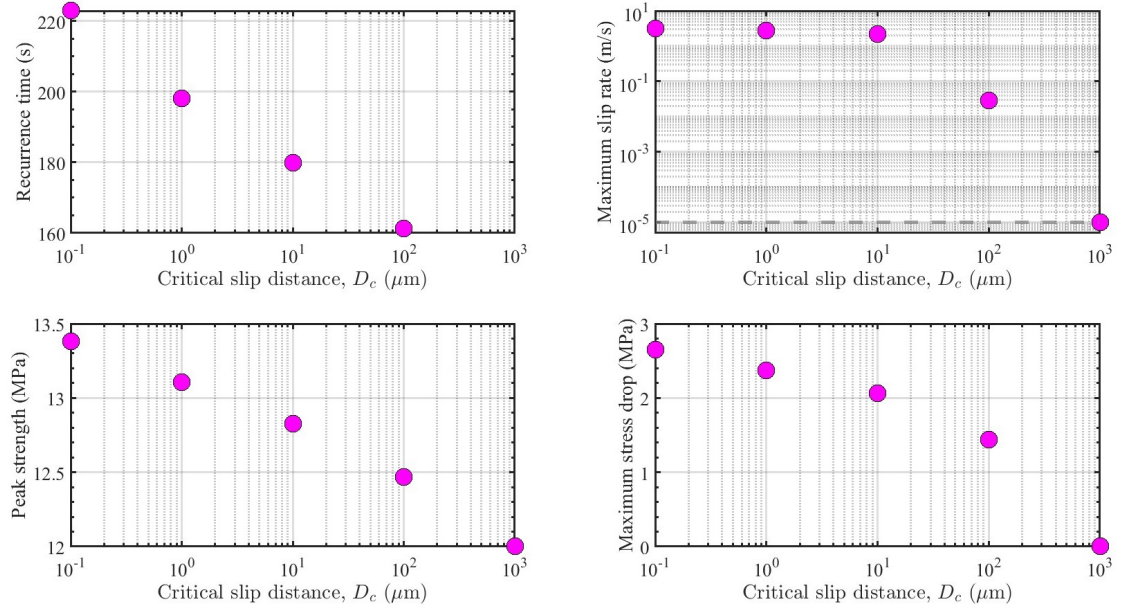
Figure 3.10: Recurrence time, maximum slip rate, peak strength, and maximum stress drop of the earthquake sequences simulated under different critical slip distances, D_c. The thick gray dashed line in the right top panel indicates the reference slip rate of the spring-block system. No recurrence time is plotted at the critical slip distance of 1000 μm due to the steady sliding of the system. In the stick-slip regime, the recurrence time, the peak strength, and the maximum stress drop evidently decrease with the critical slip distance, while the maximum slip rate slightly decreases when the critical slip distance is less than 10 μm.

3.2   One-Dimensional Model

Based on the spring-block model established above, we extend it to a one-dimensional model considering the viscoelastic interactions between asperities. We start with a simple version that includes two identical asperities coupled to each other by a spring defined by the Maxwell viscoelastic model while keeping the other assumptions the same as the single spring-block model. Such a model is illustrated schematically in Figure 3.11, where the viscoelasticity the interacting spring, 2.2×10^7 Pa·s, is determined from the silicone sample characterization in Section 2.1.2. We acknowledge that the thick PMMA plate in our experimental setup also has a viscoelastic characteristic (McLoughlin & Tobolsky, 1952) which can be translated into the vertical viscoelastic spring that connects the block and the loading plate (Figure 3.11). However, as the PMMA plate (with a Young's modulus of about 2.32 GPa (Park et al., 2017)) is about a thousand times stiffer than the silicone block (with a Young's modulus of 1.1 MPa), the vertical spring is considered purely elastic for the current modeling. By keeping the other assumptions unchanged, the behaviors of the two asperities can be described by the following ODE system:
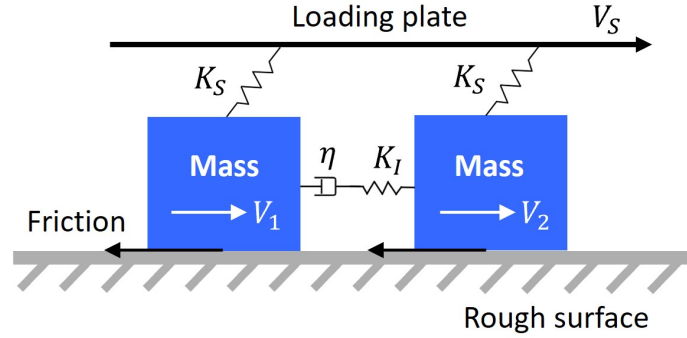
Figure 3.11: Scheme of the simple one-dimensional model containing two identical asperities. The viscoelastic interaction between the asperities is quantitatively described by the Maxwell spring with both the elasticity K_I and viscosity η. The other assumptions are the same as the spring-block model shown in Figure 3.1.

$$\begin{cases} \dot{u}_1 = V_1 - V_0 \\ \dot{V}_1 = -\dfrac{1}{M}\left(K_S \cdot u_1 + \mu_1\sigma_n + \mathcal{I}_1 + \dfrac{G}{2C_S}V_1\right) \\ \dot{\theta}_1 = 1 - \dfrac{V_1\theta_1}{D_c} \\ \dot{u}_2 = V_2 - V_0 \\ \dot{V}_2 = -\dfrac{1}{M}\left(K_S \cdot u_2 + \mu_2\sigma_n + \mathcal{I}_2 + \dfrac{G}{2C_S}V_2\right) \\ \dot{\theta}_2 = 1 - \dfrac{V_2\theta_2}{D_c} \end{cases} \tag{3.6}$$

with

$$\begin{cases} \mathcal{I}_1 = -K_I(u_2 - u_1) - \eta(V_2 - V_1) \\ \mathcal{I}_2 = -K_I(u_1 - u_2) - \eta(V_1 - V_2) \end{cases} \tag{3.7}$$

where the subscripts 1 and 2 indicate the two asperities while the others remain the same as equation 3.1. $\mathcal{I}_1$ and $\mathcal{I}_2$ are the viscoelastic interaction terms for the first and the second asperities, respectively. We follow the same non-dimensionalization presented before (equation 3.3) and the initial ODE system is derived into the non-dimensionalized one as:

$$\begin{cases} \dot{u}_1^{nd} = V_1^{nd} - 1 \\ \dot{V}_1^{nd} = -\gamma^2\left(\zeta V_1^{nd} + u_1^{nd} + \mathcal{I}_1^{nd} + \dfrac{1}{\xi}\left(\dfrac{\mu_0}{a} + \ln(V_1^{nd}) + (1+\epsilon)\ln(\kappa\theta_1^{nd})\right)\right) \\ \dot{\theta}_1^{nd} = \dfrac{1}{\kappa} - V_1^{nd}\theta_1^{nd} \\ \dot{u}_2^{nd} = V_2^{nd} - 1 \\ \dot{V}_2^{nd} = -\gamma^2\left(\zeta V_2^{nd} + u_2^{nd} + \mathcal{I}_2^{nd} + \dfrac{1}{\xi}\left(\dfrac{\mu_0}{a} + \ln(V_2^{nd}) + (1+\epsilon)\ln(\kappa\theta_2^{nd})\right)\right) \\ \dot{\theta}_2^{nd} = \dfrac{1}{\kappa} - V_2^{nd}\theta_2^{nd} \end{cases} \tag{3.8}$$

with

$$\begin{cases} \mathcal{I}_1^{nd} = -\phi(u_2^{nd} - u_1^{nd}) - \chi(V_2^{nd} - V_1^{nd}) \\ \mathcal{I}_2^{nd} = -\phi(u_1^{nd} - u_2^{nd}) - \chi(V_1^{nd} - V_2^{nd}) \end{cases} \tag{3.9}$$

and with

$$
\begin{cases}
\gamma = \sqrt{\dfrac{K_S}{M}} \dfrac{D_c}{V_0} \\[2ex]
\zeta = \dfrac{G}{2C_S} \dfrac{V_0 D_c}{K_S} \\[2ex]
\xi = \dfrac{K_S D_c}{a\sigma_n} \\[2ex]
\epsilon = \dfrac{b - a}{a} \\[2ex]
\kappa = a\sigma_n \dfrac{V_0}{D_c} \\[2ex]
\phi = \dfrac{K_I}{K_S} \\[2ex]
\chi = \dfrac{\eta V_0}{K_S D_c}
\end{cases}
\tag{3.10}
$$

Similarly, the non-dimensionalized ODE system above can be solved numerically in MATLAB through the variable-step, variable-order stiff solver (Shampine & Reichelt, 1997; Shampine et al., 1999).

3.2.1 Preliminary Simulations

Table 3.2: Parameters used in the one-dimensional viscoelastic model

Parameter	Symbol	Value
Mass	M	6×10^{-3} kg
Shear modulus	G	2.28 GPa
Shear wave speed	C_S	1330 m/s
Normal stress	σ_n	20 MPa
Loading rate	V_S	10.0 μm/s
Direct effect	a	0.00936
Evolution effect	b	0.01440
Critical slip distance	D_c	1×10^{-5} m
Stiffness of the loading	K_S	1.0 GPa
Elasticity of the Maxwell spring	K_I	1.1 MPa
Viscosity of the Maxwell spring	η	2.2×10^7 Pa·s
Reference friction coefficient	μ_0	0.6
Reference slip rate	V_0	10.0 μm/s
Simulation time	t	3000 s

Table 3.2 lists the parameters used for the preliminary simulations of the one-dimensional viscoelastic model, where the viscoelasticity of the Maxwell spring linking the two blocks is obtained from the viscoelastic properties of the silicone block, while the other parameters are the same as those used for the spring-block model (Table 3.1).

A preliminary simulation is run with the established one-dimensional model by setting the same initial conditions for the two blocks. Figure 3.12 displays the earthquake sequences produced by the one-dimensional viscoelastic model. The consistent behaviors of the two blocks are observed at the beginning of the simulation (see also Figure 3.13a). Then, the viscous damping takes effect on the behaviors of the two blocks. Specifically, the rapid slipping of one block will cause the less rapid slipping of the other block along an opposite direction (see also Figure 3.13b).
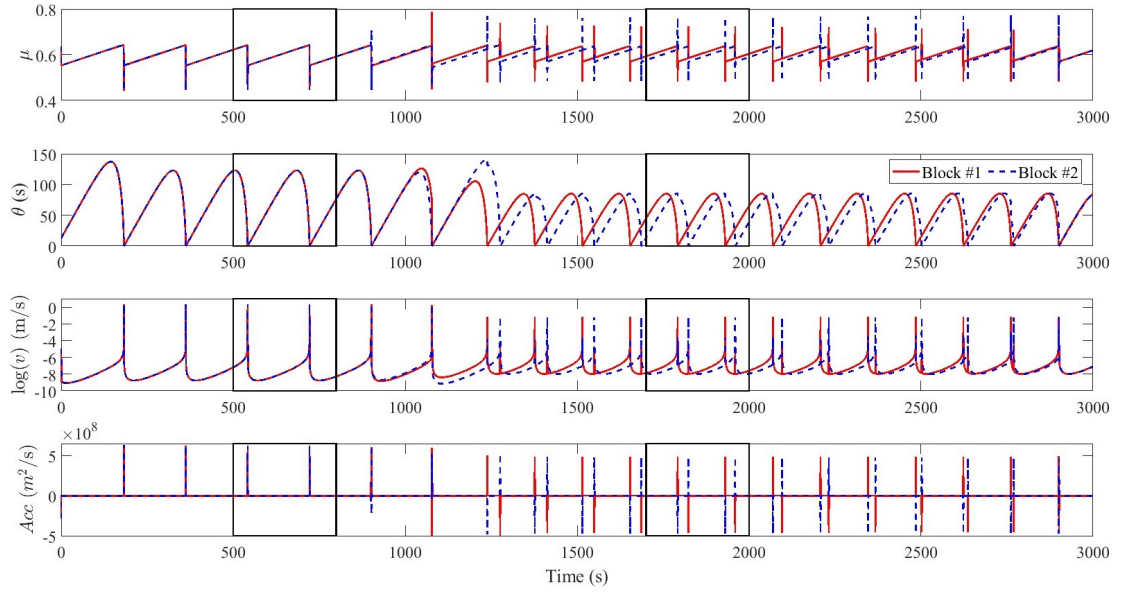
Figure 3.12: Earthquake sequences simulated by the one-dimensional viscoelastic model using the parameters listed in Table 3.2. The same initial conditions are set for the two blocks. The black rectangles represent two zoom-in views, where the one ranging from 500 s to 800 s is shown in Figure 3.13a and the other ranging from 1700 s to 2000 s is shown in Figure 3.13b.
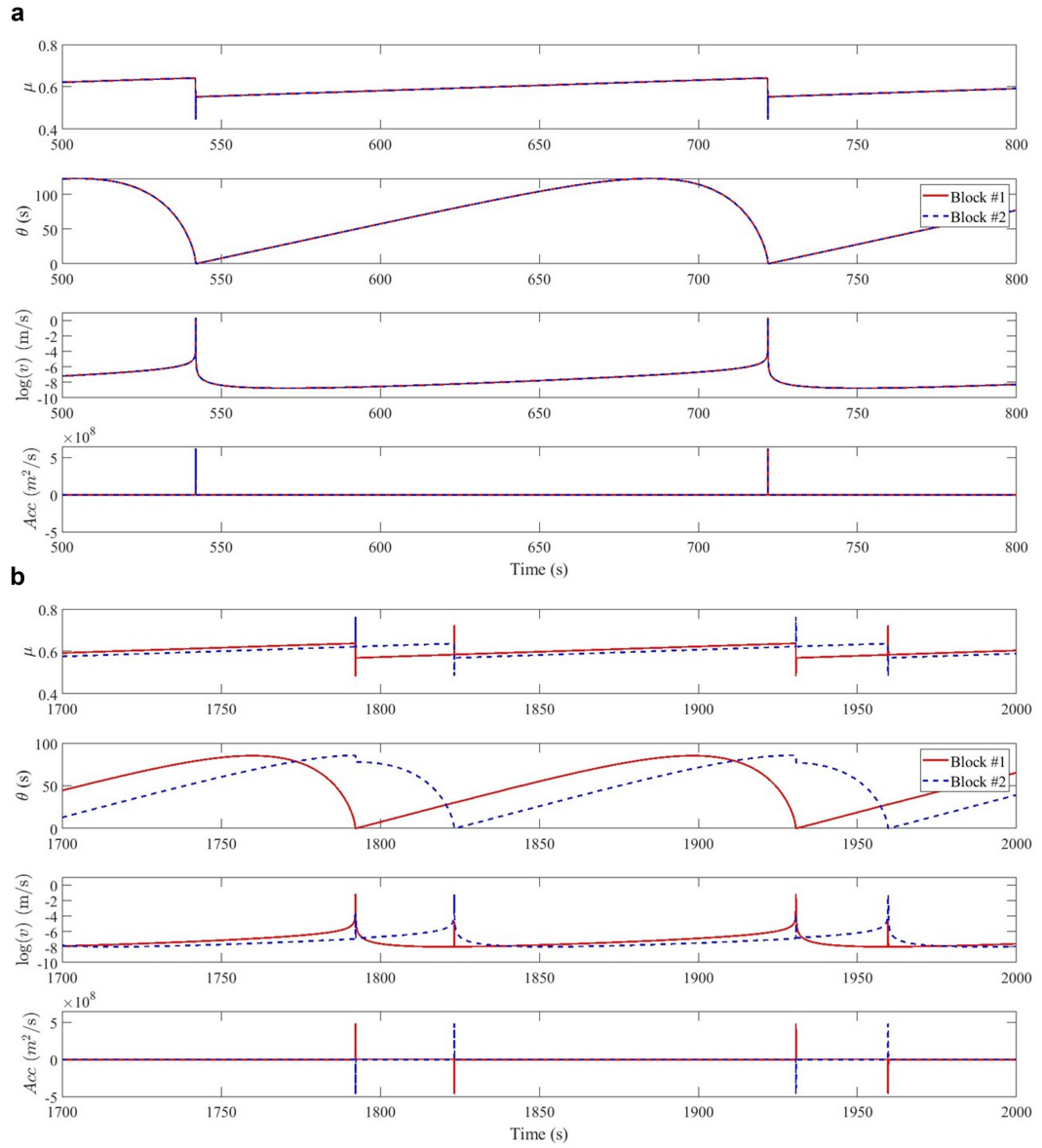
Figure 3.13: a: Zoom-in view of Figure 3.12 ranging from 500 s to 800 s, showing the consistent behaviors of the two blocks. **b:** Zoom-in view of Figure 3.12 ranging from 1700 s to 2000 s, showing the inconsistent behaviors of the two blocks affected by the viscous damping.

The detailed underlying physics of this one-dimensional viscoelastic model is still under investigation. Here we simply test the effect of the viscous damping on the behavior of the one-dimensional system by changing the values of the viscosity of the Maxwell spring.

Four different values of viscosity, which are 2.2×10^5 Pa·s (Figure 3.14), 2.2×10^3 Pa·s (Figure 3.15), 2.2×10^1 Pa·s (Figure 3.16), and 0 (Figure 3.17), are used to run the one-dimensional viscoelastic model while keeping the other parameters the same as Table 3.2. By comparing Figures 3.12 to 3.17, it is observed that the two blocks are gradually easier to be synchronized to present consistent behaviors with a decrease in viscosity, which means that the effect of viscous damping gradually diminishes with the decreasing viscosity. In the case of zero viscosity (Figure 3.17), the two blocks present elastic interactions, similar to those reported in the one-dimensional Burridge-Knopoff model.
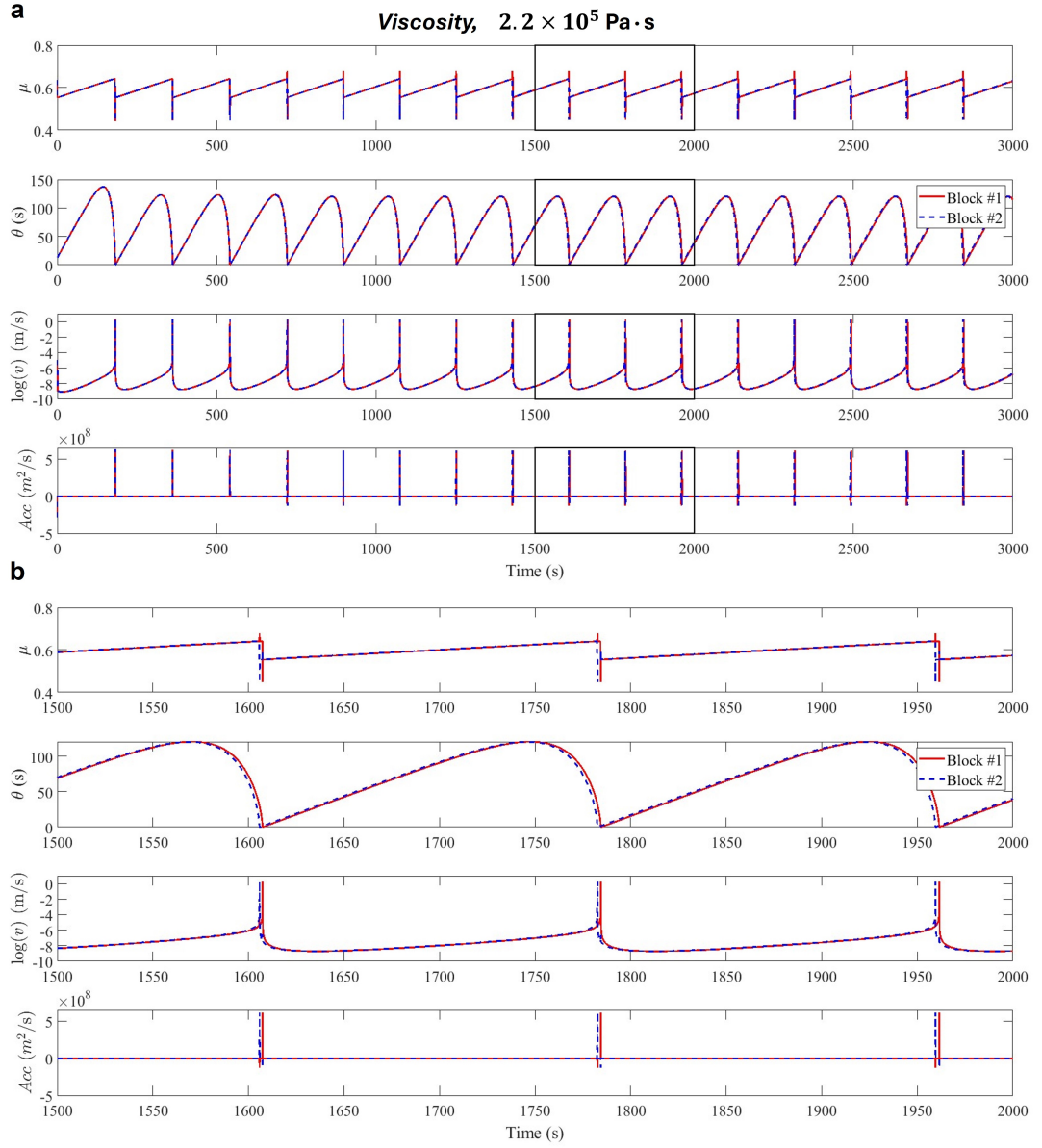
Figure 3.14: a: Earthquake sequences simulated by the one-dimensional viscoelastic model using the parameters listed in Table 3.2, except the viscosity is modified as 2.2×10^5 Pa·s. The initial conditions are set the same for the two blocks. The black rectangle represent the zoom-in view ranging from 1500 s to 2000 s. **b:** Zoom-in view of the black rectangle region shown in Figure 3.14a.
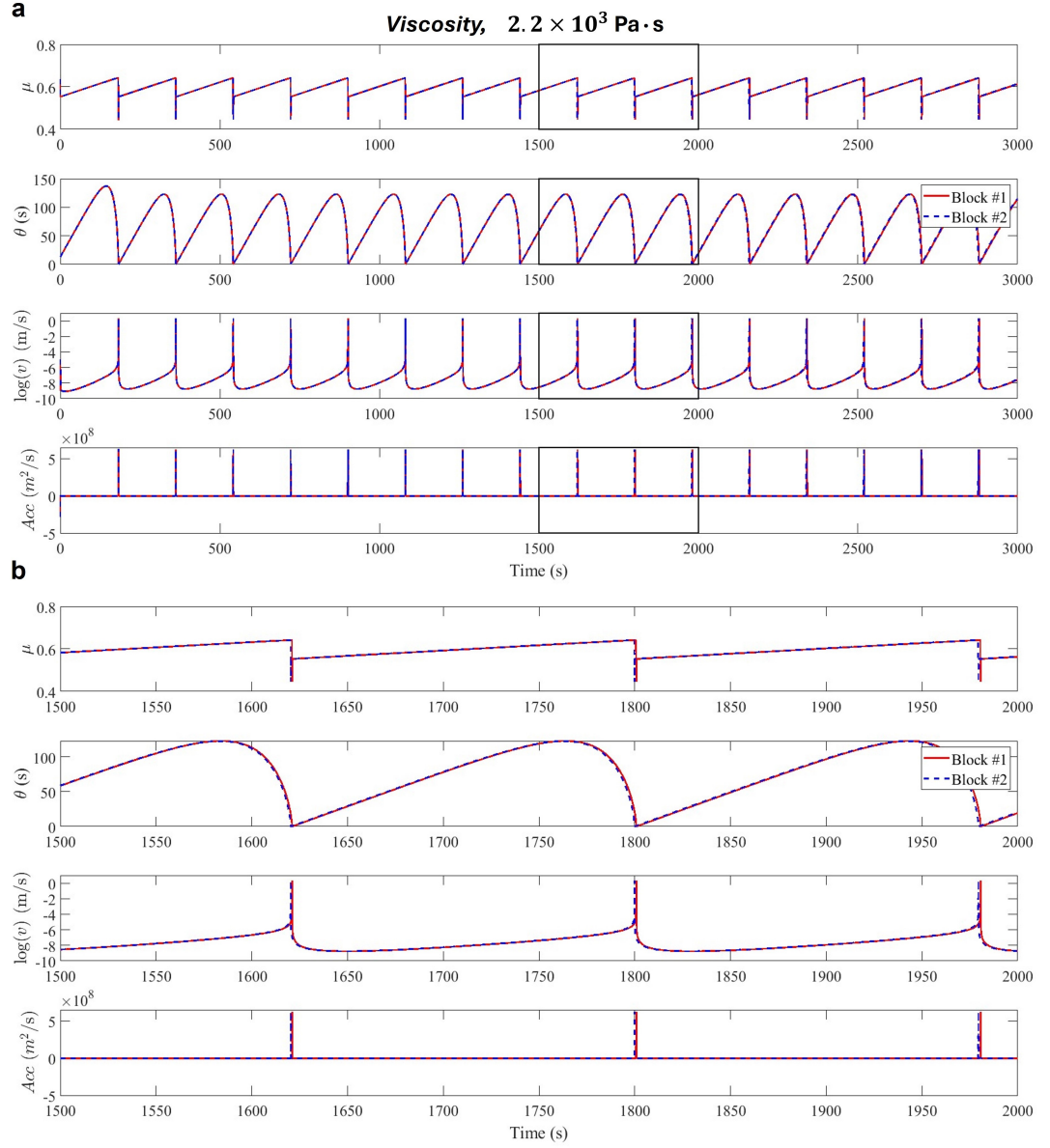
Figure 3.15: a: Earthquake sequences simulated by the one-dimensional viscoelastic model using the parameters listed in Table 3.2, except the viscosity is modified as 2.2×10^3 Pa·s. The initial conditions are set the same for the two blocks. The black rectangle represent the zoom-in view ranging from 1500 s to 2000 s. **b:** Zoom-in view of the black rectangle region shown in Figure 3.15a.
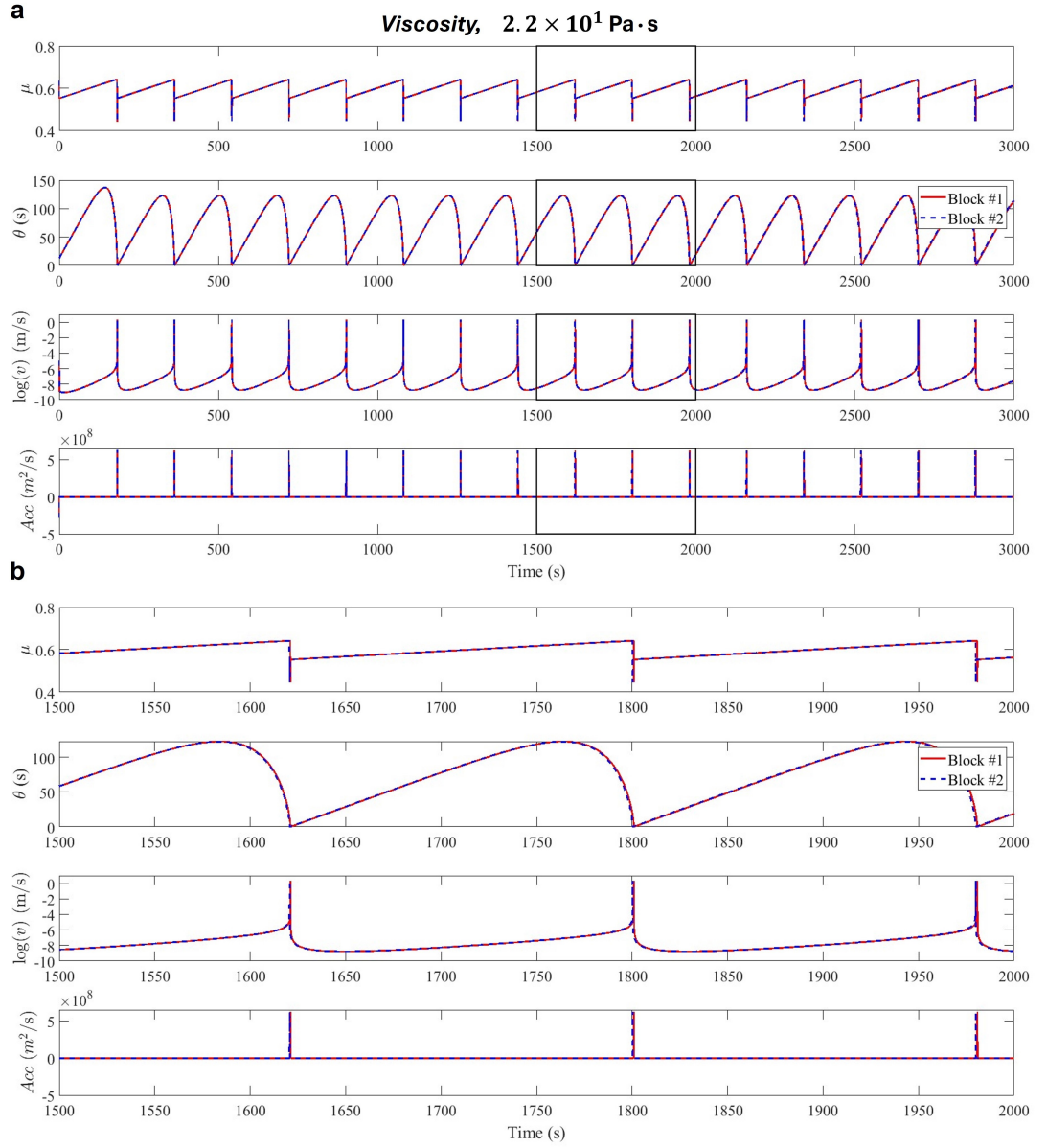
Figure 3.16: a: Earthquake sequences simulated by the one-dimensional viscoelastic model using the parameters listed in Table 3.2, except the viscosity is modified as 2.2×10¹ Pa·s. The initial conditions are set the same for the two blocks. The black rectangle represent the zoom-in view ranging from 1500 s to 2000 s. **b:** Zoom-in view of the black rectangle region shown in Figure 3.16a.
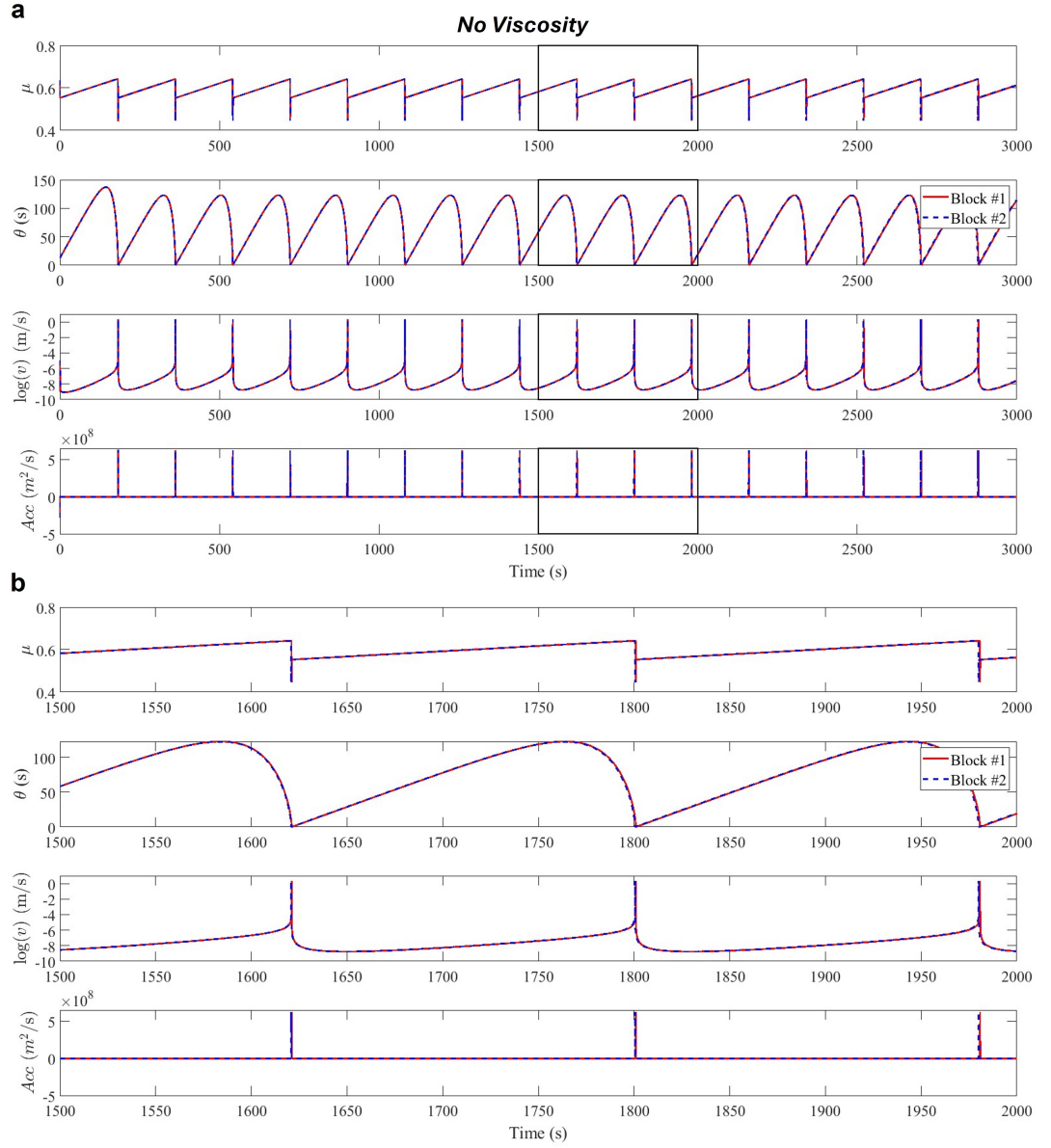
Figure 3.17: a: Earthquake sequences simulated by the one-dimensional viscoelastic model using the parameters listed in Table 3.2, but no viscosity is applied. The initial conditions are set the same for the two blocks. The black rectangle represent the zoom-in view ranging from 1500 s to 2000 s. **b:** Zoom-in view of the black rectangle region shown in Figure 3.17a.

3.3   Two-Dimensional Model

We further extend the one-dimensional model to a modified two-dimensional Burridge-Knopoff model, which contains numerous identical asperities whose number and positions are the same as our analog fault model. Figure 3.18 shows the scheme of this two-dimensional numerical model, where the color-coded spheres indicate asperities with different peak heights (extracted from the high-resolution topographical map, see Figure 4.3 for details). All these asperities are coupled with a elastic spring with a stiffness of K_S to another side of the fault. By considering the position of each asperity as a vertex, a two-dimensional Delaunay triangulation (D.-T. Lee & Schachter, 1980) is applied to the fault interface to determine the spatial connections between asperities, shown as the gray lines in Figure 3.18 that represent the interactions between asperities (see also Section 4.5.1 for more details). The viscoelastic interactions between asperities all over the interface are then quantified based on the updated spatial connections and the Maxwell spring that couples two connected asperities. We are aware that the interaction stiffness depends on the distance between each pair of asperities due to the irregular 2D topography. However, to run a preliminary simulation, we just set it to be constant for the moment. Note that, the normal stresses sustained by all asperities are assumed to be homogeneous in this preliminary numerical model, although the normal stress heterogeneity induced from the various peak heights of asperities exists in the analog model. More measurements that employ pressure-sensitive films to precisely quantify the normal stress on each asperity at a given nominal normal load are required in the future to better complement the input of this two-dimensional model.

The dynamics of each asperity in this modified two-dimensional Burridge-Knopoff model is controlled by the following ODE system:

$$
\begin{cases}
\dot{u}_i = V_i - V_0 \\
\dot{V}_i = -\dfrac{1}{M}\left(K_S \cdot u_i + \mu_i \sigma_n + \mathcal{I}_i + \dfrac{G}{2C_S}V_i\right) \\
\dot{\theta}_i = 1 - \dfrac{V_i \theta_i}{D_c}
\end{cases}
\tag{3.11}
$$

The interaction term $\mathcal{I}_i$ is defined as the sum of the viscoelastic interactions be-
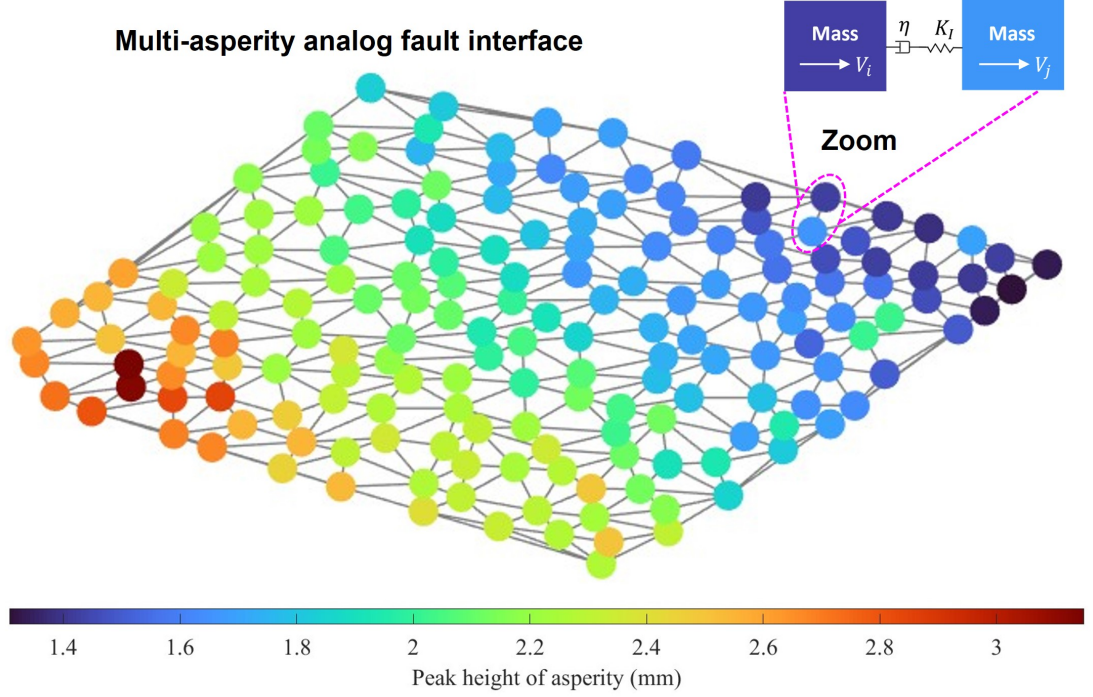
Figure 3.18: Scheme of the two-dimensional numerical model with the number and positions of asperities the same as the analog fault interface. Through the Delaunay triangulation, the spatial connections between asperities are determined and shown as gray lines indicating the viscoelastic interactions between asperities. The zoom view shows that such a viscoelastic interaction between two asperities is quantitatively described by the Maxwell spring with both the elasticity K_I and viscosity η. Note that the normal stress heterogeneity induced from the various peak heights of asperities has not been considered in this preliminary model. The same normal stress on each asperity is assumed in the current model. The other assumptions are the same as the spring-block model shown in Figure 3.1.

tween the asperity i and all the asperities determined by the updated spatial connections:

$$\mathcal{I}_i = - \sum_{i}^{j=D(i)} \Big(K_I(u_i - u_j) + \eta(V_i - V_j) \Big) \qquad (3.12)$$

where j denotes the index of the asperity spatially connected with the asperity i and D is the function of the updated Delaunay triangulation. Following the same non-dimensionalization (equation 3.3), we derive the original ODE system (equation 3.11) into the non-dimensionalized one as:

$$\begin{cases} \dot{u}_i^{nd} = V_i^{nd} - 1 \\ \dot{V}_i^{nd} = -\gamma^2 \Big(\zeta V_i^{nd} + u_i^{nd} + \mathcal{I}_i^{nd} + \dfrac{1}{\xi}\Big(\dfrac{\mu_0}{a} + \ln(V_i^{nd}) + (1+\epsilon)\ln(\kappa \theta_i^{nd})\Big) \Big) \\ \dot{\theta}_i^{nd} = \dfrac{1}{\kappa} - V_i^{nd}\theta_i^{nd} \end{cases} \quad (3.13)$$

with

$$\mathcal{I}_i^{nd} = - \sum_{i}^{j=D(i)} \Big(\phi(u_i - u_j) + \chi(V_i - V_j) \Big) \qquad (3.14)$$

and the other variables are the same as those shown in equation 3.10.

Finally, the dynamics of each asperity on the fault interface is obtained by numerically resolving the non-dimensionalized ODE system (equation 3.13) in MATLAB through the same variable-step, variable-order stiff solver (Shampine & Reichelt, 1997; Shampine et al., 1999).

3.3.1 Preliminary Simulation

A preliminary simulation is run with the established two-dimensional model using the same parameters listed in Table 3.2. But, the reference friction coefficient, μ_0, is changed to 0.1. Otherwise, the computation will fail at the very beginning (of time at around 1×10^{-15} s), because it is unable to meet integration tolerances without reducing the step size below the smallest value allowed. All the asperities are set to have the same initial conditions.

Figure 3.19a displays the earthquake sequences produced by the two-dimensional viscoelastic model, and a zoom-in view ranging from 1500 s to 2000 s is shown in
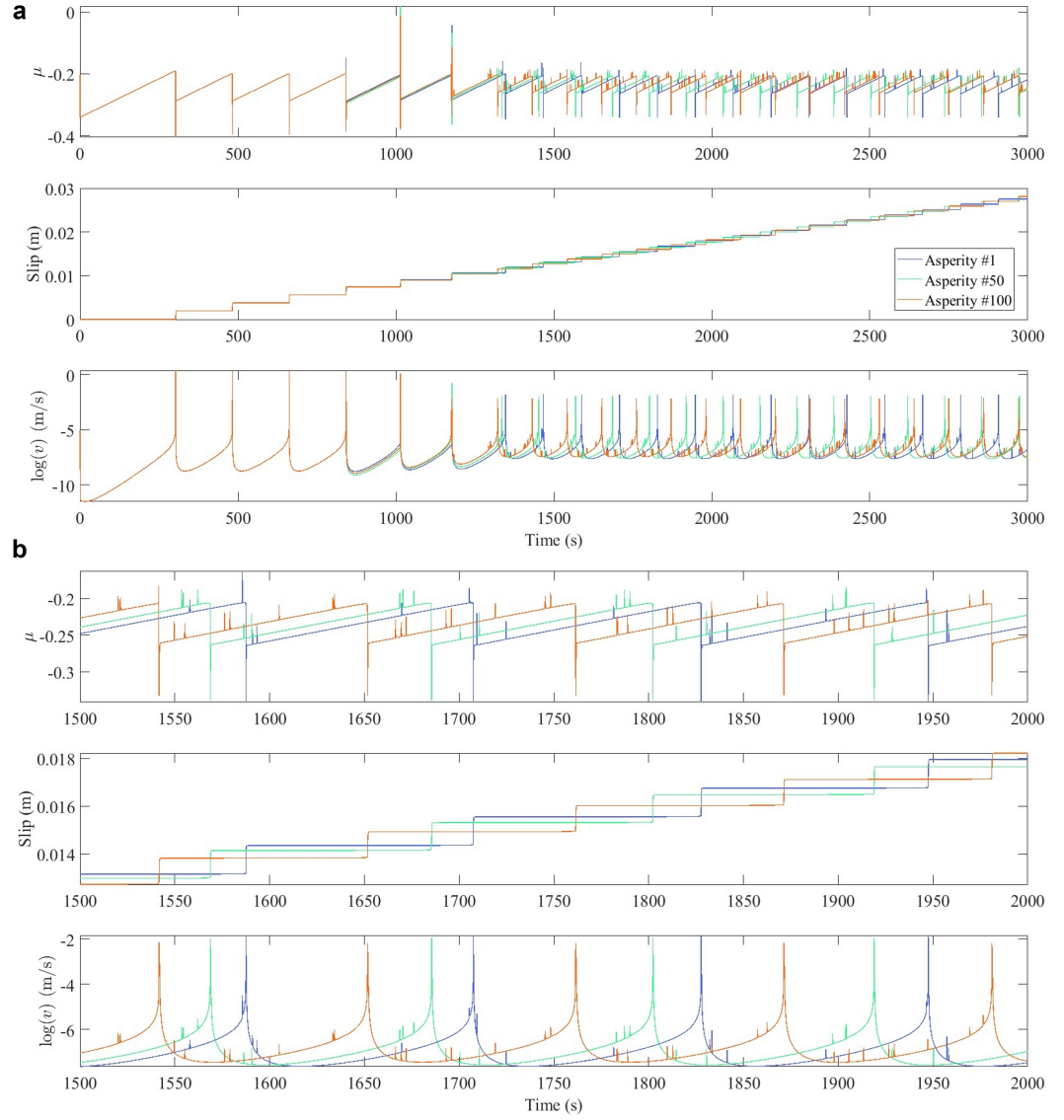
Figure 3.19: a: Earthquake sequences simulated by the two-dimensional viscoelastic model using the parameters listed in Table 3.2, but the reference friction coefficient, μ_0, is changed to 0.1. The initial conditions are set the same for the two blocks. The behaviors of three asperities are displayed for clear visualization. **b:** Zoom-in view of Figure 3.19a ranging from 1500 s to 2000 s.

Figure 3.19b. It is weird that the friction coefficient computed by the model is negative. We suspect this may come from the wrong computation of the interacting term in the numerical model. We acknowledge that this two-dimensional model is a very preliminary one that is not totally correct. Multiple questions, such as why the model is not executable with a reference friction coefficient of 0.6 and why a negative friction coefficient is computed, remain to be figured out. Here we will not try to further discuss the physical process presented in Figure 3.19 until the apparent technical problems are fixed.

3.4   Concluding Remarks

In this chapter, we attempt to establish a modified two-dimensional Burridge-Knopoff numerical model physically based on our aforementioned multi-contact analog fault model and corresponding experimental setup. The dynamics of each asperity obeys Newton's laws of motion, and the friction is governed by the rate and state frictional law, in which the relevant parameters such as a, b, and D_c are expected to be measured from the slide-hold-slide and velocity step experiments with a customized single-asperity interface. The viscoelastic interactions between asperities all over the interface are illustrated by the spatial connections derived from the two-dimensional Delaunay triangulation and the viscoelasticity of the Maxwell spring characterized by the silicone block.

We established the spring-block model considering the block with unit basal area, which has been validated through the benchmark with the Quasi-DYNamic (QDYN) earthquake simulator. The performance of this spring-block model is tested by separately varying different parameters, which are the normal stress, the loading rate, the ratio a/b between the direct effect a and the evolution effect b, and the critical slip distance. Four variables, which include the recurrence time, the maximum slip rate, the peak strength, and the maximum stress drop, are extracted from the earthquake sequences simulated using different parameters to examine the effectiveness of the spring-block model.

The one-dimensional model considering the viscoelastic interaction between two

asperities is also developed. The effect of the viscous damping on the behavior of the one-dimensional system is investigated by changing the viscosity values of the Maxwell spring. Five simulations with the same parameters except varying viscosity values ranging from seven orders of magnitude are run with the one-dimensional model. We observe that the two blocks are gradually more and more synchronized to present consistent behaviors with the decreasing viscosity, which means that the effect of viscous damping gradually diminishes with the decreasing viscosity. However, the detailed underlying physics of this one-dimensional viscoelastic model is still under exploration, and more benchmark works are necessary to fully validate the one-dimensional model.

The two-dimensional model, which comprises the same number and position of asperities as the analog fault model, is also developed. A preliminary simulation is performed with the two-dimensional model, where the slip behavior of each asperity is characterized. However, some technical problems have emerged in this current model, which forces us to correct the current model before trying to further interpret the physical process presented by this system. Moreover, we acknowledge that several more points need to be considered to model the analog fault interface. For instance, the normal stress at each asperity is assumed to be the same in the current version, which is not exactly correspondent to our analog fault model comprising asperities with different peak heights. The normal stress at each asperity relies on the pressure-sensitive film measurement that can resolve the normal stress and real contact area at local asperity. This is my ongoing work and more details can be found in Section 5.2.1. Considering the varying lengths of different Maxwell springs that connect interacting asperities is another issue to be addressed, as the distribution of asperities on our analog fault interface is not homogeneous. The normalization of the lengths of these viscoelastic springs needs to be incorporated into the ODE system of the two-dimensional model. Based on these optimizations, further benchmarks need to be conducted to validate the two-dimensional model. To eventually demonstrate the effectiveness of such a physics-based two-dimensional model, it is expected to reproduce our experimental results generated through the analog fault interface by using the same loading

characteristics.

Chapter 4

Collective Behavior of Asperities before Large Stick-Slip Events

With all the experimental facilities aforementioned in detail, a novel experimental setup capable of measuring directly the subtle motion of individual asperities on a heterogeneous faulting interface is proposed. In this chapter, only optical monitoring of the interface is employed during the direct-shear experiments to couple with the macroscopic measurement of the shear force. The temporal evolution of the slip of each asperity is captured. The close relationship between the mechanical behavior of the global fault and the collective behavior of local asperities is demonstrated. The spatiotemporal interactions of asperities are quantified as slip episodes to mimic the ruptures including both stable and unstable slips. With the catalog of slip episodes, we reproduce the significant characteristics and scaling laws observed in natural faults, such as the magnitude-frequency distribution and the moment-duration scaling. Such upscaling suggests that our results can be extrapolated to natural faults and provide insights into fault physics and mechanics.

This study was conducted with my advisors Olivier Lengliné and Jean Schmittbuhl. This work has been published in *Journal of Geophysical Research: Solid Earth* in 2023. For a comprehensive description of the work, here I merge the published article and the corresponding supporting information into a complete chapter as follows.

4.1 Abstract

The multi-scale roughness of a fault interface is responsible for multiple asperities that establish a complex and discrete set of real contacts. Since asperities control the initiation and evolution of the fault slip, it is important to explore the intrinsic relationships between the collective behavior of local asperities and the frictional stability of the global fault. Here we propose a novel analog experimental approach, which allows us to capture the temporal evolution of the slip of each asperity on a faulting interface. We find that many destabilizing events at the local asperity scale occurred in the slip-strengthening stage which is conventionally considered as the stable regime of a fault. We compute the interseismic coupling to evaluate the slipping behaviors of asperities during the slip-strengthening stage. We evidence that the interseismic coupling can be affected by the elastic interactions between asperities through the embedding soft matrix. Scaling laws of natural slow slip events are reproduced by our setup in particular the moment-duration scaling. We also evidence an unexpected persistency of a disordering of the asperities through the seismic cycles despite the relaxation effects of the large slip events.

4.2 Introduction

Crustal fault interfaces display geological heterogeneities at various scales (Faulkner et al., 2003; Chester et al., 1993; Ben-Zion & Sammis, 2003). In particular, exhumed fault surfaces exhibit a complex topography characterized by height variations at all scales (Candela et al., 2009, 2012; Power et al., 1987; Schmittbuhl, Gentier, & Roux, 1993; Schmittbuhl et al., 1995; Scholz, 2019). Supposing that the roughness of these interfaces is similar to those of active faults at depth, it implies that the frictional interface is formed by a complex set of junctions across the two opposite surfaces in contact (Schmittbuhl et al., 2006; Pohrt & Popov, 2012). These junctions are commonly known as asperities (Bhushan, 1998). They have been characterized at the laboratory scale as microcontacts (Dieterich & Kilgore, 1994) where the resistance to an imposed shear stress is shown to be governed by

the initiation and evolution of the fault slip (Scholz, 2019).

The presence of these asperities on the fault is supported by the observation of small repeating earthquakes, supposedly representing cohesive zones that fail periodically under constant loading (Nadeau & Johnson, 1998; Frank, 2016). The role of such asperities in the behavior of earthquakes has long been recognized. For example, it is suggested that small and scattered asperities on a subduction interface may lead only to a minor release of the seismic moment (Ruff & Kanamori, 1983). On the other hand, a great earthquake may involve the simultaneous rupture of multiple asperities, such as the 1960 M_W 9.5 Chile earthquake (Moreno et al., 2009) or the 2004 M_W 9.2 Sumatra-Andaman earthquake (Subarya et al., 2006). Such examples have been interpreted in a framework drawing a strong link between the rupture synchronization of asperities and the magnitude of the impending earthquake (Lay & Kanamori, 1981; Lay et al., 1982). The role of asperities on the behavior of the faulting interface is not limited to dynamic rupture events. Indeed, the interseismic phase is also strongly impacted by the presence of such strong contact areas. This notably arises as locked patches can create stress shadows which lead to reduced interseismic slip rates on the surroundings of the asperity (Bürgmann et al., 2005) and thus a spatial modulation of the interseismic coupling (Perfettini et al., 2010).

Numerical models have addressed the behavior of a fault interface comprising multiple asperities. A number of simulations represent the interface notably in the context of the rate-and-state friction framework (Dieterich, 1979; Ruina, 1983; Marone, 1998b) and asperities are presented as distinct patches spatially distributed over the fault plane with distinct frictional parameters (Ariyoshi et al., 2009; Dublanchet et al., 2013; Luo & Ampuero, 2018; Li & Rubin, 2017). In these numerical models, the asperities are usually considered as velocity-weakening patches and are therefore defined to be potentially unstable. These models indicate that the mechanical response of a fault is evidently affected by the interactions of discrete asperities surrounded by aseismic creep areas. For instance, a variable density of asperities (Dublanchet et al., 2013), which is the ratio between the total area covered by asperities and the total area of the fault plane is proposed and

utilized to explain at which condition the fault will be ruptured entirely or locally. Incorporating roughness on the fault plane (as fluctuations of the normal stress), Cattania and Segall (2021) show that this heterogeneity modulates the slip stability across the fault. Finally, Romanet et al. (2018) demonstrate that the sliding diversity of a fault can be obtained from geometrical complexities alone, without the need for the complexity of the friction law. All these numerical approaches, therefore, point to the importance of these asperities and their interactions in controlling fault mechanics. However, these models are severely limited by the computational cost of simulating heterogeneities with a variable size over a large time and space domain and inherently only describe a limited aspect of the ongoing physics.

At the laboratory scale, numerous experiments on rock samples have also shown that fault roughness plays a crucial role in fault slip behavior (Goebel et al., 2017; Harbord et al., 2017; Morad et al., 2022; S. Xu et al., 2023; Yamashita et al., 2021) as it controls actual stress conditions at contacting asperities (Aubry et al., 2020). These results imply that the stress heterogeneity at local asperities is significant for influencing fault slip behavior. However, these experiments usually analyze the effects of asperities by comparing the initial and final roughness of the fault interface as the nontransparent rock slabs cannot provide the possibility to capture what is happening on the interface during the fault slip process. On the contrary, some other experiments take advantage of the transparency of analog materials (e.g., Poly-methyl-methacrylate, PMMA) to optically observe the asperities distributed on the interface (Lengliné et al., 2012; Jestin et al., 2019; Selvadurai & Glaser, 2015a, 2017), which provides a possibility for the direct monitoring of the faulting interface. Although the contacts were captured during these experiments, it was not possible to track the slip at each point during shearing.

Here we present a novel experimental setup that aims at capturing the slip as a function of time for each asperity on a sheared interface. Our experimental setup is much simpler than a complex fault zone system, which has no mineralogy, no fluid, and no chemical transformation, but the fundamental process of interest, the relationship between the collective behavior of local asperities and the sta-

bility regime of the global fault system, remains similar. Specifically, this novel experimental approach allows a thick transparent PMMA plate to slide slowly on a customized surface with height variations, on which asperities are modeled by numerous identical spherical PMMA beads embedded in a softer polymer base. Thanks to a high-resolution camera, our setup is capable of measuring directly the subtle motion of local asperities on the interface during the whole slipping process, which helps to understand the time-and-space dependent behavior of each single asperity. The mechanical response of the global fault system is well recorded and explained through the collective behavior of local asperities. The link between the fault topography and the interseismic coupling is also investigated. In addition, the spatio-temporal interactions of asperities are quantified as collective slip episodes mimicking fault ruptures including both stable and unstable slips. To give some geophysical implications, the effective upscaling from the analog interface to natural faults is demonstrated by reproducing significant characteristics and scaling-laws observed in natural fault systems.

4.3   Experimental Setup

We build an analog model of a shear interface that aims at reproducing the typical mechanical structure of a natural fault core. We consider that a fault zone consists of several key elements. At the interface, the roughness of the fault topography creates contacts on a number of discrete sites, i.e. asperities, that are here modeled as PMMA beads. The core of the fault, which consists generally in a heavily fractured medium (Chester & Chester, 1998; Schulz & Evans, 2000) is represented in our setup with a soft material surrounding the PMMA beads. At a greater distance from the fault, the number of damage decreases (Ben-Zion & Sammis, 2003; Mitchell & Faulkner, 2009; Stierman, 1984), and the fault becomes stiffer which translates in our setup in a rigid base attached to the soft material (Figure 4.1). The asperities are in contact with a top rigid block and establish a rough slip plane, while the soft embedding block fixed within the bottom rigid frame is easily deformed. This thick, rough, and deformable interface allows us to

study the interactions of asperities and their collective behavior with respect to the frictional stability of the fault interface.
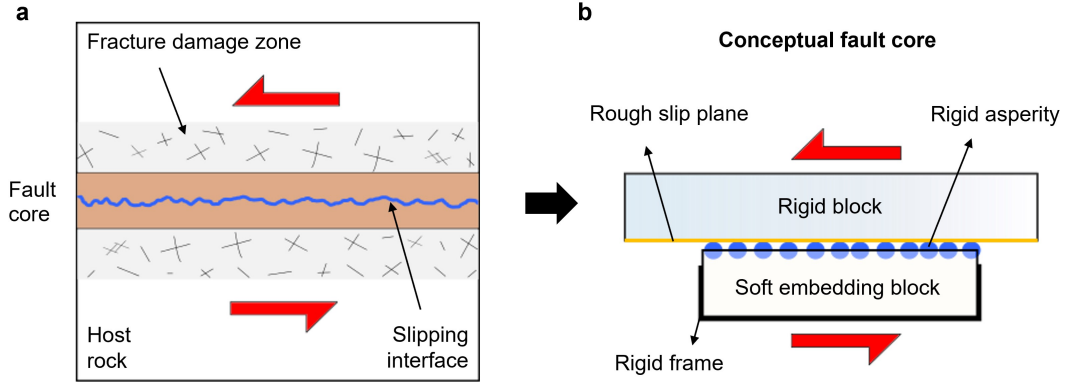
Figure 4.1: a: Sketch of a typical natural fault zone showing a rough frictional slipping interface subjected to shear. **b:** Conceptual model of the analog shear interface derived from the natural fault core structure. The rigid asperities embedded in the soft thick block establish a rough slip plane beneath the top rigid block. Retrieved from Shu et al. (2023).

4.3.1 Sample Preparation and Characterization

To prepare such a model of multi-asperity contact, numerous identical spherical PMMA beads (a total number of 175) with a radius R of 3 mm are embedded in a soft block. The soft block is composed of silicone (BLUESIL RTV 3428 A&B product from the Elkem company), with dimensions $10 \times 10 \times 3.0$ cm. The preparation of the sample consists in first pouring a thin layer (of the thickness of a bead radius) of edible gelatin mixed with water at the bottom of a mold. Then PMMA beads are dropped randomly in this layer all over the interface. After the gelatin layer solidifies, we then pour the liquid silicon into the mold to cover the beads and wait for at least 24 hours at room temperature for its solidification. Finally, we take out the upside-down sample and remove the mixture of gelatin and water. Following the procedures above, we customize an experimental sample where multiple frictional asperities are embedded in the viscoelastic silicone block.

Such an experimental design is supported by growing geological evidence suggesting that a mixture of frictional and viscous deformation is responsible for the emerging diversity of fault slip behaviors (Behr & Bürgmann, 2021; Kirkpatrick et al., 2021). The resulting sample is made such that all beads have nearly the same height while being scattered randomly over the sample and its picture is displayed in Figure 4.2. Physical characteristics of the silicone are derived from the technical datasheet, the relation of Gent (1958) for converting durometer values to Young's modulus, and laboratory measurements of the P-wave velocity of the material. We obtain a P-wave velocity for this material of 1000 m/s, an S-wave velocity of 19 m/s, a Young's modulus of 1.1 MPa, and a density of 1100 kg/m^3. The viscoelasticity of the silicone block is also measured and quantified (Figure 2.2 and Figure 2.3).

In order to precisely describe the so-formed interface and get the summit heights of all the beads, we measure a high-resolution topographical map for the interface. The data are acquired by a digital microscope profiler (RH-2000, HIROX) and a non-contact Nano Point Scanner (NPS, HIROX). The system uses a white light confocal LED beam with grids of 28 μm and 100 μm in the x- and y-directions, respectively. The topographical map of the interface is shown in Figure 4.3a, where the blueish part indicates the embedding silicone block while the discrete circles represent the asperities with different heights. We determine the peak heights of all the asperities (Figure 4.3b) and statistically analyze their distribution (Figure 4.3c). The peak heights of asperities (relative to the average silicone upper face level) range from 1.31 mm to 3.15 mm, with most of them within the peak height interval $[1.4, 2.6]$. The average peak height is 2.02 mm and the standard deviation of the peak heights is 0.39 mm, which indicates a small variance in the peak heights of asperities. We notice that there is a large-scale trend across the entire sample of this peak bead height. This is most likely due to the non-perfect planarity of the gelatin layer. Removing this large-scale trend, we observe that the height difference between neighboring asperities is low. In addition, we compute the average peak height difference between two asperities as a function of the distance in x and y direction (Figure 4.3d). We find a pattern highlighting the large scale variation of the peak height but no other correlation of the peak heights emerges.
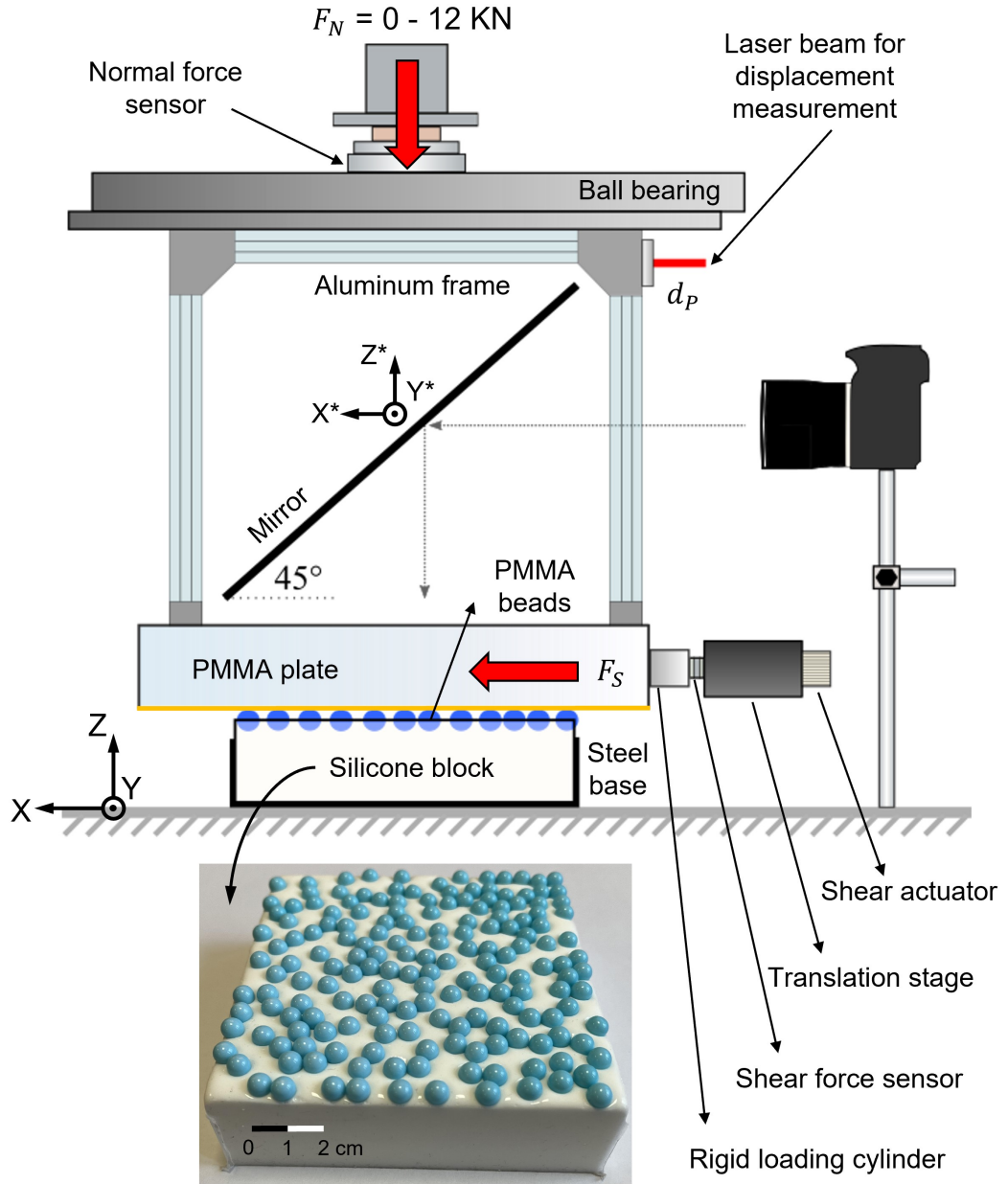
Figure 4.2: Schematic diagram of the technical experimental setup (side view). The normal force, F_N, and shear force, F_S, are measured by their corresponding sensors. A laser is employed to measure the displacement of the PMMA plate, d_P. A high-resolution camera is utilized with a mirror to monitor the positions of the PMMA beads during the whole shear process. Two axis systems, one attached to the ground and another one attached to the mirror, are represented. The yellow line indicates a rough slip plane established between the PMMA plate and the PMMA beads. The inset shows an image of the PMMA beads embedded in the soft silicone block. Retrieved from Shu et al. (2023).
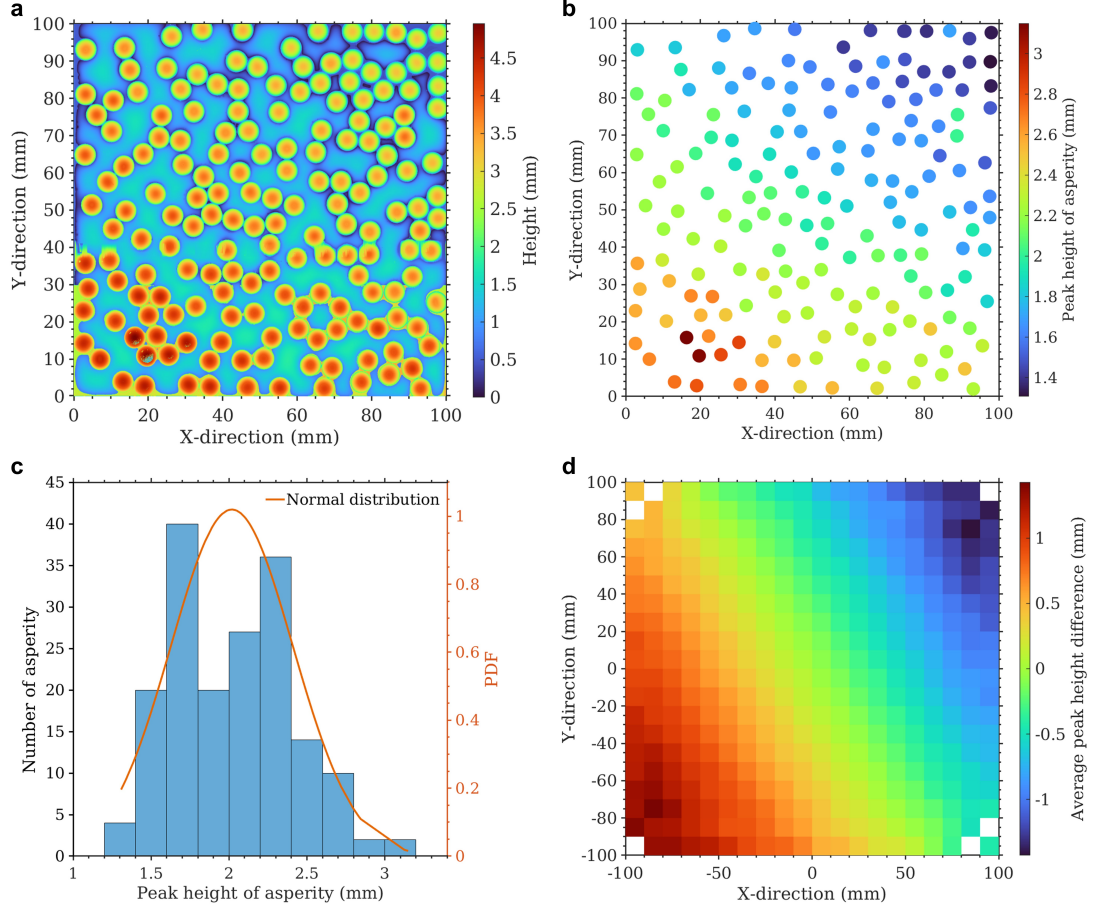
Figure 4.3: a: Topographical map of the analog fault interface. The blueish part is the embedding silicone block while the colored circles are the asperities created by the PMMA beads. There are a few non-measured points in the bottom-left corner that have little effect on characterizing the interface. **b:** Peak height of each asperity. The minimum and the maximum are 1.31 mm and 3.15 mm, respectively. **c:** Distribution of the peak heights of all the asperities. The asperities with peak heights ranging from 1.4 to 2.6 mm account for the majority. A standard deviation of 0.39 mm indicates a small variance in the peak heights. **d:** Average peak height difference as a function of the x and y direction. This highlights the large scale variation of the peak heights. Retrieved from Shu et al. (2023).

Table 4.1: Parameters of each experiment

| Normal load (N) | Displacement rate (μm/s) | | |
	5.0	10.0	15.0
10	Exp.26		
25	Exp.25		
50	Exp.24		
100	Exp.6	Exp.7	Exp.8, Exp.27, Exp.28
200	Exp.1, Exp.9	Exp.10	Exp.11
400	Exp.2, Exp.12	Exp.13	Exp.14
600	Exp.15	Exp.3, Exp.16	Exp.17
700	Exp.18	Exp.19	Exp.20
800	Exp.21	Exp.4, Exp.22	Exp.23
1000			Exp.5

4.3.2 Mechanical Loading

To simulate a large-scale, far-field, loading imposed on a fault, the shear of the whole analog interface system is induced by imposing a small displacement rate to the PMMA plate under well-controlled normal loads (Figure 4.2). Multiple normal loads ranging from 10 N to 1000 N and three displacement rates ranging from 5.0 μm/s to 15.0 μm/s are imposed in the experiments (Table 4.1). We consider a simple Hertz model consisting of the serial assembly of the PMMA beads and the silicone block both modeled as elastic materials (K. Johnson, 1987). As the displacement is imposed on the PMMA beads, the contact area increases and both the PMMA beads and the silicone are deforming. The typical normal stress on the PMMA beads is around 60 MPa, while the typical radius of contact is 200 micrometers.

PMMA has been widely used, as an analog material, to simulate numerous mechanical processes taking place within the Earth. In particular, frictional processes taking place on natural faults have been investigated using this material, such as fault creep and nucleation phases (e.g., McLaskey & Glaser, 2011; McLaskey et al., 2012; Selvadurai & Glaser, 2015a) but also ruptures (e.g., Ben-David, Cohen, & Fineberg, 2010; Gvirtzman & Fineberg, 2021; Schmittbuhl & Måløy, 1997). Due to its transparency, the PMMA enables a clear direct observation of the deforming medium (Lengliné et al., 2012; Jestin et al., 2019). The shear modulus of the

PMMA is estimated as 2277.1 MPa (Selvadurai & Glaser, 2015a).

The normal force F_N is applied by the vertical movement of the rigid load platen driven by a high-precision micro stepper motor (LoadTrac II), and uniformly transferred to the PMMA plate through the ball bearing and the rigid aluminum frame. A sensor of resolution 0.01 N is utilized to record the normal force and maintain a constant normal load throughout the whole duration of an experiment. We run the shear actuator, a combination of servo and stepper motor, with a constant displacement rate V_S to drive the translation stage and the rigid loading cylinder to impose the shear force F_S while maintaining a normal force F_N on the PMMA plate. The loading cylinder is composed of the aluminium alloy 2017A, with a stiffness of 78 N/μm. The shear force F_S is measured using a sensor placed between the cylinder and the translation stage, with a resolution of 0.01 N. The stiffness of this sensor is 1 N/μm, thus most of the loading stage deformation is actually taking place within the force sensor. We employ a laser (Keyence IL-S025), range 10 mm and resolution 0.1 μm, to measure the displacement of the PMMA plate, d_P (Figure 4.2). For all the experiments, we keep the initial value of d_P the same to ensure each fault slip starts from the same position.

Prior to performing the experiments, we fix the PMMA plate to the aluminum frame and attach the silicone block to the rigid steel base and clamp it. We use a digital level to make sure that the whole experimental system, especially the slip plane, is flat horizontal. Each experiment begins at the moment when the shear force starts to increase on the PMMA plate, given the analog fault has been previously loaded by a stable normal load. The duration of each experiment is set to 600 s. We performed 28 experiments by applying various normal loads and displacement rates (Table 4.1). We define the x-direction as the sliding direction of the PMMA plate while the direction y is set perpendicular to the x-direction.

To demonstrate the transition from steady slip to stick-slip in our analog fault system, the evolution of the shear force, F_S, under multiple normal loads, F_N, maintaining the same loading rate V_S of 5.0 μm/s is presented in Figure 4.4. We clearly observe the steady sliding of the interface when the normal load is quite small (e.g., $F_N = 10$ N). On the other hand, multiple stick-slips are observed when
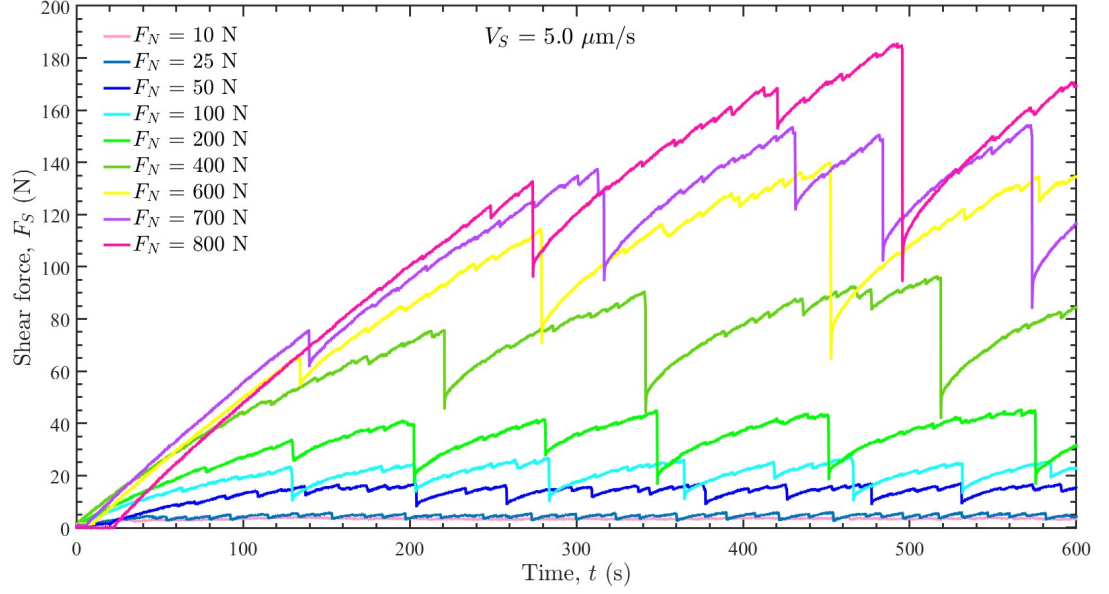
Figure 4.4: Temporal evolution of the shear force under multiple normal loads. The interface slips steadily when the normal load is quite small while evident stick-slips occur when the normal load becomes greater than 50 N. With the increase of the normal load, the shear force drop also increases. Retrieved from Shu et al. (2023).

the normal load becomes greater than 50 N (Figure 4.4). In addition, the shear force drop of each stick-slip increases with the increase of the normal load.

4.3.3 Optical Monitoring

To capture the positions of asperities and compute their slips during the experiments, we use a high-resolution camera (Nikon D800) with a lens (Nikon 105mm f/2.8D AF Micro-Nikkor) in automatic focus mode to record videos. A mirror fixed inside the aluminum frame, which is inclined at 45 degrees, reflects the interface and moves with the sliding of the PMMA plate during the experiments (Figure 4.2). The main settings of the optical system are as follows: aperture size f/14, exposure time 1/30 s, and photosensitivity (ISO) 100. Two LED lights are placed behind the camera to supplement sufficient light for the clear observation of the interface. We record videos of dimensions in 1920 × 1080 pixels with a sampling

rate of 29.97 frames per second. In addition, to synchronize the force measurement and the optical monitoring, we send an electrical synchronization signal and correct the time base of each record.

For each experiment, we extract all pictures taken by the camera between the times t_0 and t_f which are respectively the times at the beginning and the end of an experiment. From this set of pictures, we extract the slip of each individual asperity as a function of time. Denoting $x_i(t)$ and $y_i(t)$ the positions of the center of asperity i in a fixed reference frame (attached to the ground) we can define the displacement, $d_i(t)$, of an asperity along the loading direction in this fixed frame,

$$d_i(t) = x_i(t) - x_i(t_0). \tag{4.1}$$

Similarly, we define $x_P(t)$ as the position of the center of the mirror in the same fixed frame and then its displacement (which corresponds to the displacement of the PMMA plate as well), is computed as:

$$d_P(t) = x_P(t) - x_P(t_0). \tag{4.2}$$

The cumulative slip of asperity i at time t is defined as the difference of the displacement between the two sides of the interface (i.e., the asperity and the PMMA plate):

$$u_i(t) = d_i(t) - d_P(t). \tag{4.3}$$

As the camera and the silicone block are both fixed to the ground while the mirror moves with the sliding PMMA plate, the position of each asperity, i, on pictures taken by the camera is relative to the moving frame of the mirror and is noted $(x_i^*(t), y_i^*(t))$. It follows that the displacement of an asperity in this moving frame is simply $d_i^*(t) = x_i^*(t) - x_i^*(t_0)$. From the definition of the cumulative slip introduced before, this displacement, $d_i^*(t)$, corresponds exactly to the cumulative slip, $u_i(t)$ of asperity i. Consequently, the cumulative slip of each asperity is obtained by tracking the evolution of its position, $x_i^*(t)$, between time t_0 and time t_f.

We developed a two steps procedure for tracking the evolution of the position $x_i^*(t)$ of each asperity i in the moving frame of the mirror. In the first step, we applied the circular Hough transform algorithm implemented within MATLAB for automatically detecting circular objects (Yuen et al., 1990; Davies, 2005). From the first and last pictures at times t_0 and t_f respectively, we extract the initial position $x_i^*(t_0)$ and final position $x_i^*(t_f)$ of asperity i. We also estimate the initial position of the beads, $y_i^*(t_0)$ in the direction perpendicular to the slip direction.

The initial positions of asperities detected at time t_0 are shown in Figure 4.5. The asperities marked by red circles, with a total number of $N = 144$, are retained in our analysis while the asperities with blue markers are excluded from the subsequent image analysis because they are located too close to one of the image edges. We note the value of N may change with different experiments mainly due to the field view of the camera, but it fluctuates around 140. In addition, we obtain the radius R, which is 36 pixels, and compute the scaling of the image from the known radius of the PMMA beads ($R = 3$ mm), 12 pixels/mm. Based on the initial and final positions of asperities, we are able to estimate the total slip $u_i(t_f) = x_i^*(t_f) - x_i^*(t_0)$ of each asperity. Due to the constant loading rate, a simple linear trend between these two positions gives an approximate position, $x_i^*(t)$ of asperity i at each time step. This provides a first-order estimate of each asperity location during the experiment. In the second step, in order to obtain the most accurate locations, we applied an image correlation technique (Sutton et al., 2009) to refine these first measurements.

To quantify the slip of each asperity, a square window for image correlation with a size of $\sqrt{2}R$ is defined at the center of each asperity based on our previous estimates of $x_i^*(t_0)$ and $y_i^*(t_0)$. We extract the image defined by the square correlation window of each asperity at all frames. For each asperity, we compute the FFT (fast Fourier transform)-based two-dimensional cross-correlation between the extracted window defined at time t_k and the window defined at time t_{k-1}. From the correlation map, we isolate the position of the maximum value which gives the displacement of the bead. We then shift the correlation window of the second frame based on this displacement and repeat the procedure until the computed
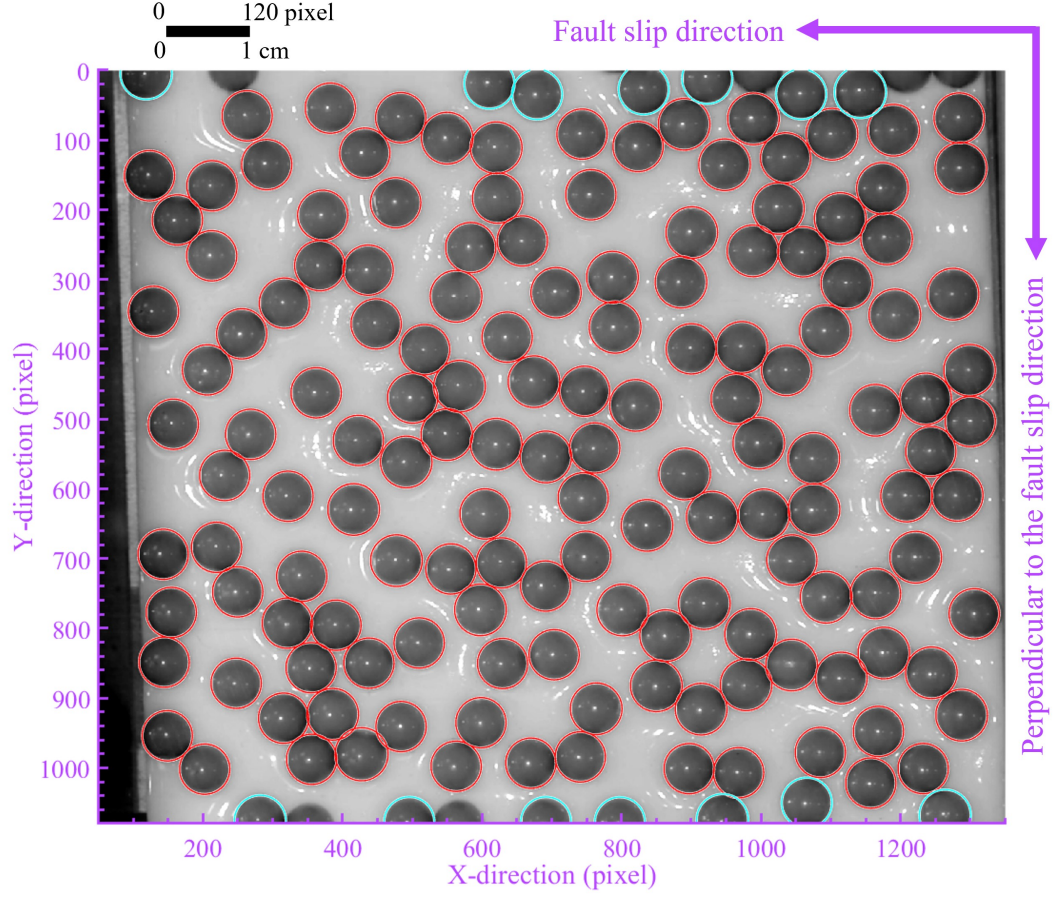
Figure 4.5: Typical automatic detection results indicating the initial positions of asperities at time t_0, on the interface within a region of interest of dimensions 1300 $\times$ 1080 pixels (i.e., 108.33 $\times$ 90 mm). The asperities without markers represent the undetected ones while the asperities with blue circles correspond to the excluded ones as their correlation windows exceed the image boundary. A total of $N = 144$ asperities marked by red circles are kept and their positions $x_i^*(t_0)$ are taken as the initial positions for computing the slip through the image correlation. Retrieved from Shu et al. (2023).

displacement is null. At this last stage, we then extract a sub-sample displacement by interpolating the correlation map around its maximum. The final displacement of the bead between the two time frames is then obtained by summing all displacements computed during this iterative process. Repeating this procedure for all time frames and for each bead we are able to obtain the cumulative slip of each asperity during the whole duration of an experiment. The typical resolution of the resolved displacement in each direction is of the order of 0.01 mm.

Due to the geometry of our experimental setup, the non-parallelism which may result from the non-perfect 45-degree inclination of the mirror and/or the non-parallel view between the camera lens and the slip plane (Figure 4.2), can create a non-linear scaling along the x axis. In order to eliminate this effect, we correct the cumulative slip of asperity i based on its total slip $u_i(t_f)$, which is supposed to be no greater than the displacement $d_P(t_f)$ of the PMMA plate at time t_f. Given the corrected cumulative slip $u_i(t)$ of asperities, we then update the displacement $d_i(t)$ of asperities following the equation (4.3).

Finally, we also note that the asperities also exhibit slips perpendicular to the loading direction. These cumulative slips are near-evenly distributed around zero and the maximum cumulative slip is quite small compared to the cumulative slip along the faulting direction. We present the trajectories of all the asperities during the whole experimental duration in Figure 4.6, where the onset of the trajectory of each asperity is set to be at the origin $(0, 0)$. The total slip during this experiment is of the order of the asperity size, $R = 3$ mm, and the slip in the x direction is about 10 times larger than that in the y direction. There is a fan shape of the trajectories with a mean y-direction that is close to zero. We observe several prominent gaps that correspond to the large stick-slip events during the faulting. For the other experiments under different loading characteristics, the total slip of asperities in the x direction is dependent on the loading rate and the experimental duration while that in the y direction is generally of the same order of ~ 0.3 mm.
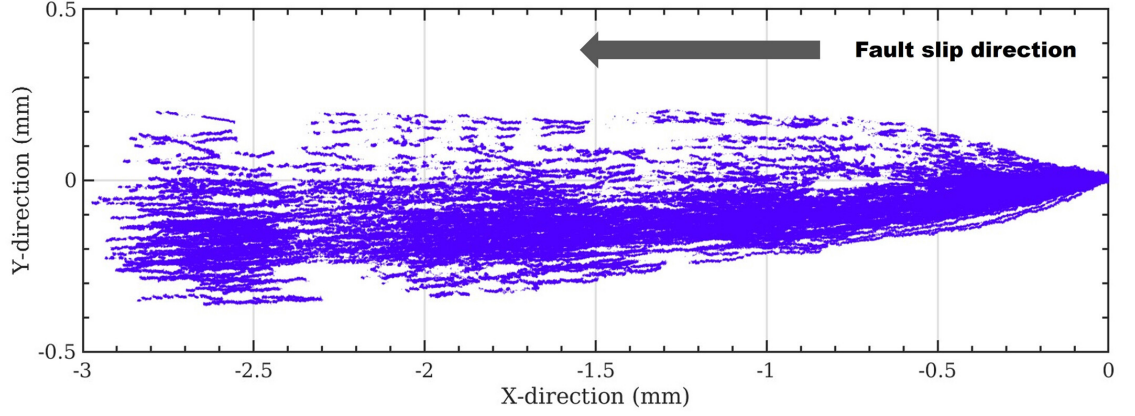
Figure 4.6: Trajectories of all the asperities during the whole duration of an experiment under a normal load of 400 N and a loading rate of 5 μm/s. The onset of each trajectory is superimposed to be at the origin $(0, 0)$. The prominent gaps correspond to the large stick-slip events. Retrieved from Shu et al. (2023).

4.4 Collective Behavior of Asperities

4.4.1 Temporal Evolution of the Cumulative Slips of Asperities

To understand the individual behaviors of asperities as well as the relationship between each local asperity and the whole interface, we present the temporal evolution of the cumulative slips of individual asperities. For a better visibility, only 20 asperities, randomly selected out of 144 asperities, are presented in Figure 4.7. The cumulative slips of the 20 asperities are color-coded by their initial positions $y_i(t_0)$. We also indicate in Figure 4.7 the loading rate of the interface which is 15.0 μm/s here. Any asperity following this trend could be considered then as fully sliding. On the contrary, a fully sticking asperity would accumulate no relative slip with respect to the loading plate. Its behavior would appear as a horizontal line in Figure 4.7.

The stepping feature of cumulative slip evolution of the asperities in Figure 4.7 illustrates the repetitive stick-slip events of the interface (20 events in Figure 4.7a and a zoom on one of them in Figure 4.7b). These events involve all the asperities of the interface. In the time interval between these whole stick-slip episodes, during
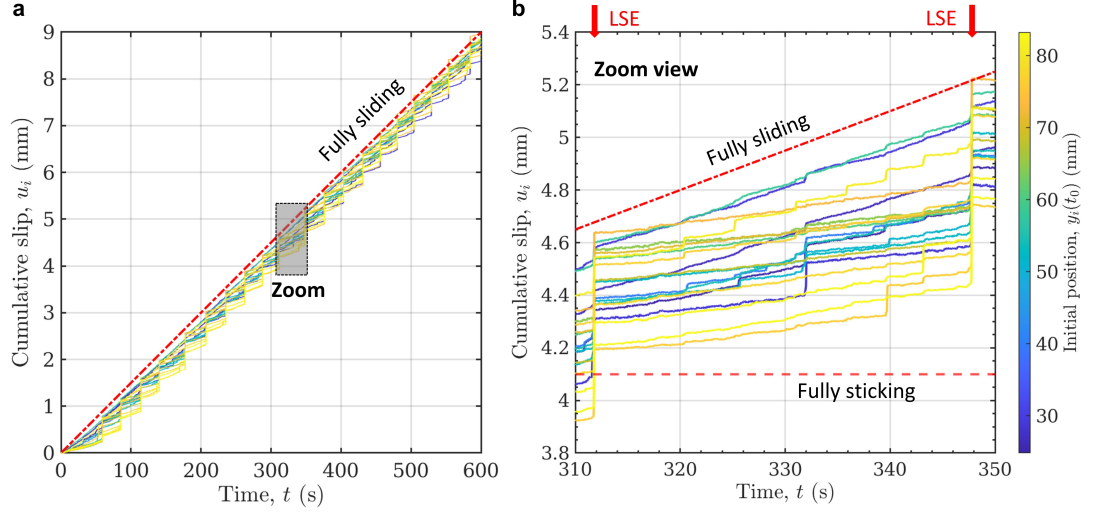
Figure 4.7: a: Temporal evolution of the cumulative slip in the x direction for 20 asperities during an experiment under a normal load of 200 N and a loading rate of 15.0 μm/s. The cumulative slips of the 20 asperities are colored-coded by their initial y positions at time t_0. **b:** Zoom view of Figure 4.7a showing the detailed behaviors of asperities during one time interval between two large stick-slip events (LSE) and ranging from 310 s to 350 s. Fully sticking indicates a locked state while fully sliding gives the slope of the imposed displacement rate to the system. Retrieved from Shu et al. (2023).

the sticking phase, the asperities show distinct behaviors. We observe that all the slipping rates are smaller than that of the imposed loading rate (see the slopes of the cumulative slip of the asperities and the PMMA plate) but with a non-horizontal trend, which indicates that, actually, the asperities are slipping at a low rate during the sticking phase, instead of being fully locked.

It is noteworthy that the slips accumulated during each sticking period are not the same for different asperities. This proves that different asperities can slip at different rates, though they are all in the quasi-static regime (i.e. the sticking phase of the interface stick-slip behavior). Another interesting finding is that there are also some small visible slips that occurred at different single asperities during the overall sticking phase and correspond to small stick-slip events at the scale of several asperities. These small episodes contrast with global slip episodes, when all

the local asperities slip rapidly in a synchronous way and that we define as a large stick-slip event (LSE). Moreover, the observation that the slips on all asperities after a LSE do not reach the imposed loading slip, indicates that accumulated stress is only partly released during such a whole scale event.

4.4.2 Slip Velocity of Asperities

Slip velocity reflects the slipping rate of asperities, which is estimated using a given discretization of the time (i.e., time step) during the whole experiment. The slip velocity $v_i(t_k)$ of each asperity i is computed as

$$v_i(t_k) = \frac{s_i(t_k)}{\Delta t} = \frac{u_i(t_k) - u_i(t_{k-1})}{\Delta t}, \tag{4.4}$$

where $s_i(t_k)$ is the slip of the asperity i at time t_k and Δt is the fixed time step of 1/29.97 s determined by the sampling rate of the camera, i.e., $t_k - t_{k-1}$. Following the same experimental data used in Figure 4.7, for illustration, the slip velocity of all the 144 asperities ranging from time 330 s to time 350 s is shown in Figure 4.8, where the asperities are sorted in ascending order by their initial positions $x_i(t_0)$. A LSE involving the synchronous slipping of all the asperities is observed at the time 348 s. We also observe several small stick-slip events that share the same characteristic, which is the synchronized sliding of only a part of the asperities.

4.4.3 Mechanical Response of the Interface

In order to document the mechanical response of the frictional interface, we analyze how the shear force evolves as a function of slip. Here we define the shear-to-normal force ratio, $\mu_f = F_S/F_N$, as the effective friction coefficient during the slip of the sticking phase, while the shear-to-normal force ratio, $\mu = F_S/F_N$, is defined as the friction coefficient at the onset of a large stick-slip event. We compute the spatial average of the cumulative slip, $\langle u(t) \rangle$, over all asperities, N, following
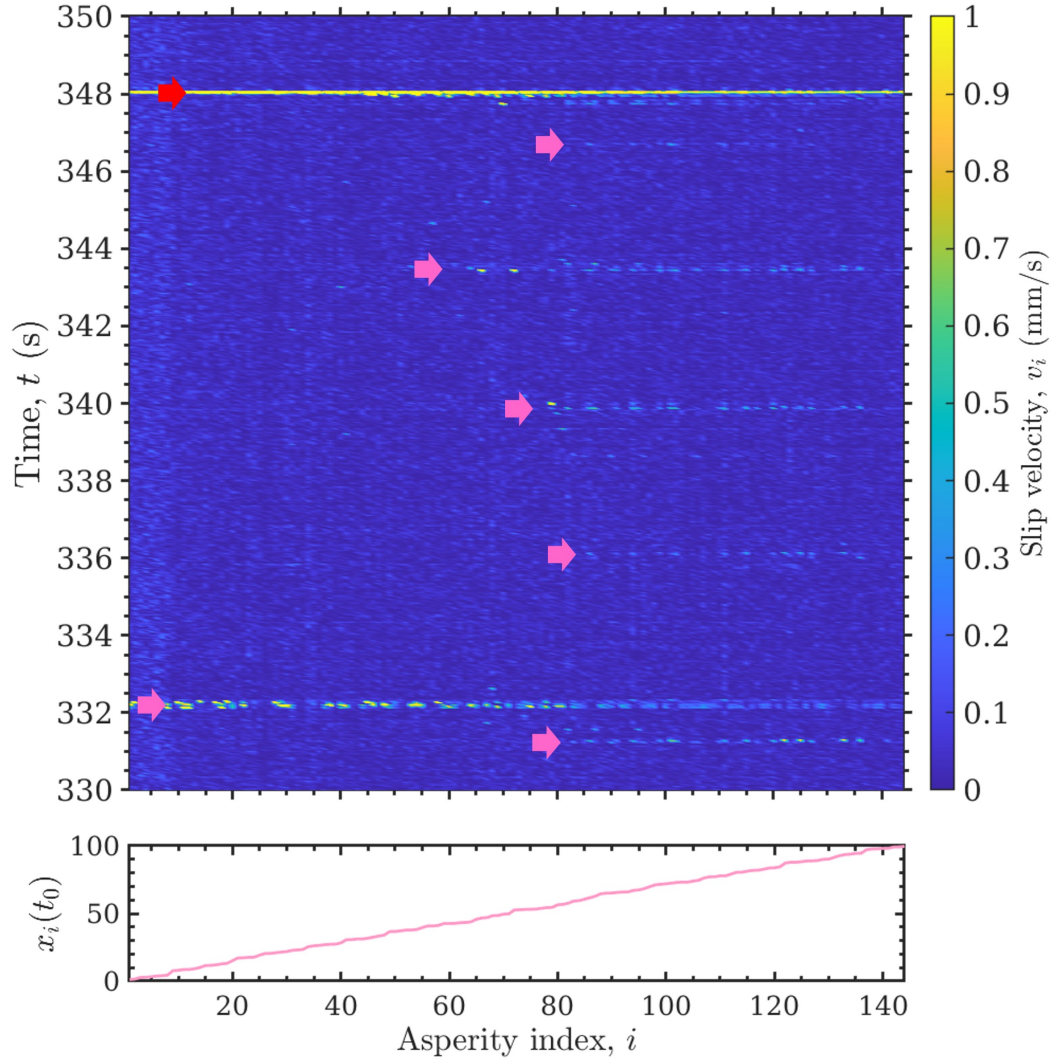
Figure 4.8: Slip velocity of all the asperities during the time period ranging from 330 s to 350 s of the same experiment shown in Figure 4.7. The asperities are sorted in ascending order by their initial x positions at time t_0, $x_i(t_0)$. A large stick-slip event (LSE) indicated by the red arrow occurred at time 348 s observed, where all the asperities are synchronously slipping. During the sticking phase, there are also several small stick-slip events (SEs) which are indicated by the pink arrows involving the slipping of a part of asperities. We note that the slip velocity is thresholded as 1 mm/s to clearly show the slipping of local asperities. The maximum slip velocity is about 11 mm/s which is a rough proxy as this might be strongly sensitive to the sampling rate of the camera. Retrieved from Shu et al. (2023).

$$\langle u(t) \rangle = \frac{1}{N} \sum_{i=1}^{N} u_i(t), \tag{4.5}$$

which is a global indicator of the collective behavior of all the asperities. As multiple seismic cycles (i.e., large stick-slip events) are produced during a single experiment, we report in Figure 4.9a the evolution of μ_f as a function of $\langle u(t) \rangle$, for all the cycles of a single experiment. Each cycle is separated based on the onset of a large scale slip event LSE (observed when μ_f reaches a local maximum before an abrupt decrease, i.e., when $\mu_f = \mu$). The value of the friction coefficient mainly ranges between 0.10 and 0.23, which is a low value but comparable to the values in other PMMA-PMMA interfaces (Baumberger & Caroli, 2006; Selvadurai & Glaser, 2015a). We observe, in each cycle, a stage with an overall increase of the effective friction coefficient, μ_f, during the slow slipping phase and a weakening stage during the fast slipping phase.

To focus on the slow slipping phase of the whole faulting process, the variations of the effective friction coefficient, $\Delta\mu_f$, and of the average cumulative slip, $\Delta\langle u(t) \rangle$, are both computed relative to their respective values at the onset of these large scale slips. We plot the variation of the effective friction coefficient, $\Delta\mu_f$, as a function of the variation of the average cumulative slip of all the asperities, $\Delta\langle u(t) \rangle$, by superimposing all the slow and the fast slipping phases, where each onset of the fast slipping phase is set to be $\Delta\mu_f = 0$ and $\Delta\langle u(t) \rangle = 0$ (Figure 4.9b). The curves represent the slow slipping phase while the circles represent only a few time steps after the onset of the LSE. We observe a good similarity between all seismic cycles, proving the repeatability of our observations. We observe that the effective friction coefficient during the period preceding the large scale event (LSE) is increasing. This strengthening of the interface is occurring while the interface is slipping. We observe that during this overall increase of the effective friction coefficient, there exist multiple instances where μ_f actually drops significantly compared to the error of the effective friction coefficient measurement. The strengthening of the interface (an overall increase of μ_f) is thus not a homogeneous process and is slip-controlled in a non-linear manner. It should be noted that slip-strengthening is defined here at the global scale (i.e., the entire fault interface) as phenomenological behavior, i.e.,
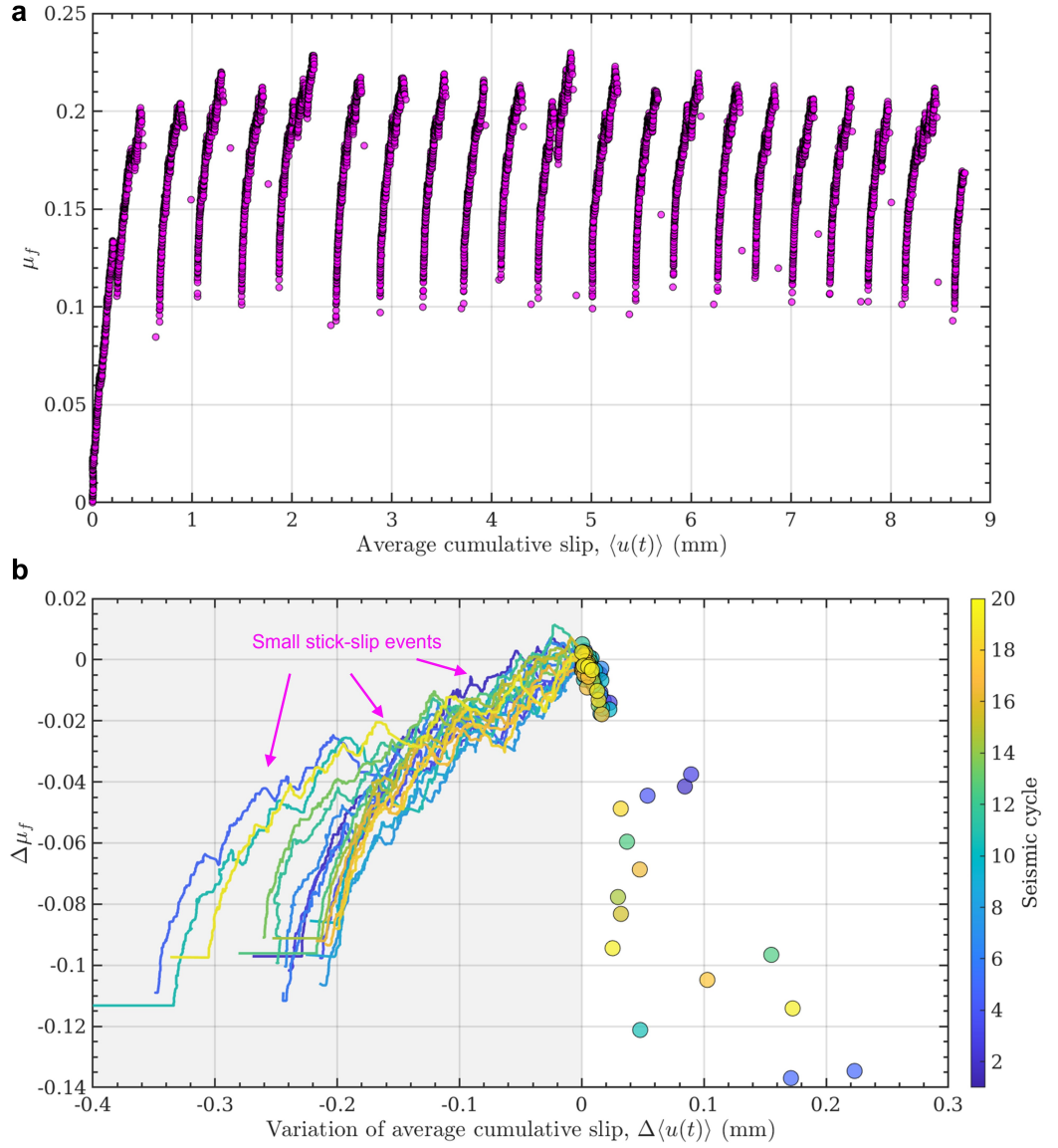
Figure 4.9: a: Evolution of the shear-to-normal force ratio, μ_f, as a function of the average cumulative slip, $\langle u(t) \rangle$, during the same experiment shown in Figure 4.7 with multiple seismic cycles. **b:** Variation of the effective friction coefficient, $\Delta \mu_f$, as a function of the variation of the average cumulative slip of all the asperities, $\Delta \langle u(t) \rangle$, for the same experiment shown in Figure 4.9a. All the seismic cycles represented by different colors are superimposed together by setting the onset of each fast slipping phase as the origin. The colored curves in the shadow indicate different slow slipping phases while the circles denote the corresponding fast slipping phases. Retrieved from Shu et al. (2023).

the increase in frictional strength with mean interface slip. This definition of slip-strengthening also applies elsewhere in this paper (e.g., key points, discussion, etc.). This shows as well that this slip-strengthening stage, conventionally considered as the stable regime of a fault, actually consists of many small-scale destabilizing events. The rapid slip that occurs during a LSE is not well captured by our experiments mainly because of the limited time resolution of the camera that does not allow a sufficient time sampling during this stage. It is also possible that the weakening part is velocity dependent which is not well captured here since Figure 4.9b represents the effective friction coefficient, μ_f, as a function of slip with no information on the velocity.

4.4.4 Topographical Effect on Interseismic Slipping Behaviors

Our results show that many small stick-slip events accompanied by effective friction coefficient drops are found during every slip-strengthening stage (Figure 4.9). These interseismic, small stick-slip events result from the slip of a limited number of asperities on the interface. In order to identify what controls the number and the amount of these partial slips, we document the interseismic slipping behaviors of the asperity using the interseismic coupling coefficient (Hyndman et al., 1997). We denote the onset times of the j and the $j+1$ large stick-slip events as $t(\mathrm{LSE}(j))$ and $t(\mathrm{LSE}(j+1))$, respectively. To describe the extent of the slipping of the asperity i during the interseismic phase between $t(\mathrm{LSE}(j))$ and $t(\mathrm{LSE}(j+1))$, the interseismic coupling, $\lambda_{i,j+1}$, is computed as

$$\lambda_{i,j+1} = 1 - \frac{u_i(t(\mathrm{LSE}(j+1))) - u_i(t(\mathrm{LSE}(j)))}{d_P(t(\mathrm{LSE}(j+1))) - d_P(t(\mathrm{LSE}(j)))}. \tag{4.6}$$

We note that λ is in the range $[0,1]$, where $\lambda = 0$ indicates no coupling or fully sliding while $\lambda = 1$ denotes a fully coupled interface or sticking. For experiments with multiple seismic cycles, we compute the final interseismic coupling for each asperity i by averaging λ_i over all of the interseismic phases.

With the experimental data used in Figure 4.9, we present the interseismic cou-

pling of these asperities along the interface (Figure 4.10). We observe a large scale trend of this interseismic coupling that we can link with the same trend observed from the peak height of asperity derived from the topographical map (Figure 4.3b). A higher peak height of asperity corresponds to a higher interseismic coupling while a smaller peak height is corresponding to a lower interseismic coupling. This can be interpreted in terms of normal stress on the asperity where a higher peak height causes a greater normal stress, and therefore creates the locking of the asperity which increases the interseismic coupling. On the contrary, the asperities with smaller peak heights have a low normal stress and thus cannot accumulate large shear stress (and consequently large slip deficit) and will fail more often during the interseismic phase and have a low coupling, i.e., low values of λ.

We also investigate the direct effect of the macroscopic normal load on the interseismic coupling, as shown in Figure 4.11. For all experiments with the same normal load, we compute the interseismic coupling of each asperity, which is indicated by the colored circles. The average evolution of the interseismic coupling with peak heights conceals some scattering. Indeed, we can observe from Figure 4.11 that for the same normal load and the same asperity height, different values of λ are computed. To present the evolution of the interseismic coupling as a function of the peak height of asperity, we average the interseismic coupling values over peak heights within a bin width of 0.10 mm. It evidences that, when the normal load is low: 10 N and 25 N, all the asperities have a quite small interseismic coupling, a value that is not distinguishable from zero. The interseismic coupling shows no dependence on the peak height. This is consistent with the mechanical response of the fault system shown in Figure 4.4, where the global fault slips almost steadily under the normal loads of 10 N and 25 N.

As the normal load increases and becomes large enough such that large stick-slips of the whole fault system are observed, we evidence that interseismic coupling is then dependent on the peak height of asperities. The asperities with low peak heights correspond to low normal stresses, thus inducing the small stick-slip events observed in between the large stick-slip events due to a small interseismic coupling. For the same peak height of asperity, the interseismic coupling increases with the
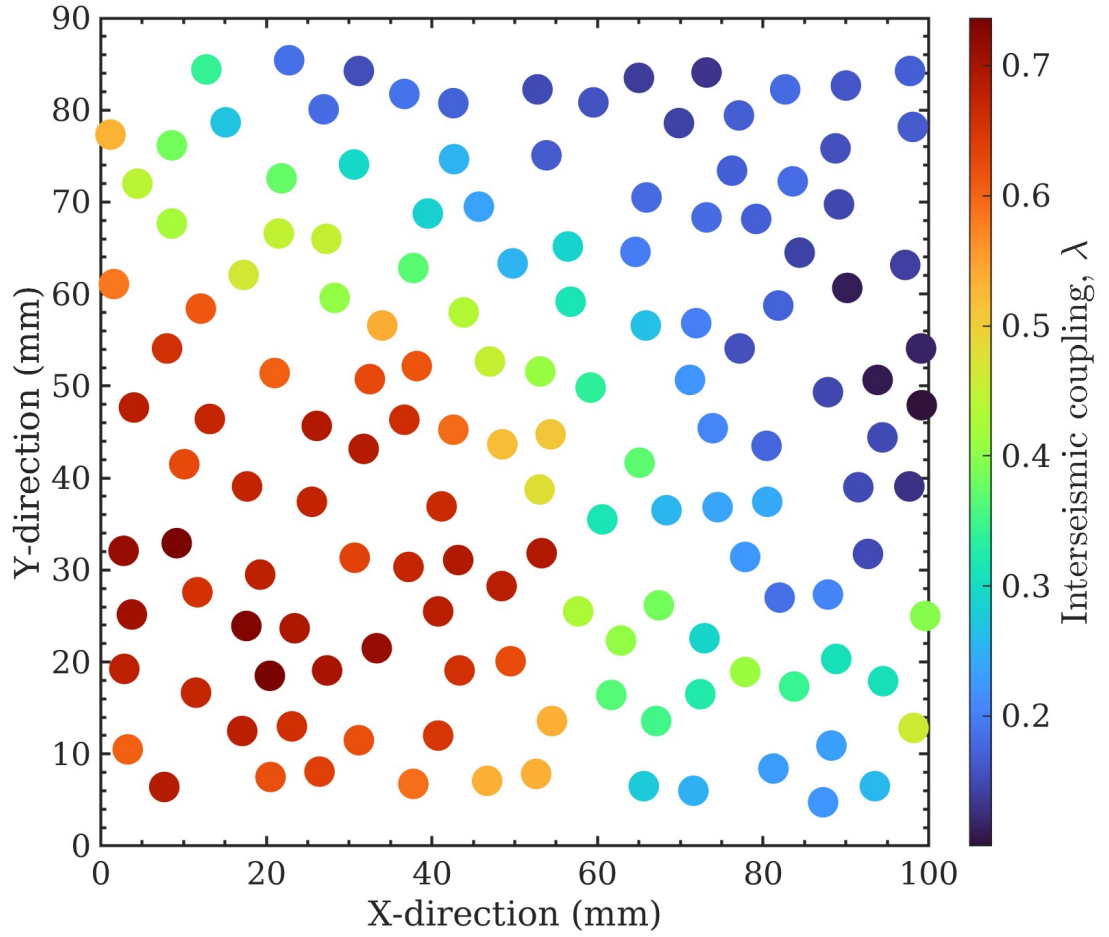
Figure 4.10: Map of the interseismic coupling of asperities along the interface using the same experimental data shown in Figure 4.9. A similar pattern between the peak heights of asperity (Figure 4.3b) and the interseismic coupling is observed, which shows that a larger peak height corresponds to a larger interseismic coupling whereas a smaller peak height corresponds to a lower interseismic coupling. Retrieved from Shu et al. (2023).
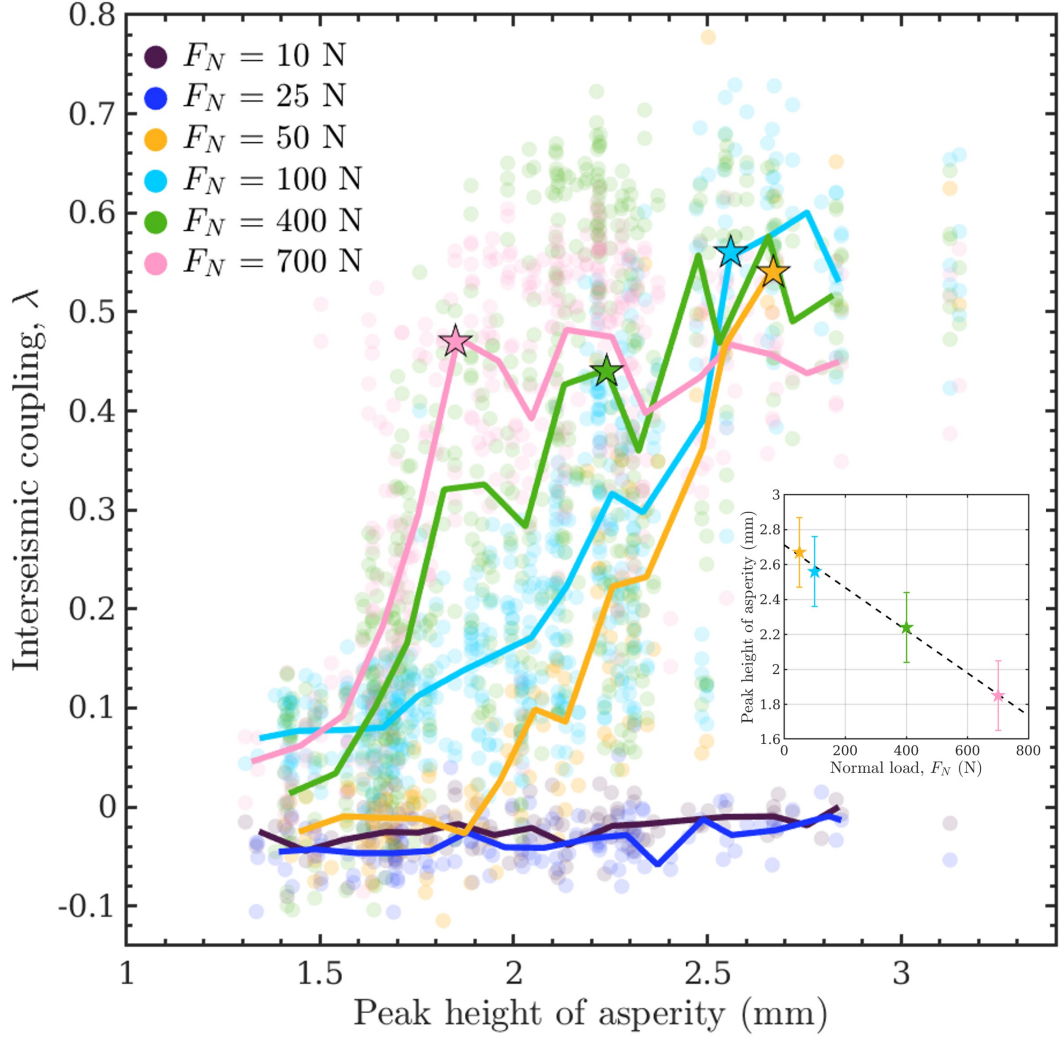
Figure 4.11: Evolution of the interseismic coupling at different peak heights of asperity under multiple normal loads. The circles with one filled color are the dataset computed for all the experiments under the corresponding normal load. Each curve is obtained by averaging the interseismic coupling over the peak height of asperity with a bin width of 0.10 mm. The inset displays the peak height of asperity at transitions from high to low coupling (stars) as a function of the normal load, where the peak height of asperity decreases with the increase of the normal load. Retrieved from Shu et al. (2023).

increase of normal stress, which strengthens the locking of the asperities. The maximum value of the interseismic coupling is about 0.55 which is significantly lower than 1. This is consistent with the partial slipping of asperities shown in Figure 4.7b and Figure 4.8. It is interesting to note a transition of the interseismic coupling, for a given normal load, at a specific peak height threshold. This peak height threshold is decreasing as a function of the increased normal stress (from about 2.67 mm at 50 N to about 1.85 mm at 700 N). The interseismic coupling above this peak height threshold converges for all loading conditions to a constant value of around 0.6. Below the threshold, λ decreases towards 0.

4.5 Interactions between Asperities during the Slip-Strengthening Phase

4.5.1 Collective Slip Episodes

To investigate the spatiotemporal interactions of asperities, we use a two-step procedure in order to define and characterize slip episodes (SEs). In the first step, we analyze individually each asperity to isolate individual asperity slips (IASs) from their slip history. In the second step, we identify collective behavior by clustering IASs based on their time and space connection to build slip episodes. The first step is realized by thresholding the velocity $v_i(t)$ for each asperity i. We use a threshold Γ_i specifically for each asperity i, which is determined by considering the median $\tilde{v}_i$ and the median absolute deviation D_i^{med} of the slip velocity $v_i(t)$,

$$\Gamma_i = \tilde{v}_i + c \cdot D_i^{med}, \tag{4.7}$$

We test several values of the coefficient c in front of D_i^{med} by considering the percentage of isolated slip episodes as a function of the coefficient c. As shown in Figure 4.12, we find that in a transition from a sharp decrease to a relatively constant the percentage of isolated slip episodes occurs when the coefficient value is 6. Since natural earthquakes usually show the characteristic of the cluster of seismicity rather than the distributed isolated events, we, therefore, determine that
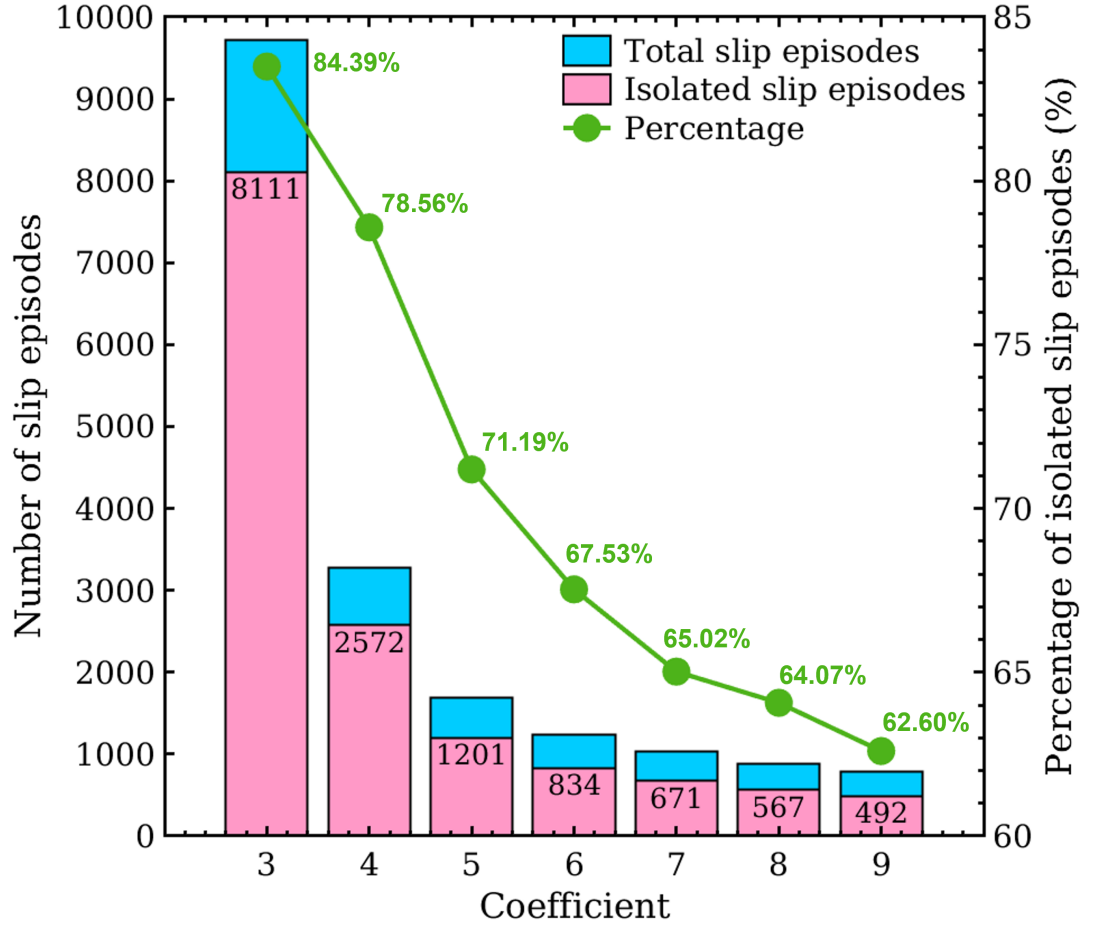
Figure 4.12: Number and percentage of isolated slip episodes under different values of the coefficient c of D_i^{med}. With the increase of the coefficient value, the percentage of isolated slip episodes first decreases sharply and then remains relatively stable. The value $c = 6$ that controls the transition is determined as the optimal coefficient of D_i^{med}. Retrieved from Shu et al. (2023).
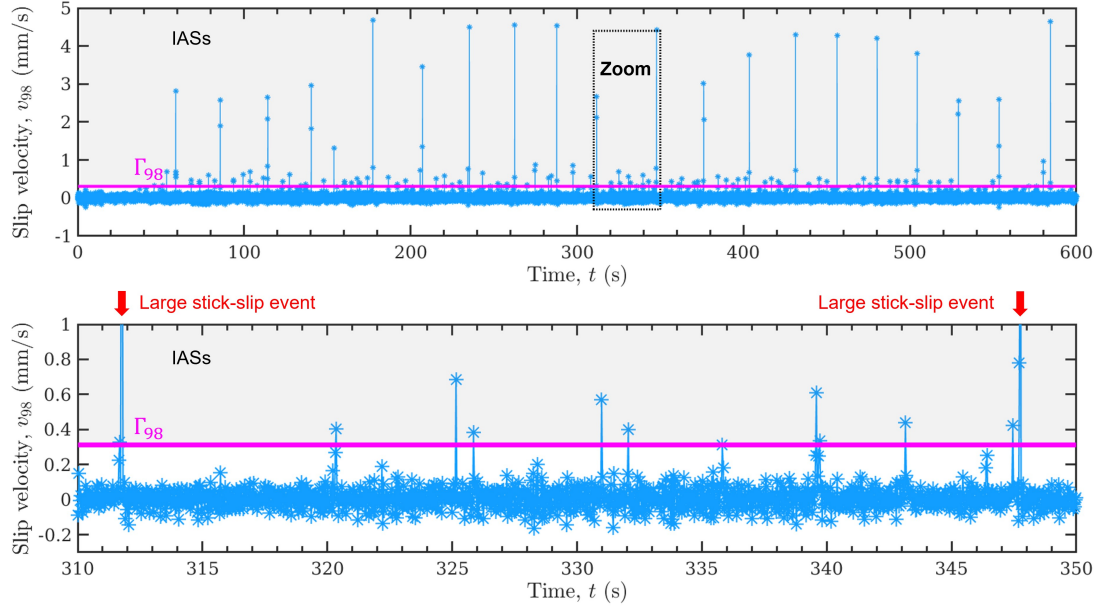
Figure 4.13: Time-localized slip events produced by a single asperity ($i = 98$) in the same experiment shown in Figure 4.7. The blue stars and the thick magenta line represent slip events and the corresponding threshold Γ_{98} specifically computed for this asperity. The slip events localized in the shadow region with slip velocity greater than the threshold are defined as IASs while the others indicating minor slip events and noise are removed. A zoom view showing the low amplitude IASs during an interseismic phase ranging from 310 s to 350 s is presented below. Several IASs with low slip velocities are observed. Retrieved from Shu et al. (2023).

the value retained here ($c = 6$) is the best able to separate noise from slip event.

Following equation (4.7), we define the IASs as periods with $v_i(t) > \Gamma_i$ while the others with $v_i(t) \leq \Gamma_i$ are taken as minor slip events and possible noise, and are not included in the catalog of IASs. Figure 4.13 presents the slip events (blue stars) of one single asperity ($i = 98$) for the same experiment displayed in Figure 4.7 and its corresponding threshold Γ_{98} (thick magenta line). We find a diversity of slip velocities of IASs. To display the IASs with low slip velocities during the interseismic phase, we zoom in on Figure 4.13 during a time interval between two large stick-slip events, ranging from 310 s to 350 s (the same time period exhibited

in Figure 4.7b). The observation that several IASs with moderate maximum slip velocity are observed for this asperity is actually consistent with the small stick-slip events found during the slip-strengthening stage shown in Figure 4.9. For each experiment, we establish a complete catalog of IASs by computing the slip velocity $v_i(t)$ of all the asperities and the corresponding threshold Γ_i.

To cluster in space and time all the IASs defined at different asperities into collective SEs covering multiple asperities and time steps, we analyze the time and space connections of these IASs. We define a link between a pair of IASs if the two events are separated in time by one or less time step and if they have a spatial connection (i.e., they are nearest neighbor), introducing a two-dimensional Delaunay triangulation, and considering the location of each asperity as a vertex (D.-T. Lee & Schachter, 1980). The edges of the resulting triangulation give the spatial connection between asperities used to make clusters. Additionally, we assume that an asperity is always spatially linked with itself. The IASs simultaneously connected in time and space scales are clustered as a new SE using a single linkage clustering algorithm (Gan et al., 2020). IASs that are not linked to other neighboring IASs are considered as individual SEs. Figure 4.14 shows one SE lasting only one time step, and composed of nine IASs. The polygons with different colors represent the slip area allocated to each IAS and are determined by the Voronoi diagram corresponding to the performed triangulation (Fortune, 1995). We, therefore, are able to build the catalog of spatiotemporal SEs for each experiment.

4.5.2 Magnitude-Frequency Distribution

In order to characterize the so-formed slip events, we first investigate their magnitude distribution. The magnitude of the slip event is estimated based on the computation of their moment, M_0. For one SE containing n IASs, its seismic moment is computed as:

$$M_0 = \sum_{i=1}^{n} G \cdot A_i \cdot s_i, \tag{4.8}$$

where G is the shear modulus of the PMMA, A_i and s_i are respectively the slip
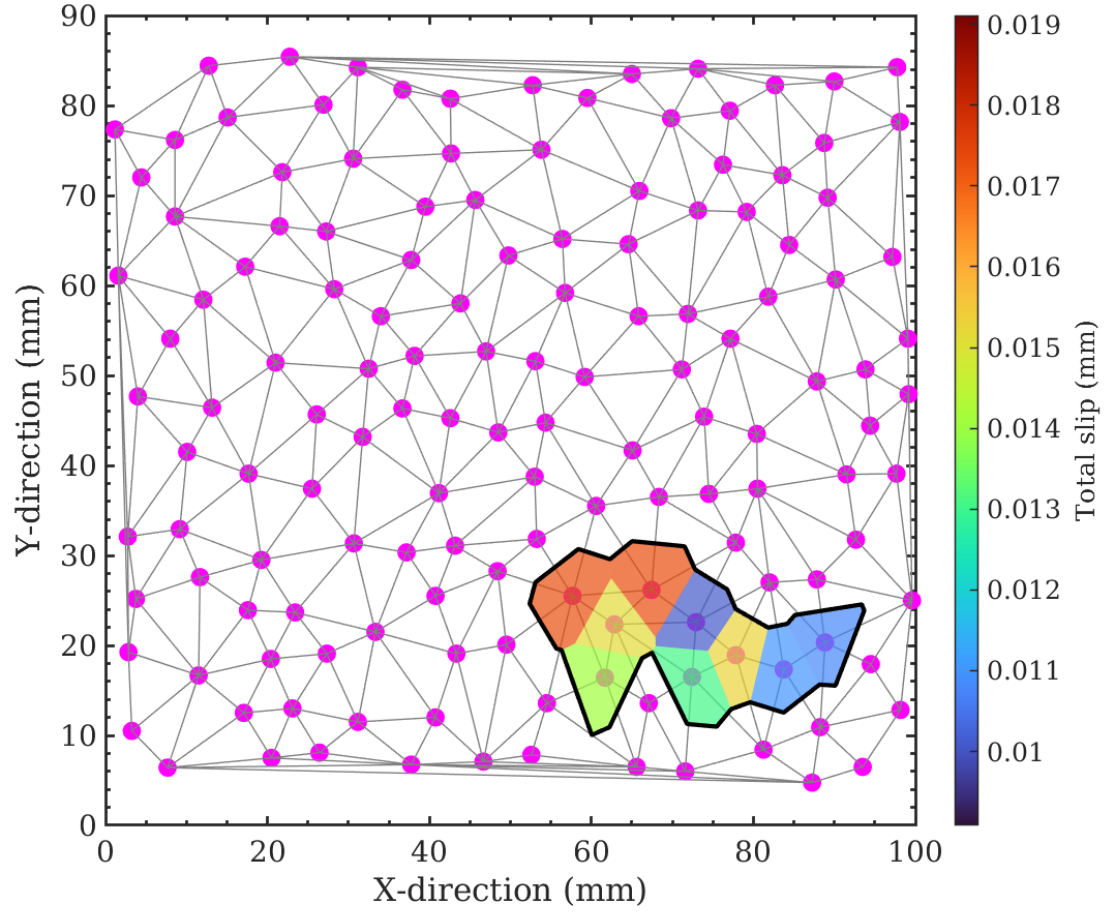
Figure 4.14: Example of one SE lasting one time step which is composed of nine IASs (polygons with different colors) colored by their total slips. The magenta dots and gray lines indicate the asperities locations and the spatial connections all over the interface determined by the Delaunay triangulation, respectively. Retrieved from Shu et al. (2023).

area and the slip of each IAS i that compose this SE. We note that the slip area, A_i, defined here is the effective slip area rather than the real slip area during an IAS since there is no frictional contact between asperities in our model. The estimation of such effective slip area, due to the difficulty of determining the discontinuity of slip zones, also exists when studying natural earthquakes originating from faults at depth. Another ambiguity comes from the selection of the shear modulus in equation 4.8 as the analog fault interface is composed of bimaterial, that is, PMMA and silicone with different shear moduli. We thus emphasize that the moment computed here should be interpreted as relative values, instead of absolute values. More details about the definition of the slip area, the computation of the moment, and the choice of the shear modulus, will be further discussed in Section 4.6.5. Then, we can calculate the magnitude M of each SE following (Hanks & Kanamori, 1979) as:

$$M = (\log_{10} M_0 - 9.05)/1.5. \tag{4.9}$$

The magnitude-frequency distributions of the SEs extracted from three experiments, which are under the same normal load of 400 N but with three different loading rates, are presented in the top panel of Figure 4.15. The shadow region marks the magnitudes of the ruptures of a single asperity in these three experiments, with a range of $M = -6.09 \pm 0.22$. The symbols with crosses represent the large stick-slip events that involve all the asperities of the interface and subsequently with a size controlled by the finite size of the interface. As evidenced already for finite systems, the distribution of events is bimodal: exponentially distributed size for the events not reaching the interface and a peak for system-wide events (Fisher et al., 1997). Excluding system-wide events, the observed distributions follow a typical Gutenberg-Richter distribution (Gutenberg & Richter, 1944): $\log_{10} N(m) = a - bm$. For the three experiments under loading rates of 5.0 μm/s, 10.0 μm/s, and 15.0 μm/s and a normal load $F_N = 400$ N, their b values and corresponding uncertainties are estimated as 1.21±0.04, 1.49±0.10, and 1.33±0.13, respectively, using the maximum likelihood method (Aki, 1965). A gray dashed line showing a reference b value of 1.3 is displayed in Figure 4.15. We can observe
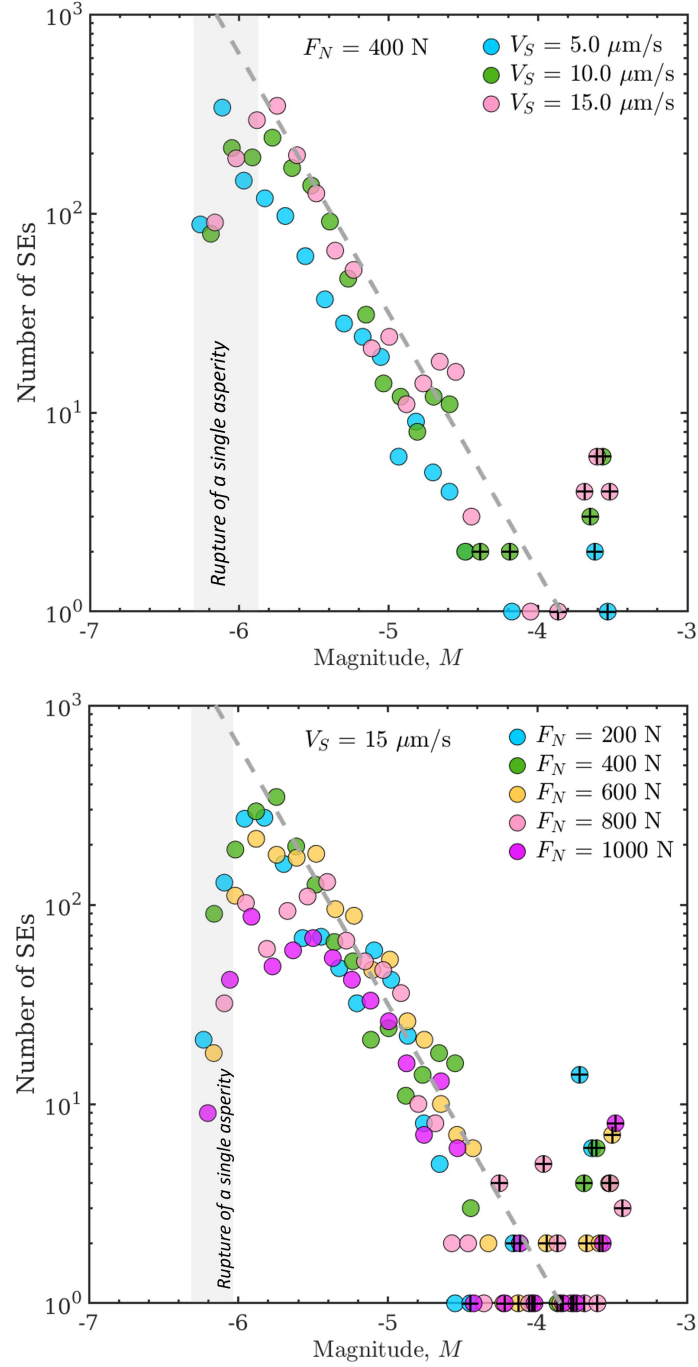
Figure 4.15: Magnitude-frequency distributions at different loading rates under the same normal load of 400 N (top) and at different normal loads under the same loading rate of 15 μm/s (bottom). The circle symbols marked by crosses indicate the large stick-slip events at the global fault scale, which are excluded from the computation of the b value since they are reaching the boundaries of the model and accordingly are limited in size. The gray dashed line indicates a reference line with a b value of 1.3. The shadow represents the range of the magnitudes corresponding to the ruptures of a single asperity, with an average value of $M = -6.09$. Modified from Shu et al. (2023).

that all these three experiments have a b value nearly similar to this reference. It shows that the b value has no clear dependence on the loading rate of the system. In addition, our experimental results show that the b value is insensitive as well to the imposed normal load (Figure 4.15 and Table 4.2). Such observation seems to be contradictory to the previous studies on natural faults and laboratory faults which have shown that the b value is dependent on the imposed stress (Amitrano, 2003; Rivière et al., 2018; Scholz, 2015). We however speculate that the limited range of tested normal loads, and the uncertainties attached to the b value, cannot provide a sufficient resolution to evidence a clear dependence of the b value on the imposed normal load.

4.5.3   Moment-Duration Scaling Relation

For regular earthquakes, a scaling relation between the moment and the duration is commonly observed and takes the form $M_0 \propto T^3$ (Kanamori & Anderson, 1975). This relation can be understood from the representation of an earthquake as a circular crack expanding at a constant speed and with a constant stress drop. Another scaling relation has also been resolved for slow slip events observed in subduction megathrusts which follows the form $M_0 \propto T$ (Gao et al., 2012; Ide, Beroza, et al., 2007).

Since the confined and unconfined ruptures are produced in our experiments, it is important to exclude the influence of the edge effect for SEs, as the SEs reaching the boundaries of the experimental model accordingly are limited in size. We investigate whether the edge effect of SEs impacts the moment-duration scaling by changing the slip area threshold, which can be used to exclude the SEs reaching the edge of the sample. Meanwhile, we plot the moment-duration statistics of SEs under different normal loads and loading rates, as shown in Figure 4.16 and Figure 4.17, respectively, to explore whether such scaling is dependent on the normal load or the loading rate in our experiments. The duration, T, is defined as the time difference between the onset and end of each SE.

We also represent from our SEs the relation between their duration, T, and their moment, M_0, for all experiments with various normal loads and loading rates

Table 4.2: Parameters and b value of each experiment

Experiment	Normal load (N)	Displacement rate (μm/s)	b value
1	200	5.0	1.01±0.11
2	400	5.0	1.18±0.10
3	600	10.0	1.18±0.11
4	800	10.0	1.17±0.13
5	1000	15.0	1.05±0.13
6	100	5.0	1.21±0.09
7	100	10.0	1.30±0.12
8	100	15.0	1.13±0.09
9	200	5.0	1.30±0.09
10	200	10.0	1.30±0.13
11	200	15.0	1.42±0.17
12	400	5.0	1.21±0.04
13	400	10.0	1.49±0.10
14	400	15.0	1.33±0.13
15	600	5.0	1.26±0.11
16	600	10.0	1.14±0.08
17	600	15.0	1.39±0.08
18	700	5.0	1.29±0.08
19	700	10.0	1.17±0.10
20	700	15.0	1.46±0.09
21	800	5.0	1.09±0.14
22	800	10.0	1.12±0.10
23	800	15.0	1.81±0.19
24	50	5.0	-
25	25	5.0	-
26	10	5.0	-
27	100	15.0	1.34±0.07
28	100	15.0	1.18±0.05
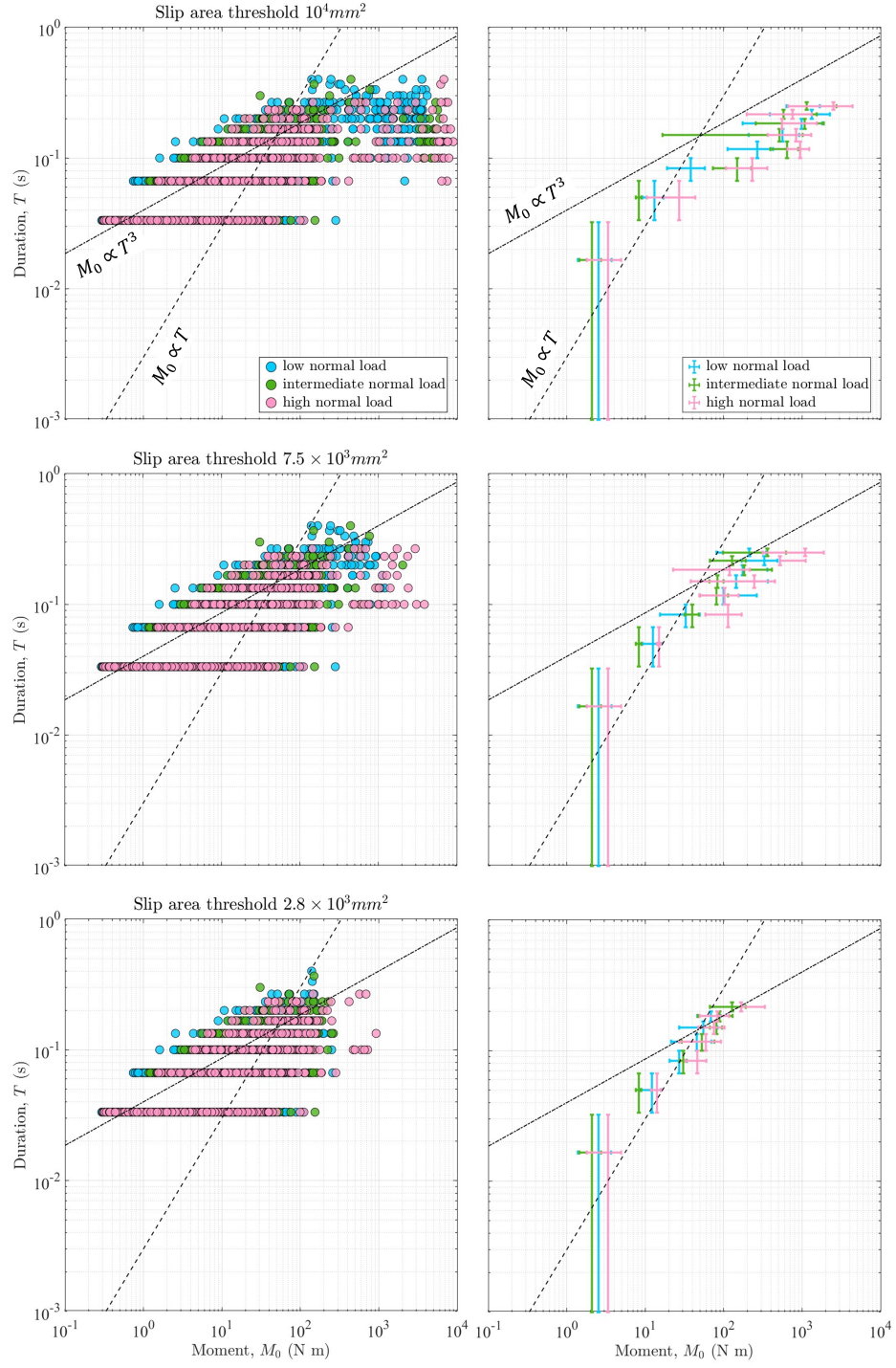
Figure 4.16: Moment-duration scaling relation of SEs from multiple experiments under different normal loads with a decreasing slip area threshold. The slip area threshold decreases from 1.0×10^4 mm^2 (top, i.e., the whole interface) to 7.5×10^3 mm^2 (middle) and to 2.8×10^3 mm^2 (bottom). The low, intermediate, and high normal loads correspond to the values of no greater than 200 N, between 200 N and 600 N, and no less than 800 N, respectively. The linear and cubic scaling relations are plotted for a guide. The left panel shows the distribution of all the SEs while the right panel displays the average moment for each duration. Modified from Shu et al. (2023).
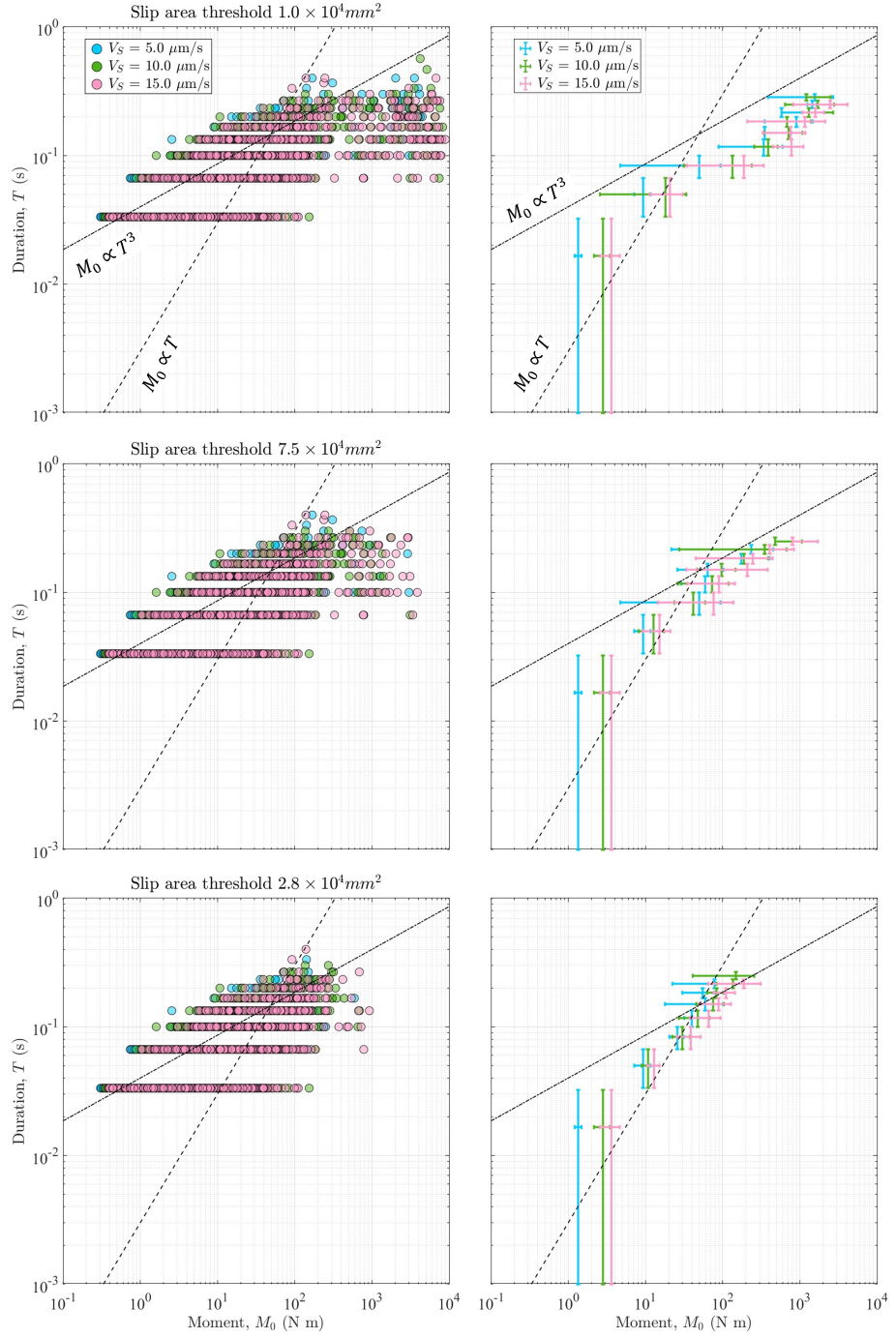
Figure 4.17: Moment-duration scaling relation of SEs from multiple experiments under different loading rates with a decreasing slip area threshold. The slip area threshold decreases from 1.0×10^4 mm^2 (top, i.e., the whole interface) to 7.5×10^3 mm^2 (middle) and to 2.8×10^3 mm^2 (bottom). The values of loading rates are color-coded as shown in the legend. The linear and cubic scaling relations are plotted for a guide. The left panel shows the distribution of all the SEs while the right panel displays the average moment for each duration. Modified from Shu et al. (2023).

(Figure 4.18a). Two populations of SEs, where one is the small and moderate SEs in blue and another is the large SEs in red, are evidenced. To retain only the confined ruptures, we set a threshold of 2.8×10^3 mm^2 by considering the slip area of SEs to exclude the large slip events reaching the edge of the sample. We evidence a linear scaling relation close to $M_0 \propto T$ for all the experiments for $M_0 <$ 100 N m and a transition to the scaling for earthquakes ($M_0 \propto T^3$) for the large events (Figure 4.18b). We note that such a transition mainly results from the value of the threshold as some confined and unconfined events might be mixed. By changing the value of the slip area threshold, we observe that the linear scaling relation becomes more evident with the decrease of the threshold (Figure 4.16 and Figure 4.17). Thus, we conclude that the scaling of the small and moderate events (compared to the system size) is in $M_0 \propto T$ and not in $M_0 \propto T^3$ which is an artifact of the existence of two populations. The moments corresponding to the ruptures of a single asperity are marked by the shadow region, with a range of $M_0 = 2.32 \pm 0.91$ N m, which is also compatible with the magnitudes shown in Figure 4.15. Additionally, we find that such a scaling relation is also insensitive to the imposed normal load (Figure 4.16) and the loading rate (Figure 4.17). We still note however that the fitted range of duration is limited and further experiments with a wider range of event duration would be helpful to reinforce this result.

Excluding the large slip events reaching the edge of the sample by using the same slip area threshold (2.8×10^3 mm^2), we then compute the distance between the first and last slipping asperities for each retained SE. The duration and expanding distance are averaged to present their relation, as shown in Figure 4.18c. We observe a square-root scaling relation between the expanding distance and the duration.

4.5.4 Temporal Decay of Slip Episodes

In order to investigate the possible time interaction between our identified SEs, we compute the time correlation between them, $C(t)$ with
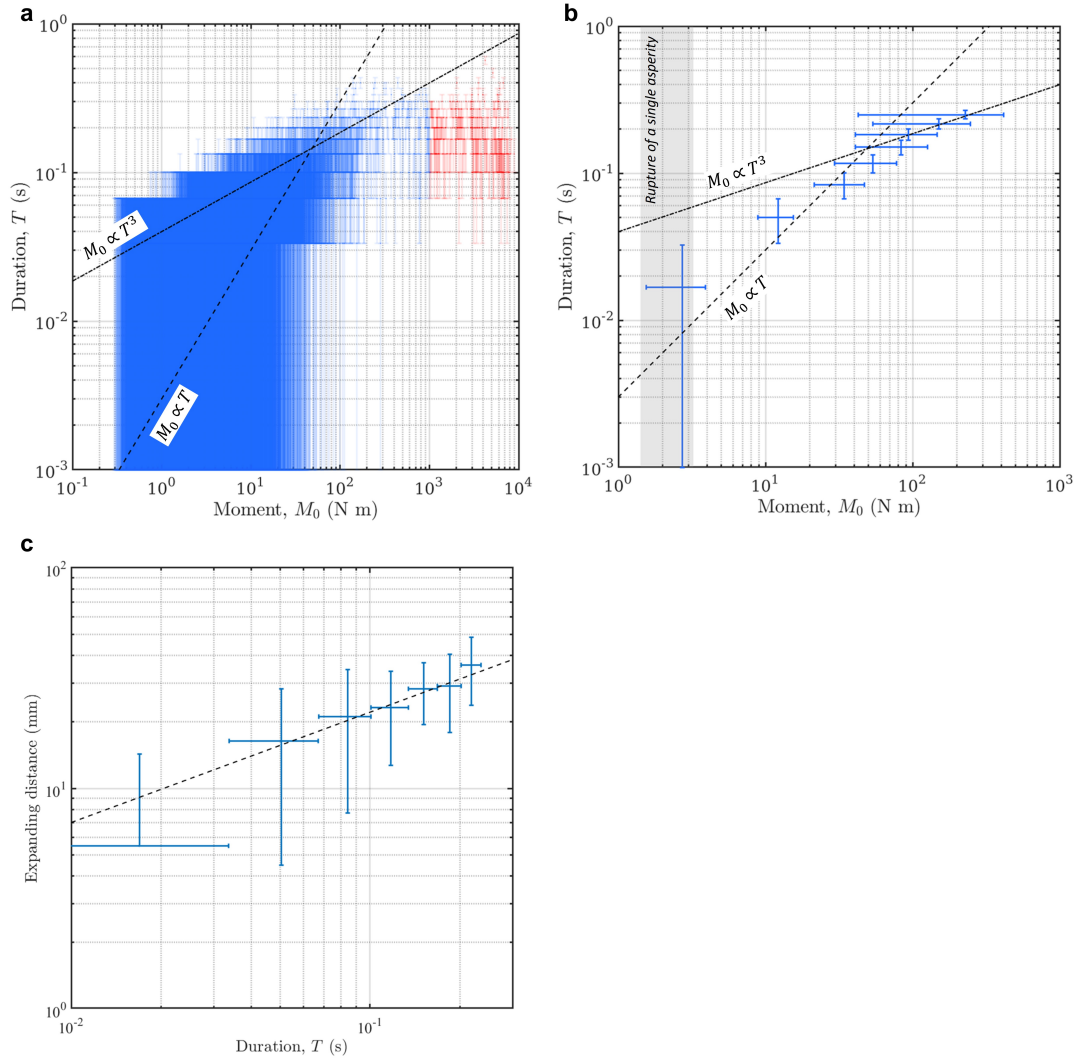
Figure 4.18: a: Moment-duration distribution obtained using SEs from all experiments at various normal loads and loading rates, with a slip area threshold of 1.0×10^4 mm^2 (i.e., the whole interface). The black dash-dotted line and dashed line represent the scaling relations of $M_0 \propto T^3$ and $M_0 \propto T$ for the guide, respectively. Two populations of events indicating small and moderate events (blue) and large events (red) are evidenced. **b:** Average moment-duration scaling relation obtained using small and moderate SEs from all experiments as the large slip events reaching the edge of the sample have been excluded using a slip area threshold of 2.8×10^3 mm^2. The shadow indicates the moments corresponding to the ruptures of a single asperity, with a range of $M_0 = 2.32 \pm 0.91$ N m. **c:** Scaling relation between the expanding distance of SEs and their duration using the same dataset in **(b)**. The black dashed line represents the square-root scaling relation between the expanding distance and the duration. Retrieved from Shu et al. (2023).

$$C(t) = \frac{1}{Tn_t} \sum_{i=1}^{n_t} \sum_{j=i+1}^{n} \Theta \left(t_j - t_i \in [t; t+T] \right), \tag{4.10}$$

where $\Theta(\mathcal{P})$ of proposition $\mathcal{P}$ is 1 if $\mathcal{P}$ is true and 0 otherwise. In order to take into account the time finiteness of the catalog, the first sum is performed up to n_t which is the largest index i such that $t_n - t_i < t + T$, where T is the duration of the time bin. The equation (4.10) actually gives the average rate of SEs at time t following a preceding slip event. We represent examples of $C(t)$ computed for multiple experiments under different normal loads and the same loading rate, as shown in the top panel of Figure 4.19. We observe that, for all of these experiments, a rapid decrease of $C(t)$ at a short time range, following a power law decay similar to $1/t$. After a duration of about 1 s, the average rate of SE stabilizes to a background rate of around 1 or 2 SE(s) per second. This indicates that interactions between SE exist for a short time and that they quickly decay. This evolution of the event's rate bears some analogy with Omori's law observed after large earthquakes or LFEs which gives as well a decay of the earthquake rate following $1/t$ (Lengliné et al., 2017; Utsu et al., 1995). The observation of the same decay rate under different normal loads indicates that the decay rate has no clear dependence on the imposed normal load. Our experimental results also show that the decay rate is independent of the loading rate (Figure 4.19).

4.6 Discussion

4.6.1 Interseismic Coupling

Our results indicate that the interseismic slip rate relative to the loading rate, i.e. the interseismic coupling, λ, is related at first order to the normal stress imposed on the asperities. The transition from small to high coupling is a function of the normal load (the height of the asperity at this transition is decreasing with normal stress) but the value of the coupling at high or low normal stress is the same for any normal load. This is visible first as a global macroscopic effect affecting all asperities when we change the imposed normal load in our experiments (Figure
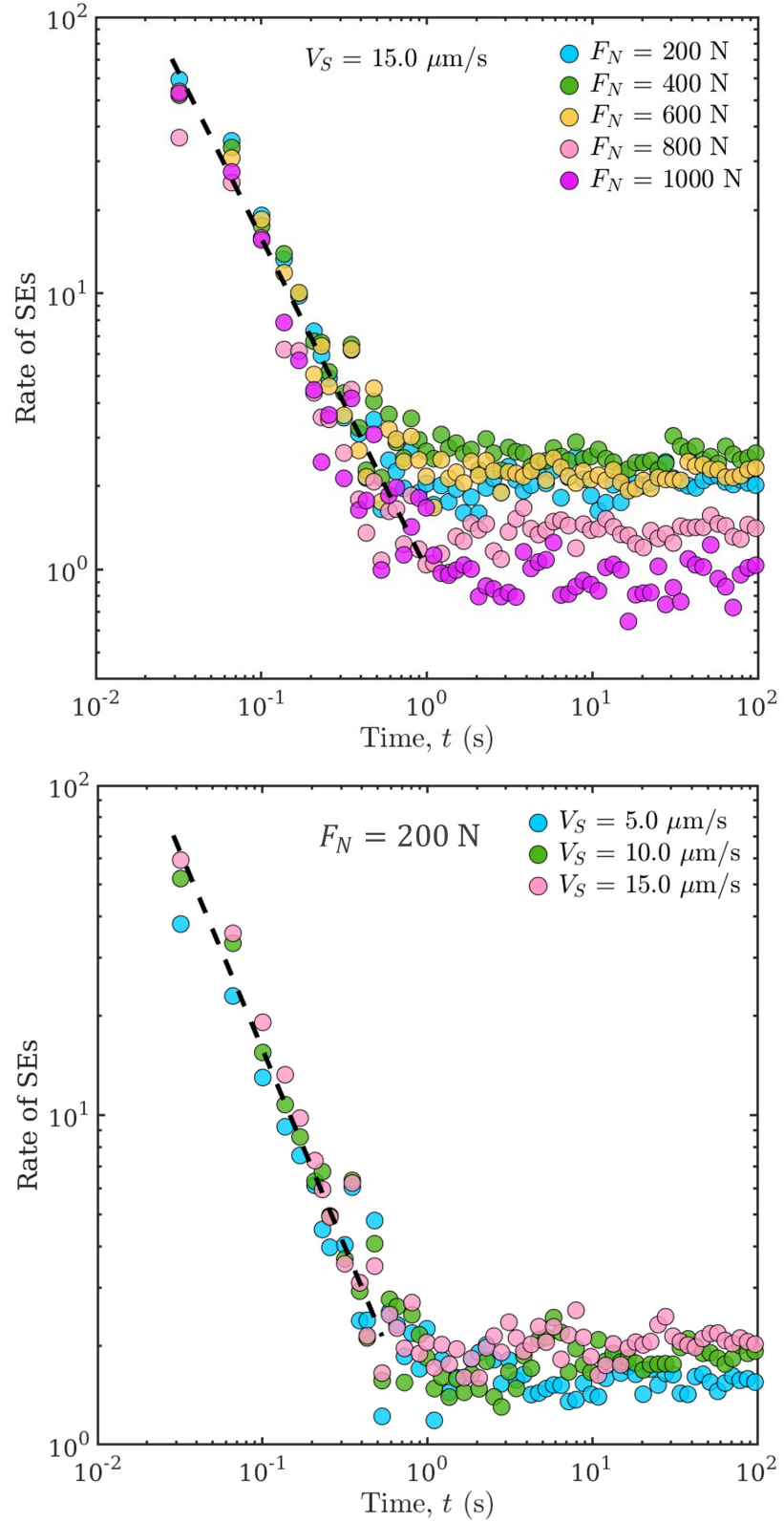
Figure 4.19: Temporal decay of SEs defined in multiple experiments under different normal loads and the same loading rate of 15 μm/s (top) and under different loading rates and the same normal load of 200 N (bottom). The rate of SEs first decays rapidly with $1/t$ during about 1 s and then keeps stable as a background value of about 1 or 2 SE(s) per second. Modified from Shu et al. (2023).

4.11). This can also be observed at the individual asperity scale where we observe that the asperity peak height is correlated with λ. Indeed, considering a simple Hertz contact model, a higher asperity height results in higher normal stress. The distribution of asperity heights in our experiments, therefore, leads to a distribution of normal stresses and a continuum of values of λ (Figure 4.11).

It is tempting to relate the characteristic asperity height in our experiment to the critical reduction in the normal force, ΔF_N^*, that controls the transition from low to high coupling, as identified in the model of Scholz and Campos (1995, 2012). However, since the interface is regarded as homogeneous, it should be noted that in this model the transition is only caused by the impact of the global normal load. This approach is thus describing the effective seismic coupling of the interface but not that of the asperities, which we can achieve in our experiments. According to our interpretation, the fault's quenched disorder influences the interface's effective coupling, which is then indirectly influenced by the normal stress. For example, there wouldn't be any variation in interseismic coupling at various asperities if we assumed that all of the asperities were the same height. Therefore the whole interface would have the same behavior as that of the asperities. Here we emphasize that, in contrast to the traditional normal stress level effect, a fault topography with changes in asperity heights has an impact on the effective seismic coupling of the fault.

Finally, we acknowledge that the definition of interseismic coupling is not completely satisfactory as it fails to capture the variation of the slip velocity inferred on some asperities in between two large scale stick-slip events. Indeed, we highlighted some transient activity and non-steady slipping rate for asperities which indicate that the value we computed only represents an effective behavior of the asperity at the time scale between two large scale stick-slip events.

4.6.2 Interfacial Elastic Energy

Our results evidence that for an interface composed of multiple asperities, as in our system, local slip events with various sizes (see Figure 4.15) are taking place at all times. We also note that large scale events that involve slips on all asperities

of the interface are also observed. These large scale slip events can only happen when sufficient large stress has been accumulated on the strongest asperities. This requires that asperities at some time are synchronized such that initiating the failure at one location triggers the cascading rupture of all the asperities on the interface, thus generating the large scale stick-slip event. This is equivalent to a collective depinning (i.e., the transition of the physical system from a locked state to a slipping state; (Perfettini et al., 2001; Alava et al., 2006)) induced by the long range elastic interactions in a slowly (quasi-static) loaded system.

We quantitatively illustrate such synchronization effect by computing the evolution of the interfacial elastic energy, E_h, and of the bulk elastic energy, E_t, following the definition of Schmittbuhl et al. (1996). The interfacial elastic energy, E_h, is quantified through the sum of the relative distance between two asperities over all the spatial links defined by the two-dimensional Delaunay triangulation:

$$E_h(t) = K_N \sum_{k=1}^{D} \left(l_k(t) - l_k(t_0) \right)^2 , \tag{4.11}$$

where l_k is the relative distance computed through the x positions of two asperities linked spatially and D is the number of the spatial links between two asperities defined by the Delaunay triangulation. K_N is the compressive stiffness between asperities, computed through $K_N = E_s \langle d_{asp} \rangle$, where E_s denotes Young's modulus of the silicone block and $\langle d_{asp} \rangle$ is the average distance between asperities which estimated to be 6 mm. The interfacial elastic energy, E_h, actually quantifies the variance of the change of distance between neighboring asperities, thus is related to the elastic force interactions between asperities. The bulk elastic energy, E_t, is the total elastic energy stored on the interface through the global loading, which is characterized by the collective change in the absolute positions of all the asperities along the x direction:

$$E_t(t) = K_S \sum_{i=1}^{N} (d_i(t))^2, \tag{4.12}$$

where K_S is the shear stiffness estimated using $K_S = G_s L$. G_s is the shear modulus of the silicone block and is estimated from its Young's modulus, 1.1 MPa,

while L is the size of the interface, 10 cm. N is the total number of asperities and d_i is the displacement of each asperity.

Such energies and the definition of links between close asperities originate in the reference spring array model of Burridge-Knopoff (Burridge & Knopoff, 1967; J. Carlson & Langer, 1989). However, our model is also different from the Burridge-Knopoff model which has only short-range elastic interactions as the silicone block induces long-range elastic interactions and viscous damping. We present the interfacial elastic energy, E_h, and the bulk elastic energy, E_t, as a function of the PMMA plate displacement, d_P, for different experiments with various normal loads but the same loading rate, as shown in Figure 4.20. We identify multiple large scale stick-slip events and the corresponding slip-strengthening phases from the large abrupt drops of E_t and the slow accumulation of E_t, respectively. We also observe a similar pattern for the evolution of E_h, which is equivalent to the direct measure of the spreading of the x positions of the asperities apart from their initial position where $E_h = 0$. Additionally, we observe a clear dependence of E_h and E_t on the normal load, which is consistent with the mechanical response of the fault system shown in Figure 4.4. With the increase of normal load, the interfacial elastic energy, E_h, and the bulk elastic energy, E_t, also increase.

Such evolution of the elastic energies during successive seismic cycles illustrates the disordering effect of asperities (i.e., the absence of correlation with their original positions; (Alava et al., 2006)) and the build-up of the elastic energy during the slip-strengthening phase. We interpret the rising E_h as the disordering process of asperities, that is the strong perturbation from the initial position which is supposed to be quenched in the system. The sticking phases correspond to a period of increase of E_h during which the asperities increase disordering, while a large scale event corresponds to the rapid decrease of E_h (re-ordering of the asperities). We note that during such a large scale event, while E_t drops significantly and returns to zero, the drop of E_h is only partially such that a disorder, and elastic energy, is still present after a large event. It implies that there is a memory effect over the cycles from the relative positions of the asperities.

We also observe a transient period at the beginning of the shearing where the
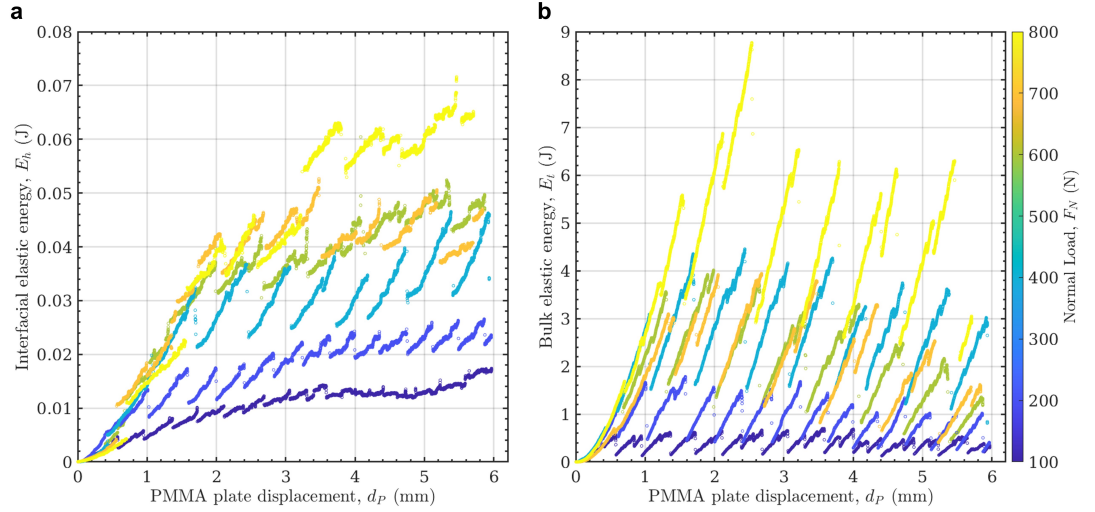
Figure 4.20: Evolution of **(a)** the interfacial elastic energy, E_h, and of **(b)** the bulk elastic energy, E_t, under different normal loads and the same loading rate. Both E_h and E_t accumulate slowly during the slip-strengthening phases and drop when a large stick-slip event occurs. Both E_h and E_t show a clear dependence on the normal load. Retrieved from Shu et al. (2023).

evolution of E_h is similar for all experiments. As the normal stress is increased a larger level of E_h is reached in the system, so a larger disordering of the asperities. It implies that higher normal stress prevents the interface to come back to its initial state (with low E_h) even during a LSE and so maintains a larger disorder in the system with internal stresses along the interface at any time.

The process of synchronization has been well documented notably in numerical simulations and shows that only for forces larger than a critical force, that constitute a critical point, the system will become unstable and sliding will extend to all sites of the interface (Fisher et al., 1997; Tanguy et al., 1998; Kammer et al., 2015; de Geus et al., 2019; Albertini et al., 2021). This constitutes a depinning transition and this phenomenology leads to stick-slip. In such models, this critical force is linked to a critical length scale, L_c, of an initiating slip pulse, that will invade all the interface if its extension becomes larger than L_c. Most of these results were inferred from a homogeneous fault model. Here, both the evolution of the macro-

scopic force (Figure 4.9) and the distribution of slip events in Figure 4.15 are not in agreement with these predictions. Indeed, we first observe in Figure 4.9 that the macroscopic force required to propagate a full scale event is not perfectly constant but rather displays some fluctuations from one rupture to the other. Secondly, the distribution of event magnitudes (Figure 4.15) shows almost no gap between the largest avalanche and the whole interface avalanche. It, therefore, implies that avalanches of all sizes can exist in the system without necessarily leading above a certain size to a complete failure. In such a case one would expect a larger gap in event size between the maximum observed avalanche and the system wide event. Such different nucleation mode can arise in the heterogeneous system as interactions between arrested small events could exist and significantly modifies the process leading to a major rupture (Albertini et al., 2021). Interpreting these results in terms of fault mechanics suggests that creeping faults correspond to the interface with an asperity disorder and a slip-strengthening regime with the disordering of the interface by small destabilizing events that increase elastic interaction between asperities but without impacting the global fault loading.

4.6.3 Slip Intermittency

Our system is driven by a constant displacement rate for each experiment and we measure a macroscopic velocity of the PMMA plate that is indeed constant (except during a large-scale event, where a small but noticeable displacement step is observed). This macroscopic measurement mimics the measure that could be made around natural faults by geodetic instruments located at the surface, and thus necessarily far away from the slipping area at depth. It implies that such kind of measurement actually misses the actual complexity of the slip distribution taking place on the interface at a short time and spatial scale. Some fine measurements of the slip distribution in both time and space for shallow creeping faults indeed reveal that the long term continuous creeping of faults is actually accommodated during bursts of aseismic slip of various sizes (Jolivet et al., 2013, 2015; Rousset et al., 2016; Khoshmanesh & Shirzaei, 2018). During slow slip events, the analysis of GPS signal in conjunction with the recording of low frequency earthquakes (LFEs)

also reveals that the large scale motion along the slab consists in the superposition of numerous small slip episodes each acting for a limited duration (Frank, 2016; Frank & Brodsky, 2019). The analysis of LFEs as a proxy for local slip on the interface reveals as well that these slip episodes span a wide range of sizes and present both temporal and spatial correlation (Lengliné et al., 2017). All these results are well in agreement with the observations performed in this study where the interseismic slip on the fault is characterized by slip events (SEs) of different sizes that act in a close temporal relationship.

The slip events we characterized here are slow events in the sense that the ratio of their size with respect to their duration is much lower than the Rayleigh wave speed of the material that constitutes the interface. Indeed, supposing a typical PMMA Rayleigh velocity of 1255 m/s (Gvirtzman & Fineberg, 2021), this would imply that in one time frame (1/29.97 s) a dynamic rupture front travels up to 42 m. This is inconsistent with the observations of SEs that last several time frames. If we suppose that most of the stress transfer between asperities is actually mediated by the silicone base embedding the PMMA beads, this gives a Rayleigh wave velocity of the order of 20 m/s, and then the propagation of a rupture front of 66 cm in one time frame. As the largest SEs have a typical duration of 0.3 s and cover a maximum area with a characteristic dimension of half the sample length (5 cm), this suggests that the SEs formed by our criterion actually correspond to slow events. Such a slow process is achieved as the stress is mainly transmitted through the bulk of the silicone block due to the absence of frictional contact in between asperities, and could be damped by the bulk viscosity, which is similar to some numerical models composed of discrete frictional patches embedded in a viscous matrix (Ando et al., 2010, 2012; Behr et al., 2021; Nakata et al., 2011). It does not preclude local dynamic rupture to take place during such SEs, but their size might be limited to a single bead contact area (or smaller). This implies that the moment-duration scaling we report in Figure 4.18 should be interpreted as scaling attached to slow ruptures on the interface. The best-resolved trend shows $M_0 \propto T$ in agreement notably with the observations of (Ide, Beroza, et al., 2007) that show that many slow slip events on subduction zones follow this scaling

law. We note however that the scaling in our experiment is only resolved over a restricted range of moments. This calls for future further experiments involving an increase in the number of beads and the sampling rate of the optical device. This moment-duration scaling is also in agreement with the observed evolution of the slip event characteristic distance with the square root of duration. This, therefore, suggests that the slip events are driven by a diffusion process controlling the propagation of the rupture, similar to slow-slip events tracked with tremor migration (Ide, 2010). The recognition of these SEs as slow events also suggests that the magnitude-frequency distributions shown in Figure 4.15 can be considered as a scaling attached typically to such slow events as inferred, for example, from non-volcanic tremors (Wech et al., 2010), rather than a Gutenberg-Richter relation for ordinary earthquakes. The fact that the whole-fault-scale scaling relations presented by these slow events can be derived from the collective spatiotemporal slips of local asperities is also supported by some numerical studies of Ide (2008) and Ide and Yabe (2019). Additionally, the depinning transition leading to stick-slip constituted in the synchronization process is also consistent with the model of Ben-Zion (2012), which proposes that the depinning transition is a mechanism for the generation of tremors.

The slip event, SEs are characterized as a single rupture following the clustering procedure we defined. It is not obvious how to select the merging condition which is imposed partially in our case by the acquisition rate of the optical device. However, what is the exact definition and extent of a slip event is not a question limited to our experiment. Indeed, the analysis of earthquakes for example, generally indicates that they are actually composed of several sub-events. The identification of these sub-events, therefore, questioned the definition of the earthquake rupture that consists of several connected local slip episodes. As we discussed above, the same problem of definition arises for a slow slip event which is actually made of a sum of local transient slip episodes connected in time and space. Decreasing the time interval required to merge individual asperity slips into the same cluster would ultimately lead to only isolated local slip events. On the opposite, increasing this time interval would lead to a single slip event comprising all the beads. Finally, we

conclude that SEs are thus analyzed at the spatial and temporal scale imposed by our acquisition system which is a constraint imposed as well to observations made on natural fault systems.

4.6.4   Mechanics of the Slip-Strengthening Regime

Our system resolves confined rupture that takes place during the slip-strengthening phase. This contrasts with most frictional setups where only large scale ruptures are analyzed during the weakening phase. Unlike these large scale ruptures that are largely controlled by the machine loading stiffness (Leeman et al., 2016; Wu & McLaskey, 2019), partial ruptures provide the opportunity to study the slip events taking place on an interface without being actually influenced by the loading system. In our system, the events are arrested because of stress heterogeneity that arises notably from the variable asperity heights creating spatial differences in frictional strengths. We stress that the heterogeneous nature of the interface only arises as a result of the topography and the position distribution of the asperities with respect to their initial position (assessed by the interfacial elastic energy E_h), but that there is no variation of the material properties that constitute the interface. In particular, it implies that the complex dynamic that we recovered during our experiment is not the result of a heterogeneous spatial distribution of the a and b parameters of the rate-and-state friction model as employed in several simulations of faulting (Barbot et al., 2012). We note that such approaches are based on a continuum description of the interface and do not model the failure of individual asperities where locations in between are contact-free, similar to the inclusion-in-matrix models (e.g., Behr et al., 2021) and the fiber-bundle models (e.g., Daub et al., 2011; Stormo et al., 2016), and hence have zero frictional strength like in our case.

Our results indicate that the slip-strengthening phase, which could be seen as the preparatory phase of large ruptures, includes a population of events that are multi-scale in size (Gutenberg-Richter relation in Figure 4.15) and in duration (Figure 4.18). A similar multi-scale size distribution has also been reported for events occurring during the slip-strengthening phase along a sheared fault gouge layer

simulated by spherical glass particles that are similar to our asperities (Nasuno et al., 1998). Combined with our results, it implies that this preparatory phase, before a large rupture, is very long with many local events strongly related to the quenched disorder. This result is highly reproducible with the same disorder in the asperity positions.

4.6.5 Limitations of the Experimental Setup

Our novel experimental setup builds a heterogeneous shear interface of multi-asperity contacts. An important point resulting from the designed configuration is that the elevated adhesion of the silicone block to the asperities is strong enough such that there is no rolling of asperities caused by the shearing imposed on the PMMA plate. Similarly, we also make sure that the silicone block is at no time in contact with the PMMA plate during the experiment. Indeed, in such a case, the high adhesion of the silicone would cause a local resistance to slip and modify the modeled physical process (from friction to adhesion). This limits the maximum normal load we can impose on the system to approximately 1500 N, at a higher imposed normal load, the silicone block starts to have some local contacts with the PMMA plate.

The sampling rate of the camera employed directly determines the time resolution for tracking the slips of asperities. Thus, the rapid slipping phase involving multiple asperities cannot be analyzed in detail. For example, it is not sampled with a high enough time resolution to capture a clear trend of the decay of the shear force as a function of slip during these episodes (see Figure 4.9). Furthermore, the precise timing, migration, or interactions of local bead slips during the high slipping phase is not accessible. Finally, as we evidence, the overall rupture during such SEs is slow but it does not preclude that locally during such slow transient, local dynamic rupture occurs such that some proportion of the resolved slip is actually taking place during such dynamic phase and radiate elastic wave. The proportion of the slip taking place on the asperities as dynamic events is presently not measurable but remains to be investigated for future studies. However, we note that such a time-resolution issue also exists when studying natural

earthquakes and/or slow slip events. Meanwhile, the velocity threshold defined for each asperity to distinguish IASs and non-IASs is another fundamental parameter that will influence how we treat the temporal slips of asperities, which works the same also for natural geological faults. We argue that increasing the sampling rate would eventually lead to only isolated local slip events. With the current technical setup, the collective SEs clustered with such a relatively low sampling rate are able to reveal some important aspects of the fault physics at scales of both the whole fault and the local asperity.

The derivation of the moment, M_0, of the slip events required the computation of an area, A_i, attached to each asperity (see Eq. 4.8). Here we take for each asperity the area returned by the Voronoi cell including the asperity. Such a definition of the slip area attached to an asperity defines the effective slip area rather than the real slip area during an IAS, which is also commonly seen in natural earthquakes due to the difficulty of determining the discontinuity of slip zones. Indeed, the locked area of an asperity is presumably much lower than a circle of the asperity radius (considering a Hertz contact model) (K. Johnson, 1987). Although some slip deficit can extend beyond the fully locked area, it becomes negligible at a distance typically greater than one asperity radius (L. Johnson, 2010). It then leads to an overestimation of the computed moment. However, as the contact area for each asperity should be nearly similar (considering again the Hertz contact model and the low stiffness of the silicone) we can expect that the conclusion of the magnitude distribution presented in Figure 4.15 would be unchanged if one could obtain a precise measurement of the slipping area of each IAS. We thus acknowledge that the reported moment of slip events should be mostly interpreted relatively than as absolute values. Such complexity of the slip distribution is also observed for natural earthquakes with zones of little or no slip (Freymueller et al., 2021).

Another ambiguity is involved in the calculation of the moment from equation (4.8). Indeed, the shear modulus used in this equation is taken as the shear modulus of the PMMA. However the PMMA is the dominant material only on one side of the system, the other side is composed of the PMMA beads embedded in

the silicone block. Characterizing the shear modulus for such bi-material is not a trivial task and again further warns against a direct interpretation of the absolute values of M_0.

4.7   Concluding Remarks

This study analyzes the collective behavior of numerous discrete asperities ($N \approx 140$) modeled on an analog fault interface during multiple seismic cycles. We show that an interface composed of multiple discrete asperities can have a macroscopic behavior that is distinct from that of its individual elements. The asperities present a diversity of slips at various speeds. We evidence the dependence of the interseismic coupling of the interface with the topographical map of the asperity summits and the normal load imposed on the system. We notably show that topographic variations of the asperity summits have a pronounced effect on this coupling. The slip intermittency of the activity of clustered asperities indicates that the interface undergoes local episodes of creep that ultimately lead to the global slip of the interface. The analysis of the evolution of the elastic energy along the interface helps to track the disordering of the asperities with respect to their initial position. We show that this energy is typically higher for large normal stress, which supports the conclusion that normal stress maintains a larger disorder in the system. It shows as well that the disorder increases during the slip-strengthening phase and is only partially reduced during large slip events. Significant statistical features of slip widely observed in natural faults are reproduced by our experiments like the Gutenberg–Richter law, Omori's law, and the moment-duration scaling, suggesting that the obtained results can be extrapolated to natural fault systems.

Chapter 5

Discussion and Conclusions

Throughout the previous chapters, the motivation of my PhD project (Chapter 1), all the experimental setups required for our laboratory experiments (Chapter 2), the development for modeling the analog fault interface (Chapter 3), and the experimental characterization of such an interface that explains the collective behaviors of asperities before large stick-slip events (Chapter 4) have been explained in this dissertation.

In this final chapter, I first discuss the stress drops of the slip episodes produced in our experiments. In particular, we discuss the observation that the seismological stress drops of the tectonic earthquakes are invariant with the depth through the confined ruptures produced in our experiments. We then emphasize the importance of understanding the links between the seismicity induced in geothermal reservoirs, the aseismic slip of a fault, and the interfacial properties of the fault, since this induced seismicity is suggested to originate from the aseismic slip of the fault which is affected by its interfacial properties. In addition, the perspectives of our work are discussed in four major directions: the pressure-sensitive films used to measure the normal stresses and real contacts at local asperities modeled on the analog interface, the analog fault model itself, the numerical modeling of the analog fault interface, and the experimental characterization of the analog fault interface. At last, I present a concise conclusion to summarize what we have done and learned from this dissertation.

5.1 Implications

5.1.1 Stress Drops of Slip Episodes

Except for the discussion presented in Section 4.6, where the interseismic coupling, the interfacial elastic energy, the slow-slip nature of our slip episodes generated by the frictional-viscous experimental setup, the slip intermittency of the slip episodes, and the mechanics of the slip-strengthening regime are discussed, another noteworthy point is the stress drops of the slip episodes.

Excluding the elastic-property dependence with depth, seismological observations usually show that the stress drop is independent of the depth (Figure 5.1a) (Allmann & Shearer, 2007; Denolle & Shearer, 2016), which can be translated as the stress drop being independent of the normal stress since the normal stress increases with the depth. However, many laboratory experiments only focusing on system-size ruptures show the opposite trend, which is the stress drop dependent on the normal stress (Figure 5.1b) (Karner & Marone, 2000; Okubo & Dieterich, 1984). Such discrepancy can be reconciled by studying the stress drops of confined and unconfined ruptures generated in our experiments. As already discussed in Section 4.6.4, many confined ruptures that takes place during the slip-strengthening phase are observed in our experiments. These confined ruptures (i.e., non-system-size ruptures) can be further classified into several subgroups by identifying how many sample edges have they reached during the rupture process. For comparison, the large-scale stick-slip events rupturing the whole fault interface are also taken into account. We then need to compute the stress drops of all slip episodes that are divided into different subgroups under different nominal normal loads.

The stress drop of a tectonic earthquake is usually inferred from the seismic moment and the rupture length as follows (Kanamori & Anderson, 1975):

$$\Delta\sigma_s = \frac{7}{16}\frac{M_0}{L^3} \qquad (5.1)$$

where L is the rupture length by assuming a circular propagation crack and M_0 is the seismic moment. This is the indirect manner for inferring the stress drop, as the initial and the residual stresses of the fault before and after the rupture are
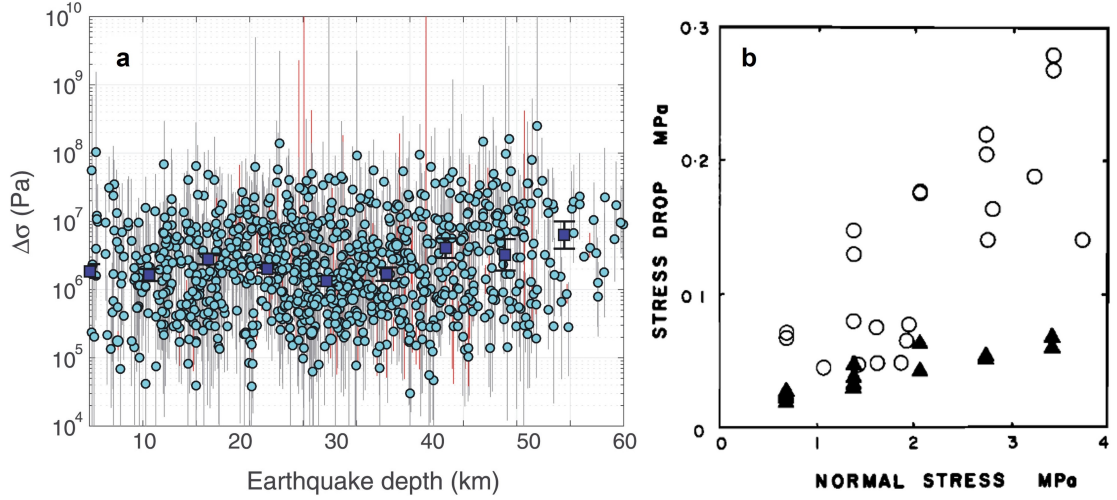
Figure 5.1: a: Variations of stress drop with source depth using the catalog of 942 thrust earthquakes of magnitude M_W 5.5 and above. Solid circles are individual measurements, and solid squares are mean (bootstrapped) over magnitude bins. Gray and red lines are uncertainty measurements. Retrieved from Denolle and Shearer (2016). **b:** Variations of average stress drop with normal stress using laboratory stick-slip events. Solid triangles and open circles respectively represent the events produced by a rough fault (a roughness of about 80 μm) and a smooth fault (a roughness of about 0.2 μm). Retrieved from Okubo and Dieterich (1984).

unknown, respectively. Yet, the small shear force drops resulting from the small-scale stick-slip events, as shown in Figure 4.9, are recorded in our experiments through the shear force measurement on the macroscopic fault. Moreover, these shear force drops are well tracked by the slip episodes in our catalogs, in which the effective rupture area of each slip episode is estimated based on the Voronoi diagram (Fortune, 1995). The shear force drop and effective rupture area obtained in our experiments provide a direct manner to compute the stress drop of each slip episode as:

$$\Delta\sigma_s = \frac{\Delta F_S}{A_r} \tag{5.2}$$

Therefore, we are also able to compute the stress drop of each slip episode in the catalogs following equations 5.1 and 5.2, which are the indirect inferring manner and the direct measurement manner, respectively. We note that a combined shear

modulus, G_{cb}, is considered since the bi-material (PMMA and silicone) is involved (Ampuero & Dahlen, 2005) in our analog fault:

$$G_{cb} = \frac{2G_p G_s}{G_p + G_s} \tag{5.3}$$

where G_p and G_s are the shear moduli of PMMA and silicone, respectively. Additionally, the rupture length L is computed through the known effective rupture area, A_r, by assuming a circular crack, which is equal to $L = \sqrt{A_r/\pi}$. The seismic moment, M_0, is computed as:

$$M_0 = G_{cb} \cdot A \cdot L \tag{5.4}$$

With the catalogs of slip episodes, the stress drops of different groups of slip episodes are computed under different nominal normal loads, using the direct and inferring manners, as shown in Figure 5.2. Six color-coded groups of slip episodes, which are the system-size events rupturing the whole fault interface, the fully confined events never reaching the sample edge, and the partially confined events reaching different numbers of edges on the interface, are classified under various normal loads. The filled and open symbols denote the stress drops computed through the direct (equation 5.2) and inferring (equation 5.1), respectively. For clear visualization, the inferring stress drops are offset by +40 N to compare with the direct stress drops.

Figure 5.2 presents the stress drops computed from the direct and inferring manners, although more scatters are found in the direct stress drops. A clear trend shows that, for the system-size slip episodes, the stress drop increases with the normal load. A similar trend, but not as evident as that of the system-size events, is also observed for the partially confined slip episodes reaching three and four edges of the interface. This less evident trend is because these intermediate-scale events are between the system-size and the fully confined ones, but they are also kindly limited by the edge effect of the analog fault. On the contrary, the stress drops of the other slip episodes, especially the fully confined ones, show little dependence on the normal load.

Figure 5.3 plots the inferring stress drop (equation 5.1) as a function of the direct stress drop (equation 5.2) to compare the consistency between the two com-
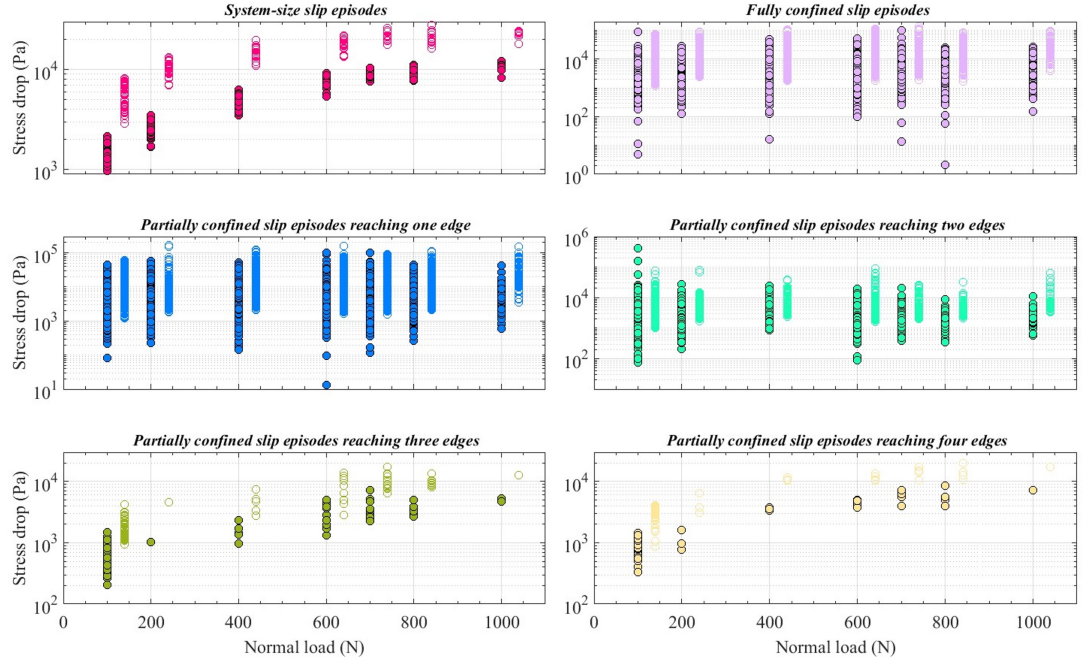
Figure 5.2: Stress drops of six types of slip episodes under different nominal normal loads. The stress drops computed through the direct manner are denoted by the filled circles, while the open circles denote the stress drops obtained from the inferring manner. The inferring stress drops are offset horizontally by +40 N for clear visualization.

putations. A cluster with a trend whose slope greater than 1 suggests that the inferring stress drop is overestimated if we assume the direct stress drop is accurate. Such overestimation may come from the overestimation of the combined shear modulus (equation 5.3), as the validity of this proxy of the PMMA beads embedded in the silicone block has not been carefully checked.

Our results reconcile the discrepancy that seismological stress drops are observed to be invariant to normal stress (Allmann & Shearer, 2007; Denolle & Shearer, 2016) while the average stress drops computed from the experimental system-size ruptures are dependent on the normal stress (Karner & Marone, 2000; Okubo & Dieterich, 1984). Similar evidence from the stress drops of confined and unconfined ruptures are also given by Steinhardt et al. (2023), as shown in Figure 5.4. This provides the implications for the appropriate interpretation of seis-
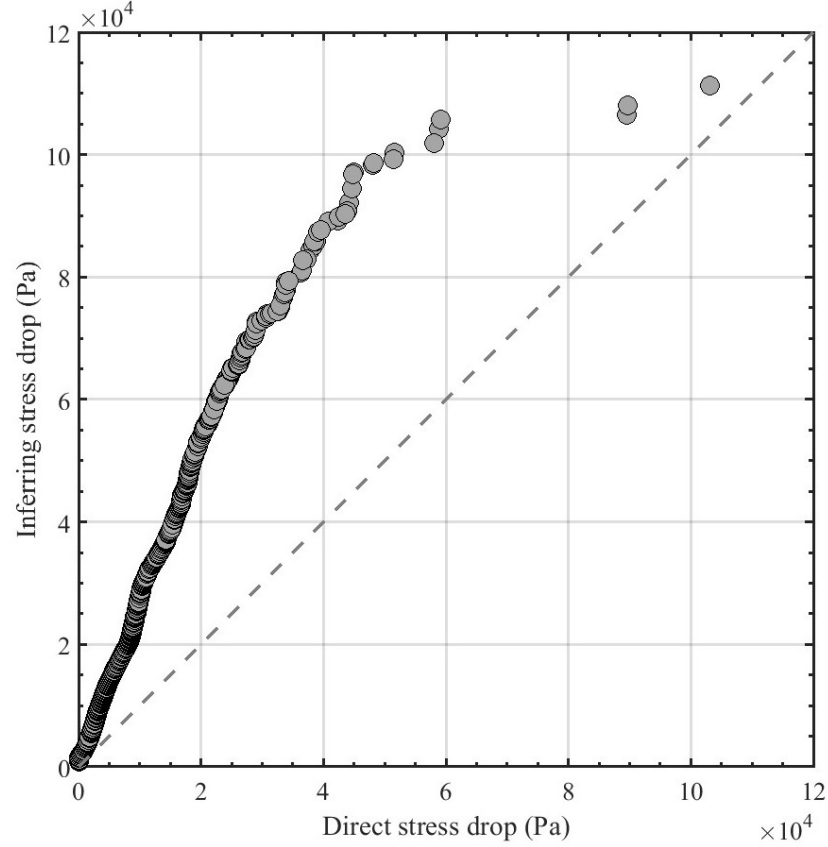
Figure 5.3: Inferring stress drop as a function of the direct stress drop. The gray dashed line represents the slope of 1 as a guide to the eye.

mological stress drops by considering the confined nature of the widely observed tectonic earthquakes that only rupture part of the fault zones. It also implies that, for those system-size ruptures created in experiments and the simple spring-block model, which also shows the depth-dependent stress drop, a more comprehensive interpretation of their stress drops is necessary. It suggests that more attention should be paid to the confined ruptures in experiments, as they are better analogies to the tectonic earthquakes that occurred in nature.

5.1.2   Implications for Geothermal Reservoirs

In geothermal reservoirs, the elevated temperature and potential circulation of hot fluid in the fault zones may not only be responsible for the viscoelastic rheol-
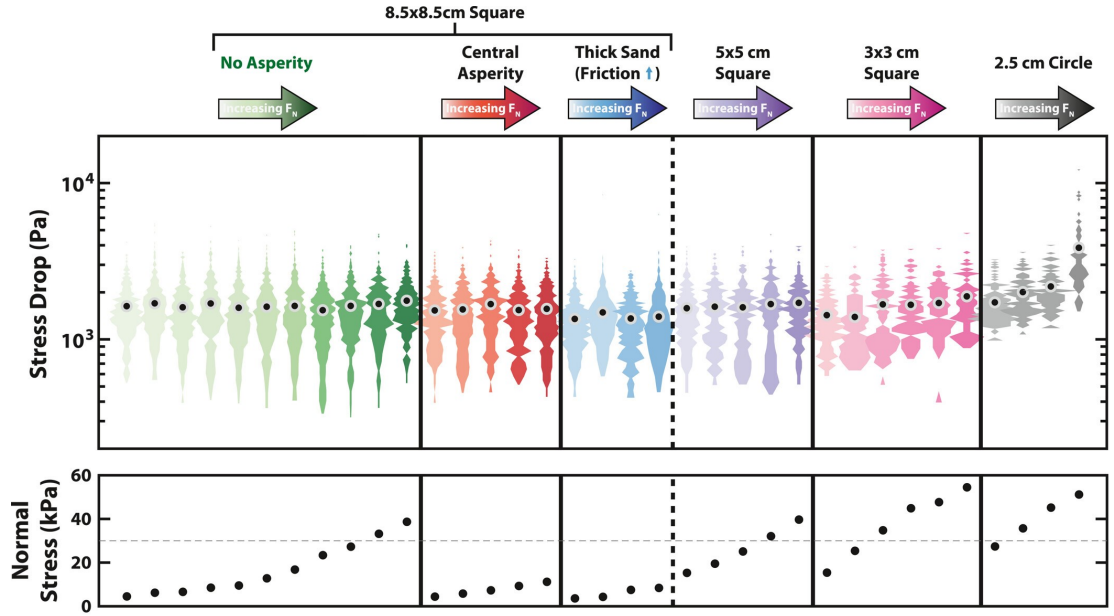
Figure 5.4: Stress drop of confined and unconfined ruptures. Top: Stress drop distributions with increasing normal stress (color intensity, values shown in bottom plot) for six unique fault conditions. The width of each shape corresponds to the probability density function for that range of stress drops. For the largest fault size with fully confined ruptures (left of thick dashed line), stress drop is invariant to changes in normal stress (green), normal stress heterogeneity (red), and even to a large extent increases in the frictional force along the fault (blue). However, as the size of the fault is reduced (right of thick dashed line) and events increasingly nucleate or terminate at the edges of the system, a large change in the stress drop, as well as an emergent normal stress dependence are observed (purple, fuchsia, gray). Black dots indicate the average stress drop of all events across the experiment. Bottom: Average normal stress for each corresponding set of experiments above. Horizontal dashed line at 30 kPa is shown as a guide to the eye. Modified from Steinhardt et al. (2023).

ogy (Kamali-Asl et al., 2019) but also for putting the faults at the transition of the frictional equilibrium between seismic and aseismic slip (Scholz, 1998; Cornet, 2016) due to the low effective normal stress. An in-situ fluid-injection experiment performed on an initially inactive fault reveals that the induced seismicity within the reservoir is mainly triggered by the aseismic slip (Guglielmi et al., 2015). Our work bears a similar physical analogy with the origin of the induced seismicity in geothermal reservoirs, which is how aseismic slip is related to the initiation of seismicity. In this dissertation, most of our work mainly focused on the characterization of the aseismic slip of the heterogeneous fault interface at both asperity and fault scales. The characterization of the seismicity would be further implemented with the analysis of acoustic emissions captured during the aseismic slip of the fault (see more perspectives in Section 5.2.4). The link between these acoustic emissions and the aseismic slip would be implicating for better understanding and eventually limit the induced seismicity.

The slip episodes clustered on the interface can be seen as the analogy of the seismicity induced within reservoirs by the partial ruptures of the interface that contains the interactions of asperities. Except for the large-scale events that rupture the whole interface, multiple events with various sizes and corresponding occurrences are observed in our experiments (Figure 4.15), which are the partial ruptures that occurred on an aseismic sliding interface and contain multiple asperities with different slip behaviors. For example, the slip rates of different asperities vary in time and space (Figure 4.8), and even the slip rate of a single asperity also varies over time (Figure 4.13). Our work helps to understand the link between the seismicity and the aseismic slip of the multi-asperity interface by focusing on the physical behavior of each asperity, which could eventually seek strategies to limit the induced seismicity within geothermal reservoirs.

5.2 Perspectives

In addition to the results and implications presented in this dissertation, we are using the pressure-sensitive film to estimate the normal stress distribution

and real contacts of the analog fault interface. Besides, several perspectives have emerged during my PhD journey that may potentially be the research ideas in the future. These perspectives could be divided into three major directions: the analog fault model itself, the numerical modeling of the analog fault interface, and the experimental characterization of the analog fault interface.

5.2.1   Pressure-Sensitive Film

A pressure-sensitive film (Prescale, Fujifilm Corporation) is flatly placed between the thick PMMA plate and the asperities embedded in the silicone block to measure the real contact area and normal stress distribution of the analog fault interface at a prescribed macroscopic normal load in the static state. The polyethylene-based film has a thickness of approximately 90 μm. Microcapsules embedded in the film will break and react with a precalibrated color-developing agent when subjected to the normal loading. The color resulting from the color-developing agent is proportional to the pressure, with a spatial resolution of ± 5 μm and a pressure resolution of ± 1.5 Pa. In our experiments, the pressure-sensitive film of medium range 12-50 MPa is employed for preliminary tests. The color intensity will be saturated (intensity ~ 0.3 candelas (cd)) in the areas with normal stress greater than 50 MPa, while no color will be displayed in the areas with normal stress smaller than 12 MPa.

Such a film is placed on the interface and then compressed under a constant normal load of 800 N for about 200 s expecting the full development of the real contacts. Once the film is carefully extracted from the interface, it is digitized through a high-resolution image scanner (Canon PIXMA TS8351a) with a resolution of 2400 DPI (Dots Per Inch) at least. The raw image of the digitized pressure-sensitive film is shown in Figure 5.5. It is found that the distribution of the colorful dots in the global view of the image is generally consistent with the distribution of the asperities in the analog fault model, except a few asperities located in the right top corner are not clearly measured, which is due to the smaller peak heights of these asperities evidenced in the high-resolution topographical map (see Figure 4.3 for details). These unmeasured asperities probably have normal
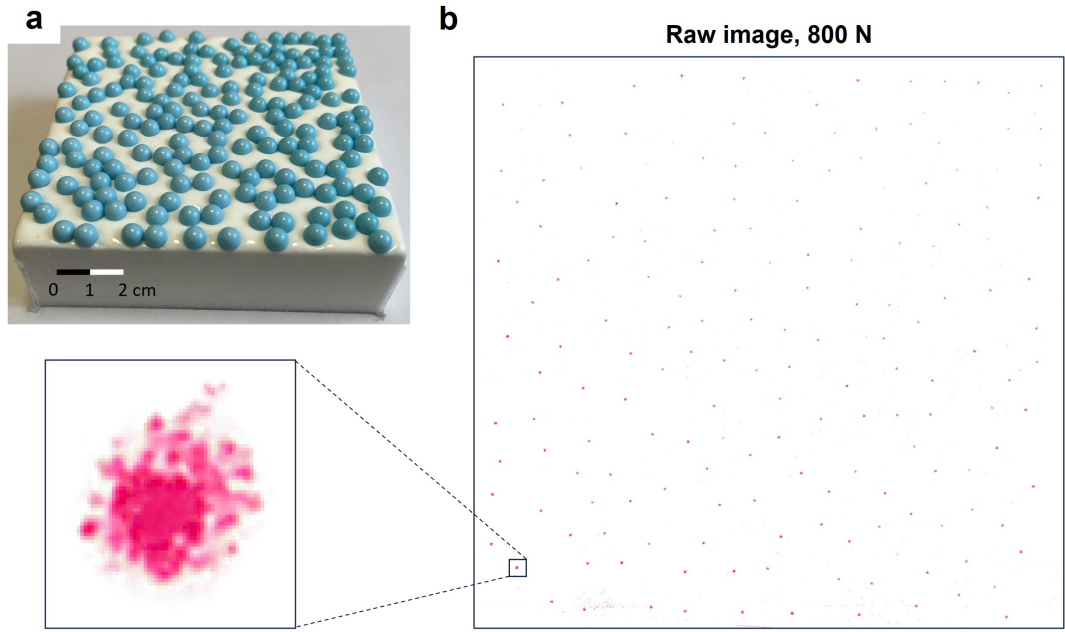
Figure 5.5: a: Picture showing numerous asperities embedded with height variations in the viscoelastic silicone block. Modified from Shu et al. (2023). **b:** Raw image (with a resolution of 2400 DPI) of the digitized pressure-sensitive film compressed under a constant macroscopic normal load of 800 N for about 200 s. A few asperities located in the right top corner are not clearly measured because they have smaller peak heights as evidenced in the high-resolution topographical map (see Figure 4.3 for details). The zoom view displays the color intensity (proportional to the pressure) and the real contact measured at one local asperity.

stresses smaller than the lower detection threshold of the pressure-sensitive film, 12 MPa. The real contact and color intensity measured at one local asperity are also displayed in a zoom-in view.

Normal Stress Distribution and Real Contacts

Each pixel contained in the raw image of the pressure-sensitive film is converted from the RGB color scheme to the luminous intensity color scheme. (Figure 5.6a). Luminous intensity is an SI (International System) photometric measurement unit that has a value between 0 and 1 cd. A higher intensity value indicates a brighter

region outside the real contact, whereas the darker region indicates the real contact with a smaller intensity. Figure 5.6a shows the luminous map of the fault interface measured at a nominal normal load of 800 N, with the black rectangles marking the zoom-in regions, from which the real contact and the luminous intensity at each pixel can be observed for each asperity. The contacts look relatively irregular, and similar irregular contacts are also observed in other measurements under different normal loads. We suspect this might be a problem of the employed pressure-sensitive film for resolving the real contacts. More measurements with other types of pressure-sensitive films with different stress ranges and resolutions need to be implemented in the future to improve the measurement. The pressure-sensitive film is calibrated in the same way documented by Selvadurai and Glaser (2015b) where indentation tests are performed and compared with the numerical modeling results. The luminous map is converted to the normal stress map, based on the calibration dataset, as shown in Figure 5.6b. The white rectangles zoom in on the same regions highlighted by the black ones, and a good agreement between the luminous map and the normal stress map is evidenced.

We identify all the pixels above a threshold of 12 MPa in the normal stress map (Figure 5.6b). The image detection algorithm (Lehmann & Legland, 2012) in MATLAB is employed to these pixels to return the properties of the clustered pixels that indicate the real contacts of asperities. For each asperity in our analog experiments, the variables including the centroid of its real contact, the average contact area, and the average normal stress are obtained to establish the catalog. Meanwhile, the equivalent contacting radius of each asperity is computed by assuming the real contact is circular. Finally, such a catalog is refined by selecting the clusters with an average contact area between 150 and 2000 pixel^2. In addition, the scaling between the pixel of the digitized pressure-sensitive film and the millimeter is given by the digitization parameters shown by the image scanner, which is 72.8 pixels/mm. Such scaling is also double-checked by the distance between two far-away known asperities in our analog model in millimeters (from the high-resolution topographical map, Figure 4.3) and in pixels (from the digitized pressure-sensitive film). The real contacts and normal stresses of 161 asperities out
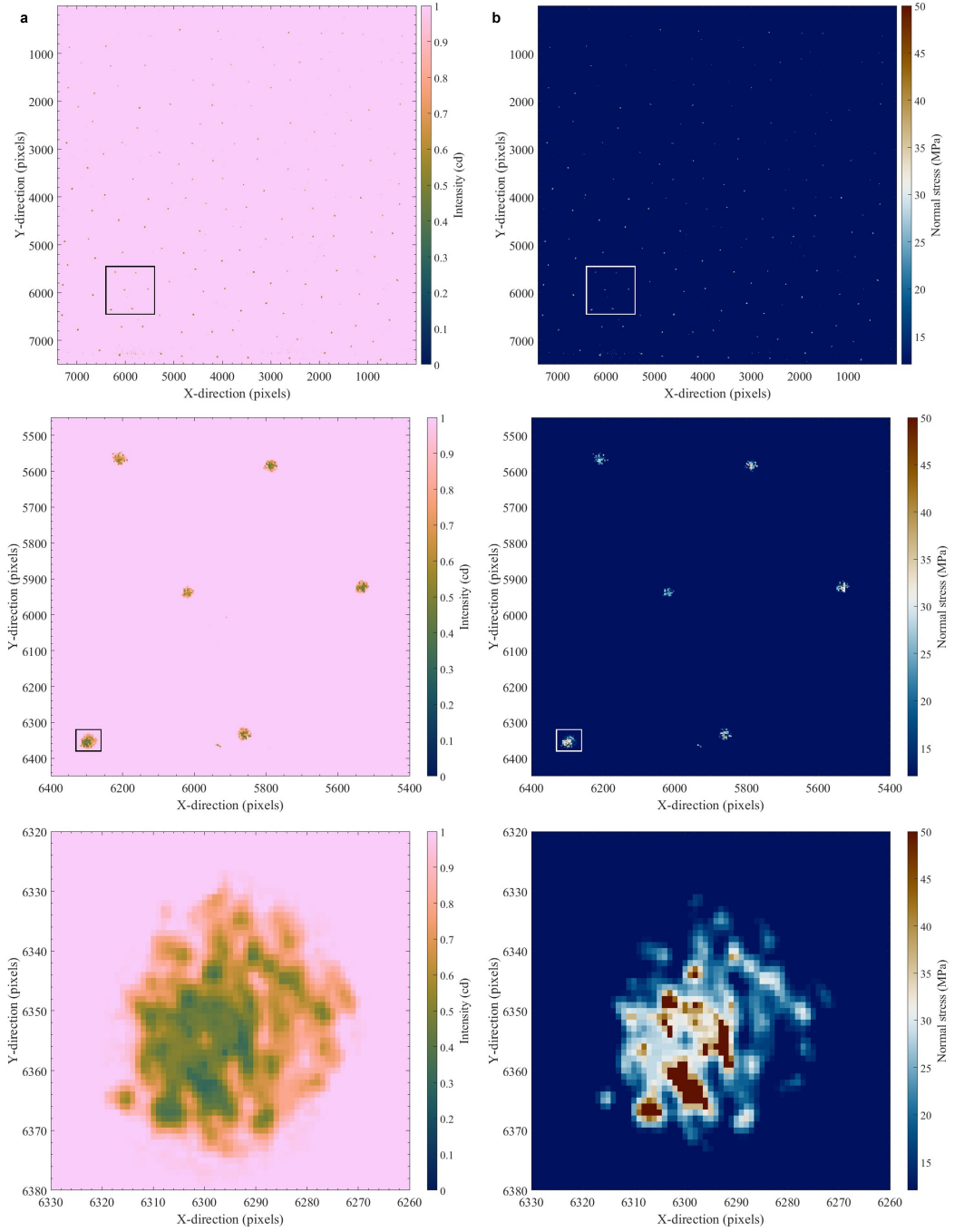
Figure 5.6: a: Luminous intensity map of the digitized pressure-sensitive film compressed under a constant macroscopic normal load of 800 N for about 200 s. The real contacts are marked by the regions with smaller intensity. The black rectangles highlight the zoom-in regions shown below, where the real contact of each asperity is displayed. **b:** Normal stress map of the same pressure-sensitive film where the white rectangles mark the same zoom-in regions. The zoom-in view of the normal stress map is consistent with that of the luminous intensity map.

of 174 asperities modeled on the analog fault interface are measured at the static state under a normal load of 800 N.

The normal stress map at each asperity can be presented (Figure 5.7b) since the centroid, the equivalent contacting radius, and the average normal stress of each asperity are given by the pressure-sensitive film. The normal stress is color-coded
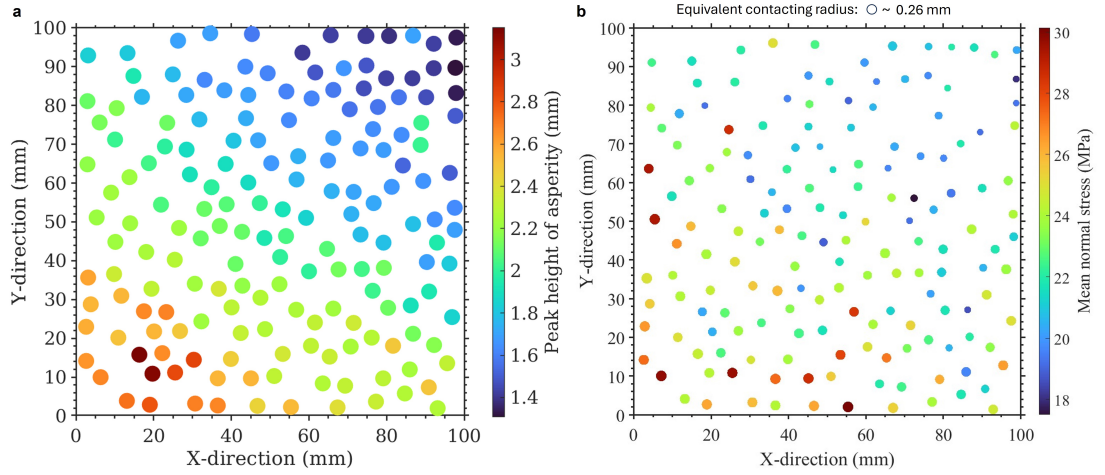
Figure 5.7: a: Peak height of each asperity extracted from the high-resolution topographical map of the analog fault interface (see also Figure 4.3). The minimum and the maximum are 1.31 mm and 3.15 mm, respectively. Such a distribution of the peak height of asperity indirectly indicates the normal stress distribution if referring to a simple Hertz contact model. Modified from Shu et al. (2023). **b:** Normal stress distribution at local asperities measured from the pressure-sensitive film compressed under a nominal normal load of 800 N. The normal stress is color-coded and the equivalent contacting radius of each asperity is up-scaled by 1000 times for clear visualization. The normal stress and the real contact of a few asperities located in the right top corner of the analog fault are not measured by the pressure-sensitive film.

and the equivalent contacting radius of each asperity is up-scaled by 1000 times for clear visualization. The peak height of each asperity (Figure 5.7a) derived from the high-resolution topographical map of the analog fault interface (see also Figure 4.3) is used to compared with the normal stress map measured from the pressure-

sensitive film (Figure 5.7b), as the distribution of the peak height of asperity is an indirect indicator of the normal stress distribution if considering a simple Hertz contact model (K. Johnson, 1987). It is observed that, generally, the distribution of the peak height (Figure 5.7a) and the local normal stress (Figure 5.7b) of asperities are consistent. But, the major trend from lower left corner to upper right corner as shown in Figure 5.7a is not evidenced. Nevertheless, the maximum normal stress is not located at the highest asperity as expected. On the contrary, a few asperities with smaller peak heights (located in the right top corner of the analog fault) are not measured by the pressure-sensitive film, which is reasonable as they are expected to sustain much less normal stress when the whole interface is subjected to a macroscopic normal load.

The distribution of the equivalent contacting radius of detected real contacts (Figure 5.8a) and the mean normal stress as a function of the equivalent contacting radius (Figure 5.8b) are also plotted to check the robustness of the pressure-sensitive film measurements. The gray dashed line in Figure 5.8b indicates the best linear fit of the whole dataset, and the color is coded by the parameter solidity, which is the area of the image object divided by the area of its convex hull. The solidity is dimensionless and has an absolute value between 0 and 1 which respectively indicate the worst and the best measurement reliability. This variable can be further used to refine the catalogs of asperity measurement. The thick magenta dashed line indicates the macroscopic normal stress computed by dividing the nominal normal load of 800 N by the sum of the real contact areas of the detected asperities. A gap between this normal stress of around 45 MPa and the cluster of normal stresses at asperities is found (Figure 5.8b). The reasons could be that some small real contacts cannot be detected by the pressure-sensitive film and/or the lower limit of our preset contact area range ($[150, 2000]$ pixel^2) is large thus some small contacts are excluded from the catalog.

Most of the detected real contacts have an equivalent contacting radius between 0.12 mm and 0.24 mm. The maximum, minimum, and average equivalent contacting radius are 0.2613, 0.0955, and 0.1833 mm, respectively. For the whole detected real contacts, they generally follow the best linear fit representing a trend,
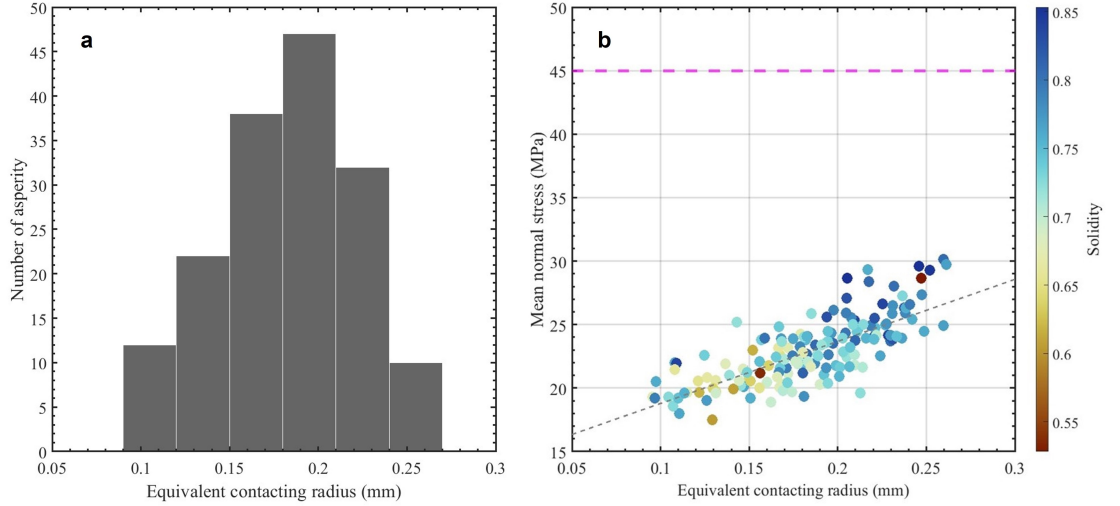
Figure 5.8: a: Distribution of the equivalent contacting radius of the real contacts detected by the pressure-sensitive film. The minimum, average, and maximum equivalent contacting radius are 0.1143 mm, 0.1740 mm, and 0.3506 mm, respectively. **b:** Mean normal stress sustained by the asperity as a function of its equivalent contacting radius. Each separate circle is color-coded by the solidity of the image detection, and the best linear fit of the whole dataset is represented by the gray dashed line. The thick magenta dashed line represents the macroscopic normal stress of the interface, which is computed by dividing the applied nominal normal load by the sum of the real contact areas of the detected asperities. The whole measurement generally follows a trend indicating an increase in real contact area increasing the mean normal stress.

that is, the larger the equivalent contacting radius the greater the mean normal stress sustained by the asperity. Such a trend is also consistent with a simple single-asperity Hertz contact model in which a greater normal stress can result in a larger real contact area.

Interfacial Statistics under Different Normal Loads

Statistical analysis is further performed on the catalogs of detected real contacts under different nominal normal loads. We first refine the catalog of detected asperities under multiple normal loads by setting a solidity threshold of 0.55. The

detection with a solidity greater than 0.55 will be taken as reliable imaging and retained in the catalog. With the refined catalogs, Figure 5.9 shows the number of asperities detected by the pressure-sensitive film as a function of the nominal normal load, where the best linear fit, represented by the dashed line, indicates a trend that the larger the normal load, the more asperities detected. Only 5 reliable asperities are detected under the normal load of 200 N, thus these asperities are not involved in the further statistical analysis.
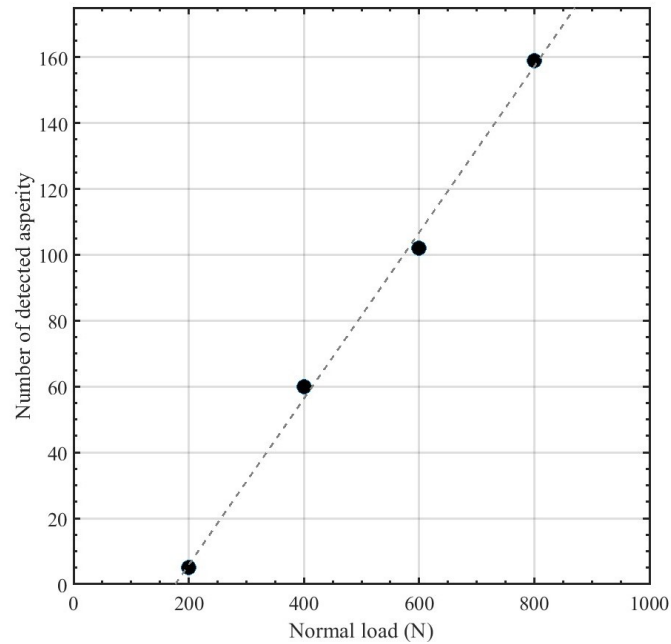
Figure 5.9: Number of detected asperities as a function of the applied nominal normal loads. The dashed line represents the best linear fit.

Similarly, for the three nominal normal loads, the distribution of the equivalent contacting radius of the real contacts (Figure 5.10a) and the mean normal stress as a function of the equivalent contacting radius (Figure 5.10b) are also superimposed to investigate the effect of normal load on the real contact.

In Figure 5.10a, we observe that the maximum equivalent contacting radius and the number of detected asperities both increase with the applied nominal normal load. In addition, the average contacting radius also increases with the normal load, which can be seen from the right shift of the histograms with rising normal
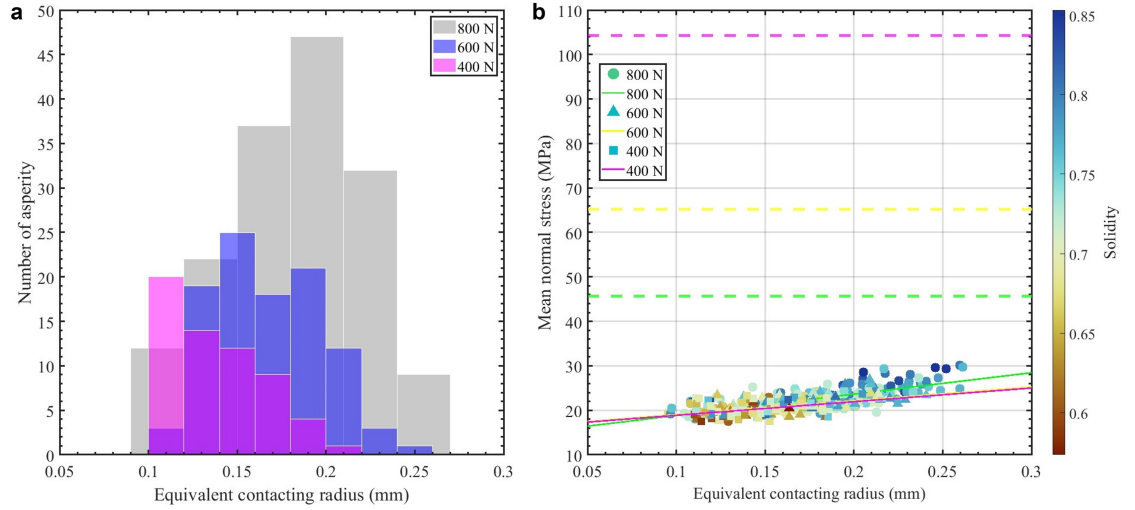
Figure 5.10: a: Distribution of the equivalent contacting radius of the detected asperities, color-coded by the nominal normal load. **b:** Mean normal stress sustained by the asperity as a function of its equivalent contacting radius. The symbols are coded by the applied nominal normal loads. Each separate symbol is color-coded by the solidity of the image detection. The color-coded thin, solid lines represent the best linear fits of the asperities detected under different normal loads. The thick dashed lines with the same color coding indicate the macroscopic normal stresses computed the same as that in Figure 5.8.

loads. As shown by the best linear fits in Figure 5.10b, a similar major trend, the larger the equivalent contacting radius the greater the mean normal stress sustained by the local asperity, is also observed under three normal loads. This trend is quite close when the normal loads are 400 N and 600 N, whereas another steeper trend is found under the normal load of 800 N. The maximum value of the mean normal stress corresponds to the normal load of 800 N. Besides, we also compute the macroscopic normal stress of the interface by dividing a nominal normal load by the sum of the real contact areas of the corresponding asperities. These macroscopic normal stress are color-coded and indicated by the thick dashed lines. We find that the gap between the macroscopic normal stress and the cluster of measurements is bigger when the applied normal load is smaller. The gap may

come from the small contacts that are not detected by the pressure-sensitive film and/or our identification process. This speculation is supported by the number of detected asperities under different normal loads (Figure 5.10), as much less asperities can be detected when the normal load is low.

Since the peak height of each asperity has been derived from the high-resolution topographical map of the analog fault interface (Figure 4.3), it is important to link the peak height of asperity with the mean normal stress measured by the pressure-sensitive film. Figure 5.11 presents the mean normal stress as a function of the peak height of asperity. The asperities that are not be detected by the pressure-sensitive film are also plotted with the same arbitrary value for each normal load. We observe a general trend between the mean normal stress and the peak height of asperity, which indicates that the higher the asperity peak, the greater the normal stress. However, for all the measurements under three different normal loads, the maximum normal stress is not evidenced at the largest peak height of asperity. Another strange point is that the peak heights of the undetected asperities overlap with those asperities detected by the pressure-sensitive film. Theoretically, these undetected asperities should have been detected by the pressure-sensitive film. For the moment, we have not answered these questions yet. More tests are needed in the future to fully understand how the pressure-sensitive films with different resolutions resolve the real contacts. On the contrary, it allows us to estimate the normal stress sustained by these undetected asperities since they share similar peak heights to the detected ones.

To this end, Figure 5.12 presents the mean normal stress as a function of the nominal load for all the measurements given by the pressure-sensitive film. Each measurement of the mean normal stress is represented by a circle and color-coded by the peak height of asperity. We fit the best linear relation between the mean normal stress on local asperity and the nominal normal load if this asperity is detected by the pressure-sensitive film under all three normal loads. The relation allows us to estimate, for most of the asperities with intermediate to large peak heights, the mean normal stress at various nominal normal loads. For the asperities with small peak heights, if we assume they obey the same relation, we can also
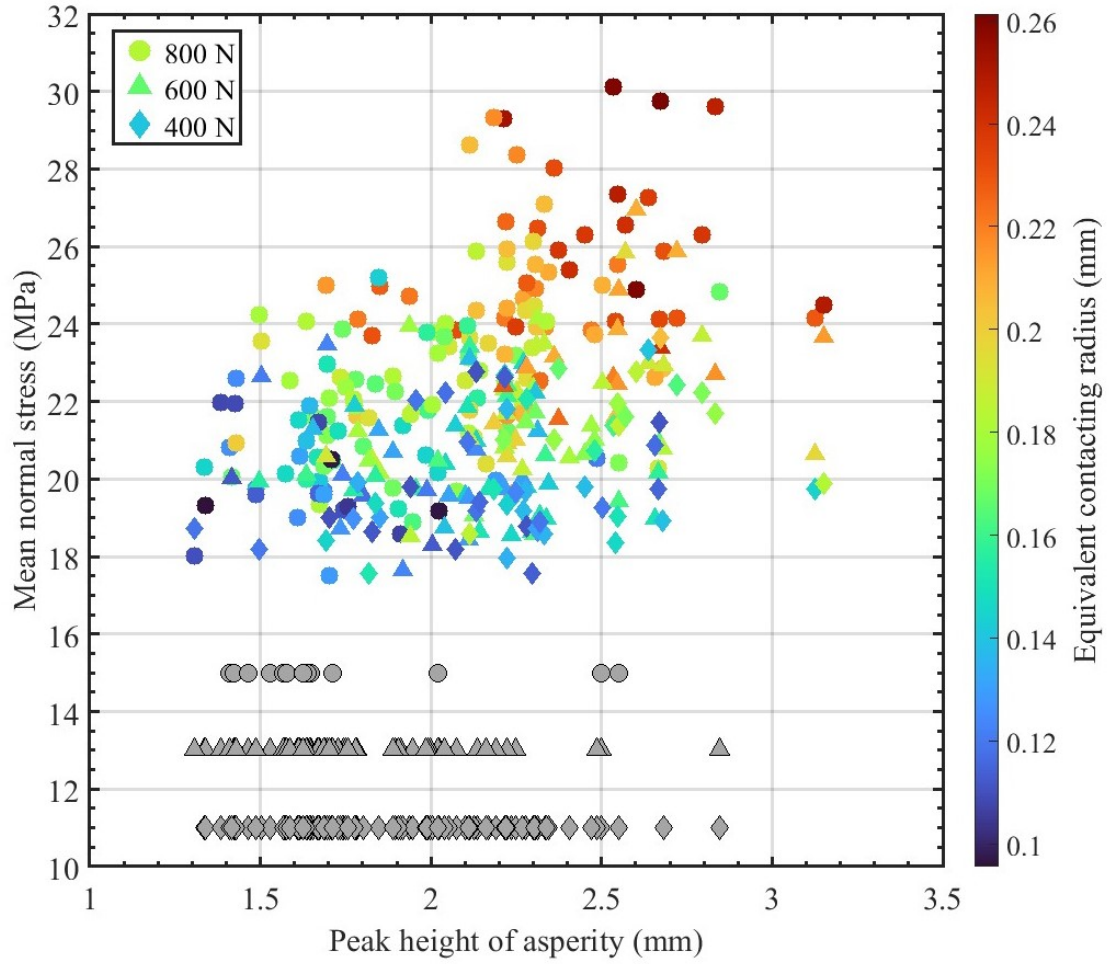
Figure 5.11: Mean normal stress as a function of the peak height of asperity derived from the topography of the analog fault interface. The symbols are coded by the normal load, and the color indicates the equivalent contacting radius measured by the pressure-sensitive film. The gray symbols represents the undetected asperities with unknown mean normal stresses. For each normal load, the undetected asperities are plotted using the same arbitrary value. A vertical offset of 2 MPa is applied to all the undetected asperities under three normal loads for clear visualization.

estimate their mean normal stress under low nominal loads since their mean normal stress under 800 N are known.

Concluding Remarks

Taking the pressure-sensitive film measurement under the normal load of 800 N as a typical example, the real contacts and normal stresses of 161 asperities out of 174 asperities modeled on the analog fault interface are measured at the static state. It is found that the normal stress map constrained by the pressure-sensitive film presents some similarity with the topographical map which can be considered as an indirect indicator of the normal stress distribution. Moreover, the measurements of the real contact area and normal stress on each asperity give a roughly linear trend, which indicates a positive relationship between the real contact area and the sustained normal stress.

The pressure-sensitive film measurements under three normal loads are analyzed statistically. With increasing normal loads, we evidence the increase of the number of detected asperities, of the maximum and average equivalent contacting radius. A similar linear trend indicating the larger the equivalent contacting radius the greater the mean normal stress is observed for all three measurements. In addition, we link the mean normal stress given by the pressure-sensitive film with the peak height of asperity derived from the high-resolution topography of the analog fault interface. A general relation, in which the mean normal stress increases with the peak height of asperity, is observed. Furthermore, the linear relationships between the mean normal stress and the applied nominal normal load are established for asperities with specific peak heights. These relationships not only allow us to estimate the mean normal stress on a local asperity at various normal loads but also estimate the mean normal stress on undetected asperities that share similar peak heights with detected ones.

Some problems have also emerged with the pressure-sensitive film measurements. For example, the real contacts seem relatively irregular, which requires us to find the most appropriate pressure-sensitive film with the best resolution adaptive to our analog fault model. Meanwhile, it is also necessary to find the best
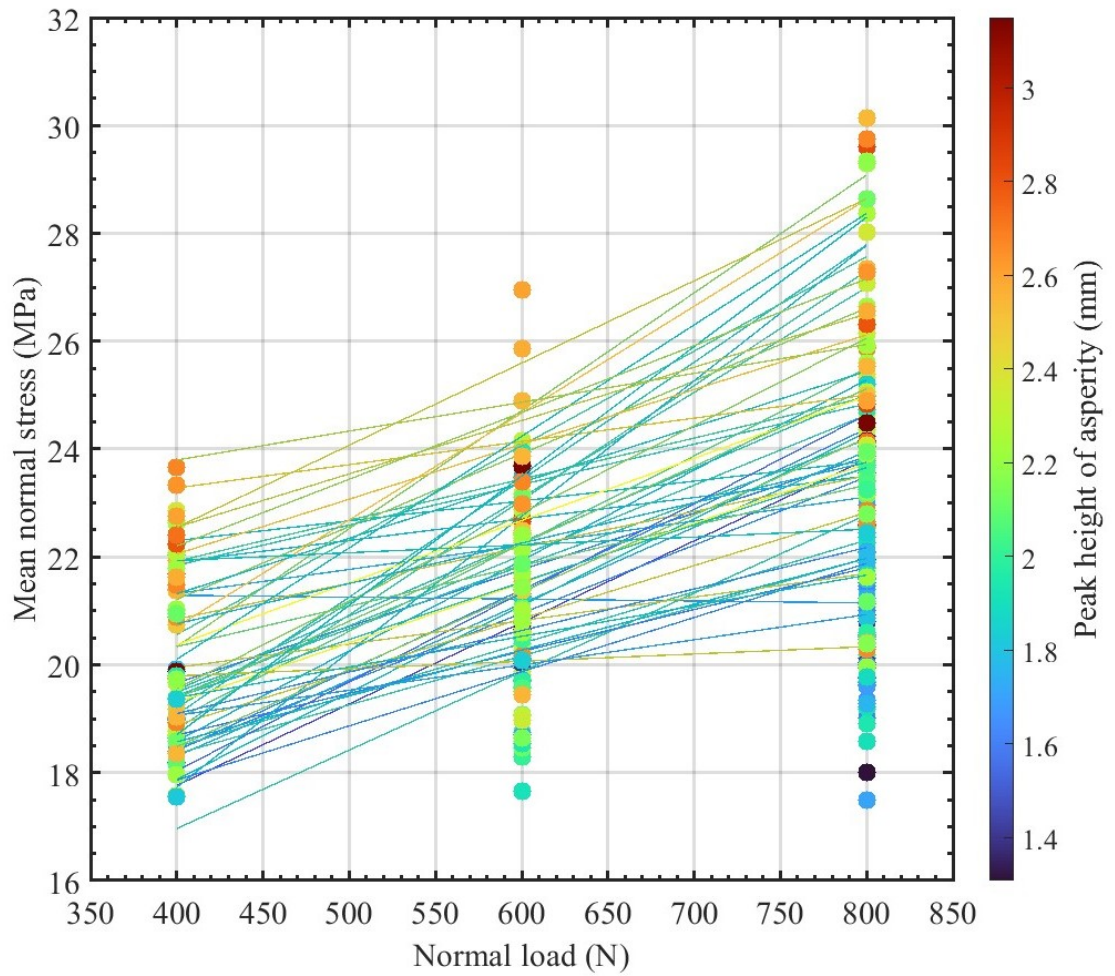
Figure 5.12: Mean normal stress as a function of the nominal normal load. The symbols are the measurements given by the pressure-sensitive film and are coded by the peak height of asperity. A best linear fit is presented when the asperity is detected by the pressure-sensitive film under all three normal loads, which is color-coded by the peak height of this asperity. It gives the linear relationship between mean normal stress on a local asperity with a specific peak height and the applied nominal normal load.

way to place the pressure-sensitive film to resist its gravity in the areas without contact for precise measurement. Besides, a large discrepancy is found between the normal stress given by the pressure-sensitive film and the macroscopic normal stress computed from the preset nominal normal load divided by the sum of the real contact area. How to reconcile such a discrepancy is important for us to validate the precise normal stress and real contact at each asperity. For each test, comparing the pressure-sensitive film measurements and the results computed by the Hertz contact model will help us to double-check the pressure-sensitive film measurements. For instance, the relationship between the mean normal stress and the nominal load for each asperity with a specific peak height can be better constrained by comparing with the results from the contact model. This relationship is important for inputting accurate values of normal stress on local asperities into the ongoing two-dimensional Burridge-Knopoff model, which is based on the physical properties of the experimental setup.

5.2.2   Perspectives for the Analog Fault Model

The first aspect is the analog fault model itself. The slip episodes clustered from the spatiotemporal interactions of asperities are partly controlled by the spatial discretization of the whole interface by taking the asperities as vertices (Figure 4.14, see Section 4.5.1 for details). It also means that the effective slip area allocated to each asperity is fixed since the position of each asperity on the interface has been fixed since the analog fault was prepared. It is straightforward that a smaller effective slip area to each asperity will be allocated if more asperities are modeled on the interface, which can lead to better spatial resolution of the spatiotemporal slip episodes. One approach is to model each asperity using a PMMA bead of a smaller radius that can still be tracked by our optical monitoring system and then randomly distribute more identical asperities with height variations all over the interface, following the same sample preparation procedures. Figure 5.13a shows another multi-contact analog fault model with more identical asperities of a smaller radius (2 mm), which will discretize the resulting fault interface more densely. Such denser spatial connections between asperities would allow us to constrain the stress
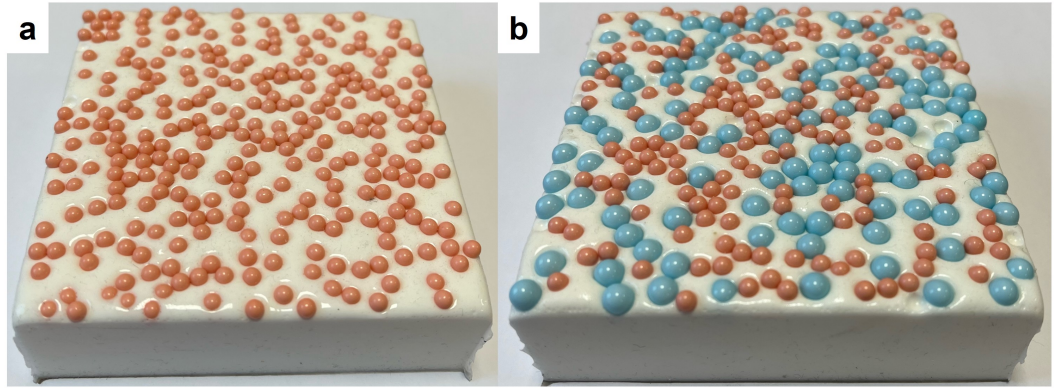
Figure 5.13: Pictures showing another two multi-contact analog fault models. **a:** Numerous identical spherical rigid PMMA beads with a radius of 2 mm are randomly embedded with height variations in the same viscoelastic block. **b:** Two sizes of spherical rigid PMMA beads, one in a radius of 2 mm (red) and the other in a radius of 3 mm (blue) are randomly embedded with height variations in the same viscoelastic block.

transfer-based triggering of individual asperity slipping with better resolution, thus enabling catalogs of the slip episodes through the finer spatiotemporal clustering. Several preliminary experiments demonstrate that our optical monitoring system can not only detect these smaller asperities but also track their slips during the whole faulting process. More experiments with such an interface (Figure 5.13a) could be an extension of our current results.

The effect of the size of asperity on the fault slip behavior and resulting earthquake sequences is also important (Lay & Nishenko, 2022; L. Johnson, 2010). For example, the rupture of a huge asperity is prone to synchronize the ruptures of surrounding asperities and lead to a large earthquake event, whereas the failure of a small asperity may only trigger a slow earthquake event with non-prominent seismic radiation (Lay & Nishenko, 2022). The effect of asperity size also acts on the static regime of a fault as an asperity with a greater radius will cause a larger stress shadow region compared to a smaller one (L. Johnson, 2010; L. R. Johnson & Nadeau, 2002). By remodeling the asperities on the fault interface, the effect of asperity size also can be investigated. Figure 5.13b displays the analog fault

model comprising two sizes of spherical rigid PMMA beads, red ones in a radius of 2 mm and blue ones in a radius of 3 mm, which are randomly embedded with height variations in the same viscoelastic block. Meanwhile, all the asperities are densely distributed on the fault interface. The advantage of such an analog model is that the two sizes of asperities concurrently exist on the fault interface, which is more realistic to the natural faults, instead of two analog fault models where each one contains asperities with an identical size, which will cause technical difficulty for keeping the same position and height distribution of asperities in the two samples. Except for the dense spatial connections between asperities, the effect of the asperity size will also be studied during both the macroscopic stable and unstable phases of the interface. Since the detection and image correlation of the smaller asperity are proven to be applicable, the experiments with the mixture of two sizes of asperities could also be implemented following the same protocols.

The density of asperity, a variable proposed by Dublanchet et al. (2013), which defines the ratio between the total area covered by asperities and the total area of the fault plane, is another interesting effect that can be investigated through our analog fault model. We can assume that the maximum density of asperity is obtained in one of our original analog fault models (e.g., Figure 2.1 and Figure 5.13). We can then obtain multiple values of the density of asperity for each analog fault model by removing different numbers of asperities from the original analog model, as long as a minimum number of asperities has remained to guarantee the zero contact between the silicone block and the thick PMMA plate. Such a strategy uses the same silicone block for all the experiments and avoids the repeating preparation of samples with different numbers of asperities. We expect to estimate a relationship between the density of asperity and the features of events (earthquakes and/or slow slip events) generated during the slow-sliding interface, such as the frequency of occurrence and magnitude, with sufficient datasets.

5.2.3   Perspectives for the Numerical Modeling

As shown in Figure 4.18, the diffusive processing controlling the rupture propagation is observed in our experimental results, which are obtained without the

presence of fluid in the fault system. Such observation seems to contrast with the widely accepted assumption that the diffusive events are contributed by the fluid in the real fault systems (Ide, 2010). We suspect that such diffusive rupture propagation is due to the viscoelastic bulk rheology in our experimental setup since if excluding this rheological heterogeneity, our experiments will be inherently the same as the other dry PMMA-PMMA frictional experiments (Selvadurai & Glaser, 2015a, 2017) that seldom report such diffusive phenomena. However, experimentally testing the effect of bulk viscoelasticity on the diffusive events is not straightforward, as varying diverse values of the viscoelasticity for the silicone block requires the appropriate material properties of the corresponding silicone products. A tougher technical difficulty is that the thick PMMA plate will contact the silicon block if a smaller elasticity makes the silicone block easier to deform. Given the reasons above, we aim to build the modified two-dimensional Burridge-Knopoff numerical model, as described in Chapter 3, to study the effect of the bulk viscoelastic rheology on the manner of the rupture propagation. For the moment, this work is still ongoing. The next step is to reproduce the experimental results using this numerical model under the same loading characteristics and with the input parameters measured from the physical properties of our experimental setup, which proves the successful validation of the effectiveness of the numerical model. With this validated numerical model, the effect of the bulk viscoelastic rheology on the diffusive process could be researched in detail by numerically varying multiple viscoelastic values.

By changing the spatial distribution of asperities, we could also study what controls the triggering of individual asperity slipping and the features of such asperity slipping. For instance, Corbi, Funiciello, Brizzi, Lallemand, and Rosenau (2017) studied the role of asperities spacing on the resulting slip rate, maximum magnitude, and seismicity rate through two identical asperities in analog experiments. In our numerical model physically based on the analog fault model, numerous asperities with varying normal stress could be placed in positions that establish a distribution with uniform spacing, and the spacing can vary among different simulations. With known spacing distance, the relationship between the normal stress

sustained by the first slipping asperity, the number of asperities it triggered, and the maximum and/or minimum triggering distance could be illustrated. Furthermore, the behaviors of asperities with the same distance away from the slipping asperity, which is assumed to emit a circular rupture front, could be compared to find if the normal stress heterogeneity stabilizes the slipping or contributes to the slipping. If a contribution to the slipping is found, a coalesce of rupture front would be expected, and will this coalesced rupture front trigger more individual asperity slipping in a cascading manner (Ellsworth & Beroza, 1995; McLaskey, 2019) remains another question to be understood. On the contrary, if a suppression of the slipping is found, this asperity serves as a barrier that inhibits the passage of the rupture front. These ideas are preliminary but could be tested as long as the two-dimensional numerical model is validated.

In speaking of the barrier, two very recent papers (Molina-Ormazabal et al., 2023; Cebry et al., 2023) present the diverse behaviors of the barrier that have been less discussed in the past. Molina-Ormazabal et al. (2023) numerically demonstrated that the velocity-weakening fault segments (indicated by the white dashed lines in Figure 5.14) display a wide range of behaviors, including permanent barrier behavior, during which they are fully locked and arrest the rupture. On the other hand, they can also release their accumulated energy either seismically or aseismically (Figure 5.14). Similarly, the experimental work (Cebry et al., 2023) artificially creates a small bump by placing different numbers of identical thin steel shims, which are assumed to be infinitely stiff since their Young's modulus is much greater than that of experimental PMMA fault, between the PMMA plates and the steel load frame (top panel, Figure 5.15). Varying local normal stress at the bump is induced through the varying numbers of shims (middle panel, Figure 5.15). Diverse behaviors of the labquake sequences are produced with different normal stress heterogeneities (bottom panel, Figure 5.15). In particular, the labquake sequence is consistent (i.e., all complete rupture events, bump never stopped rupture) when the ratio between the local normal stress at the bump, $\Delta\sigma_{bt}$, and the average normal stress along the macroscopic experimental fault, $\overline{\sigma_n}$, is smaller than 6. On the contrary, the variable labquake sequences (i.e., at least one partial rupture
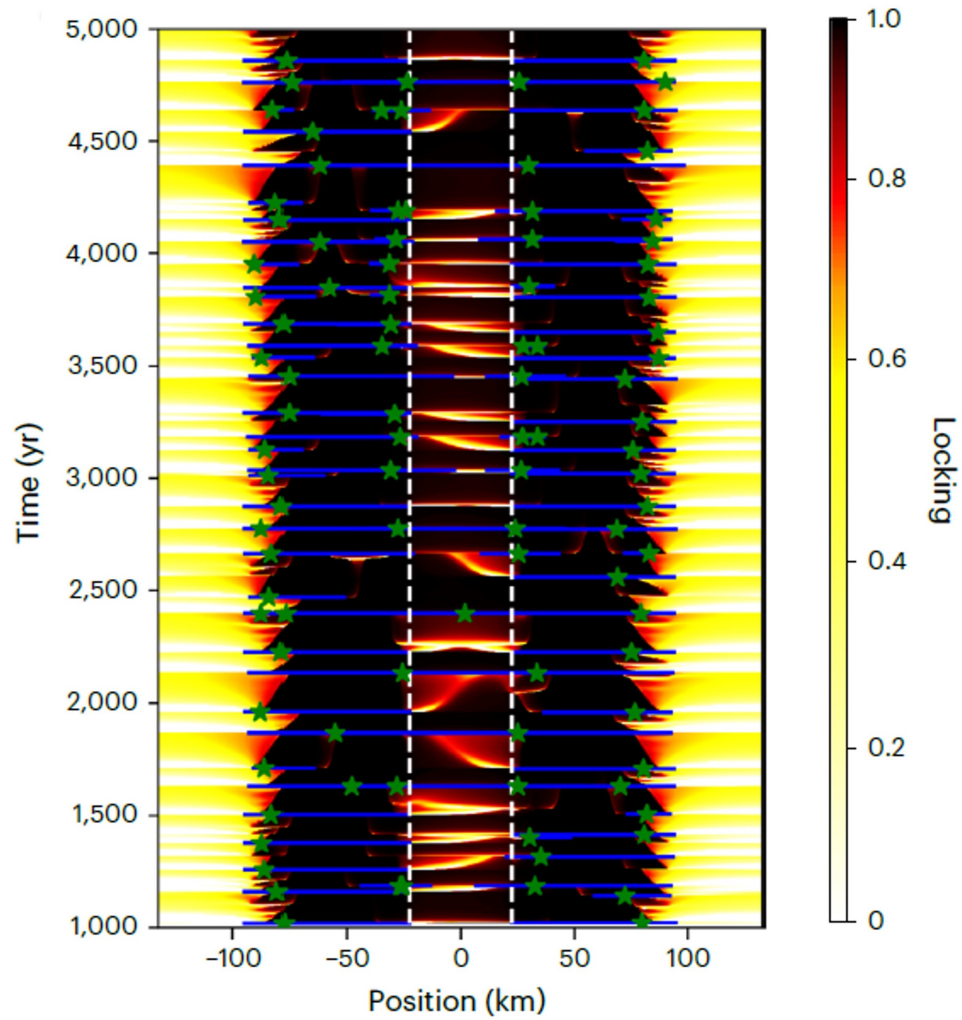
Figure 5.14: Spatiotemporal evolution of the instantaneous interseismic coupling along the simulated fault. Blue solid lines denote the earthquake rupture segments and green stars their epicentres. The position of the barrier is indicated by the white dashed lines. Retrieved from Molina-Ormazabal et al. (2023).
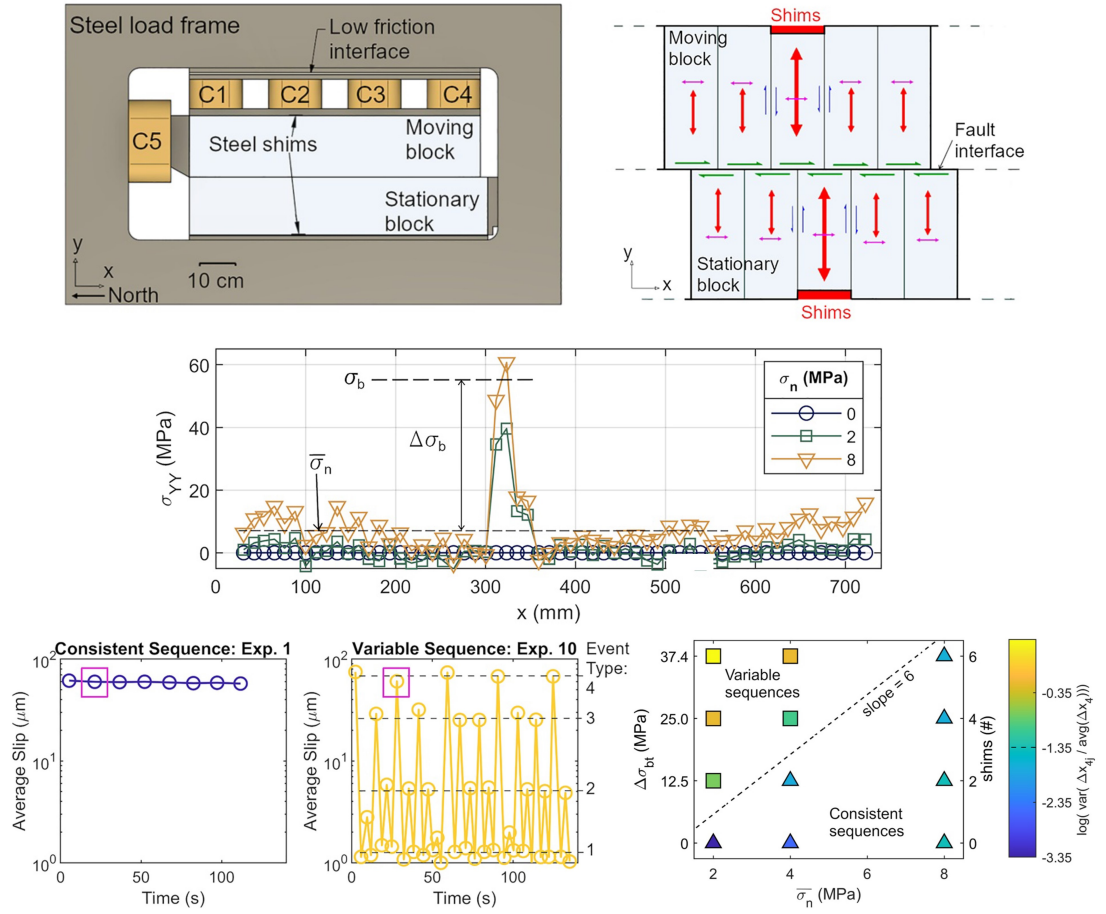
Figure 5.15: Top: Experimental setup, where a bump can be artificially created by placing different numbers of identical thin steel shims (assumed to be infinitely stiff since their Young's modulus is much greater than that of PMMA) between the PMMA plates and the steel load frame. Middle: Local normal stress distribution along the experimental PMMA-PMMA fault. Bottom (left): Temporal evolution of the average slip for two experiments under the same conditions ($\overline{\sigma_n} = 2$ MPa), except the left one has no bump (0 shim) while the right one has a bump (6 identical shims) that induces a local normal stress of about 37.4 MPa. Bottom (right): Complexity of the labquake sequences as a function of the average normal stress along the macroscopic experimental fault, $\overline{\sigma_n}$, and the local normal stress at the bump (proportional to the number of shims), $\Delta\sigma_{bt}$. The color indicates the variance of the normalized average slip. Each marker denotes the labquake sequences during an experimental run. Triangles indicate consistent sequences (all complete rupture events, bump never stopped rupture) while squares indicate variable sequences (at least one partial rupture where the bump did not slip). The dashed line with a slope of 6 separates the map into two phases: consistent and variable sequences. Modified from Cebry et al. (2023).

where the bump did not slip) with the average slip ranging about two orders of magnitude will emerge due to the complexity induced by the large normal stress heterogeneity at the bump (Figure 5.15). Both the numerical (Figure 5.14) and experimental (Figure 5.15) works emphasize the importance of the local patch with normal stress heterogeneity on the behaviors of the macroscopic fault. The role of such a patch can evolve from fully locking (i.e., barrier), partial rupture, and seismic rupture (i.e., seismic asperity).

Compared with the two works above, our analog experiments also show similar results, including that the interseismic coupling mainly ranges from 0 to 0.6 (Figure 4.11) and the complex sequences of slipping asperities with a large slip range (Figure 4.7). However, no permanent barrier, which is the fully locked patch during the interseismic phase and keeps static regardless of the slipping of other asperities, is observed in our experimental results. The absence of such a barrier may be due to the small local normal stress compared with the average normal stress on the whole fault interface, which is controlled by the peak height of asperity. Increasing the normal stress on one/several PMMA bead(s) in the validated numerical model is straightforward, and the contact area(s) of the bead(s) can be estimated from the function between the normal stress and the contact area, which is measured from the pressure-sensitive film. Multiple simulations could be implemented by systematically varying the local normal stress distribution on PMMA beads to further study the dynamics of such patch(es) and the effect on fault behaviors.

Another possibility with the validated two-dimensional numerical model is to consider the frictional heterogeneity among the PMMA beads, as frictional heterogeneous materials along the fault have been reported in many fault zones, such as the creeping and locked sections of the San Andreas Fault (Barbot et al., 2012) and the depth-dependent changes within subduction zones (Luo & Liu, 2019), which could potentially be the candidate for explaining the diverse slip behaviors of a macroscopic fault and the resulting earthquake sequences.

5.2.4   Perspectives for the Experimental Measurement

The last perspective is regarding the experimental measurement of the analog fault interface. As shown in Figure 4.9 and discussed in Section 4.6.5, the data captured during the rapid coseismic phases are sparse due to the limited sampling rate of the employed optical monitoring system. As discussed in Section 5.2.2, a denser distribution will contribute to better spatial resolution for clustering the spatiotemporal interactions of asperities into the slip episodes. Similarly, a higher sampling rate of the optical system will also promote the time resolution of the catalogs of the slip episodes. With a higher time resolution, it would be possible to obtain a clear trend of the slip-weakening or slip rate-weakening of the fault interface during the coseismic phases. Also, it would enable better access to the interactions between asperities during their rapid slipping. However, we note that a trade-off between the time and space resolution always exists. Keeping the same analog fault interface, an alternative to the high-speed camera is acoustic monitoring with an even higher sampling rate, which can capture the elastic waves emitted during small dynamic events that the camera cannot measure.

Our preliminary experiments synchronized the measurements of the shear force on the global fault, the acoustic emissions of four accelerometers, and the mean slip averaged over all the asperities (Figure 2.9), whereas a large time delay (about 4 s) between the optical and acoustic events is found using the current synchronization configuration (Figure 2.11). Moreover, the shear force drops and acoustic spikes can track events at both large and small scales (Figure 2.10). This allows us to further understand the acoustic features of dynamic ruptures that occurred during these multi-scale events. We expect to locate the source of the detected acoustic signal and quantify its amplitude in the next step. The relationship between the occurrences and magnitudes of events and the physical properties of these multi-scale events could be investigated. Moreover, the partition of seismic and aseismic slips at different events could also be explored and linked with the slipping asperities that create the corresponding events. This link would enable explaining the features of the seismicity of a fault from the physical motions of the interfacial microcontacts. In addition, such experimental measurements includ-

ing optical and acoustic monitoring could also be coupled with the perspective of the analog fault model (see details in Section 5.2.2) to further enrich the potential future studies, such as investigating how the occurrences and sizes of acoustic events are modified by the properties of the fault interface (size and density of asperity) and also the loading conditions (normal load and loading rate). These studies will eventually help us understand how and which parameters associated with the aseismic slip of the heterogeneous multi-contact fault interface influence the development and characteristics of seismicity. Besides, the energy partition on the fault interface, such as the radiated seismic energy and fracture energy, could also be inferred from seismological source models (Selvadurai, 2019). The scale dependence of these energies could be investigated through our multi-asperity interface, on which numerous slip episodes with different slips and durations emerge, and it would provide insights into the energy estimations of earthquake rupture on natural faults.

5.3 Conclusions

This dissertation is dedicated to understand the slip behavior of a global fault and the resulting earthquake sequences through the collective behavior of local discrete asperities that establish a set of complex contacts on the fault interface (Pohrt & Popov, 2012; Schmittbuhl et al., 2006). To overcome the difficulty of imaging an exhaustive spatiotemporal variability of a natural fault interface at depth and the limited computational efficiency of the numerical models when heterogeneities span a large time and space domain, we developed a novel analog fault model, in which numerous identical rigid spherical PMMA beads ($N = 174$) are randomly embedded with height variations into a soft viscoelastic silicone block. By contacting these PMMA beads with a thick, flat, transparent PMMA plate on the top, the multi-contact analog fault interface is created, on which each bead serves as a discrete frictional asperity. The normal stress variations induced by peak height variations of asperities, along with the mixture of the frictional-viscous deformation lead to a heterogeneous interface comparable to a natural rough fault interface

with bulk viscoelastic rheology, which is commonly distributed at greater depth or within the high-temperature environment (Behr & Bürgmann, 2021; Kirkpatrick et al., 2021). We studied the physical processes on and of such an interface when it is subjected to a large-scale, far-field, slow-rate shearing, which is analogical to a crustal fault interface slowly imposed by the tectonic loading.

The experimental study of such a slow-sliding interface, which produces multiple large-scale stick-slip sequences that are analogical to the earthquake cycles, is the major part of this dissertation. Taking advantage of the transparency of the thick PMMA plate, a high-resolution camera is employed to track the evolution of the position of each asperity during the shearing, and this tracking further gives the cumulative slip of each asperity. We find that the stick-slip behavior of the macroscopic fault, indicated by the temporal evolution of the shear force, can be well explained by the collective behavior of local asperities. Specifically, the unstable large-scale stick-slip events of the macroscopic fault with large shear force drops result from the synchronization of the rapid slips at all local asperities. Interestingly, many partial slips that are accompanied by small shear force drops, and consist of several to dozens of asperities that present a wide range of slip rates, while not destabilizing the strengthening of the whole interface, are observed during the interseismic phases. These partial slips are investigated by computing the interseismic coupling of each asperity. We find that the interseismic coupling is affected by the global normal load on a fault, the local normal stress caused by the interfacial topography, and the elastic interactions between asperities. Such characteristics are compatible with the observations along the subduction zones (Scholz & Campos, 2012; Vaca et al., 2018).

By considering the slip history of each asperity, a specific threshold is customized for each asperity to define the individual asperity slipping. We further cluster these individual asperity slipping in time and space scales as slip episodes to quantify the spatiotemporal interactions of asperities, which, for each experiment, enables generating a catalog that includes the average slip, effective rupture area, duration, and relative seismic moment of each slip episode. We find that these slip episodes are slow slip events by estimating the rupture speed and com-

paring it with the Rayleigh wave speed of the silicone block since it is the medium for the stress transfer between asperities. Our experimental evidence supports that the viscoelastic rheology of the complex fault zone could be an effective candidate for explaining the physical mechanism of the slow earthquakes observed worldwide (Behr et al., 2021; Fagereng et al., 2014). Our slip episodes also present the intermittent characteristic that has been reported for the slow slip events observed in subduction zones, in which a long-term slow slip event can be decomposed into several short-term slow slip events each acting for a limited duration (Frank et al., 2018).

Statistical analysis are also performed with these catalogs obtained at different loading conditions. We reproduce the magnitude-frequency distributions following a typical Gutenberg-Richter distribution where events with multiple sizes are observed. A best-resolved trend close to $M_0 \propto T$ is reproduced for the moment-duration scaling using all the catalogs, which is in agreement with the observations of slow earthquakes cataloged from multiple subduction zones (Ide & Beroza, 2023). Our slip episodes containing a cluster of slipping asperities induced by shearing also present an analogy to the low-frequency earthquakes as they are mainly thought to be small shear ruptures (Beroza & Ide, 2011; Ide, Shelly, & Beroza, 2007) occurring on small localized asperities within an aseismic sliding fault. These experimental slip episodes show a temporal decay similar to the low-frequency earthquakes that occurred in multiple natural faults (Lengliné et al., 2017). With the reproduction of these widely found scaling relations, the effective upscaling of our experimental results is also demonstrated.

Additionally, we identify numerous confined ruptures that account for a large part of our slip episodes. The stress drops of these confined events are computed in two different manners: one is from the direct measurement of shear force drop and the effective rupture area, and the other is inferred from the relative seismic moment and rupture length (Kanamori & Anderson, 1975). Both computations prove that the stress drop is independent on the nominal normal load that can be translated to the depth of natural faults, which supports the seismological observation of the depth-independent stress drop because most tectonic earthquakes are

confined ruptures in fault zones (Steinhardt et al., 2023).

To capture the seismic characteristics of dynamic ruptures that occurred during slow transients, acoustic monitoring is further coupled with the experimental setup. Acoustic events are automatically detected by the STA/LTA algorithm (Earle & Shearer, 1994) using the seismograms recorded in four channels. A good synchronization of the three measurements, which are the shear force on the macroscopic fault, the mean acoustic signal averaged over the four channels, and the mean cumulative slip averaged over all asperities, are achieved, where both the small-scale events with less shear force drops and the large-scale events accompanied by large shear force drops can be tracked by the mean acoustic signals with low amplitudes and small average cumulative slip and by the mean acoustic signals with high amplitudes and large average cumulative slip, respectively. Analyzing the detected acoustic events will be the next focus of our experimental work, which aims to better illustrate the link between the slow transients and the development of seismicity since the optical system can directly visualize the subtle motions of slow transients on the interface.

We attempt to develop a numerical model of the analog fault interface by establishing a modified two-dimensional Burridge-Knopoff model. This model is physically based on the analog model and the experimental setup. In detail, the viscoelastic interactions between discrete asperities are quantified through the Maxwell springs characterized by the silicone block's viscoelasticity. The friction of each asperity is governed by the rate and state frictional law (Marone, 1998b), and the empirical parameters including the direct effect a, evolution effect b, and critical slip distance D_c, are measured through the slide-hold-slide and velocity step experiments with a single-asperity interface. Besides, we are employing the pressure-sensitive film to measure the normal stress at each asperity under different nominal normal loads. We aim to use the modified two-dimensional Burridge-Knopoff model to reproduce the experimental results obtained before, after inputting all the realistic parameters directly constrained from the experimental measurements of the analog fault model. The resulting numerical model allows a complementary understanding of the effects of some fault parameters that

are not easy to control in the experiments on the fault slip behavior. For example, the viscoelasticity of the silicone block can be varied to numerically investigate the diffusive process of the experimental slip episodes, which is often observed in tremor migration in subduction zones (Ide, 2010) and fluid injection sites (Goebel & Brodsky, 2018) and is suspected to have a close relationship with the presence of fluid. Our numerical study will shed light on explaining the possible mechanism for the elusive diffusion phenomena of seismicity.

References

Aki, K. (1965). Maximum likelihood estimate of b in the formula log N= a-bM and its confidence limits. *Bull. Earthquake Res. Inst., Tokyo Univ.*, *43*, 237–239.

Aki, K., & Richards, P. G. (2002). *Quantitative Seismology*.

Alava, M. J., Nukala, P. K., & Zapperi, S. (2006). Statistical models of fracture. *Advances in Physics*, *55*(3-4), 349–476.

Albertini, G., Karrer, S., Grigoriu, M. D., & Kammer, D. S. (2021). Stochastic properties of static friction. *Journal of the Mechanics and Physics of Solids*, *147*, 104242.

Allam, A., Kroll, K., Milliner, C., & Richards-Dinger, K. (2019). Effects of fault roughness on coseismic slip and earthquake locations. *Journal of Geophysical Research: Solid Earth*, *124*(11), 11336–11349.

Allmann, B. P., & Shearer, P. M. (2007). Spatial and temporal stress drop variations in small earthquakes near parkfield, california. *Journal of Geophysical Research: Solid Earth*, *112*(B4).

Alwahedi, M. A., & Hawthorne, J. C. (2019). Intermediate-magnitude postseismic slip follows intermediate-magnitude (M 4 to 5) earthquakes in California. *Geophysical Research Letters*, *46*(7), 3676–3687.

Amitrano, D. (2003). Brittle-ductile transition and associated seismicity: Experimental and numerical studies and relationship with the b value. *Journal of Geophysical Research*, *108*(B1).

Ampuero, J.-P., & Dahlen, F. (2005). Ambiguity of the moment tensor. *Bulletin of the Seismological Society of America*, *95*(2), 390–400.

Ampuero, J.-P., & Rubin, A. M. (2008). Earthquake nucleation on rate and state faults–aging and slip laws. *Journal of Geophysical Research: Solid Earth*,

113(B1).

Ando, R., Nakata, R., & Hori, T. (2010). A slip pulse model with fault heterogeneity for low-frequency earthquakes and tremor along plate interfaces. *Geophysical Research Letters*, *37*(L10310).

Ando, R., Takeda, N., & Yamashita, T. (2012). Propagation dynamics of seismic and aseismic slip governed by fault heterogeneity and Newtonian rheology. *Journal of Geophysical Research*, *117*(B11308).

Ariyoshi, K., Hori, T., Ampuero, J.-P., Kaneda, Y., Matsuzawa, T., Hino, R., & Hasegawa, A. (2009). Influence of interaction between small asperities on various types of slow earthquakes in a 3-D simulation for a subduction plate boundary. *Gondwana Research*, *16*(3-4), 534–544.

Aslam, K. S., & Daub, E. G. (2018). Effect of fault roughness on aftershock distribution: Elastic off-fault material properties. *Journal of Geophysical Research: Solid Earth*, *123*(11), 9689–9711.

Aslam, K. S., & Daub, E. G. (2019). Effect of fault roughness on aftershock distribution: Plastic off-fault material properties. *Journal of Geophysical Research: Solid Earth*, *124*(7), 6989–7012.

Aubry, J., Passelègue, F., Escartín, J., Gasc, J., Deldicque, D., & Schubnel, A. (2020). Fault stability across the seismogenic zone. *Journal of Geophysical Research: Solid Earth*, *125*(8), e2020JB019670.

Barbot, S. (2019). Modulation of fault strength during the seismic cycle by grain-size evolution around contact junctions. *Tectonophysics*, *765*, 129–145.

Barbot, S., Lapusta, N., & Avouac, J.-P. (2012). Under the hood of the earthquake machine: Toward predictive modeling of the seismic cycle. *Science*, *336*(6082), 707–710.

Baumberger, T., & Caroli, C. (2006). Solid friction from stick–slip down to pinning and aging. *Advances in Physics*, *55*(3-4), 279–348.

Behr, W. M., & Bürgmann, R. (2021). What's down there? The structures, materials and environment of deep-seated slow slip and tremor. *Philosophical Transactions of the Royal Society A*, *379*(2193), 20200218.

Behr, W. M., Gerya, T. V., Cannizzaro, C., & Blass, R. (2021). Transient slow

slip characteristics of frictional-viscous subduction megathrust shear zones. *AGU Advances*, *2*(3), e2021AV000416.

Ben-David, O., Cohen, G., & Fineberg, J. (2010). The dynamics of the onset of frictional slip. *Science*, *330*(6001), 211–214.

Ben-David, O., Rubinstein, S. M., & Fineberg, J. (2010). Slip-stick and the evolution of frictional strength. *Nature*, *463*(7277), 76–79.

Ben-Zion, Y. (2012). Episodic tremor and slip on a frictional interface with critical zero weakening in elastic solid. *Geophysical Journal International*, *189*(2), 1159–1168.

Ben-Zion, Y., & Sammis, C. G. (2003). Characterization of fault zones. *Pure and Applied Geophysics*, *160*(3), 677–715.

Beroza, G. C., & Ide, S. (2011). Slow earthquakes and nonvolcanic tremor. *Annual Review of Earth and Planetary Sciences*, *39*, 271–296.

Berthoud, P., Baumberger, T., G'sell, C., & Hiver, J.-M. (1999). Physical analysis of the state-and rate-dependent friction law: Static friction. *Physical review B*, *59*(22), 14313.

Bhushan, B. (1998). Contact mechanics of rough surfaces in tribology: multiple asperity contact. *Tribology Letters*, *4*(1), 1–35.

Bolotskaya, E., & Hager, B. H. (2022). A 1d spring-slider model with a simple poly-linear failure law produces rich variations in slip behavior. *Bulletin of the Seismological Society of America*, *112*(6), 2795–2811.

Brace, W., & Byerlee, J. (1966). Stick-slip as a mechanism for earthquakes. *Science*, *153*(3739), 990–992.

Brener, E. A., Aldam, M., Barras, F., Molinari, J.-F., & Bouchbinder, E. (2018). Unstable slip pulses and earthquake nucleation as a nonequilibrium first-order phase transition. *Physical Review Letters*, *121*(23), 234302.

Bürgmann, R. (2018). The geophysics, geology and mechanics of slow fault slip. *Earth and Planetary Science Letters*, *495*, 112–134.

Bürgmann, R., Kogan, M. G., Steblov, G. M., Hilley, G., Levin, V. E., & Apel, E. (2005). Interseismic coupling and asperity distribution along the Kamchatka subduction zone. *Journal of Geophysical Research*, *110*(B07405).

Burridge, R., & Knopoff, L. (1967). Model and theoretical seismicity. *Bulletin of the Seismological Society of America*, *57*(3), 341–371.

Candela, T., Renard, F., Bouchon, M., Brouste, A., Marsan, D., Schmittbuhl, J., & Voisin, C. (2009). Characterization of fault roughness at various scales: Implications of three-dimensional high resolution topography measurements. *Pure and Applied Geophysics*, 1817–1851.

Candela, T., Renard, F., Klinger, Y., Mair, K., Schmittbuhl, J., & Brodsky, E. E. (2012). Roughness of fault surfaces over nine decades of length scales. *Journal of Geophysical Research*, *117*(B8), B08409.

Cao, T., & Aki, K. (1987). Seismicity simulation with a rate-and state-dependent friction law. *Friction and Faulting*, 487–513.

Carlson, J. (1991a). Time intervals between characteristic earthquakes and correlations with smaller events: An analysis based on a mechanical model of a fault. *Journal of Geophysical Research*, *96*(B3), 4255–4267.

Carlson, J. (1991b). Two-dimensional model of a fault. *Physical Review A*, *44*(10), 6226.

Carlson, J., & Langer, J. (1989). Mechanical model of an earthquake fault. *Physical Review A*, *40*(11), 6470.

Carlson, J. M., & Langer, J. (1989). Properties of earthquakes generated by fault dynamics. *Physical Review Letters*, *62*(22), 2632.

Carlson, J. M., Langer, J. S., & Shaw, B. E. (1994). Dynamics of earthquake faults. *Reviews of Modern Physics*, *66*(2), 657.

Carlson, J. M., Langer, J. S., Shaw, B. E., & Tang, C. (1991). Intrinsic properties of a burridge-knopoff model of an earthquake fault. *Physical Review A*, *44*(2), 884.

Cattania, C., & Segall, P. (2021). Precursory slow slip and foreshocks on rough faults. *Journal of Geophysical Research: Solid Earth*, *126*(4), e2020JB020430.

Cebry, S. B., Sorhaindo, K., & McLaskey, G. C. (2023). Laboratory earthquake rupture interactions with a high normal stress bump. *Journal of Geophysical Research: Solid Earth*, *128*(11), e2023JB027297.

Chen, X., Carpenter, B. M., & Reches, Z. (2020). Asperity failure control of stick–slip along brittle faults. *Pure and Applied Geophysics*, *177*, 3225–3242.

Chester, F. M., & Chester, J. S. (1998). Ultracataclasite structure and friction processes of the Punchbowl fault, San Andreas system, California. *Tectonophysics*, *295*(1-2), 199–221.

Chester, F. M., Evans, J. P., & Biegel, R. L. (1993). Internal structure and weakening mechanisms of the San Andreas fault. *Journal of Geophysical Research*, *98*(B1), 771–786.

Cocco, M., Aretusini, S., Cornelio, C., Nielsen, S. B., Spagnuolo, E., Tinti, E., & Di Toro, G. (2023). Fracture energy and breakdown work during earthquakes. *Annual Review of Earth and Planetary Sciences*, *51*.

Corbi, F., Funiciello, F., Brizzi, S., Lallemand, S., & Rosenau, M. (2017). Control of asperities size and spacing on seismic behavior of subduction megathrusts. *Geophysical Research Letters*, *44*(16), 8227–8235.

Cornet, F. H. (2016). Seismic and aseismic motions generated by fluid injections. *Geomechanics for Energy and the Environment*, *5*, 42–54.

Daub, E. G., Shelly, D. R., Guyer, R. A., & Johnson, P. A. (2011). Brittle and ductile friction and the physics of tectonic tremor. *Geophysical Research Letters*, *38*(10).

Davies, E. R. (2005). *Machine vision: theory, algorithms, practicalities*. Elsevier.

de Geus, T. W., Popović, M., Ji, W., Rosso, A., & Wyart, M. (2019). How collective asperity detachments nucleate slip at frictional interfaces. *Proceedings of the National Academy of Sciences*, *116*(48), 23977–23983.

Denolle, M. A., & Shearer, P. M. (2016). New perspectives on self-similarity for shallow thrust earthquakes. *Journal of Geophysical Research: Solid Earth*, *121*(9), 6533–6565.

Dieterich, J. H. (1978). Time-dependent friction and the mechanics of stick-slip. *Rock Friction and Earthquake Prediction*, 790–806.

Dieterich, J. H. (1979). Modeling of rock friction: 1. Experimental results and constitutive equations. *Journal of Geophysical Research*, *84*(B5), 2161–2168.

Dieterich, J. H. (1992). Earthquake nucleation on faults with rate-and state-

dependent strength. *Tectonophysics*, *211*(1-4), 115–134.

Dieterich, J. H., & Kilgore, B. D. (1994). Direct observation of frictional contacts: New insights for state-dependent properties. *Pure and Applied Geophysics*, *143*(1), 283–302.

Ding, X., Xu, S., Xie, Y., van den Ende, M., Premus, J., & Ampuero, J.-P. (2023). The sharp turn: Backward rupture branching during the 2023 Mw 7.8 Kahramanmaraş (Türkiye) earthquake. *Seismica*, *2*(3).

Dragert, H., Wang, K., & James, T. S. (2001). A silent slip event on the deeper Cascadia subduction interface. *Science*, *292*(5521), 1525–1528.

Dresen, G., Kwiatek, G., Goebel, T., & Ben-Zion, Y. (2020). Seismic and aseismic preparatory processes before large stick–slip failure. *Pure and Applied Geophysics*, *177*(12), 5741–5760.

Dublanchet, P., Bernard, P., & Favreau, P. (2013). Interactions and triggering in a 3-D rate-and-state asperity model. *Journal of Geophysical Research: Solid Earth*, *118*(5), 2225–2245.

Earle, P. S., & Shearer, P. M. (1994). Characterization of global seismograms using an automatic-picking algorithm. *Bulletin of the Seismological Society of America*, *84*(2), 366–376.

Ellsworth, W., & Beroza, G. (1995). Seismic evidence for an earthquake nucleation phase. *Science*, *268*(5212), 851–855.

Engelder, J. T. (1974). Cataclasis and the generation of fault gouge. *Geological Society of America Bulletin*, *85*(10), 1515–1522.

Erickson, B., Birnir, B., & Lavallée, D. (2008). A model for aperiodicity in earthquakes. *Nonlinear Processes in Geophysics*, *15*(1), 1–12.

Fagereng, Å., & Beall, A. (2021). Is complex fault zone behaviour a reflection of rheological heterogeneity? *Philosophical Transactions of the Royal Society A*, *379*(2193), 20190421.

Fagereng, Å., Hillary, G. W., & Diener, J. F. (2014). Brittle-viscous deformation, slow slip, and tremor. *Geophysical Research Letters*, *41*(12), 4159–4167.

Fagereng, Å., & Toy, V. G. (2011). Geology of the earthquake source: an introduction. *Geological Society, London, Special Publications*, *359*(1), 1–16.

Faulkner, D., Lewis, A., & Rutter, E. (2003). On the internal structure and mechanics of large strike-slip fault zones: field observations of the Carboneras fault in southeastern Spain. *Tectonophysics*, *367*(3-4), 235–251.

Fisher, D. S., Dahmen, K., Ramanathan, S., & Ben-Zion, Y. (1997). Statistics of earthquakes in simple models of heterogeneous faults. *Physical Review Letters*, *78*(25), 4885.

Fontiela, J., Rosset, P., Wyss, M., Bezzeghoud, M., Borges, J., & Cota Rodrigues, F. (2020). Human Losses and Damage Expected in Future Earthquakes on Faial Island–Azores. *Pure and Applied Geophysics*, *177*(4), 1831–1844.

Fortune, S. (1995). Voronoi diagrams and Delaunay triangulations. *Computing in Euclidean Geometry*, 225–265.

Frank, W. B. (2016). Slow slip hidden in the noise: The intermittence of tectonic release. *Geophysical Research Letters*, *43*(19), 10–125.

Frank, W. B., & Brodsky, E. E. (2019). Daily measurement of slow slip from low-frequency earthquakes is consistent with ordinary earthquake scaling. *Science Advances*, *5*(10), eaaw9386.

Frank, W. B., Rousset, B., Lasserre, C., & Campillo, M. (2018). Revealing the cluster of slow transients behind a large slow slip event. *Science advances*, *4*(5), eaat0661.

Freymueller, J. T., Suleimani, E. N., & Nicolsky, D. J. (2021). Constraints on the slip distribution of the 1938 MW 8.3 Alaska peninsula earthquake from tsunami modeling. *Geophysical Research Letters*, *48*(9), e2021GL092812.

Fryer, B., Giorgetti, C., Passelègue, F., Momeni, S., Lecampion, B., & Violay, M. (2022). The influence of roughness on experimental fault mechanical behavior and associated microseismicity. *Journal of Geophysical Research: Solid Earth*, *127*(8), e2022JB025113.

Gan, G., Ma, C., & Wu, J. (2020). *Data clustering: theory, algorithms, and applications*. SIAM.

Gao, H., Schmidt, D. A., & Weldon, R. J. (2012). Scaling relationships of source parameters for slow slip events. *Bulletin of the Seismological Society of America*, *102*(1), 352–360.

Gent, A. N. (1958). On the relation between indentation hardness and Young's modulus. *Rubber Chemistry and Technology*, *31*(4), 896–906.

Goebel, T. H., & Brodsky, E. E. (2018). The spatial footprint of injection wells in a global compilation of induced earthquake sequences. *Science*, *361*(6405), 899–904.

Goebel, T. H., Brodsky, E. E., & Dresen, G. (2023). Fault roughness promotes earthquake-like aftershock clustering in the lab. *Geophysical Research Letters*, *50*(8), e2022GL101241.

Goebel, T. H., Kwiatek, G., Becker, T. W., Brodsky, E. E., & Dresen, G. (2017). What allows seismic events to grow big?: Insights from b-value and fault roughness analysis in laboratory stick-slip experiments. *Geology*, *45*(9), 815–818.

Gu, J.-C., Rice, J. R., Ruina, A. L., & Simon, T. T. (1984). Slip motion and stability of a single degree of freedom elastic system with rate and state dependent friction. *Journal of the Mechanics and Physics of Solids*, *32*(3), 167–196.

Guérin-Marthe, S., Kwiatek, G., Wang, L., Bonnelye, A., Martínez-Garzón, P., & Dresen, G. (2023). Preparatory slip in laboratory faults: Effects of roughness and load point velocity. *Journal of Geophysical Research: Solid Earth*, e2022JB025511.

Guglielmi, Y., Cappa, F., Avouac, J.-P., Henry, P., & Elsworth, D. (2015). Seismicity triggered by fluid injection–induced aseismic slip. *Science*, *348*(6240), 1224–1226.

Gutenberg, B., & Richter, C. F. (1944). Frequency of earthquakes in California. *Bulletin of the Seismological Society of America*, *34*(4), 185–188.

Gvirtzman, S., & Fineberg, J. (2021). Nucleation fronts ignite the interface rupture that initiates frictional motion. *Nature Physics*, *17*(9), 1037–1042.

Hanks, T. C., & Kanamori, H. (1979). A moment magnitude scale. *Journal of Geophysical Research*, *84*(B5), 2348–2350.

Hansen, A., Schmittbuhl, J., Batrouni, G. G., & de Oliveira, F. A. (2000). Normal stress distribution of rough surfaces in contact. *Geophysical research letters*,

27(22), 3639–3642.

Harbord, C. W., Nielsen, S. B., De Paola, N., & Holdsworth, R. E. (2017). Earthquake nucleation on rough faults. *Geology*, *45*(10), 931–934.

Hawthorne, J. C., & Rubin, A. M. (2013). Laterally propagating slow slip events in a rate and state friction model with a velocity-weakening to velocity-strengthening transition. *Journal of Geophysical Research: Solid Earth*, *118*(7), 3785–3808.

Hirose, H., & Obara, K. (2010). Recurrence behavior of short-term slow slip and correlated nonvolcanic tremor episodes in western Shikoku, southwest Japan. *Journal of Geophysical Research: Solid Earth*, *115*(B6).

Hyndman, R. D., Yamano, M., & Oleskevich, D. A. (1997). The seismogenic zone of subduction thrust faults. *Island Arc*, *6*(3), 244–260.

Ide, S. (2008). A Brownian walk model for slow earthquakes. *Geophysical Research Letters*, *35*(17).

Ide, S. (2010). Striations, duration, migration and tidal response in deep tremor. *Nature*, *466*(7304), 356–359.

Ide, S., & Beroza, G. C. (2023). Slow earthquake scaling reconsidered as a boundary between distinct modes of rupture propagation. *Proceedings of the National Academy of Sciences*, *120*(32), e2222102120.

Ide, S., Beroza, G. C., Shelly, D. R., & Uchide, T. (2007). A scaling law for slow earthquakes. *Nature*, *447*(7140), 76–79.

Ide, S., Imanishi, K., Yoshida, Y., Beroza, G. C., & Shelly, D. R. (2008). Bridging the gap between seismically and geodetically detected slow earthquakes. *Geophysical Research Letters*, *35*(10).

Ide, S., Shelly, D. R., & Beroza, G. C. (2007). Mechanism of deep low frequency earthquakes: Further evidence that deep non-volcanic tremor is generated by shear slip on the plate interface. *Geophysical Research Letters*, *34*(3).

Ide, S., & Yabe, S. (2019). Two-dimensional probabilistic cell automaton model for broadband slow earthquakes. *Pure and Applied Geophysics*, *176*, 1021–1036.

Igarashi, T. (2020). Catalog of small repeating earthquakes for the Japanese Islands. *Earth, Planets and Space*, *72*(1), 1–8.

Ito, Y., Obara, K., Shiomi, K., Sekine, S., & Hirose, H. (2007). Slow earthquakes coincident with episodic tremors and slow slip events. *Science*, *315*(5811), 503–506.

Jestin, C., Lengliné, O., & Schmittbuhl, J. (2019). Energy partitioning during subcritical mode I crack propagation through a heterogeneous interface. *Journal of Geophysical Research: Solid Earth*, *124*(1), 837–855.

Jia, Z., Jin, Z., Marchandon, M., Ulrich, T., Gabriel, A.-A., Fan, W., ... others (2023). The complex dynamics of the 2023 Kahramanmaraş, Turkey, Mw 7.8-7.7 earthquake doublet. *Science*, *381*(6661), 985–990.

Johnson, K. (1987). *Contact Mechanics*. Cambridge University Press.

Johnson, L. (2010). An earthquake model with interacting asperities. *Geophysical Journal International*, *182*(3), 1339–1373.

Johnson, L. R., & Nadeau, R. M. (2002). Asperity model of an earthquake: Static problem. *Bulletin of the Seismological Society of America*, *92*(2), 672–686.

Jolivet, R., Candela, T., Lasserre, C., Renard, F., Klinger, Y., & Doin, M.-P. (2015). The Burst-Like Behavior of Aseismic Slip on a Rough Fault: The Creeping Section of the Haiyuan Fault, China. *Bulletin of the Seismological Society of America*, *105*(1), 480–488.

Jolivet, R., Lasserre, C., Doin, M.-P., Peltzer, G., Avouac, J.-P., Sun, J., & Dailu, R. (2013). Spatio-temporal evolution of aseismic slip along the Haiyuan fault, China: Implications for fault frictional properties. *Earth and Planetary Science Letters*, *377*, 23–33.

Kamali-Asl, A., Kc, B., Foroutan, M., Ghazanfari, E., Cladouhos, T. T., & Stevens, M. (2019). Stress-strain response and seismic signature analysis of phyllite reservoir rocks from blue mountain geothermal field. *Geothermics*, *77*, 204–223.

Kammer, D. S., Radiguet, M., Ampuero, J.-P., & Molinari, J.-F. (2015). Linear elastic fracture mechanics predicts the propagation distance of frictional slip. *Tribology Letters*, *57*(3), 1–10.

Kanamori, H., & Anderson, D. L. (1975). Theoretical basis of some empirical relations in seismology. *Bulletin of the Seismological Society of America*,

65(5), 1073–1095.

Kano, M., Fukuda, J., Miyazaki, S., & Nakamura, M. (2018). Spatiotemporal evolution of recurrent slow slip events along the southern Ryukyu subduction zone, Japan, from 2010 to 2013. *Journal of Geophysical Research: Solid Earth*, *123*(8), 7090–7107.

Karner, S. L., & Marone, C. (2000). Effects of loading rate and normal stress on stress drop and stick-slip recurrence interval. *Geocomplexity and the Physics of Earthquakes*, *120*, 187–198.

Kato, A., Obara, K., Igarashi, T., Tsuruoka, H., Nakagawa, S., & Hirata, N. (2012). Propagation of slow slip leading up to the 2011 Mw 9.0 Tohoku-Oki earthquake. *Science*, *335*(6069), 705–708.

Kawamura, H., Ueda, Y., Kakui, S., Morimoto, S., & Yamamoto, T. (2017). Statistical properties of the one-dimensional burridge-knopoff model of earthquakes obeying the rate-and state-dependent friction law. *Physical Review E*, *95*(4), 042122.

Kawamura, H., Yoshimura, K., & Kakui, S. (2019). Nature of the high-speed rupture of the two-dimensional Burridge–Knopoff model of earthquakes. *Philosophical Transactions of the Royal Society A*, *377*(2136), 20170391.

Khoshmanesh, M., & Shirzaei, M. (2018). Multiscale dynamics of aseismic slip on Central San Andreas Fault. *Geophysical Research Letters*, *45*(5), 2274–2282.

Kirkpatrick, J. D., Fagereng, Å., & Shelly, D. R. (2021). Geological constraints on the mechanisms of slow earthquakes. *Nature Reviews Earth & Environment*, *2*(4), 285–301.

Kodaira, S., Fujiwara, T., Fujie, G., Nakamura, Y., & Kanamatsu, T. (2020). Large coseismic slip to the trench during the 2011 Tohoku-Oki earthquake. *Annual Review of Earth and Planetary Sciences*, *48*, 321–343.

Kodaira, S., Iinuma, T., & Imai, K. (2021). Investigating a tsunamigenic megathrust earthquake in the Japan Trench. *Science*, *371*(6534), eabe1169.

Kwiatek, G., Martínez-Garzón, P., Becker, D., Dresen, G., Cotton, F., Beroza, G., ... Bohnhoff, M. (2023). Months-long seismicity transients preceding the 2023 MW 7.8 Kahramanmaraş earthquake, Türkiye. *Nature Communi-*

cations, *14*(1), 1–10.

Lapusta, N., Rice, J. R., Ben-Zion, Y., & Zheng, G. (2000). Elastodynamic analysis for slow tectonic loading with spontaneous rupture episodes on faults with rate-and state-dependent friction. *Journal of Geophysical Research: Solid Earth*, *105*(B10), 23765–23789.

Lay, T. (2015). The surge of great earthquakes from 2004 to 2014. *Earth and Planetary Science Letters*, *409*, 133–146.

Lay, T. (2018). A review of the rupture characteristics of the 2011 Tohoku-oki Mw 9.1 earthquake. *Tectonophysics*, *733*, 4–36.

Lay, T., & Kanamori, H. (1981). An asperity model of large earthquake sequences. *Earthquake Prediction: An International Review*, *4*, 579–592.

Lay, T., Kanamori, H., Ammon, C. J., Koper, K. D., Hutko, A. R., Ye, L., . . . Rushing, T. M. (2012). Depth-varying rupture properties of subduction zone megathrust faults. *Journal of Geophysical Research: Solid Earth*, *117*(B4).

Lay, T., Kanamori, H., & Ruff, L. (1982). The asperity model and the nature of large subduction zone earthquakes. *Earthquake Prediction Research*, *1*, 3–71.

Lay, T., & Nishenko, S. P. (2022). Updated concepts of seismic gaps and asperities to assess great earthquake hazard along South America. *Proceedings of the National Academy of Sciences*, *119*(51), e2216843119.

Lee, D.-T., & Schachter, B. J. (1980). Two algorithms for constructing a Delaunay triangulation. *International Journal of Computer & Information Sciences*, *9*(3), 219–242.

Lee, S.-J., Huang, B.-S., Ando, M., Chiu, H.-C., & Wang, J.-H. (2011). Evidence of large scale repeating slip during the 2011 Tohoku-Oki earthquake. *Geophysical Research Letters*, *38*(19).

Leeman, J., Saffer, D., Scuderi, M., & Marone, C. (2016). Laboratory observations of slow earthquakes and the spectrum of tectonic fault slip modes. *Nature Communications*, *7*(1), 1–6.

Lehmann, G., & Legland, D. (2012). Efficient n-dimensional surface estimation using crofton formula and run-length encoding. *Kitware INC*.

Lengliné, O., Elkhoury, J., Daniel, G., Schmittbuhl, J., Toussaint, R., Ampuero, J.-P., & Bouchon, M. (2012). Interplay of seismic and aseismic deformations during earthquake swarms: An experimental approach. *Earth and Planetary Science Letters*, *331*, 215–223.

Lengliné, O., Frank, W. B., Marsan, D., & Ampuero, J.-P. (2017). Imbricated slip rate processes during slow slip transients imaged by low-frequency earthquakes. *Earth and Planetary Science Letters*, *476*, 122–131.

Li, T., & Rubin, A. M. (2017). A microscopic model of rate and state friction evolution. *Journal of Geophysical Research: Solid Earth*, *122*(8), 6431–6453.

Lovery, B., Chlieh, M., Norabuena, E., Villegas-Lanza, J., Radiguet, M., Cotte, N., ... others (2024). Heterogeneous locking and earthquake potential on the south peru megathrust from dense gnss network. *Journal of Geophysical Research: Solid Earth*, *129*(2), e2023JB027114.

Luo, Y., & Ampuero, J.-P. (2018). Stability of faults with heterogeneous friction properties and effective normal stress. *Tectonophysics*, *733*, 257–272.

Luo, Y., Ampuero, J. P., Galvez, P., van den Ende, M., & Idini, B. (2017). Qdyn: a quasi-dynamic earthquake simulator (v1. 1). *Zenodo*.

Luo, Y., & Liu, Z. (2019). Rate-and-state model casts new insight into episodic tremor and slow-slip variability in cascadia. *Geophysical Research Letters*, *46*(12), 6352–6362.

Luo, Y., & Liu, Z. (2021). Fault zone heterogeneities explain depth-dependent pattern and evolution of slow earthquakes in Cascadia. *Nature communications*, *12*(1), 1–13.

Madariaga, R. (1998). Complex heterogeneous faulting models. *SMR*, *1059*, 22.

Marone, C. (1998a). The effect of loading rate on static friction and the rate of fault healing during the earthquake cycle. *Nature*, *391*(6662), 69–72.

Marone, C. (1998b). Laboratory-derived friction laws and their application to seismic faulting. *Annual Review of Earth and Planetary Sciences*, *26*(1), 643–696.

Matsuzawa, T., Igarashi, T., & Hasegawa, A. (2002). Characteristic small-earthquake sequence off Sanriku, northeastern Honshu, Japan. *Geophysical*

Research Letters, *29*(11), 38–1.

McLaskey, G. C. (2019). Earthquake initiation from laboratory observations and implications for foreshocks. *Journal of Geophysical Research: Solid Earth*, *124*(12), 12882–12904.

McLaskey, G. C., & Glaser, S. D. (2011). Micromechanics of asperity rupture during laboratory stick slip experiments. *Geophysical Research Letters*, *38*(12), L12302.

McLaskey, G. C., Thomas, A. M., Glaser, S. D., & Nadeau, R. M. (2012). Fault healing promotes high-frequency earthquakes in laboratory experiments and on natural faults. *Nature*, *491*, 101–104.

McLoughlin, J., & Tobolsky, A. (1952). The viscoelastic behavior of polymethyl methacrylate. *Journal of Colloid Science*, *7*(6), 555–568.

Mitchell, T., & Faulkner, D. (2009). The nature and origin of off-fault damage surrounding strike-slip fault zones with a wide range of displacements: A field study from the Atacama fault system, northern Chile. *Journal of Structural Geology*, *31*(8), 802–816.

Molina-Ormazabal, D., Ampuero, J.-P., & Tassara, A. (2023). Diverse slip behaviour of velocity-weakening fault barriers. *Nature Geoscience*, 1–8.

Morad, D., Sagy, A., Tal, Y., & Hatzor, Y. H. (2022). Fault roughness controls sliding instability. *Earth and Planetary Science Letters*, *579*, 117365.

Moreno, M. S., Bolte, J., Klotz, J., & Melnick, D. (2009). Impact of megathrust geometry on inversion of coseismic slip from geodetic data: Application to the 1960 Chile earthquake. *Geophysical Research Letters*, *36*(L16310).

Mori, T., & Kawamura, H. (2008). Simulation study of the two-dimensional burridge-knopoff model of earthquakes. *Journal of Geophysical Research: Solid Earth*, *113*(B6).

Myers, C. R., & Langer, J. (1993). Rupture propagation, dynamical front selection, and the role of small length scales in a model of an earthquake fault. *Physical Review E*, *47*(5), 3048.

Myers, C. R., Shaw, B. E., & Langer, J. S. (1996). Slip complexity in a crustal-plane model of an earthquake fault. *Physical Review Letters*, *77*(5), 972.

Nadeau, R. M., & Johnson, L. R. (1998). Seismological studies at Parkfield VI: Moment release rates and estimates of source parameters for small repeating earthquakes. *Bulletin of the Seismological Society of America*, *88*(3), 790–814.

Nadeau, R. M., & McEvilly, T. V. (1999). Fault slip rates at depth from recurrence intervals of repeating microearthquakes. *Science*, *285*(5428), 718–721.

Nakata, R., Ando, R., Hori, T., & Ide, S. (2011). Generation mechanism of slow earthquakes: Numerical analysis based on a dynamic model with brittle-ductile mixed fault heterogeneity. *Journal of Geophysical Research*, *116*(B08308).

Nasuno, S., Kudrolli, A., Bak, A., & Gollub, J. P. (1998). Time-resolved studies of stick-slip friction in sheared granular layers. *Physical Review E*, *58*(2), 2161–2171.

Nishikawa, T., Ide, S., & Nishimura, T. (2023). A review on slow earthquakes in the Japan Trench. *Progress in Earth and Planetary Science*, *10*(1), 1–51.

Obara, K. (2020). Characteristic activities of slow earthquakes in Japan. *Proceedings of the Japan Academy, Series B*, *96*(7), 297–315.

Obara, K., & Kato, A. (2016). Connecting slow earthquakes to huge earthquakes. *Science*, *353*(6296), 253–257.

Ohmura, A., & Kawamura, H. (2007). Rate-and state-dependent friction law and statistical properties of earthquakes. *Europhysics Letters*, *77*(6), 69001.

Okubo, P. G. (1989). Dynamic rupture modeling with laboratory-derived constitutive relations. *Journal of Geophysical Research: Solid Earth*, *94*(B9), 12321–12335.

Okubo, P. G., & Dieterich, J. H. (1984). Effects of physical fault properties on frictional instabilities produced on simulated faults. *Journal of Geophysical Research*, *89*(B7), 5817–5827.

Ozawa, S. W., Hatano, T., & Kame, N. (2019). Longer migration and spontaneous decay of aseismic slip pulse caused by fault roughness. *Geophysical Research Letters*, *46*(2), 636–643.

Park, J. S., Lee, S. M., Joo, B. S., & Jang, H. (2017). The effect of material

properties on the stick–slip behavior of polymers: A case study with pmma, pc, ptfe, and pvc. *Wear*, *378*, 11–16.

Peng, Z., & Gomberg, J. (2010). An integrated perspective of the continuum between earthquakes and slow-slip phenomena. *Nature Geoscience*, *3*(9), 599–607.

Perfettini, H., & Avouac, J.-P. (2007). Modeling afterslip and aftershocks following the 1992 Landers earthquake. *Journal of Geophysical Research: Solid Earth*, *112*(B7).

Perfettini, H., Avouac, J.-P., Tavera, H., Kositsky, A., Nocquet, J.-M., Bondoux, F., . . . others (2010). Seismic and aseismic slip on the Central Peru megathrust. *Nature*, *465*(7294), 78–81.

Perfettini, H., Schmittbuhl, J., & Vilotte, J.-P. (2001). Slip correlations on a creeping fault. *Geophysical Research Letters*, *28*(10), 2137–2140.

Pohrt, R., & Popov, V. L. (2012). Normal contact stiffness of elastic solids with fractal rough surfaces. *Physical Review Letters*, *108*(10), 104301.

Power, W., Tullis, T., Brown, S., Boitnott, G., & Scholz, C. (1987). Roughness of natural fault surfaces. *Geophysical Research Letters*, *14*(1), 29–32.

Radiguet, M., Perfettini, H., Cotte, N., Gualandi, A., Valette, B., Kostoglodov, V., . . . Campillo, M. (2016). Triggering of the 2014 Mw 7.3 Papanoa earthquake by a slow slip event in Guerrero, Mexico. *Nature Geoscience*, *9*(11), 829–833.

Reid, H. (1911). The elastic-rebound theory of earthquakes. *Univ. California Publ. Bull. Dept. Geol.*, *6*, 413–444.

Rice, J. R. (1993). Spatio-temporal complexity of slip on a fault. *Journal of Geophysical Research*, *98*(B6), 9885–9907.

Rivière, J., Lv, Z., Johnson, P., & Marone, C. (2018). Evolution of b-value during the seismic cycle: Insights from laboratory experiments on simulated faults. *Earth and Planetary Science Letters*, *482*, 407–413.

Rogers, G., & Dragert, H. (2003). Episodic tremor and slip on the Cascadia subduction zone: The chatter of silent slip. *Science*, *300*(5627), 1942–1943.

Romanet, P., Bhat, H. S., Jolivet, R., & Madariaga, R. (2018). Fast and slow slip events emerge due to fault geometrical complexity. *Geophysical Research*

Letters, *45*(10), 4809–4819.

Rousset, B., Jolivet, R., Simons, M., Lasserre, C., Riel, B., Milillo, P., ... Renard, F. (2016). An aseismic slip transient on the North Anatolian Fault. *Geophysical Research Letters*, *43*(7), 3254–3262.

Rowe, C. D., & Griffith, W. A. (2015). Do faults preserve a record of seismic slip: A second opinion. *Journal of Structural Geology*, *78*, 1–26.

Rubin, A. M., & Ampuero, J.-P. (2005). Earthquake nucleation on (aging) rate and state faults. *Journal of Geophysical Research: Solid Earth*, *110*(B11).

Rubinstein, S. M., Cohen, G., & Fineberg, J. (2004). Detachment fronts and the onset of dynamic friction. *Nature*, *430*(7003), 1005–1009.

Ruff, L., & Kanamori, H. (1983). The rupture process and asperity distribution of three great earthquakes from long-period diffracted P-waves. *Physics of the Earth and Planetary Interiors*, *31*(3), 202–230.

Ruina, A. (1983). Slip instability and state variable friction laws. *Journal of Geophysical Research*, *88*(B12), 10359–10370.

Ruiz, S., Metois, M., Fuenzalida, A., Ruiz, J., Leyton, F., Grandin, R., ... Campos, J. (2014). Intense foreshocks and a slow slip event preceded the 2014 Iquique Mw 8.1 earthquake. *Science*, *345*(6201), 1165–1169.

Saffer, D. M., & Wallace, L. M. (2015). The frictional, hydrologic, metamorphic and thermal habitat of shallow slow earthquakes. *Nature Geoscience*, *8*(8), 594–600.

Schmittbuhl, J., Chambon, G., Hansen, A., & Bouchon, M. (2006). Are stress distributions along faults the signature of asperity squeeze? *Geophysical Research Letters*, *33*(13).

Schmittbuhl, J., Gentier, S., & Roux, S. (1993). Field measurements of the roughness of fault surfaces. *Geophysical Research Letters*, *20*(8), 639–641.

Schmittbuhl, J., & Måløy, K. J. (1997). Direct observation of a self-affine crack propagation. *Physical Review Letters*, *78*(20), 3888–3891.

Schmittbuhl, J., Schmitt, F., & Scholz, C. (1995). Scaling invariance of crack surfaces. *Journal of Geophysical Research*, *100*(B4), 5953–5973.

Schmittbuhl, J., Vilotte, J.-P., & Roux, S. (1993). Propagative macrodislocation

modes in an earthquake fault model. *Europhysics letters*, *21*(3), 375.

Schmittbuhl, J., Vilotte, J.-P., & Roux, S. (1996). A dissipation-based analysis of an earthquake fault model. *Journal of Geophysical Research*, *101*(B12), 27741–27764.

Scholz, C. (1998). Earthquakes and friction laws. *Nature*, *391*(6662), 37–42.

Scholz, C. (2015). On the stress dependence of the earthquake b value. *Geophysical Research Letters*, *42*(5), 1399–1402.

Scholz, C. (2019). *The mechanics of earthquakes and faulting*. Cambridge University Press.

Scholz, C., & Campos, J. (1995). On the mechanism of seismic decoupling and back arc spreading at subduction zones. *Journal of Geophysical Research*, *100*(B11), 22103–22115.

Scholz, C., & Campos, J. (2012). The seismic coupling of subduction zones revisited. *Journal of Geophysical Research*, *117*(B05310).

Schulz, S. E., & Evans, J. P. (2000). Mesoscopic structure of the Punchbowl Fault, Southern California and the geologic and geophysical structure of active strike-slip faults. *Journal of Structural Geology*, *22*(7), 913–930.

Scuderi, M., Collettini, C., & Marone, C. (2017). Frictional stability and earthquake triggering during fluid pressure stimulation of an experimental fault. *Earth and Planetary Science Letters*, *477*, 84–96.

Scuderi, M., Marone, C., Tinti, E., Di Stefano, G., & Collettini, C. (2016). Precursory changes in seismic velocity for the spectrum of earthquake failure modes. *Nature Geoscience*, *9*(9), 695–700.

Selvadurai, P. A. (2019). Laboratory insight into seismic estimates of energy partitioning during dynamic rupture: An observable scaling breakdown. *Journal of Geophysical Research: Solid Earth*, *124*(11), 11350–11379.

Selvadurai, P. A., Galvez, P., Mai, P. M., & Glaser, S. D. (2023). Modeling frictional precursory phenomena using a wear-based rate-and state-dependent friction model in the laboratory. *Tectonophysics*, *847*, 229689.

Selvadurai, P. A., & Glaser, S. D. (2015a). Laboratory-developed contact models controlling instability on frictional faults. *Journal of Geophysical Research:*

Solid Earth, *120*(6), 4208–4236.

Selvadurai, P. A., & Glaser, S. D. (2015b). Novel monitoring techniques for characterizing frictional interfaces in the laboratory. *Sensors*, *15*(5), 9791–9814.

Selvadurai, P. A., & Glaser, S. D. (2017). Asperity generation and its relationship to seismicity on a planar fault: A laboratory simulation. *Geophysical Journal International*, *208*(2), 1009–1025.

Shampine, L. F., & Reichelt, M. W. (1997). The matlab ode suite. *SIAM Journal on Scientific Computing*, *18*(1), 1–22.

Shampine, L. F., Reichelt, M. W., & Kierzenka, J. A. (1999). Solving index-1 DAEs in MATLAB and Simulink. *SIAM Review*, *41*(3), 538–552.

Shaw, B. E. (1994). Complexity in a spatially uniform continuum fault model. *Geophysical Research Letters*, *21*(18), 1983–1986.

Shaw, B. E., Carlson, J. M., & Langer, J. S. (1992). Patterns of seismic activity preceding large earthquakes. *Journal of Geophysical Research*, *97*(B1), 479–488.

Shelly, D. R., Beroza, G. C., & Ide, S. (2007). Non-volcanic tremor and low-frequency earthquake swarms. *Nature*, *446*(7133), 305–307.

Shu, W., Lengliné, O., & Schmittbuhl, J. (2023). Collective behavior of asperities before large stick-slip events. *Journal of Geophysical Research: Solid Earth*, *128*(9), e2023JB026696.

Sibson, R. H. (1986). Brecciation processes in fault zones: inferences from earthquake rupturing. *Pure and Applied Geophysics*, *124*, 159–175.

Socquet, A., Valdes, J. P., Jara, J., Cotton, F., Walpersdorf, A., Cotte, N., … Norabuena, E. (2017). An 8 month slow slip event triggers progressive nucleation of the 2014 Chile megathrust. *Geophysical Research Letters*, *44*(9), 4046–4053.

Steinhardt, W., Dillavou, S., Agajanian, M., Rubinstein, S. M., & Brodsky, E. E. (2023). Seismological stress drops for confined ruptures are invariant to normal stress. *Geophysical Research Letters*, *50*(9), e2022GL101366.

Stierman, D. J. (1984). Geophysical and geological evidence for fracturing, water

circulation and chemical alteration in granitic rocks adjacent to major strike-slip faults. *Journal of Geophysical Research*, *89*(B7), 5849–5857.

Stormo, A., Lengliné, O., Schmittbuhl, J., & Hansen, A. (2016). Soft-clamp fiber bundle model and interfacial crack propagation: Comparison using a non-linear imposed displacement. *Frontiers in Physics*, *4*, 18.

Subarya, C., Chlieh, M., Prawirodirdjo, L., Avouac, J.-P., Bock, Y., Sieh, K., . . . McCaffrey, R. (2006). Plate-boundary deformation associated with the great Sumatra–Andaman earthquake. *Nature*, *440*(7080), 46–51.

Sutton, M. A., Orteu, J. J., & Schreier, H. (2009). *Image correlation for shape, motion and deformation measurements: basic concepts, theory and applications*. Springer Science & Business Media.

Svetlizky, I., Bayart, E., & Fineberg, J. (2019). Brittle fracture theory describes the onset of frictional motion. *Annual Review of Condensed Matter Physics*, *10*, 253–273.

Svetlizky, I., & Fineberg, J. (2014). Classical shear cracks drive the onset of dry frictional motion. *Nature*, *509*(7499), 205–208.

Takagi, R., Obara, K., & Maeda, T. (2016). Slow slip event within a gap between tremor and locked zones in the Nankai subduction zone. *Geophysical Research Letters*, *43*(3), 1066–1074.

Takagi, R., Uchida, N., & Obara, K. (2019). Along-strike variation and migration of long-term slow slip events in the western Nankai subduction zone, Japan. *Journal of Geophysical Research: Solid Earth*, *124*(4), 3853–3880.

Tal, Y., & Faulkner, D. (2022). The effect of fault roughness and earthquake ruptures on the evolution and scaling of fault damage zones. *Journal of Geophysical Research: Solid Earth*, *127*(1), e2021JB023352.

Tal, Y., Goebel, T., & Avouac, J.-P. (2020). Experimental and modeling study of the effect of fault roughness on dynamic frictional sliding. *Earth and Planetary Science Letters*, *536*, 116133.

Tal, Y., Hager, B. H., & Ampuero, J. P. (2018). The effects of fault roughness on the earthquake nucleation process. *Journal of Geophysical Research: Solid Earth*, *123*(1), 437–456.

Tanguy, A., Gounelle, M., & Roux, S. (1998). From individual to collective pinning: Effect of long-range elastic interactions. *Physical Review E*, *58*(2), 1577.

Thomas, A., Beeler, N. M., Bletery, Q., Burgmann, R., & Shelly, D. R. (2018). Using low-frequency earthquake families on the San Andreas Fault as deep creepmeters. *Journal of Geophysical Research: Solid Earth*, *123*(1), 457–475.

Tse, S. T., & Rice, J. R. (1986). Crustal earthquake instability in relation to the depth variation of frictional slip properties. *Journal of Geophysical Research: Solid Earth*, *91*(B9), 9452–9472.

Tullis, T. E., Richards-Dinger, K., Barall, M., Dieterich, J. H., Field, E. H., Heien, E. M., ... others (2012). Generic earthquake simulator. *Seismological Research Letters*, *83*(6), 959–963.

Uchida, N., & Bürgmann, R. (2019). Repeating earthquakes. *Annual Review of Earth and Planetary Sciences*, *47*, 305–332.

Uchida, N., & Matsuzawa, T. (2013). Pre-and postseismic slow slip surrounding the 2011 Tohoku-oki earthquake rupture. *Earth and Planetary Science Letters*, *374*, 81–91.

Utsu, T., Ogata, Y., & S. Matsu'ura, R. (1995). The centenary of the Omori formula for a decay law of aftershock activity. *Journal of Physics of the Earth*, *43*(1), 1–33.

Vaca, S., Vallée, M., Nocquet, J.-M., Battaglia, J., & Régnier, M. (2018). Recurrent slow slip events as a barrier to the northward rupture propagation of the 2016 pedernales earthquake (central ecuador). *Tectonophysics*, *724*, 80–92.

Villegas-Lanza, J. C., Chlieh, M., Cavalié, O., Tavera, H., Baby, P., Chire-Chira, J., & Nocquet, J.-M. (2016). Active tectonics of peru: Heterogeneous interseismic coupling along the nazca megathrust, rigid motion of the peruvian sliver, and subandean shortening accommodation. *Journal of Geophysical Research: Solid Earth*, *121*(10), 7371–7394.

Wech, A. G., Creager, K. C., Houston, H., & Vidale, J. E. (2010). An earthquake-like magnitude-frequency distribution of slow slip in northern Cascadia. *Geophysical Research Letters*, *37*(L22310).

Wu, B. S., & McLaskey, G. C. (2019). Contained laboratory earthquakes ranging from slow to fast. *Journal of Geophysical Research: Solid Earth*, *124*(10), 10270–10291.

Wynants-Morel, N., Cappa, F., De Barros, L., & Ampuero, J.-P. (2020). Stress perturbation from aseismic slip drives the seismic front during fluid injection in a permeable fault. *Journal of Geophysical Research: Solid Earth*, *125*(7), e2019JB019179.

Xia, J., Gould, H., Klein, W., & Rundle, J. (2005). Simulation of the burridge-knopoff model of earthquakes with variable range stress transfer. *Physical Review Letters*, *95*(24), 248501.

Xu, L., Mohanna, S., Meng, L., Ji, C., Ampuero, J.-P., Yunjun, Z., . . . Liang, C. (2023). The overall-subshear and multi-segment rupture of the 2023 Mw7. 8 Kahramanmaraş, Turkey earthquake in millennia supercycle. *Communications Earth & Environment*, *4*(1), 379.

Xu, S., Fukuyama, E., Yamashita, F., Kawakata, H., Mizoguchi, K., & Takizawa, S. (2023). Fault strength and rupture process controlled by fault surface topography. *Nature Geoscience*, 1–7.

Yamashita, F., Fukuyama, E., Xu, S., Kawakata, H., Mizoguchi, K., & Takizawa, S. (2021). Two end-member earthquake preparations illuminated by foreshock activity on a meter-scale laboratory fault. *Nature Communications*, *12*(1), 1–11.

Yoshino, T. (1998). Influence of crustal viscosity on earthquake energy distribution in a viscoelastic spring-block system. *Geophysical Research Letters*, *25*(19), 3643–3646.

Yuen, H., Princen, J., Illingworth, J., & Kittler, J. (1990). Comparative study of Hough transform methods for circle finding. *Image and Vision Computing*, *8*(1), 71–77.

Zhang, Y., Tang, X., Liu, D., Taymaz, T., Eken, T., Guo, R., . . . Sun, H. (2023). Geometric controls on cascading rupture of the 2023 Kahramanmaraş earthquake doublet. *Nature Geoscience*, 1–7.

Zhou, X., He, Y., & Shou, Y. (2021). Experimental investigation of the effects of

loading rate, contact roughness, and normal stress on the stick-slip behavior of faults. *Tectonophysics*, *816*, 229027.

Zielke, O., Galis, M., & Mai, P. M. (2017). Fault roughness and strength heterogeneity control earthquake size and stress drop. *Geophysical Research Letters*, *44*(2), 777–783.

Weiwei SHU

Analogical modelling of frictional slip on faults: implications for induced and triggered seismicity

Résumé

La rugosité multi-échelle de l'interface d'une faille est à l'origine de multiples aspérités qui établissent un ensemble complexe et discret de contacts réels. Puisque les aspérités contrôlent l'initiation et l'évolution du glissement de la faille, il est important d'explorer les relations intrinsèques entre le comportement collectif des aspérités locales et la stabilité frictionnelle de la faille globale. Nous proposons ici une nouvelle approche expérimentale analogique, qui nous permet de capturer l'évolution temporelle du glissement de chaque aspérité sur une interface de faille. Nous constatons que de nombreux événements déstabilisants à l'échelle de l'aspérité locale se sont produits dans la phase de renforcement du glissement, qui est conventionnellement considérée comme le régime stable d'une faille. Nous calculons le couplage intersismique pour évaluer les comportements de glissement des aspérités pendant la phase de renforcement du glissement. Nous montrons que le couplage intersismique peut être affecté par les interactions élastiques entre les aspérités par l'intermédiaire de la matrice molle encastrée. Les lois d'échelle des événements naturels de glissement lent sont reproduites par notre configuration, en particulier l'échelle moment-durée.

Mots clés : Modélisation analogique, aspérités interfaciales, rhéologie des failles.

Résumé en anglais

The multi-scale roughness of a fault interface is responsible for multiple asperities that establish a complex and discrete set of real contacts. Since asperities control the initiation and evolution of the fault slip, it is important to explore the intrinsic relationships between the collective behavior of local asperities and the frictional stability of the global fault. Here we propose a novel analog experimental approach, which allows us to capture the temporal evolution of the slip of each asperity on a faulting interface. We find that many destabilizing events at the local asperity scale occurred in the slip-strengthening stage which is conventionally considered as the stable regime of a fault. We compute the interseismic coupling to evaluate the slipping behaviors of asperities during the slip-strengthening stage. We evidence that the interseismic coupling can be affected by the elastic interactions between asperities through the embedding soft matrix. Scaling laws of natural slow slip events are reproduced by our setup in particular the moment-duration scaling.

Keywords: Analog modeling, interfacial asperities, fault rheology.

Direction de la **recherche**
et de la **valorisation**
Collège **doctoral**
Université de Strasbourg

RÉSUMÉ ÉTENDU EN FRANÇAIS

Les failles sont des discontinuités géologiques à différentes échelles réparties à différentes profondeurs dans la croûte terrestre (Ben-Zion & Sammis, 2003), qui peuvent glisser avec divers comportements en accommodant à la charge tectonique lente, à grande échelle : du fluage asismique au glissement sismique (Bürgmann, 2018; Rowe & Griffith, 2015; par exemple, Figure 1). Ces divers comportements de glissement d'une faille sont principalement contrôlés par la stabilité du frottement de l'interface de la faille située au milieu d'une zone de faille (Barbot, 2019; Chester & Chester, 1998; Mitchell & Faulkner, 2009; Schulz & Evans, 2000), que l'on peut caractériser par une rhéologie viscoélastique. En particulier les failles situées à une grande profondeur ou dans un environnement à haute température (par exemple, les réservoirs géothermiques), peuvent présenter ce type de comportement. Grâce aux mesures topographiques sur des failles géologiques exhumées, il a été reconnu que la rugosité des interfaces de faille existe à toutes les échelles et crée de nombreuses aspérités discrètes qui établissent un ensemble complexe de contacts (Candela et al., 2012; par exemple, Figure 2). Ces aspérités contrôlent l'initiation et l'évolution du glissement de la faille car elles offrent une résistance supérieure à la contrainte de cisaillement imposée (Selvadurai & Glaser, 2015 ; Selvadurai & Glaser, 2017). L'étude des relations intrinsèques entre le comportement collectif des aspérités locales et la stabilité frictionnelle de la faille macroscopique permet de mieux comprendre l'évolution mécanique d'une faille et le processus physique des sources de tremblements de terre qui en résultent.

Un modèle de faille analogique comprenant de multiples aspérités est développé pour surmonter la difficulté à imager la variabilité spatio-temporelle exhaustive des interfaces de faille naturelle en profondeur et du fait de l'efficacité limitée des modèles numériques lorsque les hétérogénéités s'étendent sur un large domaine temporel et spatial. Plus précisément, de nombreuses billes sphériques rigides identiques en PMMA (poly-méthacrylate de méthyle), utilisées pour modéliser les aspérités de frottement discrètes, sont intégrées avec des variations de hauteur et une distribution spatiale aléatoire dans un bloc de silicone viscoélastique souple afin d'établir de nombreux micro-contacts avec une plaque de PMMA rigide et transparente située sur le dessus (Figure 3). Pendant tout le processus de cisaillement d'une telle interface de faille hétérogène, non seulement le mouvement de chaque aspérité locale peut être directement mesuré par le système de surveillance optique à haute résolution, mais les caractéristiques sismiques émises par les ruptures dynamiques qui se sont produites au niveau des aspérités locales peuvent également être capturées par le système de surveillance acoustique.
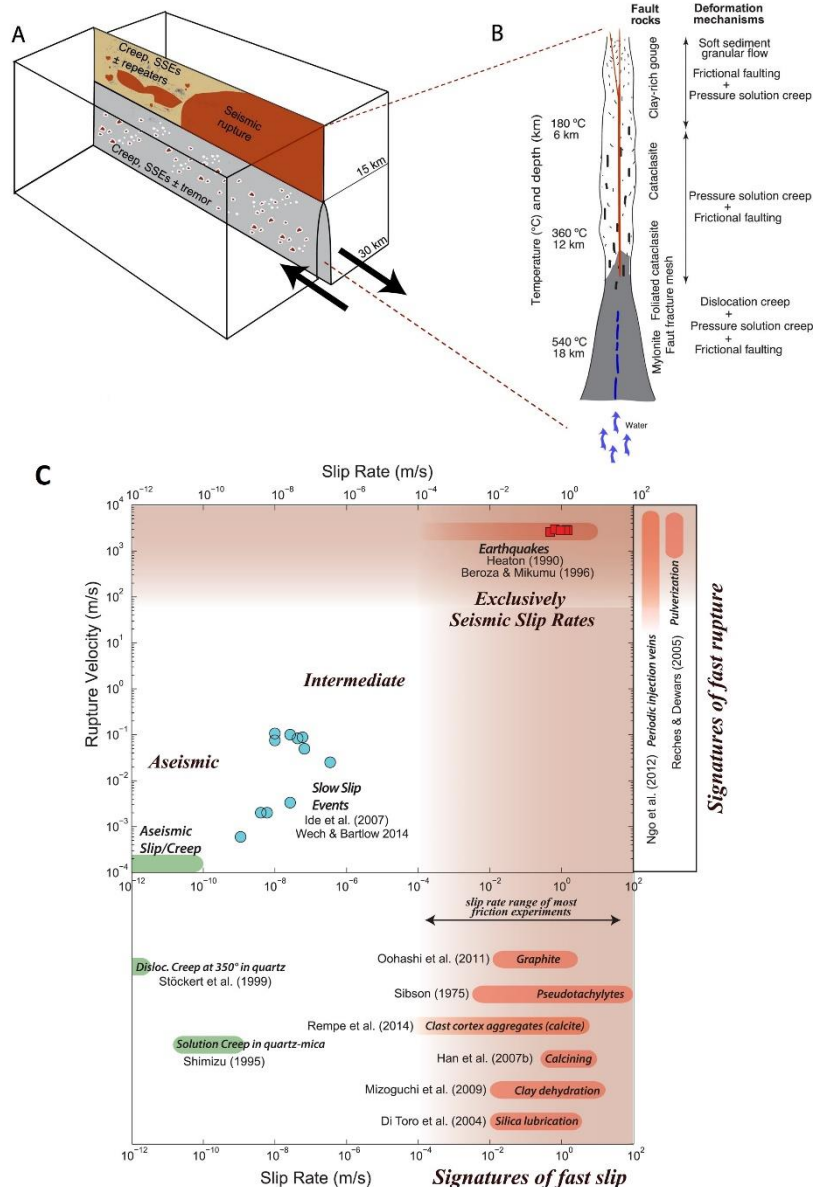
Figure 1. Comportements de glissement et structure géologique d'une faille à glissement typique. **A :** Illustration schématique de la distribution du glissement sismique, du fluage asismique, des séismes répétitifs, des SSE et des tremblements de terre sur la faille partiellement couplée de San Andreas près de Parkfield. **B :** Coupe conceptuelle d'une faille à glissement latéral illustrant la distribution en profondeur de la température, des roches de la zone de faille et des mécanismes de déformation s'accommodant de différents comportements de glissement. Modifié d'après Bürgmann (2018). **C :** Taux de glissement et vitesses de propagation de la rupture pour différents comportements de glissement de la faille. Tiré de Rowe and Griffith (2015).
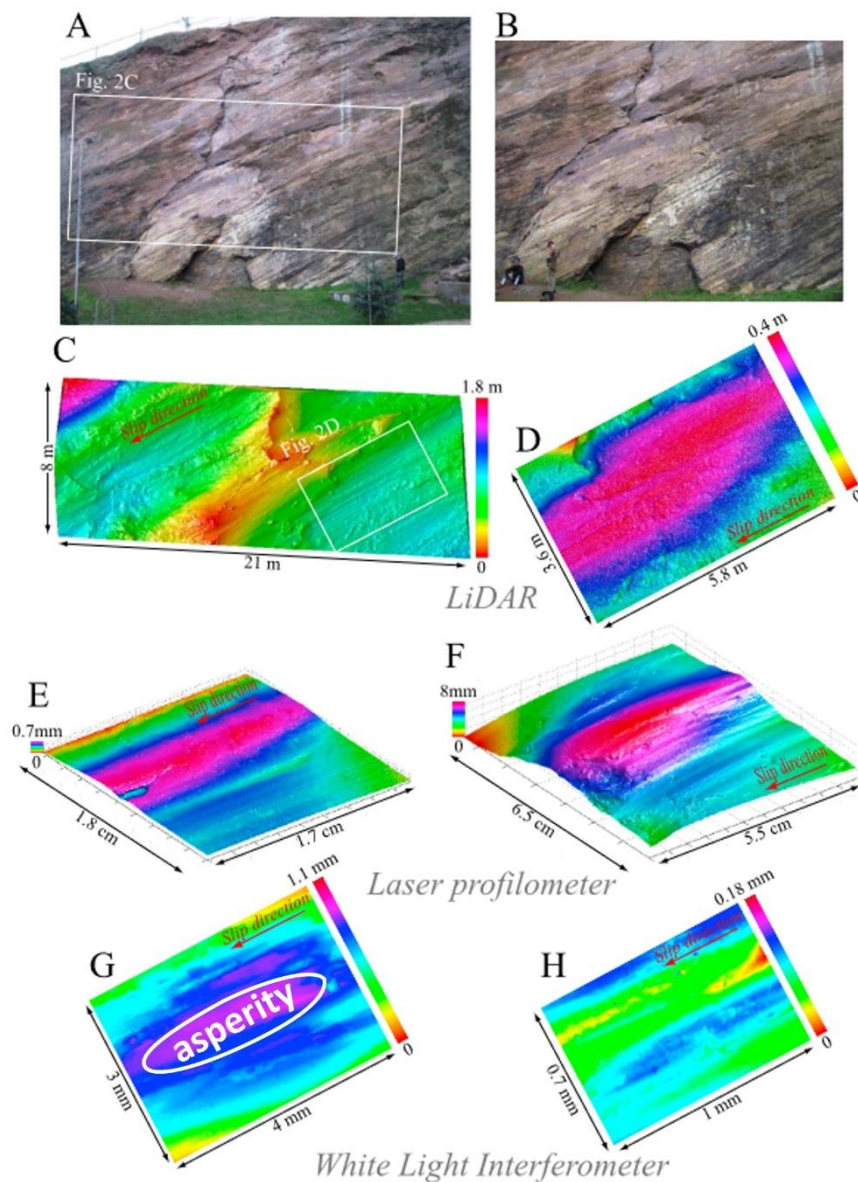
Figure 2. Mesure de la rugosité de la faille exhumée de Corona Heights en Californie, avec des échelles décroissantes et une résolution croissante (du haut vers le bas), les appareils de mesure correspondants étant indiqués sous chaque panneau. La rugosité de la faille existe à toutes les échelles. Une aspérité elliptique à l'échelle millimétrique peut être grossièrement mise en évidence en **G**. Modifié à partir de Candela et al. (2012).
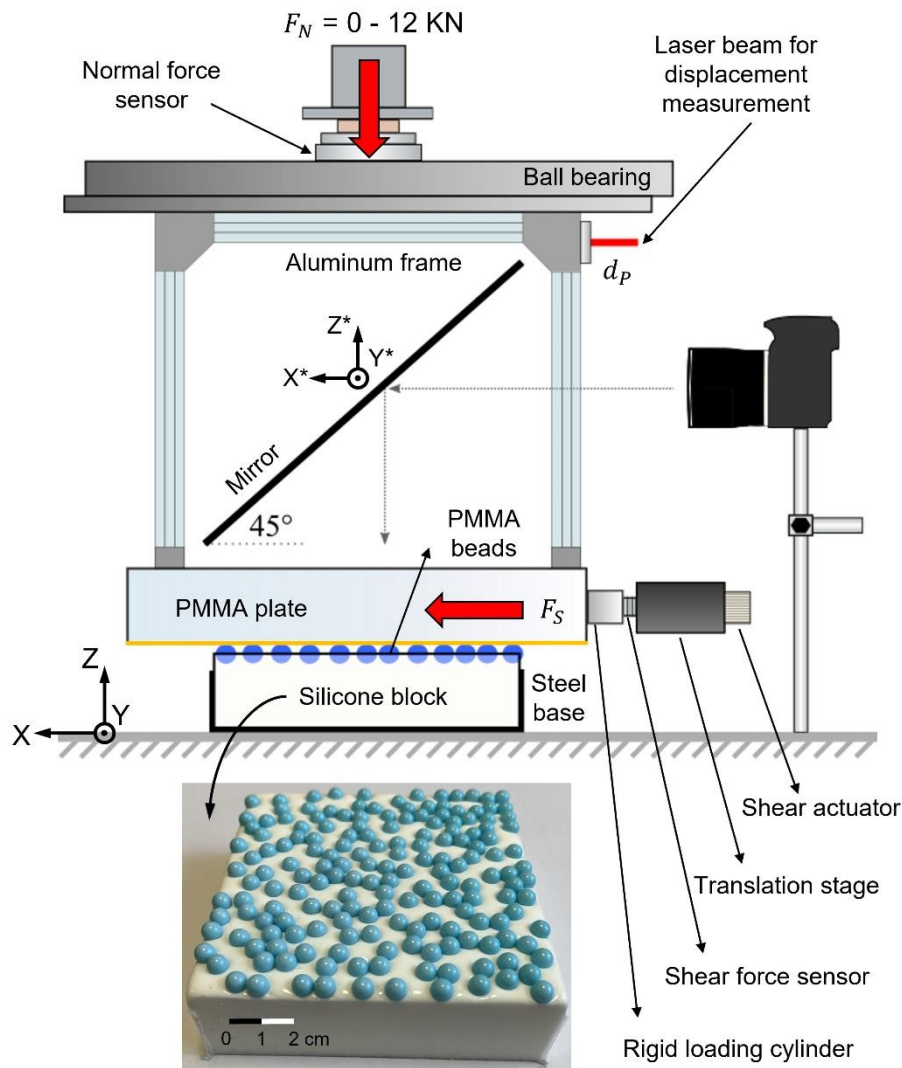
Figure 3. Schéma du dispositif technique expérimental (vue latérale). La force normale, F_N, et la force de cisaillement, F_S, sont mesurées par les capteurs correspondants. Un laser est utilisé pour mesurer le déplacement de la plaque de PMMA, d_P. Une caméra à haute résolution est utilisée avec un miroir pour surveiller les positions des billes de PMMA pendant tout le processus de cisaillement. Deux systèmes d'axes, l'un fixé au sol et l'autre au miroir, sont représentés. La ligne jaune indique un plan de glissement approximatif établi entre la plaque de PMMA et les billes de PMMA. L'encart montre une image des billes de PMMA noyées dans le bloc de silicone souple. Pour la configuration expérimentale technique associée à la surveillance acoustique, quatre accéléromètres identiques sont déployés en les collant verticalement sur la partie supérieure de la plaque épaisse de PMMA. Notez que la carte topographique tridimensionnelle de l'interface de la faille est mesurée à partir d'un profileur microscopique à haute résolution. Tiré de Shu et al. (2023).

En capturant l'évolution temporelle du glissement de chaque aspérité, nous lions la réponse mécanique de la faille macroscopique au comportement collectif des aspérités locales. Plus précisément, nous présentons l'évolution temporelle des glissements cumulés des aspérités individuelles. Pour une meilleure visibilité, seules 20 aspérités, choisies au hasard parmi 144 aspérités, sont présentées dans la Figure 4. Les glissements cumulés des 20 aspérités sont codées en couleur en fonction de leur position initiale. Nous indiquons également dans la Figure 4 le taux de chargement de l'interface qui est ici de 15,0 µm/s. Toute aspérité qui suit cette tendance peut être considérée comme entièrement glissante. Au contraire, une aspérité entièrement collée n'accumulerait aucun glissement relatif par rapport à la plaque de chargement. Son comportement apparaîtrait sous la forme d'une ligne horizontale dans la Figure 4.
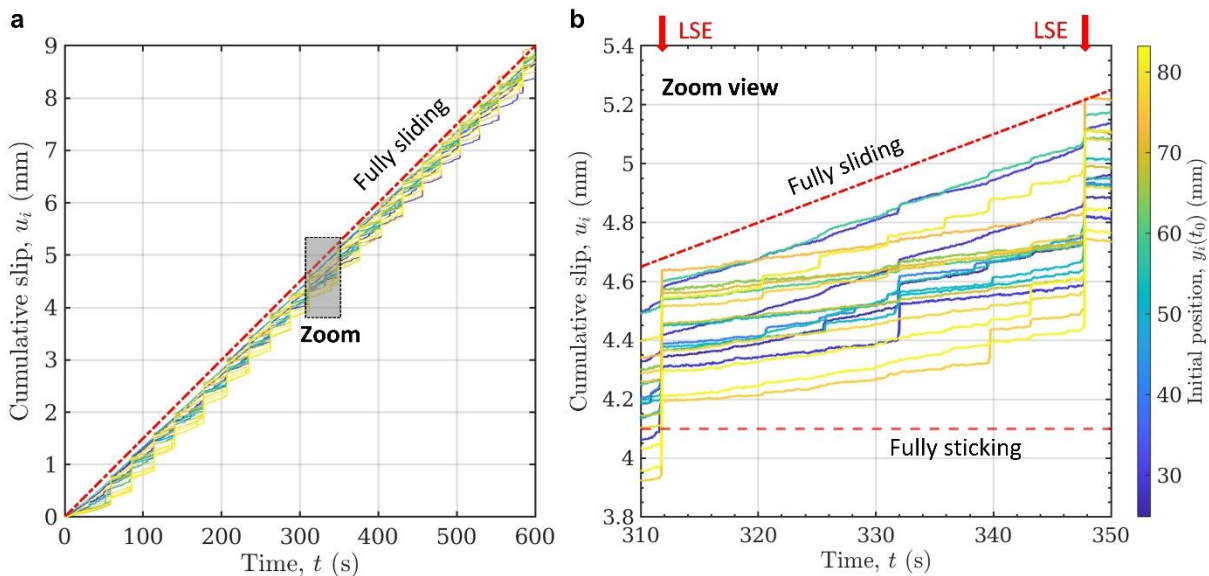
Figure 4. a : Évolution temporelle du glissement cumulé dans la direction x pour 20 aspérités au cours d'une expérience sous une charge normale de 200 N et une vitesse de chargement de 15,0 um/s. Les glissements cumulés des 20 aspérités sont codés en couleur par leurs positions y initiales au temps t0. **b :** Zoom de la Figure 4a montrant les comportements détaillés des aspérités pendant un intervalle de temps entre deux grands événements de collage-glissement (LSE) et allant de 310 s à 350 s. Un collage complet indique un état bloqué tandis qu'un glissement complet donne la pente de la vitesse de déplacement imposée au système. Tiré de Shu et al. (2023).

Direction de la **recherche**
et de la **valorisation**
Collège **doctoral**
Université de Strasbourg

L'évolution du glissement cumulatif des aspérités dans la figure 4 illustre les événements répétitifs de glissement de l'interface (20 événements dans la figure 4a et un zoom sur l'un d'entre eux dans la figure 4b). Ces événements impliquent toutes les aspérités de l'interface. Dans l'intervalle de temps entre ces épisodes de collage et de glissement, pendant la phase de collage, les aspérités présentent des comportements distincts. Nous observons que tous les taux de glissement sont inférieurs au taux de chargement imposé (voir les pentes du glissement cumulé des aspérités et de la plaque de PMMA) mais avec une tendance non horizontale, ce qui indique qu'en fait, les aspérités glissent à un faible taux pendant la phase de collage, au lieu d'être complètement bloquées.

Il convient de noter que les glissements accumulés au cours de chaque période de collage ne sont pas les mêmes pour les différentes aspérités. Cela prouve que les différentes aspérités peuvent glisser à des vitesses différentes, bien qu'elles soient toutes dans le régime quasi-statique (c'est-à-dire la phase de collage du comportement de collage-glissage de l'interface). Une autre découverte intéressante est qu'il y a également quelques petits glissements visibles qui se sont produits sur différentes aspérités uniques pendant la phase de collage globale et qui correspondent à de petits événements de stick-slip à l'échelle de plusieurs aspérités. Ces petits épisodes contrastent avec les épisodes de glissement global, lorsque toutes les aspérités locales glissent rapidement de manière synchrone et que nous définissons comme un grand événement de stick-slip (LSE). De plus, l'observation que les glissements sur toutes les aspérités après un LSE n'atteignent pas le glissement de charge imposé, indique que le stress accumulé n'est que partiellement libéré pendant un tel événement à l'échelle globale.

En résumé, la synchronisation des glissements locaux de toutes les aspérités est responsable du glissement instable de la faille macroscopique. De nombreux événements déstabilisants à l'échelle des aspérités locales sont observés alors que la contrainte sur imposée au système continue d'augmenter et ce que régime est conventionnellement considérée comme le régime stable d'une faille. Le comportement de glissement des aspérités pendant cette phase est évalué par le biais du couplage intersismique (Figure 5), qui peut être affecté par la charge normale nominale, la topographie locale de l'interface de la faille et les interactions élastiques entre les aspérités par l'intermédiaire du bloc de silicone encastré.
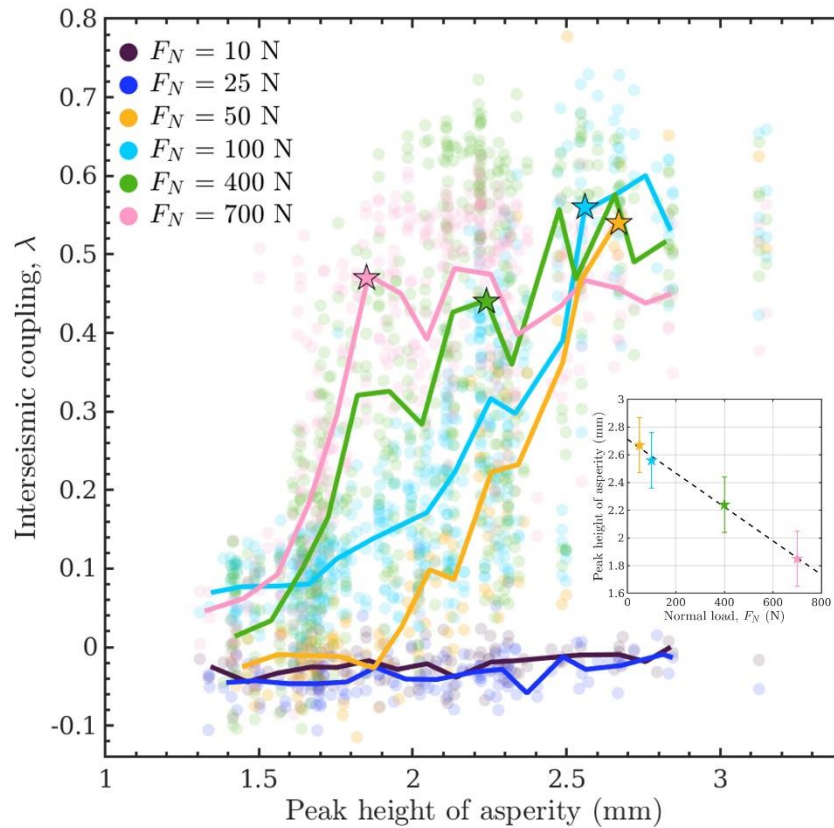
Figure 5. Évolution du couplage intersismique à différentes hauteurs de crête de l'aspérité sous des charges normales multiples. Les cercles avec une couleur remplie sont l'ensemble des données calculées pour toutes les expériences sous la charge normale correspondante. Chaque courbe est obtenue en calculant la moyenne du couplage intersismique sur la hauteur maximale de l'aspérité avec une largeur d'intervalle de 0,10 mm. L'encadré montre la hauteur maximale de l'aspérité lors des transitions entre un couplage élevé et un couplage faible (étoiles) en fonction de la charge normale, où la hauteur maximale de l'aspérité diminue avec l'augmentation de la charge normale. Tiré de Shu et al. (2023).

Les interactions spatio-temporelles des aspérités sont quantifiées en tant qu'épisodes de glissement. L'analyse statistique du catalogue des épisodes de glissement reproduit les caractéristiques significatives et les lois d'échelle observées dans les failles naturelles, telles que la distribution magnitude-fréquence (Figure 6), l'échelle moment-durée (Figure 7) et la loi d'Omori (Figure 8), démontrant l'efficacité de la mise à l'échelle des résultats expérimentaux. La transition d'un état stable à instable macroscopique des aspérités dans ce système à charge lente est illustré quantitativement par l'évolution des énergies élastiques. Une persistance inattendue de la désorganisation des aspérités à travers les cycles sismiques est mise en évidence malgré l'effet de relaxation des grands événements de glissement.
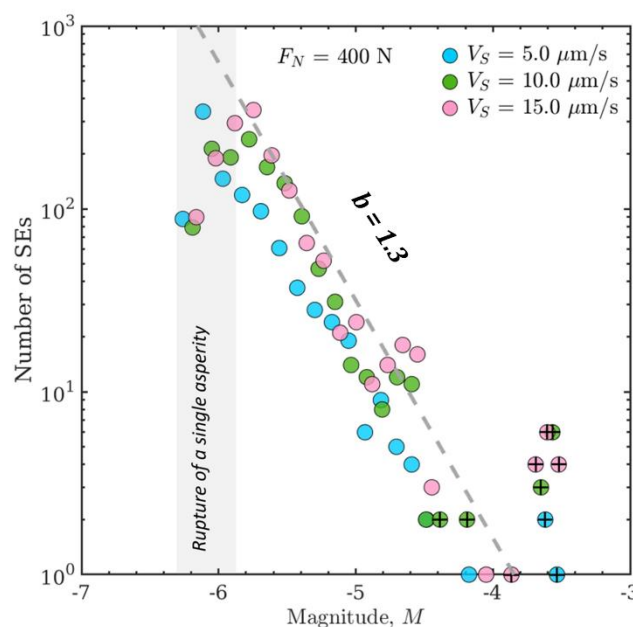
Figure 6. Distributions des fréquences de magnitude à différents taux de chargement sous la même charge normale de 400 N. Les symboles circulaires marqués par des croix indiquent les grands événements de stick-slip à l'échelle de la faille globale, qui sont exclus du calcul de la valeur b puisqu'ils atteignent les limites du modèle et sont par conséquent limités en taille. La ligne pointillée grise indique une ligne de référence avec une valeur b de 1,3. L'ombre représente la gamme des magnitudes correspondant aux ruptures d'une seule aspérité, avec une valeur moyenne de M = -6,09. Tiré de Shu et al. (2023).

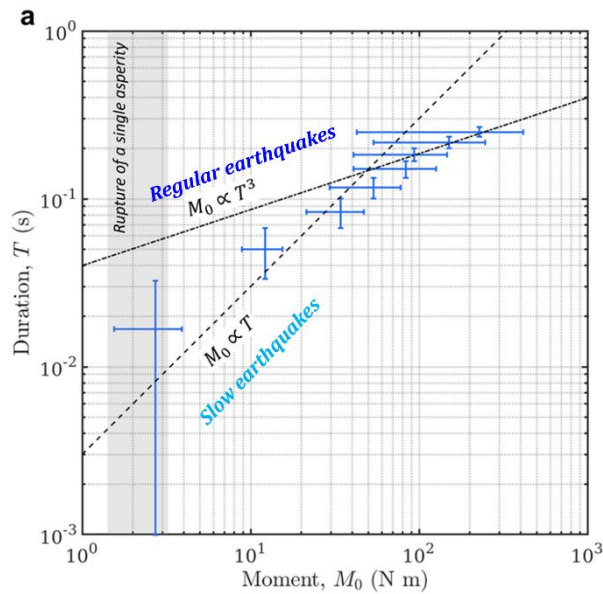**Figure 7.** Relation d'échelle moment-durée moyenne obtenue en utilisant des SE petites et modérées de toutes les expériences, car les grands événements de glissement atteignant le bord de l'échantillon ont été exclus en utilisant un seuil de zone de glissement de $2.8 \times 10^3\ mm^2$. L'ombre indique les moments correspondant aux ruptures d'une seule aspérité, avec une plage de $M_0 = 2.32 \pm 0.91$ N m. Tiré de Shu et al. (2023).
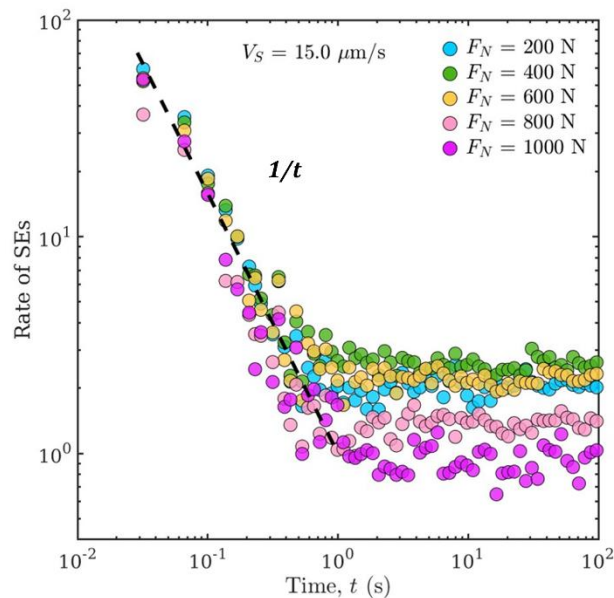

Figure 8. Décroissance temporelle des SE définie dans des expériences multiples sous différentes charges normales et le même taux de charge de 15 μm/s. Le taux de SE diminue d'abord rapidement avec $1/t$ pendant environ 1 s, puis se stabilise à une valeur de fond d'environ 1 ou 2 SE(s) par seconde. Modifié à partir deTiré de Shu et al. (2023).

Direction de la **recherche**
et de la **valorisation**
Collège **doctoral**
Université de Strasbourg

En outre, une telle interface de défaut multi-contact avec des variations de contrainte normale au niveau des aspérités et une rhéologie viscoélastique globale peut être modélisée numériquement sur la base du modèle bidimensionnel modifié de type Burridge-Knopoff, où les interactions viscoélastiques des aspérités sont quantifiées à partir des propriétés physiques de notre dispositif expérimental et où le frottement de chaque aspérité est régi par la loi de frottement du type rate-and-state (Figure 9). Les paramètres de vitesse et d'état d'une interface à aspérité unique, mesurés à partir d'expériences de glissement, sont introduits dans le modèle numérique. Ce modèle numérique basé sur la physique est efficace en termes de calcul et permet une compréhension complémentaire des effets de certains paramètres de la faille (par exemple, la viscosité du bloc de silicone, la distribution spatiale des aspérités, etc).
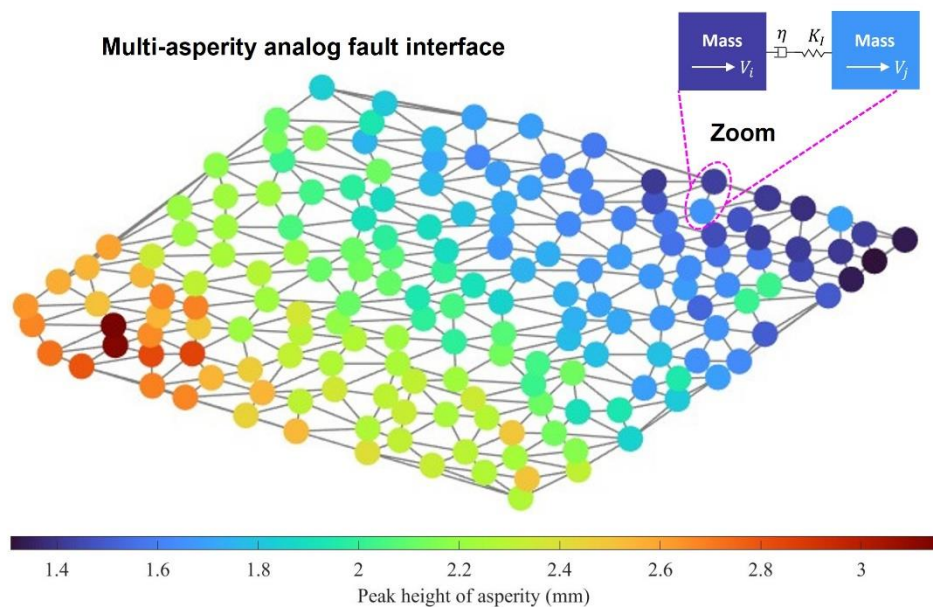

Figure 9. Schéma du modèle numérique bidimensionnel avec le même nombre et les mêmes positions des aspérités que l'interface de la faille analogique. Grâce à la triangulation de Delaunay, les connexions spatiales entre les aspérités sont déterminées et représentées par des lignes grises indiquant les interactions viscoélastiques entre les aspérités. Le zoom montre qu'une telle interaction viscoélastique entre deux aspérités est quantitativement décrite par le ressort de Maxwell avec l'élasticité et la viscosité. Il convient de noter que l'hétérogénéité de la contrainte normale induite par les différentes hauteurs de crête des aspérités n'a pas été prise en compte dans ce modèle préliminaire. La même contrainte normale sur chaque aspérité est supposée dans le modèle actuel. Les autres hypothèses sont les mêmes que celles du modèle de bloc-ressort établi.

Nos résultats démontrent que les séquences de tremblements de terre sont des manifestations phénoménologiques des divers comportements de glissement d'une faille macroscopique contrôlée par le comportement collectif des aspérités locales. Les événements de glissement lent regroupés à partir des interactions spatio-temporelles des aspérités sont générés dans notre dispositif expérimental frictionnel-visqueux sans la présence de fluide, ce qui confirme que la rhéologie viscoélastique de la zone de faille complexe pourrait être un candidat efficace pour expliquer le mécanisme physique des tremblements de terre lents observés dans le monde entier. L'intermittence du glissement de ces événements lents est également mise en évidence dans nos expériences. Cette intermittence du glissement est cohérente avec les observations selon lesquelles un événement de glissement lent à long terme peut être décomposé en plusieurs événements de glissement lent à court terme, chacun agissant pendant une durée limitée. En outre, nous avons observé l'initiation et l'arrêt des épisodes de glissement confinés qui ont lieu pendant la phase de renforcement du glissement. Cette phase de renforcement du glissement avec de multiples ruptures confinées de petite taille peut être considérée comme la phase préparatoire d'une rupture géante qui se produit dans une faille naturelle. En outre, nous montrons que le couplage intersismique sur l'interface analogique est similaire à celui observé le long des zones de subduction, où le couplage évolue en fonction de la contrainte normale et de la variation topographique. Toutes les distributions de magnitude-fréquence reproduites suivent une distribution typique de Gutenberg-Richter où des événements de tailles multiples sont observés. Notre mise à l'échelle moment-durée indique une tendance la mieux résolue proche de $M_0 \propto T$ qui est en accord avec les observations de tremblements de terre lents utilisant des catalogues de plusieurs zones de subduction. Une décroissance temporelle similaire de nos événements lents est également mise en évidence lors de l'analyse des séismes de basse fréquence (LFE) qui se sont produits dans plusieurs failles naturelles, étant donné que les LFE sont principalement considérés comme de petites ruptures de cisaillement confinées sur des aspérités localisées.

Les travaux futurs se concentreront sur les relations entre les autres caractéristiques d'un tel groupe d'aspérités (par exemple, des aspérités de tailles différentes ou des propriétés de frottement différentes sur la même interface) et le développement de la sismicité, ainsi que sur le transfert de contraintes et le déclenchement du glissement entre des aspérités discrètes, afin de mieux comprendre le lien entre la sismicité et le glissement asismique des aspérités.

Bibliographie

Barbot, S. (2019). Modulation of fault strength during the seismic cycle by grain-size evolution around contact junctions. *Tectonophysics*, *765*, 129-145.

Ben-Zion, Y., & Sammis, C. G. (2003). Characterization of fault zones. *Pure and Applied Geophysics*, *160*, 677-715.

Bürgmann, R. (2018). The geophysics, geology and mechanics of slow fault slip. *Earth and Planetary Science Letters*, *495*, 112-134.

Candela, T., Renard, F., Klinger, Y., Mair, K., Schmittbuhl, J., & Brodsky, E. E. (2012). Roughness of fault surfaces over nine decades of length scales. *Journal of Geophysical Research: Solid Earth*, *117*(B8).

Chester, F. M., & Chester, J. S. (1998). Ultracataclasite structure and friction processes of the Punchbowl fault, San Andreas system, California. *Tectonophysics*, *295*(1-2), 199-221.

Mitchell, T. M., & Faulkner, D. R. (2009). The nature and origin of off-fault damage surrounding strike-slip fault zones with a wide range of displacements: A field study from the Atacama fault system, northern Chile. *Journal of Structural Geology*, *31*(8), 802-816.

Selvadurai, P. A., & Glaser, S. D. (2015). Laboratory-developed contact models controlling instability on frictional faults. *Journal of Geophysical Research: Solid Earth*, *120*(6), 4208-4236.

Selvadurai, P. A., & Glaser, S. D. (2017). Asperity generation and its relationship to seismicity on a planar fault: A laboratory simulation. *Geophysical Journal International*, *208*(2), 1009-1025.

Shu, W., Lengliné, O., & Schmittbuhl, J. (2023). Collective Behavior of Asperities Before Large Stick-Slip Events. *Journal of Geophysical Research: Solid Earth*, *128*(9), e2023JB026696.

Rowe, C. D., & Griffith, W. A. (2015). Do faults preserve a record of seismic slip: A second opinion. *Journal of Structural Geology*, *78*, 1-26.

Schulz, S. E., & Evans, J. P. (2000). Mesoscopic structure of the Punchbowl Fault, Southern California and the geologic and geophysical structure of active strike-slip faults. *Journal of Structural Geology*, *22*(7), 913-930.